UNIVERSITY OF SOUTHAMPTON

School of Civil Engineering and the Environment

The Behaviour of Soil behind Full-height Integral Abutments

by

Ming Xu

A Thesis Submitted in Fulfillment of the Degree of Doctor of Philosophy
in the School of Civil Engineering and the Environment of the
University of Southampton

April 2005

UNIVERSITY OF SOUTHAMPTON

ABSTRACT

SCHOOL OF CIVIL ENGINEERING AND THE ENVIRONMENT

Doctor of Philosophy

THE BEHAVIOUR OF SOIL BEHIND FULL-HEIGHT INTEGRAL ABUTMENTS

by Ming Xu

Compared with conventional bridges, integral bridges have no bearings or joints between the decks and abutments, thus they can significantly reduce maintenance requirements and costs over the bridge life-time. The use of integral bridges has been encouraged over the past decade in the UK. However, because of the integral connection between the superstructure and the abutments, the integral abutments are forced to move with the deck length change caused by daily and annual variations in the effective bridge temperature. As a consequence, the soil behind the abutment is subjected to temperature-induced cyclic loading from the abutment, and uncertainties have arisen about the ultimate magnitude of the lateral earth pressure behind integral abutments.

To predict the lateral earth pressure behind integral abutments, a thorough understanding of the soil behaviour is essential. This research investigated the behaviour of a representative soil element at mid retained height under temperature-induced cyclic loading behind two typical types of full-height integral abutments. One is an embedded abutment constructed in *in situ* stiff clayey ground, and the other is a frame abutment backfilled with granular material. An automated triaxial cyclic loading system has been developed. Undisturbed Atherfield I Clay, Leighton Buzzard B sand and glass ballotini specimens have been subjected to the stress paths and levels of cyclic straining that a typical integral bridge abutment might impose on its retained soil. The results show that for stiff clay no lateral stress increase was observed, and the stress-strain behaviour and stiffness behaviour were not influenced by cycling. However, the coarse sand specimens experienced systematic increases in lateral stress for almost all cyclic strain levels, eventually reaching states of stress close to both active and passive. The underlying mechanisms of stress increase are explored, and it is concluded that particle shape is an important factor in determining the response of soil to this special type of loading. The implications for integral abutment design have been discussed.

Contents

List of Figures

List of Tables

List of Symbols

B	pore water pressure coefficient
c_u	undrained shear strength
c'	effective cohesion
Dr	relative density
E_{uh}	undrained secant horizontal Young's modulus
E_{uv}	undrained secant vertical Young's modulus
E_{tuh}	undrained tangent horizontal Young's modulus
E'_h	drained secant horizontal Young's modulus
E'_{th}	drained tangent horizontal Young's modulus
e	void ratio
Gs	specific gravity
K	coefficient of earth pressure ($K= \sigma'_r /\sigma'_v$)
K_0	coefficient of earth pressure at rest
K_a	coefficient of active earth pressure
K_p	coefficient of passive earth pressure
p'	mean effective stress(Cambridge system) ($p'_o =(\sigma'_v+2\sigma'_r)/3$)
p'_o	mean effective stress(Cambridge system) at the start of a stress excursion
p	mean total stress(Cambridge system) ($p_o =(\sigma_v+2\sigma_r)/3$)
q	deviator stress ($q=\sigma_v-\sigma_r=\sigma'_v-\sigma'_r$)
s	mean total stress (MIT system) ($s=(\sigma_v+\sigma_r)/2$)
s'	mean effective stress (MIT system) ($s'=(\sigma'_v+\sigma'_r)/2$)
t	shear stress $t=(\sigma_v-\sigma_r)/2=(\sigma'_v-\sigma'_r)/2$
u	pore water pressure
Δq	change of deviator stress from the start of stress excursion
$\Delta\varepsilon_a$	change of axial strain from the start of stress excursion
γ_d	dry density of sand
ε_a	axial strain
ε_r	radial strain
ε_{vol}	volumetric strain
v	undrained Poisson's ratio

v'	effective Poisson's ratio
σ_a	axial total stress
σ_v	vertical total stress
σ_r	radial total stress
σ'_a	axial effective stress
σ'_v	vertical effective stress
σ'_r	radial effective stress
σ_c	cell pressure
φ_μ	interparticle friction angle
φ'	effective friction angle

Acknowledgement

First of all, I would like to express my sincere thanks to my supervisors Dr Alan Bloodworth and Professor Chris Clayton for their direction, encouragement and assistance throughout the period of this work. I am especially grateful to Prof. Chris Clayton for his tireless guidance, support and enthusiasm.

I would also like to express my gratitude to Prof. Marcus Lee for his continuous encouragement and help, Prof. William Powrie for his assistance and advice.

Special thanks go to Dr David Richards and Miss Jo Clark for providing high quality undisturbed Atherfield I Clay samples, as well as lots of assistance and suggestions.

I would like to thank Harvey Skinner for all his help in the lab, Ken, Dave and Earl for their expertise in making all the special devices.

Many thanks are due to all my friends in the department for their contribution in numerous ways and particularly to Geoff, Antonios, Jeff, Martin, Michelle and Joel.

Finally, I would like to thank my parents and my sister for their immense and endless support and encouragement during my whole studies.

Chapter 1 Introduction

In this chapter, the background of this research will be introduced first. Comparison will be made between conventional bridges and integral bridges, while the problems with integral bridges will also be discussed. Then the objectives and methodology of this research will be introduced.

1.1 Background

1.1.1 Conventional bridges

Traditionally, a road bridge consists of some type of superstructure resting on an abutment at each end. Because of daily and seasonal temperature variation, the bridge superstructure tends to change dimension in its longitudinal direction. However, the supporting abutments are relatively insensitive to changes in air temperature and remain spatially fixed. To accommodate the relative movement and prevent temperature-induced stresses from developing between superstructure and abutments, expansion joints and bearings are installed between the superstructure and the abutments in conventional bridges (Figure 1.1a).

However, over the past thirty years, engineers have become increasingly aware of the disadvantages associated with the use of expansion joints and bearings. In the UK, a survey of a random sample of 200 concrete bridges (Wallbank, 1989) has confirmed that the most serious source of damage is de-icing salts leaking through or penetrating deck joints on to sub-structure components. This process causes corrosion and immobilization of movement joints and bearings located at abutments and between spans and represents a major element of conventional road bridge repair and maintenance costs.

Furthermore, joints and bearings, which have a relatively short life, are expensive to purchase, install, maintain, repair or replace (Biddle *et al.*, 1997). Replacement of bearings will inevitably cause disturbance to traffic. Along with de-icing chemicals, other debris can enter the space in a joint reserved for bridge expansion, and accumulate. The joint debris will prevent free movement of the superstructure, which may cause stresses to build up and cause damage to weaker bridge components.

1.1.2 Integral bridges

Because of the problems with conventional bridges with joints and bearings, the concept was developed to physically and structurally connect the superstructure and abutments to create what is referred to as an integral bridge (Figure 1.1b).

For integral bridges, all of the problems associated with joints and bearings, as discussed above, are avoided. An integral bridge eliminates the cost of the provision of movement joints and bearings at the ends of a bridge. More importantly, it brings the major benefits of reduced maintenance costs over the bridge life-time by eliminating the risk of damage arising from leaky joints (Biddle *et al.*, 1997).

Furthermore, without the installation of joints and bearings, which is time-consuming, faster construction may be achieved. Integral bridges are also believed to have better resistance to earthquake or high dynamic forces (Card & Carder, 1993).

Because of these advantages over conventional bridges, integral bridges have been widely adopted in the USA (Nicholson, 1997). In the UK, integral bridges have been encouraged in the past decade, especially by the publication of BD 57/95 *Design for Durability* (Highway Agency, 1995), in which it is specified that:

- "in principle bridges with lengths not exceeding 60m and skews not exceeding 30° shall in addition be designed as integral bridges, with abutments connected directly to the bridge deck without movement joints for expansion or contraction of the deck."
- and "continuous structures have proved to be more durable than structures with simply supported decks, primarily because deck joints have allowed salty water to leak through to piers and abutments. In principle all bridges shall therefore be designed as continuous over intermediate supports unless special circumstances exist."

1.1.3 Problems with integral bridges

The concept of an integral bridge has proved to be economical in initial construction and successful in reducing the maintenance costs by eliminating expansion joints and bearings. However, it is not problem free, as the integral bridge concept does nothing to alter the tendency of a bridge superstructure to undergo length changes caused by daily and annual temperature variation.

Because of the integral connection between the superstructure and the abutments, the abutments are forced to move away from the soil they retain when the temperature

decreases and the deck contracts (*e.g.* in the winter), and towards the soil when the temperature rises and the deck expands (*e.g.* in the summer). As a consequence, the soil behind the abutment is subjected to temperature-induced cyclic loading from the abutment.

Field monitoring on different types of integral abutments has revealed that the lateral earth pressures behind the abutments increase from winter to summer every year. In some extreme cases, in which shallow abutments were located at the end of a long bridge (*e.g.* Borms & Ingleson, 1971), the peak earth pressures even approached the passive state. For medium span integral bridges with a deck length of 30m to 60m, there may be a build-up of peak lateral earth pressures with repeated temperature cycles, as observed by Darley et al. (1998) (Figure 1.2). Many engineers are concerned that the peak lateral earth pressures may become far larger than the design values and eventually lead to an abutment failure in the future (Card & Carder, 1993). With the possibility of increasing pressures, the ultimate magnitude of the peak earth pressures has become a major uncertainty both for existing integral bridges and for integral abutment design.

To predict the lateral earth pressure behind an integral abutment, it is important to understand the stress-strain behaviour of soil under such a temperature-induced cyclic loading. However, only limited experimental research has been carried out previously on the behaviour of granular materials behind integral abutments (*e.g.* Springman *et al.*, 1996, England *et al.*, 2000, Goh, 2001, Cosgrove & Lehane, 2003 and Tapper & Lehane, 2004), which still remains largely unknown. It may be many years, *e.g.* decades, before field monitoring can provide an explicit conclusion to this particular problem since it involves very slow cyclic loading. Without the identification of the stress-strain behaviour of soil, numerical modelling cannot be justified and the results become doubtful. The advice from the current design standard, BA42 *The design of integral bridges*, which is based on the previous research, is generally thought to be unsatisfactory and to need a further update (Biddle *et al.*, 1997). Furthermore, no investigation has been performed on clay, which is a typical ground condition in the UK and more likely to be present behind an embedded abutment than granular materials.

1.2 Objectives

This research aims to investigate the stress-strain behaviour of soil under temperature-induced cyclic loading behind two typical types of full-height reinforced concrete integral abutments. One is an embedded abutment constructed in *in situ* stiff clayey ground, and the other is a frame abutment backfilled by granular material (Figure 1.3), both of which are widespread in the UK. A typical retained height of 8m is assumed. Since the deck length recommended by the Highway Agency for using integral bridges is up to 60m, the deck length to be studied in this research ranges from 30m to 90m.

The objective was pursued mainly by an extensive geotechnical laboratory stress path testing programme on a representative soil element, which was located at the mid retained height behind the abutments. The stress path direction experienced by the representative soil element was estimated and the cyclic horizontal strain range was predicted. An automated triaxial cyclic loading system was then developed, which was capable of carrying out long-term radial strain-controlled cyclic stress path testing on 100mm diameter specimens, with local small strain measurement. High quality undisturbed Atherfield I Clay specimens were tested, representing heavily overconsolidated stiff clay. A coarse sand, Leighton Buzzard B siliceous sand, and glass ballotini was investigated to study the behaviour of granular materials.

1.3 Organization of this thesis

Chapter 1 gives the background of integral bridges and the problems. It introduces the topic of the research and outlines the objectives and methodology.

Chapter 2 contains a comprehensive literature review on the influence of temperature on integral bridges, previous research on integral abutments and the current design standard in the UK. The development of the technique of geotechnical laboratory stress path testing, is also reviewed.

Chapter 3 describes the estimation of the stress path and the cyclic horizontal strain range experienced by the representative soil element behind an integral abutment.

Chapter 4 describes the development of an automated triaxial cyclic loading system for this project. System equipment, measuring instruments, calibration procedure and control software are introduced.

Chapter 5 outlines the testing programme on a stiff clay, Atherfield I Clay. The test results are presented and discussed.

Chapter 6 presents the testing programme on granular materials, including coarse sand (Leighton Buzzard B siliceous sand) and glass ballotini. The test results are presented and discussed.

Chapter 7 contains a comparison of test results for stiff clay and granular materials. Possible reasons are discussed. Then the findings of this research are compared with those of previous research on the behaviour of soil behind integral abutments. Implications for integral abutment design are also discussed.

Chapter 8 contains the conclusions from this research and recommendations for future research.

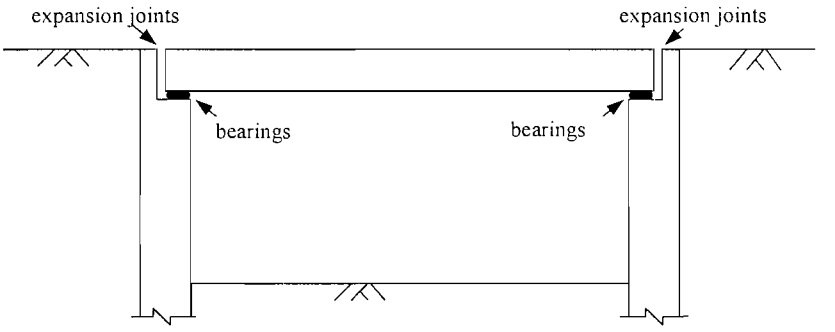

(a) Conventional bridge

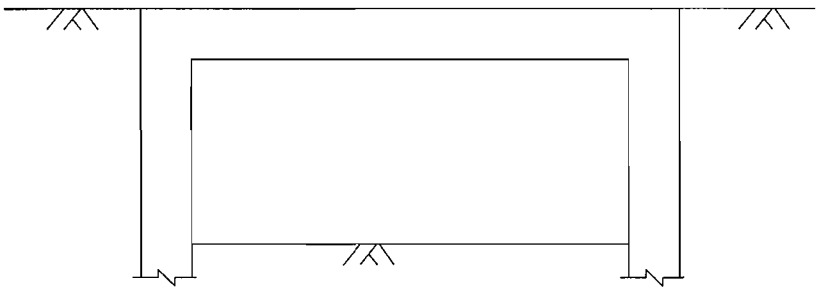

(b) Integral bridge

Figure 1.1 Comparison of conventional bridge and integral bridge

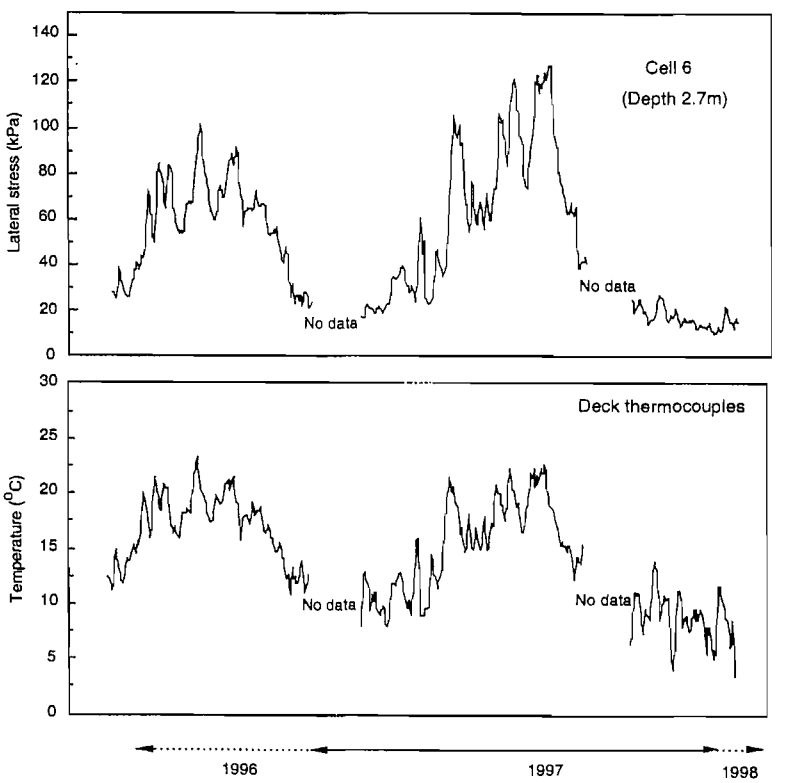

Figure 1.2 The measured lateral earth pressure at 2.7m depth behind an integral abutment (Darley *et al.*, 1998)

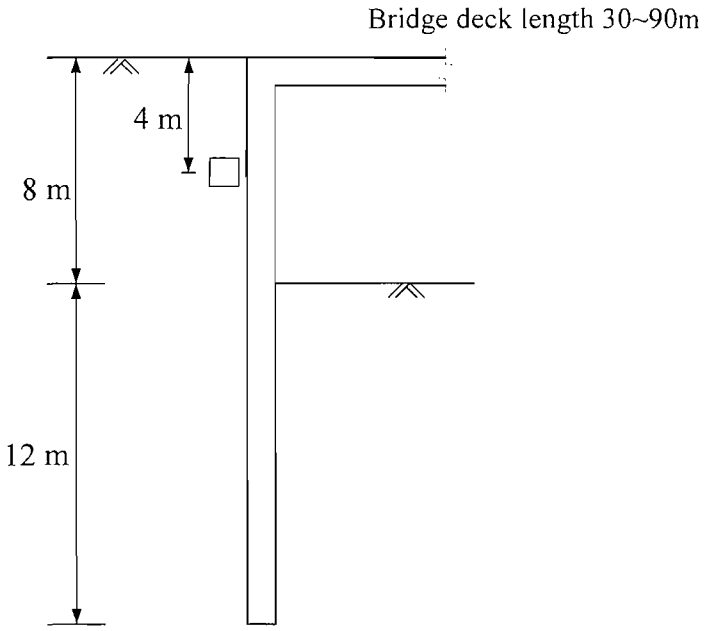

(a) Embedded integral abutment constructed in clayey ground

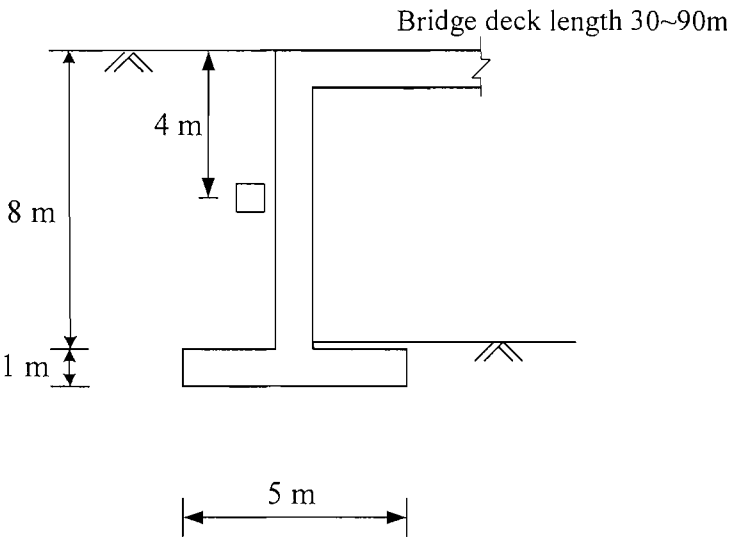

(b) Frame integral abutment backfilled by granular material

Figure 1.3 Typical full-height reinforced concrete integral abutments with a retained height of 8m and a wall thickness of 1m, with the representative soil element located at the mid retained height behind the abutment.

Chapter 2 Literature Review

2.1 Introduction

In this chapter, the literature related to integral abutments is reviewed first, including the temperature influence on a bridge deck, previous research on integral abutments and the current design standard. The major findings and the weakness of previous investigations are highlighted. It is concluded that the behaviour of soil behind integral abutments still remains unclear, and more research is needed.

In the second half of the chapter, geotechnical laboratory stress path testing is identified as a promising method to investigate the fundamental behaviour of soil behind an integral abutment. The stress path testing technique is investigated, highlighting the recent development of the technique and its contribution to the improvement of our understanding about the stress-strain behaviour of soil.

2.2 Temperature influence on a bridge deck

A bridge deck changes in length with temperature variation. The temperature of a bridge is mainly influenced by shade air temperature, solar radiation and wind speed (Emerson, 1973). Different bridge materials (*e.g.* concrete, composite or steel) have different thermal properties and will respond differently to environmental change. For example, a steel deck has a much higher thermal conductivity and responds much more quickly to shade air temperature variation than a concrete deck. In addition, the temperature is not generally uniform throughout the bridge superstructure. For these reasons, longitudinal deck movements are difficult to predict directly from shade air temperature.

Effective Bridge Temperature (EBT) is defined as an average temperature within the superstructure which governs the longitudinal movement of the deck, and has been investigated extensively by Emerson (1973, 1976). The measurement of effective bridge temperature requires extensive instrumentation and a long monitoring period. In contrast, shade air temperature is relatively easy to measure, and historic data has been recorded. The relationship between EBT and shade air temperature in the UK was investigated by

Emerson (1976), who monitored the range of temperatures experienced by various instrumented bridge decks in the UK for seven years.

Based on the research by Emerson (1976), it is suggested in BD37 *Loads for Highway Bridges* (Highway Agency, 2001) that for design purposes, minimum and maximum effective bridge temperatures in the UK for different types of superstructure can be derived from the isotherms of minimum and maximum shade air temperature, by taking account of the type of construction (*e.g.* concrete, composite or steel).

For an integral bridge with a reinforced concrete deck constructed in the London area, the annual EBT range can be approximated as 43°C, following the approach of BD37. For different deck lengths, the annual deck length change and abutment top horizontal displacement can be estimated in Table 2.1, assuming an equal movement at both ends of the deck and $\alpha = 12\times10^{-6}/^{o}C$, which is the coefficient of thermal expansion of concrete.

Table 2.1 Annual concrete deck length change and abutment top horizontal displacement

Concrete Deck length (m)	Annual total deck length change (mm)	Annual total abutment top horizontal displacement d(mm)	$\pm d/2$ (mm)
90	48	24	±12
60	32	16	±8
30	16	8	±4

2.3 Previous research on integral abutments

Relatively little research has been performed on the interaction between soil and integral abutments. Consequently, the behaviour of soil behind integral abutments has not yet been fully understood, partly because of the complicated nature of this problem and the limitations in the previous investigation methods.

The practice of integral bridges in the USA has been investigated. Although the USA has the largest number of integral bridges in the world, the design of integral bridges appears to have been somewhat empirical (Nicholson, 1997). For example, shallow bank-seat piled abutments and shallow bank-seat spread-footing abutments are preferred in the USA, mainly because the short height of such abutments limits the influence of the soil behind them (Biddle *et al.*, 1997). Most research on integral bridges in the USA has

concentrated on the bridge structures alone, without rigorous investigation of the soil behaviour (*e.g.* Arsoy *et al.*, 2002).

In this section, previous research will be examined critically in groups according to their investigation technique, which can be divided into laboratory experiments, field monitoring and numerical simulation. Alternative technology for integral bridges will also be discussed.

2.3.1 Laboratory experiments

Very limited laboratory experiments on integral abutments have been conducted in the past decade, mainly consisting of the centrifuge tests by Springman *et al.* (1996) and Tapper & Lehane (2004), and the small scale model tests under normal gravity by England *et al.* (2000), Goh (2001) and Cosgrove & Lehane (2003).

Centrifuge tests

Springman *et al.* (1996) carried out a series of centrifuge model tests on two prototype systems, which represented an embedded abutment and a spread-footing abutment respectively. These abutments had a retained height of 6m in prototype size and were located at the end of a 200m long concrete bridge deck. In both cases, two pressure transducers were installed, at depths of 1/3 and 2/3 of the retained height. The centrifuge model scale was 1:60 (Figure 2.1a) and the model walls were constructed in a fine sand, Leighton Buzzard E siliceous sand, which meant that the equivalent prototype particle size was of the order of 5~9mm.

The increase of peak earth pressure coefficient appeared to be insignificant under *small cyclic thermal movements* (±0.05% and ±0.1% for embedded abutment, and ±0.1% and ±0.2% for spread-footing abutment), but became considerable under *large cyclic thermal movements* (±0.25% and ±0.5% for embedded abutment, and ±0.5% and ±1% for spread-footing abutment), especially during the first 20 cycles (Figure 2.1b). Considering that the cyclic annual thermal movement at one end of a 60m long concrete deck is only about ±8mm, this appears to imply that temperature variation would not cause a build-up of lateral earth pressure in reality. Presumably to be cautious, recommendations for practice (for the design of medium span integral bridge abutments) were based on the results under large cyclic thermal movements for a prototype 200m deck length.

Tapper & Lehane (2004) carried out 1:20 scale centrifuge tests to model a stiff abutment with a pinned base. Medium dense uniform siliceous sand was placed behind the wall, with a mean particle size of 0.18mm. Three rotation amplitudes were investigated (±0.05%, ±0.2% and ±0.63%). The findings were generally compatible with the centrifuge tests by Springman *et al.* (1996).

Small scale tests under normal gravity

England *et al.* (2000 and 2001) carried out a series of 1:12 scale model tests under normal gravity to investigate the lateral earth pressure created on the back of a stiff vertical abutment wall with a pinned base and a retained height of 7m in prototype scale, forced to rotate about its base by simulated thermal movements applied at the level of the bridge deck (Figure 2.2a). The model wall had a retained height of 580mm and Leighton Buzzard sand was placed behind it with a relative density of 94.1±0.2%, but no details about the sand particle size are available. Three cyclic rotation magnitudes (±0.125%, ±0.25% and ±0.35%) were investigated. In all cases, significant pressure changes occurred in the first 10 cycles, after which the rates of change became considerably slower and the pressures tended towards a stationary or steady-state (Figure 2.2b), the value of which was related to the cyclic movement magnitude. In contrast, the settlement of the soil surface was progressive throughout all cycles without any indication that a limit was being approached.

To investigate the behaviour of granular materials behind shallow abutments of integral bridges, Goh (2001) carried out a series of tests on 1:15 scale model walls under normal gravity, with either a fine or a coarse Leighton Buzzard sand backfilled. It was concluded that a shallow abutment at the end of a short length bridge would not experience full passive earth pressures. A pilot experiment was also conducted, demonstrating that the earth pressure on the abutment and the settlement could be reduced by incorporating a thin layer of flexible material, *e.g.* crumbed rubber in this test, between the abutment and the backfill.

Cosgrove & Lehane (2003) carried small scale model test on a 1m high rigid abutment rotated around the toe. Loose uniform siliceous sand, with a mean particle size (D_{50}) of 0.22mm, was placed behind the wall. Two cyclic rotation magnitudes (±0.23% and ±0.63%) were investigated. In contrast to those observed by England *et al.* (2000 and

2001), the maximum lateral pressure coefficient was found to increase progressively towards the passive state and did not display a tendency to reach a constant value.

In the experiments by England *et al.* (2000 and 2001), Goh (2001) and Cosgrove & Lehane (2003), the small scale models were tested under normal gravity, in which the stresses due to soil self weight were very low. As a result, the stress-strain behaviour of soil in the field may not have been replicated in these tests, since the confining pressure has a significant effect on the soil behaviour. To account for such a limitation, the high earth pressure coefficient K obtained by England *et al.* (2000) was scaled down, by comparing the stress-strain relationship of sand during monotonic plane strain testing under two different confining pressures (20kPa and 60kPa). The new K values were recommended as an upper bound value for design purposes. Furthermore, the relative dimensions of the testing box, *e.g.* the ratio of model wall width to height, and the ratio of box length to model wall height, were small in these experiments, which may have restricted soil deformation.

2.3.2 Field monitoring

Field monitoring investigations have been carried out both in the UK and overseas on existing integral abutments. The major findings will be presented and discussed here.

Field monitoring overseas

In Sweden, two long integral bridges were monitored by Broms & Ingleson (1971 and 1972). In the first case (Broms & Ingleson, 1971), the bridge was a 150m long rigid frame concrete bridge with a shallow abutment of 2.2m in height, backfilled with uniform sand with a mean particle size (D_{50}) of 0.45mm. It was found that the measured lateral earth pressure decreased to the active value during winter seasons, while it approached the passive state in the summer. In the second case (Broms & Ingleson, 1972), the bridge had a 110m long concrete deck, and abutments 8.25m high which were backfilled with sand and gravel. The measured earth pressure coefficient K was found to drop to the active state and even to zero in the winter. In the summer, K was raised to a value above K_o, the at-rest earth pressure coefficient.

In the USA, a semi-integral bridge in Virginia has been monitored for a period of 2.5 years (Hoppe *et al.*, 1996). This bridge was a 98m long, two-span composite steel girder

structure with an integral backwall about 1.5m high. The seasonal temperature change was significant, with -22°C recorded in the winter and +34°C in the summer. It was observed that the lateral earth pressure behind the integral backwall varied considerably on a daily basis, in response to temperature changes. Full passive earth pressures were recorded behind the integral backwall in the summer. Although uniformly graded granular backfill was used because of its low compressibility, excessive settlement became evident even in the first year after the opening of the bridge.

Field monitoring in the UK

In the UK, four medium length integral bridges have been monitored by the Transport Research Laboratory (TRL), including a shallow abutment integral bridge, a portal frame abutment bridge, an embedded abutment bridge, and a frame bridge with abutments pinned at the base, which are summarized in Table 2.2. A series of reports were published (Darley *et al.*, 1996 and 1998; Barker & Carder, 2000 and 2001), from which general conclusions can be derived, as follows:

For all the bridges, the decks expanded and contracted with temperature changes. The measurements indicated that the coefficient of thermal expansion of the deck in general was about $9.0\sim9.6\times10^{-6}/°C$ (Darley *et al.*, 1996 and 1998; Barker & Carder, 2000), which was consistent with that expected when limestone aggregates are used in concrete (BD37, DMRB 1.3). The bridge deck expanded or contracted relatively freely with minor resistance from the abutment and soil, though a stiffer abutment provided larger resistance than a more flexible abutment (Barker & Carder, 2000).

Except for the embedded abutment retaining mainly *in situ* soil, all the other abutments were backfilled with granular materials (see Table 2.1). The lateral earth pressures on the abutments changed with temperature, reaching their peak values in the summer. The changes were the most significant for the shallow abutments (Darley *et al.*, 1996 and 1998), where the earth pressure coefficient K in the summer was always higher than 1. For other full height abutments, K rose to a value slightly above the at-rest earth pressure coefficient K_o in the summer. In the winter, the measured lateral earth pressures decreased significantly in all cases, even approaching the active state.

For all the three full height abutment bridges, it has been found difficult to draw conclusions about whether a build-up of the peak lateral pressures can be expected

(Barker & Carder, 2000 and 2001). Creep and shrinkage of the concrete deck is believed to be the main reason, while the monitoring periods were too short (2 to 3 years after the opening of the bridges).

The shallow integral abutment had been kept under monitoring for more than 4 years since the opening of the bridge (Darley *et al.*, 1998). By comparing the measurements on two days with almost the same temperature in the last two successive years, it was found that there was a small increase in the lateral pressure on the shallow abutment. The authors suggested that this could provide some indication about the densification of backfill and the build-up of pressures. They also suggested that a much longer monitoring period, *e.g.* more than a decade, was needed to investigate the extent of the build-up of earth pressure and its ultimate magnitude.

2.3.3 Numerical modelling

Relatively little in the way of numerical modelling has been reported in the literature. Springman *et al.* (1996) carried out Finite Element analysis to simulate their centrifuge tests in sand, using the BRICK soil model (Simpson, 1992a and 1992b) to develop pressure depth relationships under cyclic loading. England *et al.* (2000) developed a semi-empirical constitutive model to simulate the interaction between the abutment and the sand, based on the results from their small-scale model tests. Wood & Nash (2000) carried out a numerical study to analyse an integral abutment pinned at the base. Using the Mohr-Coulomb elastic perfectly plastic model to simulate the soil, they concluded that the development of earth pressure was primarily controlled by the stiffness of the fill and was hardly influenced by its strength. Only monotonic movement of the abutment was investigated, as the isotropic hardening assumption in the Mohr-Coulomb model makes it unsuitable for investigating the stress build-up due to cyclic movement.

2.3.4 Alternative technologies

As discussed above, the behaviour of soil behind an integral abutment is very complicated and has not yet been fully understood, imposing a major uncertainty on engineers. To overcome such an uncertainty and avoid the risk of build-up of high lateral earth pressure, some alternative technologies have been attempted, mainly with the aim of protecting the soil from cyclic loading.

The use of a compressible layer

Carder & Card (1997) and Darley & Carder (1998) state that one method of avoiding the development of high lateral pressures is to use a low stiffness, but compressible, elastic backfill as a stress absorbing layer behind the abutment. Various compressible materials were identified, *e.g.* polymeric and geocomposite materials, which may be suitable for use as innovative structural backfill behind integral bridge abutments. However, other problems were found to emerge, such as the durability of the compressible materials.

Semi-integral abutments

In order to avoid the problem of cyclic loading on the soil behind an integral abutment, engineers have developed the concept of semi-integral bridges, which has been widely used in the USA (Burke *et al.*, 1997). In a semi-integral bridge, only the expansion joints are eliminated, by extending the bridge superstructure over the top of the abutments. The bearings between the deck and the abutments are still present, so that the abutments may remain relatively fixed while the superstructure changes in length with temperature. However, bearing maintenance is still a problem; though it may be reduced with this type of design compared with conventional bridges, as surface water no longer has direct access to the bearings.

2.4 Current UK design document BA 42

In 1996, the Highway Agency published BA 42 *The design of integral bridges*, which provides advice on the lateral earth pressures for the design of three main classes of integral bridge abutments (shallow abutment, full height frame abutment and embedded abutment). In 2003, BA 42 was updated with minor changes, mainly revising recommendations on shallow height abutments and adding new advice on frame abutments hinged at the foundation, based on the research of England *et al.* (2000) and Goh (2001). The advice for embedded abutments and frame abutments was kept unchanged.

The suggested lateral earth pressure distributions behind the embedded abutment and full height frame abutment are represented (Figure 2.3) by:

- For the embedded abutment, a uniform value of earth pressure coefficient K^* is assumed over the top two thirds of the retained height; while for the frame abutment a uniform value of K^* is assumed over the top half of the retained height.
- Lateral earth pressure then remains constant with depth as K^*drops to the at-rest earth pressure coefficient K_0.
- If the lateral earth pressure coefficient falls to K_0, then below that depth pressures are according to the value of K_0.

K^* is calculated from the formula below,

$$K^* = \left(\frac{d}{0.05H}\right)^{0.4} K_p \qquad (2.1)$$

where d is the thermal displacement of the top of the abutment and H is the retained height. K^* is advised to be at least the at-rest earth pressure coefficient $K_0=1-\sin\varphi'$. When calculating K_p, the peak effective friction angle φ'_{peak} is recommended, aiming to take account of the densification of granular material in the long-term. Furthermore, to take consideration of the rough surface of the concrete abutment, a wall friction angle δ of $\varphi'_{peak}/2$ is assumed at the same time. The influence of δ on the active earth pressure coefficient K_a is small, but the influence on the passive earth pressure coefficient K_p can be very significant (Clayton *et al.*, 1993). In reality, the magnitude of δ depends on the wall rotation, roughness and depth, and it could be as high as the peak value of the plane strain angle of internal friction φ'_{ps} (Bica, 1991).

The publication of BA 42 has encouraged the use of integral bridges and provided guidelines for designers. However, the advice in BA 42 is based on limited research, which could not provide enough evidence to predict the earth pressure increase tendency and its ultimate magnitude, as discussed in section 2.3. It is widely believed to be unsatisfactory and that further research is necessary (*e.g.* Biddle *et al.*, 1997). Furthermore, although embedded abutments are more likely to be constructed in a clayey ground, especially overconsolidated clay, which is a typical ground condition in the UK (Padfield & Mair, 1984), there are no special recommendations for the earth pressures in such conditions, since all the previous research was carried out on granular material. As

a consequence, engineers have to face uncertainties in the design of an abutment embedded in clay (Way & Yandzio, 1997).

2.5 Previous research on the soil behaviour under cyclic loading

The behaviour of soils under cyclic loading has been studied by many researchers, particularly in the following areas:

- foundation of offshore gravity structures (*e.g.* Andersen & Lauritzsen, 1988; Bjerrum, 1973);
- cyclic behaviour of large piles with reference to offshore structures (*e.g.* Jardine, 1991);
- foundation of pavement and rail track (*e.g.* Brown, 1996);
- seismic loading (*e.g.* Ishihara, 1993);
- machine foundations (*e.g.* Davies, 1991).

It is widely recognised that the behaviour of soils under cyclic loading is complicated and depends on a number of factors, as discussed below:

Sand and clay exhibit markedly different stress-strain behaviour under cyclic loading. The property of a soil, such as the overconsolidation ratio (OCR) and plasticity index of clay (Andersen *et al.*, 1980; Vucetic & Dobry, 1991), or the relative density and grading of sand (Lekarp *et al.*, 2000), can have a significant effect on the stress-strain behaviour under cyclic loading.

The soil behaviour also depends on the drainage conditions and the frequency of cyclic loading. For saturated sand, especially fine silty sands, under high frequency cyclic loading (*e.g.* seismic loading), there is no time for the excess pore pressure to dissipate, which leads to a build-up of pore pressure and a final loss of shear strength of the soil (liquefaction) (Ishihara, 1993).

Cyclic triaxial testing can be divided into two groups in general: stress-controlled or strain-controlled cyclic loading. The amplitude of cyclic stress or strain is of great

importance and varies considerably in different cases (*e.g.* the load on the soil beneath the foundation of an oil platform or beneath road pavement).

Brown & Selig (1991) found that little strain will develop for granular materials under stress-controlled cyclic loading if the peak stress ratio is kept below a certain value, which appears to be about 70% of the stress ration at failure in most cases. Results reported by Brown *et al.* (1987) for a silty clay also identified a threshold value for the deviator stress plus (q_r) in relation to the deviator stress at yield (q_y) at he same effective stress. Only when q_r/q_y exceeded 1.3 did significant plastic strain develop.

Vucetic (1995) identified two types of cyclic threshold shear strain for strain-controlled cyclic loading: the linear cyclic threshold shear strain γ_{tl} (about 10^{-5}~10^{-4}) and the volumetric cyclic threshold shear strain γ_{tv} (about 10^{-4}~10^{-3}), both of which were found to depend on the type of soil and are correlated to soils plasticity index. For cyclic strains below γ_{tl}, soil behaves essentially as a linearly elastic material. Between γ_{tl} and γ_{tv}, soil becomes markedly nonlinear but remains largely elastic. Above γ_{tv}, soil becomes increasingly nonlinear and inelastic, with significant permanent microstructural changes taking place under cyclic loading.

The importance of stress path on the behaviour of sand during monotonic loading has been demonstrated by Lade & Duncan (1975). Show (1980) noted that for uniform granular materials under stress-controlled cyclic triaxial loading following different stress path, the accumulation of volumetric and shear strain were considerably different (Figure 2.4).

Marr & Christian (1981) carried stress-controlled cyclic triaxial testing on fine sand. Two types of tests were performed, with the same cyclic deviator stress amplitude but different stress path location. The "isotropic" test has the deviator stress cycled about an average value of zero, while the "anisotropic" test has a positive average deviator stress. Significantly difference was found in the permanent strain accumulation (Figure 2.5).

It has been found that the accumulation of strain under stress-controlled cyclic loading is far greater when the principle stress direction is rotated than when it remains constant (e.g. Wong & Arthur, 1986). The investigation of the effect of principle stress rotation needs special equipment, such as hollow cylinder apparatus (Hight *et al.*, 1981)

To assist interpretation of the settlements observed in the small scale tests on integral abutment by Cosgrove & Lehane (2003), Cosgrove *et al.* (2001) carried out cyclic axial strain-controlled triaxial testing on a fine sand with a constant cell pressure. A non-

symmetrical deviator stress-axial strain curve was observed, which was found to be markedly different from curves observed in stress-controlled cyclic testing. An increase in stiffness with cycling was also observed, which was attributed to the strain hardening. However, uncertainty arises due to the different stress path used in these tests compared to the stress path in the soil behind integral abutments.

The above review reveals that the behaviour of soils under cyclic loading is very complicated and varies considerably in different situations. The state of the soil behind an integral abutment, *e.g.* the rate of loading, cyclic strain amplitude, stress path, mean effective stress level *et al.*, determines that this problem is unique in comparison to previous research, and the soil behaviour will remain uncertain until appropriate experimental investigation has been carried out.

2.6 Laboratory investigation of soil stress-strain behaviour

From the review of previous research described in sections 2.3 and 2.5, it is evident that the behaviour of soil behind an integral abutment still remains unclear, partly because of the complicated nature of this problem and also due to the limitations of the previous research. Geotechnical laboratory stress path testing has been identified as a promising technique to investigate the fundamental behaviour of soil behind an integral abutment. It has been successfully used in the investigation of a wide range of geotechnical problems (*e.g.* Lambe, 1967). The soil specimen could be tested with well-defined boundary conditions with the drainage well controlled. With the aid of computer control and the development of local strain and stress measurement, the stress and strain could be measured and controlled accurately. Both clay and sand specimens could be tested in a reasonable period of time. But more importantly, the stress path dependency of soil behaviour can be replicated.

In this section, geotechnical stress path testing is examined, highlighting the development of the technique, especially the local small strain measurement. Recent improvement of our understanding of soil are also noted, including the pre-failure behaviour of soil, time-dependent soil behaviour, the effect of loading path and of recent stress history, and the micromechanical behaviour of granular material.

2.6.1 Stress path dependency of soil behaviour

The most common stress path in a conventional triaxial test is to change the deviator stress while keeping the lateral stress constant, since it is of practical convenience to maintain a constant cell pressure (Bishop & Henkel, 1962). However, the stress-strain behaviour of soil is in general dependent on the loading-path (Lambe & Whitman, 1979). Lade & Duncan (1975) demonstrated in triaxial tests on sand that the strains induced by changing the stresses from one stress state to another depended not only on the end points, but also on the stress path. The strain increments could be markedly different when following different stress paths, even if the initial and final stress conditions were the same.

Since soil behaviour depends on the stress path, appropriate deformation characteristics may only be obtained if the appropriate stress path is followed. Similarly, for a given deformation or strain level, realistic stress changes will not be estimated unless appropriate stress paths are followed. To overcome the restriction in following any stress path in a conventional triaxial cell, Bishop and Wesley (1975) developed a simple and versatile hydraulically operated triaxial apparatus, which was capable of testing soil over a wide range of stress paths. This equipment was used in this research and will be introduced in Chapter 4.

Lambe (1967) and Lambe & Marr (1979) proposed the "Stress path method", which consisted of a systematic approach to elucidating and solving geotechnical engineering problems. The stress path method is usually used in shallow problems, which are essentially stress-controlled and for which the stress increments could be reasonably estimated using a simple soil model. The deformation of soil can then be deduced by performing a stress path test on selected typical soil elements.

2.6.2 Small strain measurement

One of the major problems in geotechnical engineering up to the 1970s was the apparent difference between the stiffness of soils measured in laboratory tests and those back-calculated from observations of ground movements (*e.g.* Cole & Burland, 1972; Green, 1972; Hooper 1974; Burland & Hancock, 1977). It was widely reported that in order to obtain satisfactory results, the stiffness assumed for the overconsolidated soil

would have to be very much greater than that measured in laboratory tests using conventional triaxial tests or oedometer tests (Figure 2.6).

These differences have now largely been reconciled through an understanding of the principal features of soil stiffness and, in particular, the very important influence of non-linearity. This has been achieved mainly through the improvement of strain measurement technology.

Typical strain around structures

Jardine *et al.* (1986) carried out finite element analyses to examine the levels of strain around a range of construction types in London Clay. It was found that typical shear strain levels were less than about 0.1%. In cases where loading was light, or when excavations were well restrained, or in stiff ground, typical strain levels could be even less, and perhaps as low as 0.01%.

Burland (1989) summarized the site measurements by other researchers of strain in soil beneath or around different types of structures, including a tunnel and the foundations of tall buildings. It was concluded that under working conditions, the direct strain in a large mass of ground beneath and around a structure, *e.g.* an excavation or foundation, would be less than 0.1%.

A typical stiffness-strain curve for soil is summarized in Figure 2.7 (Mair, 1993), which includes typical ranges of strain for laboratory testing and for structures. It shows that the strain levels where stiffness degradation is most rapid coincide with the strain levels found for geotechnical structures in practice. This implies that the non-linear stress-strain response of geomaterials should be taken into consideration in design, and suggests that the stiffness required for use in engineering calculations must be derived at an appropriate strain level, if accurate displacement or settlement predictions are to be made.

Strain measurement

Conventional procedures for determining deformations during triaxial tests are based on measurements made externally to the cell. This practice is inadequate, particularly if the small strain behaviour of the soil is being investigated, because errors are introduced

which limit the accuracy and resolution of the measurements. A number of errors may be introduced in the externally measured strain, as specified by Baldi *et al.* (1988):

1. compliance errors, *e.g.* deformation in an internal load cell as it compresses under load;
2. seating errors due to the closing of gaps between ram or internal load cell and platen, and platens and porous stone;
3. alignment errors from equipment and specimen nonconformity;
4. non-uniform strains along the specimen height resulting from end restraint;
5. bedding errors caused by lack of fit or surface irregularities at the interfaces (top and bottom) between the specimen and loading surfaces (platens or porous stones).

Because of these errors, external strain measurement will introduce large errors in the small strain range. Although the errors due to apparatus compliance can be evaluated with reasonable certainty by careful calibration, the bedding error can be very difficult to assess since its magnitude depends on the way in which the ends of the specimen are prepared. Thus the only way to obtain accurate determinations of axial strain is to carry out the measurement remotely from the ends of the specimen, and preferably on its middle third. This measurement technique is known as local strain measurement. The advantage of local strain measurement is that it overcomes the errors listed above and thereby measures soil stiffness more accurately, especially at small strain levels, as demonstrated by Jardine *et al.* (1984) and Clayton *et al.* (1986).

It was stated earlier that there were apparent differences between the stiffness of soils measured in conventional laboratory tests and those back-calculated from observations of ground movements. Jardine *et al.* (1985) demonstrated that when local strain instrumentation was used, good agreement was found between back calculated stiffness and triaxial stiffness (Figure 2.8). This suggested that errors from external strain measurements were responsible for the lower triaxial stiffness.

Since the early 1970s, a number of purpose-made local strain instruments have been developed, including electrolevel displacement gauges (Burland & Symes, 1982), Hall effect semiconductors (Clayton & Khatrush, 1986), proximity sensors (Hird & Yung, 1987), local deformation transducers (Goto *et al.*, 1991) and miniature linear variable differential transformers (LVDTs) (Cuccovillo & Coop, 1997).

2.6.3 Pre-failure behaviour of soils

With the development of devices allowing the accurate measurement of local strains, it has become possible to examine in more detail the pre-failure stress-strain behaviour of soils.

Non-linearity of soil stress-strain behaviour

Jardine *et al.* (1991) proposed a framework for the stress-strain behaviour of soil, which can be divided into three zones (Figure 2.9).

Linear elastic Zone I corresponds to a region of true linear elastic behaviour. Zone I is very small and cannot easily be identified.

Recoverable Zone II: the stress-strain behaviour inside Zone II is non-linear and hysteretic, but complete load-unload cycles show fully recoverable behaviour. Undrained instrumented load-unload triaxial tests can be used to identify the upper and lower extent of the boundary Y2, but drained tests are required to map out the rest of the region (Smith *et al.*, 1992).

Plastic Zone: The key feature of Zone III is the development of irrecoverable strains, which become progressively more important as the path approaches the bounding surface Y3. Y3 corresponds to the onset of a pronounced change in the pattern of behaviour.

Jardine (1992) stated that the inner Y1 and Y2 yield surfaces were kinematic. When Y1 and Y2 are crossed by the effective stress path, they move with the effective stress state. If the stress path direction changes sharply at any stage, then the material will exhibit again the stiff behaviour ascribed to Zone II, or even Zone I. This behaviour was regarded to be a result of the effect of recent stress history (Jardine, 1992), but recent research revealed that this might have resulted from creep strains contributed by the previous loading path (Clayton & Heymann, 2001).

Soil behaviour at very small strain

The soil stress-strain behaviour at very small strain behaviour has recently been investigated by Clayton and Heymann (2001). Local strain measurement was made using LVDTs, which were calibrated by a Fabry-Perot laser interferometer (Heymann, 1998) to an axial strain accuracy of the order of $\pm 10^{-4}\%$. High quality undisturbed specimens,

including a soft clay (Bothkennar clay), a very stiff clay (London Clay), and weak rock (Chalk) were investigated. They were chosen to be representative of natural geomaterials with wide-ranging strengths and stiffnesses.

The stiffness behaviour of the three geomaterials was compared. Although the maximum undrained secant Young's moduli (E_{max}) measured at very small strains were markedly different, the strain at the limit of the linear elastic behaviour appeared similar for all three materials, and was found to be approximately 0.002-0.003% axial strain. Beyond this point, the stiffness decreased and exhibited highly non-linear behaviour (Figure 2.10).

Their research showed that for these relatively undisturbed specimens of natural clay, E_{max} appeared to be a function of mean effective stress level alone. More strongly bonded specimens, such as the chalk, showed little influence of mean effective stress level until destructuring took place, accompanied by significant volumetric strains. It has also been found that the maximum stiffness in the highest-quality laboratory specimens was close to that determined from field geophysics (Matthews *et al.*, 2000).

2.6.4 Creep and stress relaxation

In conventional soil mechanics theory, it is generally assumed that deformation of soil occurs only as a result of changes in effective stress. However, in reality, soils are found to continue to deform when the effective stresses are not changing. This behaviour is known as creep. On the other hand, stress relaxation may happen when the deformation of soil is restrained. In fact, soils exhibit time-dependent behaviour, or viscous behaviour, the degree of which depends on the complex interaction among soil structure, stress history, drainage conditions, change in temperature, and bio-chemical environment (Mitchell, 1993).

Although creep and stress relaxation is very complicated, especially in the field situation, it may follow some logical and predictable patterns, at least for simple stress and deformation states in the laboratory. On the basis of creep tests performed in triaxial apparatus in drained and undrained conditions on a wide range of materials, Singh & Mitchell (1968) found that a similar pattern could be observed, as that noted by Bishop (1966) (Figure 2.11). At any stress level, the logarithm of strain rate $d\varepsilon/dt$ decreases linearly with the logarithm of time t. The slope m of the graph is essentially independent

of the applied stress. An increase in applied deviator stress shifts the relationship to higher strain rates. Except at very low and very high stress levels, there is a linear relationship between the logarithm of the strain rate and the deviator stress at a given time. Based on the idealized pattern, Singh & Mitchell (1968) proposed the following equation to represent creep in soil:

$$d\varepsilon/dt = Ae^{\alpha D}(t_1/t)^m$$

where D is the stress density, equal to the applied deviator stress divided by the deviator stress at failure, t_1 is a reference time generally taken as 1 min, and α and A are creep parameters.

2.6.5 Effect of recent stress history

The effect of recent stress history on soil behaviour has been controversial. Richardson (1988) and Atkinson *et al.* (1990) investigated the effect of recent stress history by conducting four shear stages on 38 mm diameter samples of reconstituted London Clay using external strain measurement. Before each shear stage the required stress state was approached from a different direction in triaxial stress space, resulting in an angle (θ) between incoming and outgoing stress paths of 0 °, ±90 °, and 180 °. The results indicated that the stiffness at intermediate strain levels were higher for larger angles between the incoming and outgoing stress path (Figure 2.12). Based on this finding, conclusions were drawn that following a change of the direction of the stress path the stiffness may be increased by up to an order of magnitude, and that the recent stress history thus had a major effect on the subsequent stiffness. It should be noted that between reaching the required stress state and commencing shear, the samples were hold at a constant stress state for only 3 hours. The authors stated that this was twice the period required for primary consolidation to occur and the volumetric creep rate was too small to be measured by the external volume gauge after the rest period. Since then, a number of numerical models have been developed, trying to simulate such an effect, including the BRICK model (Simpson, 1992a and 1992b) and the Three Surface Kinematic Hardening (3-SKH) model (Stallebrss, 1990).

However, the effect of recent stress history has become a subject of doubt recently. Hird & Pierpoint (1997) carried out a series of drained triaxial tests on block samples of Oxford clay, an overconsolidated stiff clay, with local strains measured by proximity

transducers. Their test programme included a number of constant p' and constant q stress paths on single specimens. They found that recent stress history had almost no effect on locally measured stiffness, once creep effects were eliminated by a rest period of at least 2 to 3 days.

Clayton & Heymann (2001) carried out triaxial tests on high quality intact samples of Bothkennar clay, a lightly overconsolidated soft clay, with local strains measured by LVDTs. Three stress paths were applied to the same specimen in order to investigate the effect of recent stress history. The direction of the incoming stress path was different, while the direction of the outgoing stress path was identical in each case, with the resulting changes in stress path direction of 180°, 90° and -90°. Between completing the incoming stress excursion and commencing with the outgoing stress excursion, a rest period of between 1 and 2 days was allowed, and the local creep strain rates were reduced to less than 0.8% of the local shear rate when the shear phase commenced. It was found that the stiffness was almost identical at all strain levels for each outgoing stress path (Figure 2.13) and there was no effect of recent stress history on the stress-strain behaviour.

Clayton & Heymann (2001) suggested that the apparent effects of recent stress history on stiffness that had been previously observed on reconstituted soils might have resulted to some extent from creep strains contributed by the previous loading path. After completion of a stress excursion in any stress path test, it is always found that some volumetric and shear strains continue to occur under a constant effective stress state. If the creep rate is not allowed to decrease sufficiently, strains from creep will be included in strains measured during subsequent stress excursions. The measured stiffness after a stress path reversal would appear to be higher than that without a stress path reversal. Especially at small strain levels, if uncontrolled, these creep strains could be of the same magnitude as strains resulting from the current loading, thus leading to incorrect measurements of stiffness. Reconstituted or destructured soils were expected to undergo much larger creep at small strains than natural undisturbed soils. Furthermore, the external strain measurement could also bring significant errors, especially at small strain levels (Clayton *et al.*, 1986).

Bishop & Lovenbury (1969) investigated the creep behaviour of undisturbed London Clay over extended periods of more than three years and found that creep occurred at all deviator stress levels and that no threshold was apparent below which creep did not

occur. Depending on the deviator stress state, they found the creep rates of London Clay after three hours to range between 0.2% and 2% per day, which implied that a significant proportion of the strains measured by Atkinson *et al.* (1990) could be attributed to creep and that stiffness might be overestimated greatly after a stress path reversal, or underestimated when there was no stress path reversal.

2.6.6 Micromechanical behaviour of granular materials

The shear strength of a mass of particles depends on a number of factors, and its relationship with interparticle friction angle φ_μ has long been investigated (*e.g.* Bishop, 1954; Skinner, 1969; Ni, 2003). Bishop (1954) approximated φ_{cv}' (the effective shearing resistance at constant volume) in terms of φ_μ, both for plane strain conditions and for triaxial compression. Newland & Allely (1957) proposed a model for granular materials based on the assumption that shearing of granular soils was analogous to frictional sliding between two rigid blocks, with the only difference that sliding took place on many contact surfaces in the former but on a single plane in the latter. All these predictions suggested an increasing shear strength with φ_μ, based on a mechanism of particle sliding.

However, Skinner (1969) demonstrated that the shear strength in a shearbox was almost the same for wet and dry 1 mm glass ballotini, even though the wet glass ballotini interparticle friction angle (27°~38°) was significantly higher than that of the dry ones (2°~5°). Skinner (1969) suggested that rolling of particles became a dominant mechanism, rather than sliding, during shear when interparticle friction was high.

This conclusion was supported by Oda *et al.* (1982), who carried out biaxial tests on rod-like particles with oval cross sections cast from polyurethane rubber. For rounded particles, no dependence of peak stress ratio on φ_μ was observed when φ_μ was increased from 26° to 52°. On the other hand, for particles with a flatter cross section, the peak stress ratio increased by almost a third when φ_μ was increased from 26° to 52°. Those tests suggested that particle shape could have an effect on particle rolling and influence significantly the behaviour of granular material.

Recently these features of particle behaviour observed in tests were reproduced in three-dimensional distinct element simulations by Ni (2003). When a granular material in a shearbox was simulated as 1mm diameter spheres, the shearing resistance at the critical state (φ_{cv}') was found to be independent of the interparticle friction angle, and

considerable particle rotation was observed. However, when non-spherical particles were simulated by bonding two spheres together, the shear strength increased significantly with the interparticle friction angle. The freedom of a particle to rotate was found to be restricted by the particle shape.

Both experiments (Oda *et al.*, 1982) and numerical simulation (Iwashita and Oda, 1998; Thornton, 1997) found that the granular particles did not transmit the stress equally and that the development of column-like structure was a major feature before failure (Figure 2.14). In the hardening process up to failure, particles were arranged in chains to form column-like structures with the elongation directions approximately parallel to the major principal stress axis, and the applied stress was mainly transmitted through them. During the failure, rolling of particles, rather than sliding, took place and the column-like structures began to collapse, or "buckle". Particles inside the region forming the shear band rotated significantly more than those outside.

2.7 Stress in the ground

2.7.1 Earth pressure in clay

For embedded abutments retaining natural cohesive ground, the pre-existing or *in situ* lateral earth pressure, possibly modified by the wall installation process, is potentially important to the abutment behaviour.

Ground conditions before construction will vary from site to site, and the *in situ* lateral earth pressure coefficient $K_o=\sigma'_h/\sigma'_v$ depends on the effective stress history, ground water conditions and current stress state (Burland *et al.*, 1979). In heavily overconsolidated clay, such as London Clay, K_o may rise to well in excess of 2 near the ground surface (Skempton, 1961).

However, the effects of diaphragm wall installation are potentially significant, because they will alter the initial stress state. The exact effect depends on the details of the construction technique.

The sequence of construction of diaphragm wall panels or bored piles was described by Clayton *et al.*(1993). At the beginning of construction, a hole (which may be unsupported or may be supported by bentonite slurry) must be excavated in the soil to

form the wall section. The total horizontal stress on the boundary of this hole will reduced from the initial *in situ* horizontal total stress in the undisturbed soil to either zero (if the hole is unsupported) or to a value which is approximately equal to the pressure exerted by a fluid with the same density as bentonite. The total lateral stress acting on the soil is then increased to a value approximating to the pressure applied by the wet concrete, especially in the upper 10 meters of the wall (Figure 2.15a).

Field observation of the Bell Common Tunnel (Tedd *et al.*, 1984), both during construction and afterwards, showed not only that 30% of the measured ground surface settlement adjacent to the walls occurred during the process of the installation of the secant-bored pile, but also that this was associated with a significant reduction in horizontal total stresses, particularly in the heavily overconsolidated London Clay, where the effective lateral earth pressure coefficient decreased to a value close to unity (Figure 2.15b). Measured bending moments over five years after construction were much lower than were predicted during design, which was believed to be partly as a result of this effect.

These findings from experiment and field monitoring were consistent with theoretical research. By neglecting three dimensional effects and modelling the soil as a reversible, linear elastic and cross-anisotropic material, Powrie (1985) demonstrated that the effective lateral earth pressure coefficient would be expected to move towards unity during construction of a diaphragm wall.

Based on previous investigations, K=1.0 was recommended for the design of embedded walls (diaphragm walls and bored pile walls) in stiff overconsolidated clay to take account of the effects of wall installation (Gaba *et al.*, 2003).

2.7.2 The pressure of compacted granular backfill

Frame bridge abutments, as well as many other earth retaining structures, support soil which has been placed against the structure. Granular material is usually used, compacted in thin layers so as to optimise its strength and compressibility properties. This can lead to a lateral earth pressure coefficient much higher than K_o. Consequently, a number of design theories have been proposed by Broms (1971), Ingold (1979) and Clayton & Symons (1992).

A simple approach for assessing the lateral stress distribution caused by the compaction of a free draining granular backfill behind a smooth rigid wall has been put forward by Broms (1971). Before compaction takes place and assuming that soil has been placed uniformly and there is full drainage, the horizontal earth pressure will be equal to the earth pressure at rest. As the fill is compacted by a roller the vertical stress will temporarily increase by $\Delta\sigma'_v$ and the horizontal stress is assumed to increase by K_o $\Delta\sigma'_v$. The largest stress increase will occur at shallow depth immediately beneath the roller. As the roller moves away the vertical stress will decrease back to the original value σ'_{v0} and Broms (1971) suggested that at the soil at shallow depth will yield along an unloading line at a slope of 1/ K_o to give a final horizontal stress of σ'_{hf} after compaction (Figure 2.16a). However, the soil at greater depth will not reach the unloading line and the final horizontal stress after compaction is assumed to remain at the value with the roller in place (Figure 2.16b).

For compaction of the backfill in thin layers, summation of the residual horizontal stress distributions leads to a pressure distribution of the form shown in Figure 2.16c. Above Z_{cr} the earth pressure coefficient K is simplified as 1/ K_o. Between depths of Z_{cr} and h_c the pressure is assumed to be constant and equal to the maximum residual pressure σ'_{hrm}. Below h_c the horizontal pressure due to self weight of the overlying soil exceeds that induced by compaction.

Assuming that a roller can be adequately modelled as an infinitely long line load with an intensity of w per unit length, and that at shallow depths the self-weight of the backfill is relatively small and can be neglected, then the following equations may be derived:

$$\sigma'_{hrm} = \sqrt{2w\gamma/\pi} \qquad (2.2)$$

$$Z_{cr} = K_o\sqrt{2w/\gamma\pi} \qquad (2.3)$$

$$h_c = \sqrt{2w/\gamma\pi} / K_o \qquad (2.4)$$

where γ is the bulk unit weight of the fill. Ingold (1979) extended this approach to a smooth wall which yields during compaction. This has no effect on the predicted maximum residual horizontal pressure σ'_{hrm} but gives formulas for the depths Z_{cr} and h_c in which the K_o term in equations 2.3 and 2.4 is replaced by K_a , the active earth pressure coefficient.

Clayton & Symons (1992) demonstrate that the compaction pressure σ'_{hrm} are unlikely to exceed 20~30 kPa and the depth h_c to which compaction pressures are significant will not exceed 3~4m, below which the horizontal earth pressure coefficient could be reasonably assumed to equal to K_o for rigid walls, or K_a for flexible walls. This was supported by the results of the pilot scale experiment reported by Symons & Clayton (1991).

2.8 Summary

In the first half of this chapter, the influence of temperature on a bridge deck, previous research on integral bridge abutments, the current design standard for integral bridges, and previous research on the soil behaviour under cyclic loading were reviewed. It was found that the behaviour of soil behind an integral abutment still remains unclear, mainly because of the complexity of the problem and also due to limitations of previous model tests and field monitoring. As a result, numerical simulations of the soil-abutment interaction cannot be justified. The current UK design standard, BA42 *The Design of Integral Bridges*, is widely believed to be unsatisfactory and that more research is needed. No investigation has been conducted on the magnitude of earth pressure behind integral abutments embedded in clayey ground.

Compared with other research methods, geotechnical laboratory stress path testing has been identified as a promising technique to investigate the fundamental behaviour of soil behind an integral abutment. Therefore, in the second half of this chapter, the stress path testing technique was investigated, highlighting the recent development of technique and improvement of our understanding of soil behaviour, including local small strain measurement, pre-failure behaviour of soil, time-dependent behaviour of soil, the effect of recent stress history and the micromechanical behaviour of granular materials. Finally, research on the effects of wall installation in clay and compaction pressures in granular backfill was reviewed.

Table 2.2 Summary of the integral bridges investigated in the UK

Bridge Location	Total Deck Length (m)	Deck material (Thickness, mm)	Abutment type (Abutment thickness, mm)	Retained height (m)	Deck width (m)	Main retained soil	Length of monitoring period after opening	Reference
Glasgow	60	Concrete (700)	Shallow abutment with a spread base (900)	3.1	17	Well graded crush rockfill, $\varphi'=46^{o}$	4 years	Darley *et al.* (1996, 1998)
Manchester	40.7	Concrete (1700)	Portal frame abutment with permanent prop 4.5 m under ground level (1900)*	9.5		Granular backfill $\varphi'_{peak}=42^{o}$ $\varphi'_{residual}=37^{o}$	2.5 years	Barker & Carder (2000)
	42.9	Concrete (1700)	Integral bored pile abutment (ø1500@1820)	6.5		In situ soil (mainly Boulder Clay)	2.5 years	
Bramham	50.2	Concrete	Full hight abutment with a pinned base (800~900)	8.8 (West) 9.3 (East)	18.1	Granular backfill $c'_{peak}=9kPa$ $\varphi'_{peak}=41^{o}$	3.5 years	Barker & Carder (2001)

* There was a remedial works to the defective concrete cast, which lead to a very thick wall.

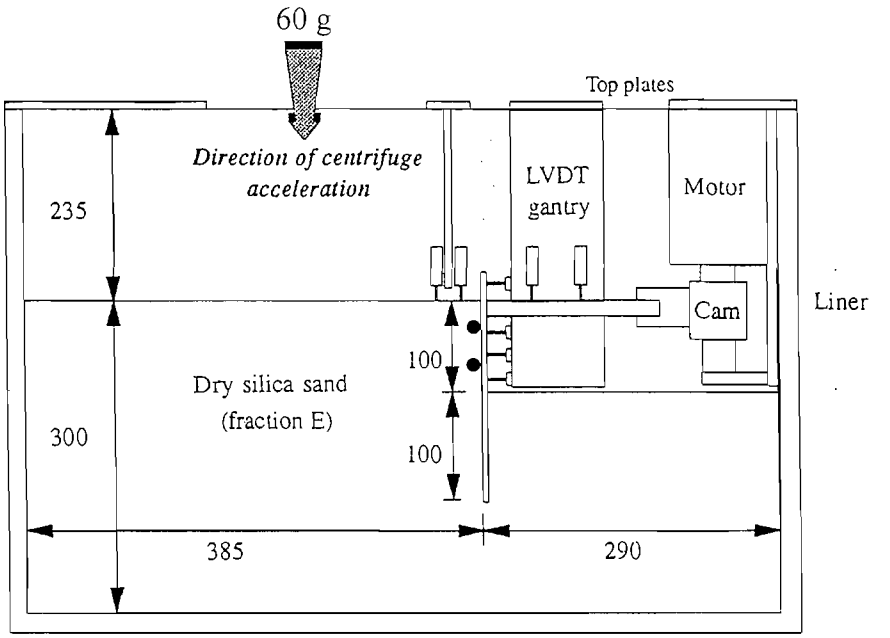

(a) Test set-up for the 1:60 scale embedded abutment
(●—the position of pressure cells at the back of the model abutment)

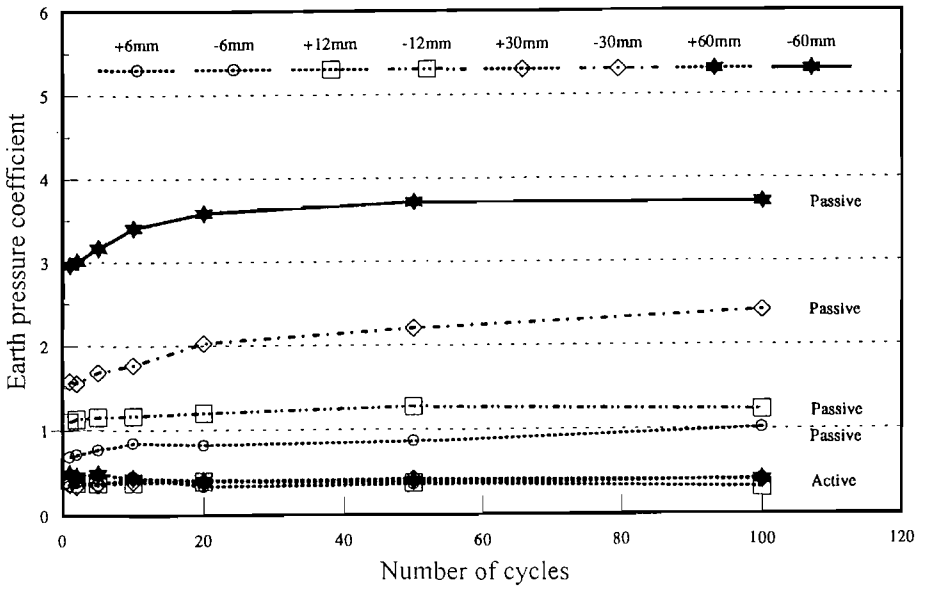

(b) Measured earth pressure coefficient (at a depth of 1/3 of the retained height) behind the spread-footing abutment backfilled by dense sand

Figure 2.1 The centrifuge tests by Springman *et al.* (1996)

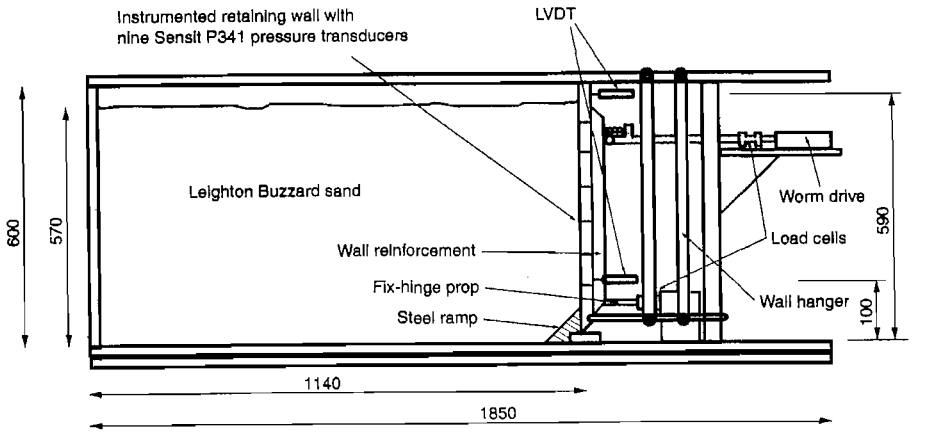

(a) The test apparatus of the 1:12 scale experiment

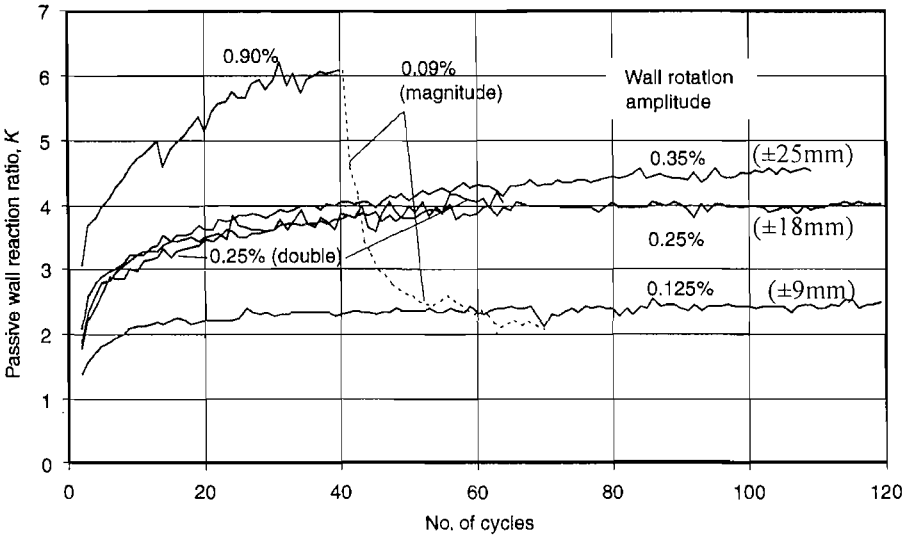

(b) Escalation of peak earth pressure coefficient with cycles

Figure 2.2 The small scale model experiment by England *et al.* (2001)

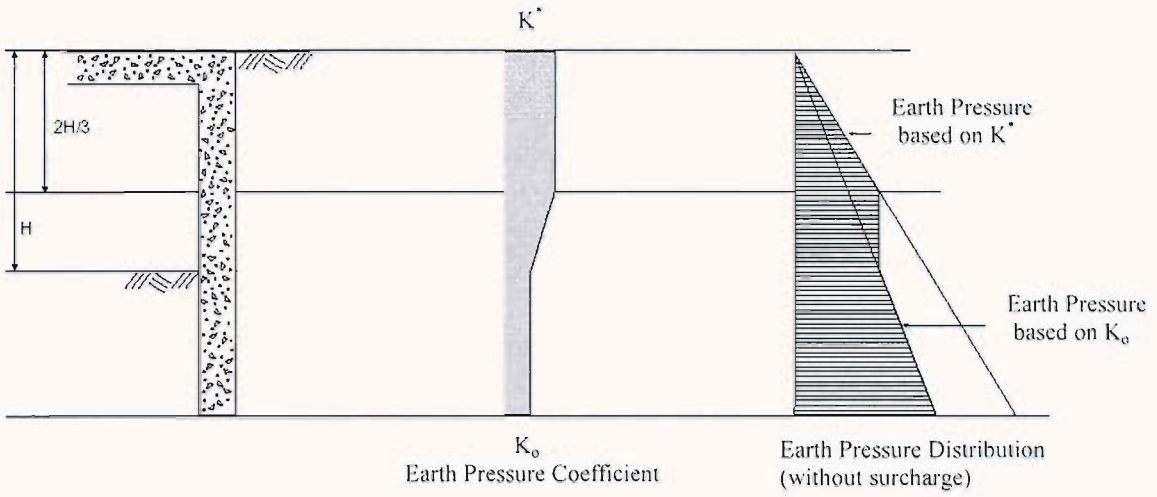

(a) Earth pressure distribution behind embedded abutments

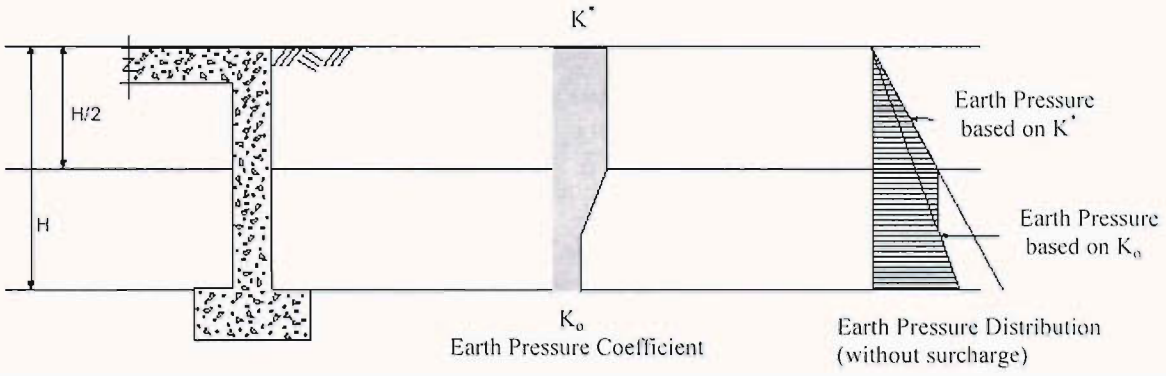

(b) Earth pressure distribution behind frame abutments

Figure 2.3 Earth Pressure Distribution behind full-height integral abutments (BA 42/96)

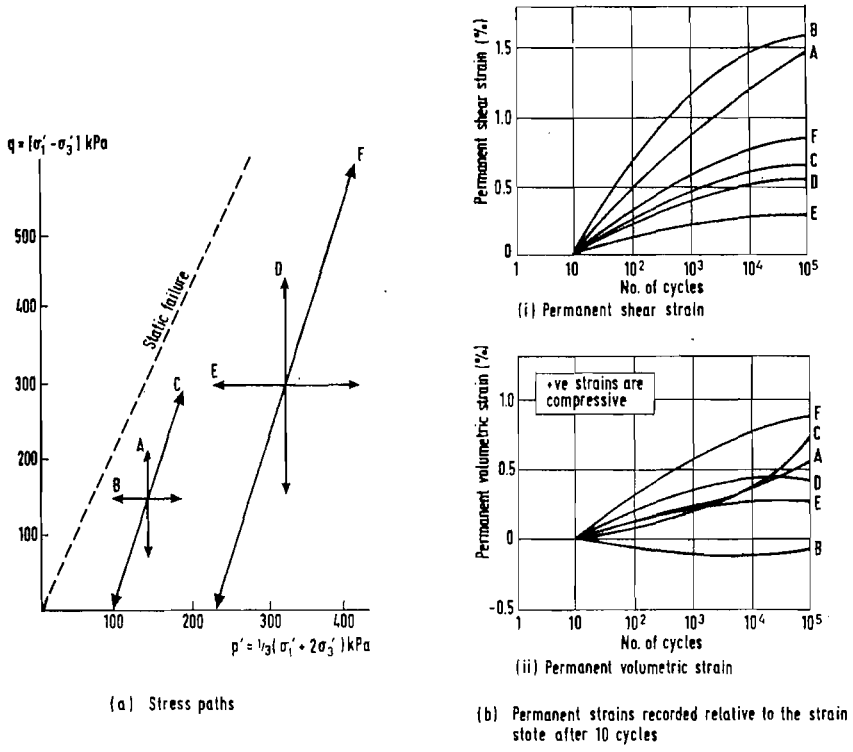

Figure 2.4 The long-term accumulation of strains during cyclic triaxial testing following different stress path (from Shaw, 1980)

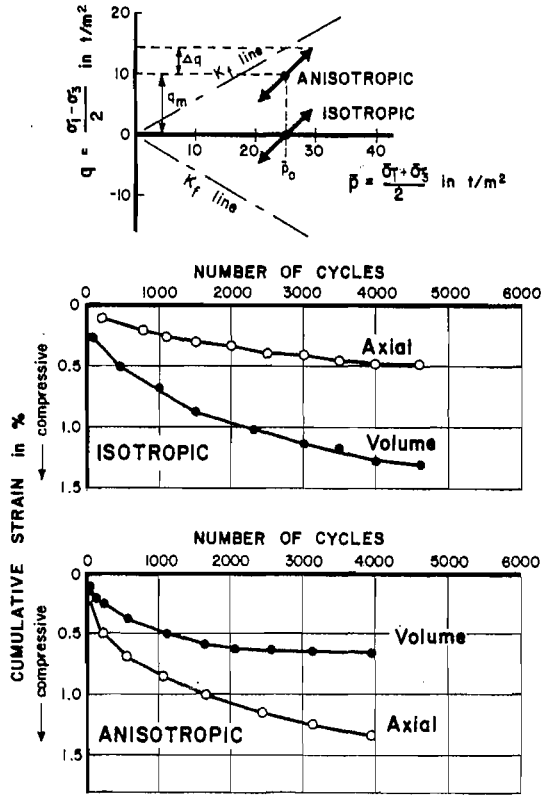

Figure 2.5 The influence of stress path location under drained stress-controlled cyclic triaxial testing (from Marr & Christian, 1981)

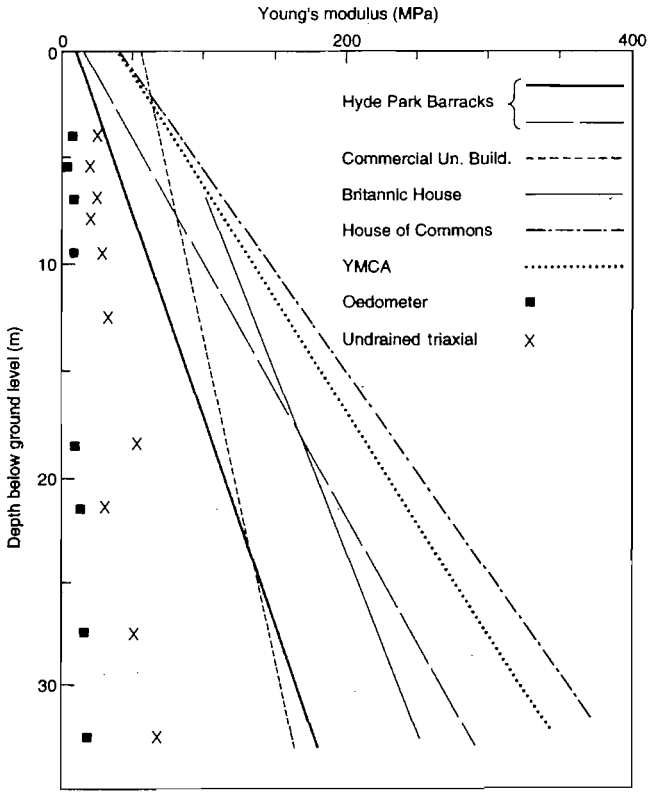

Figure 2.6 Comparison of stiffness of London Clay from conventional triaxial tests with those from back calculation for Grand Buildings, Trafalgar Square, London (Clayton *et al.*, 1991)

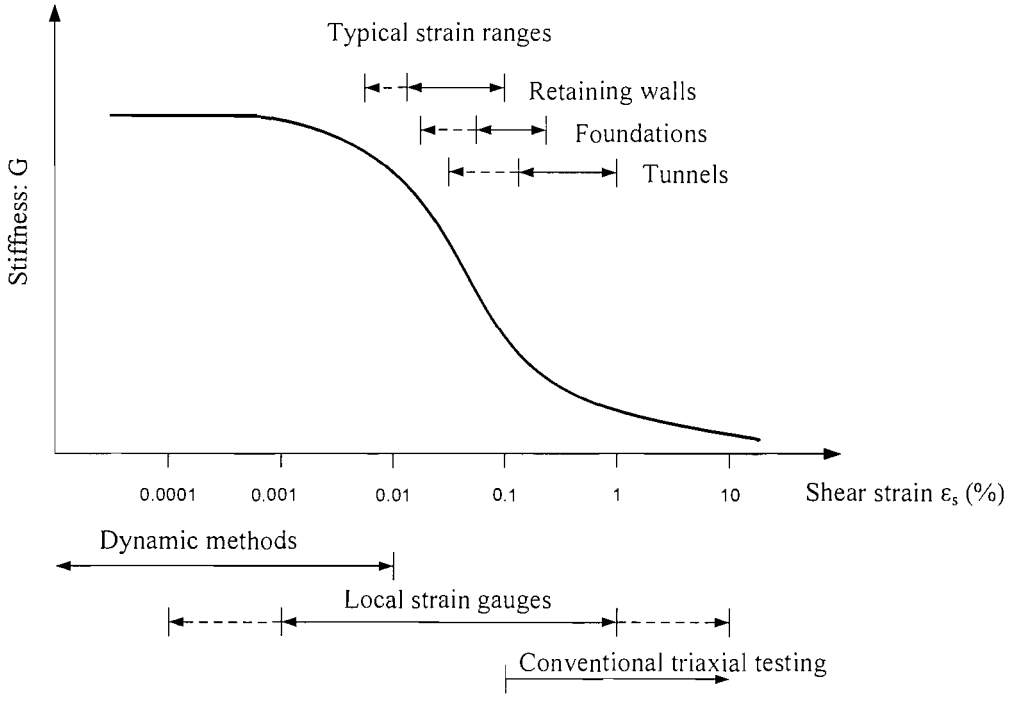

Figure 2.7 Characteristic stiffness-strain behaviour of soil with typical strain ranges for laboratory tests and structures (Mair, 1993)

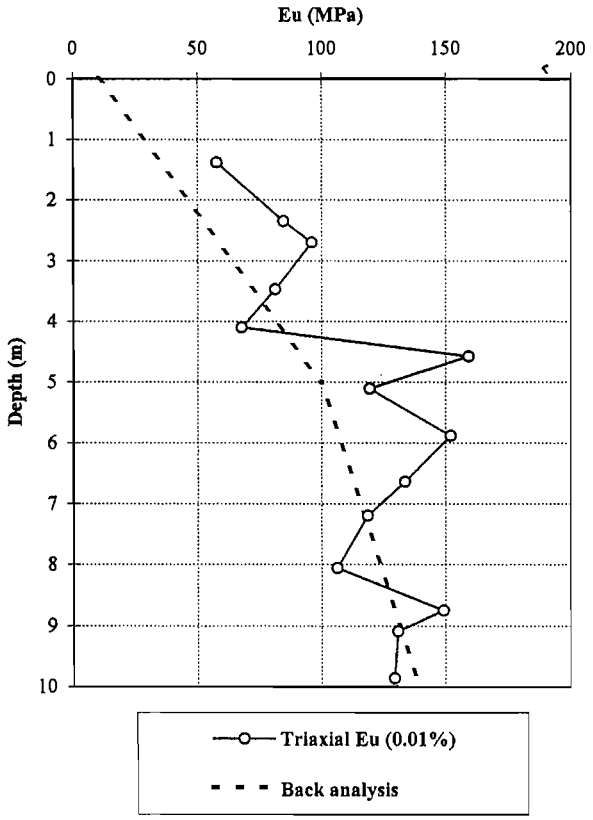

Figure 2.8 Comparison of stiffness of London Clay from triaxial tests (with local strain measurement) with those from back calculation (Jardine *et al.*, 1985)

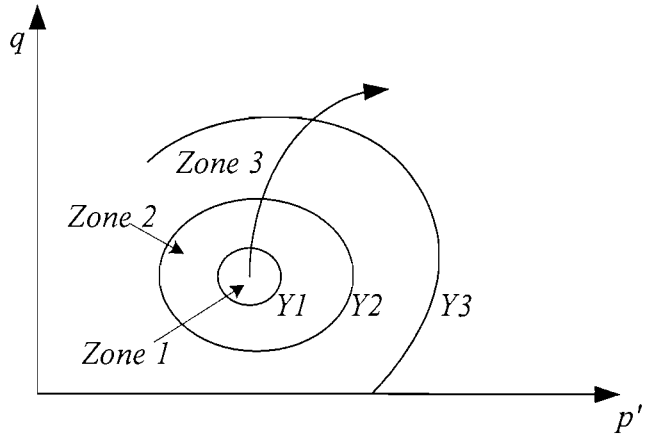

Figure 2.9 Identification of Zone I, II and III in triaxial stress space (Jardine *et al.*, 1991)

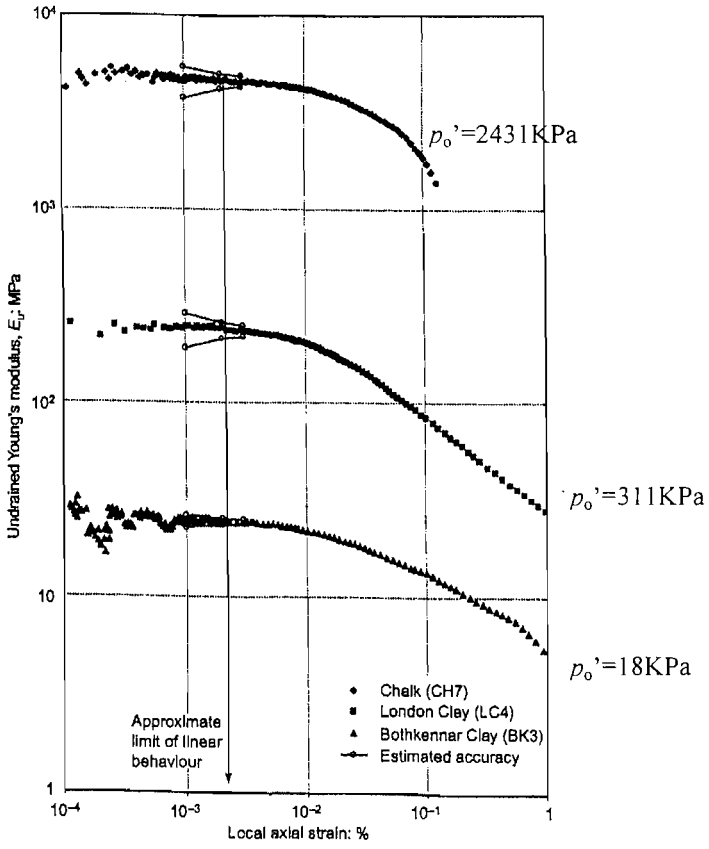

Figure 2.10 Comparison of small strain stiffness behaviour of three different natural geomaterials (Clayton & Heymann, 2001)

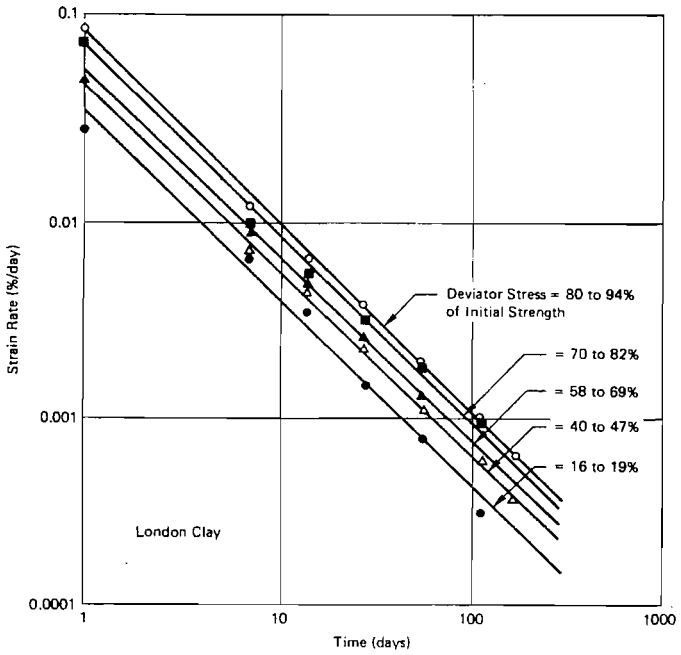

Figure 2.11 The creep behaviour of London Clay (Bishop, 1966)

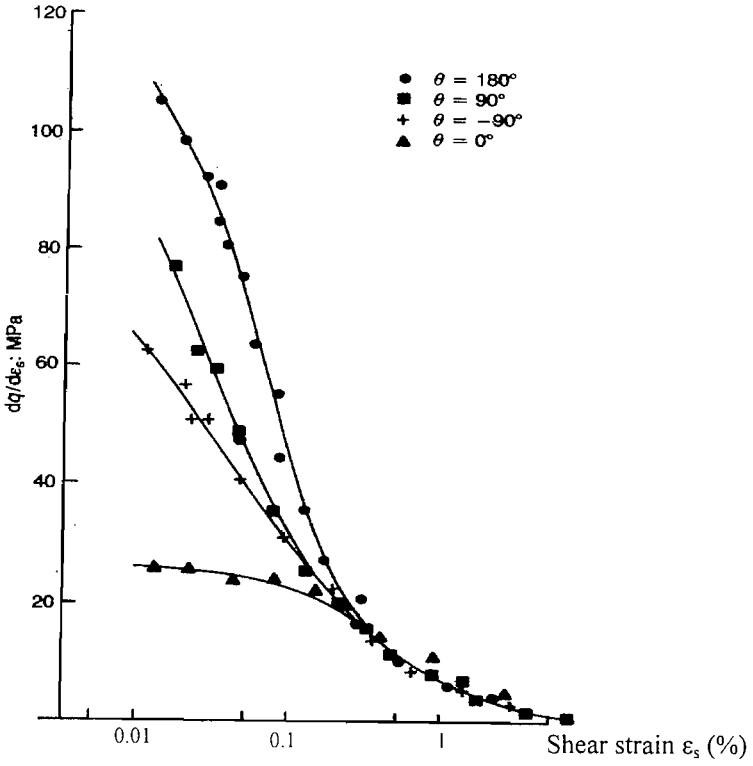

Figure 2.12 The effect of recent stress history on reconstituted London clay (Atkinson *et al.*, 1990)

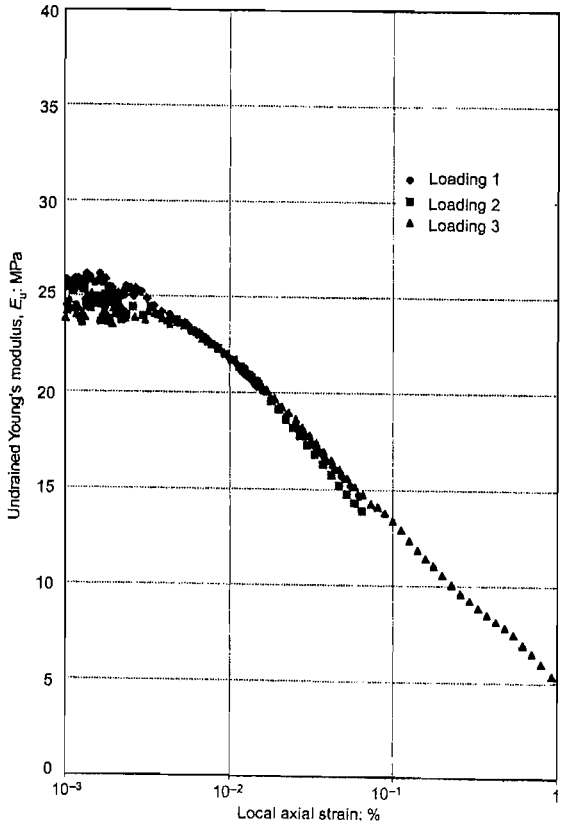

Figure 2.13 The stiffness behaviour of a single Bothkennar clay specimen subjected to three identical repeated loading paths (Clayton & Heymann, 2001)

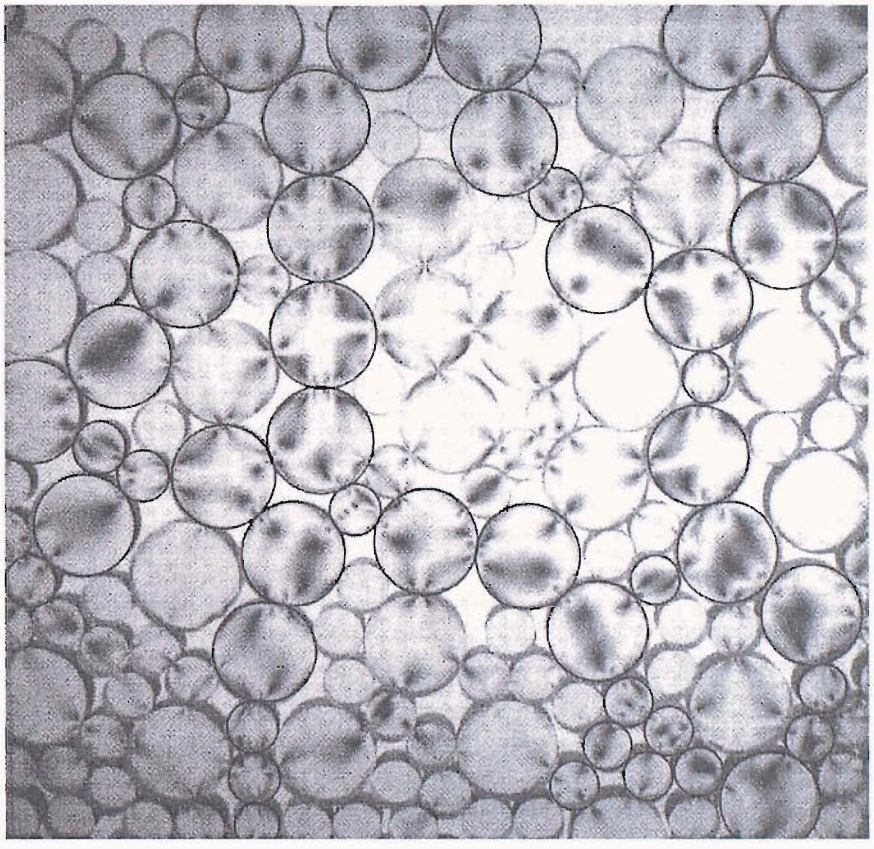

Figure 2.14 Column-like structure for granular particles under loading (from Santamarina *et al.*, 2001)

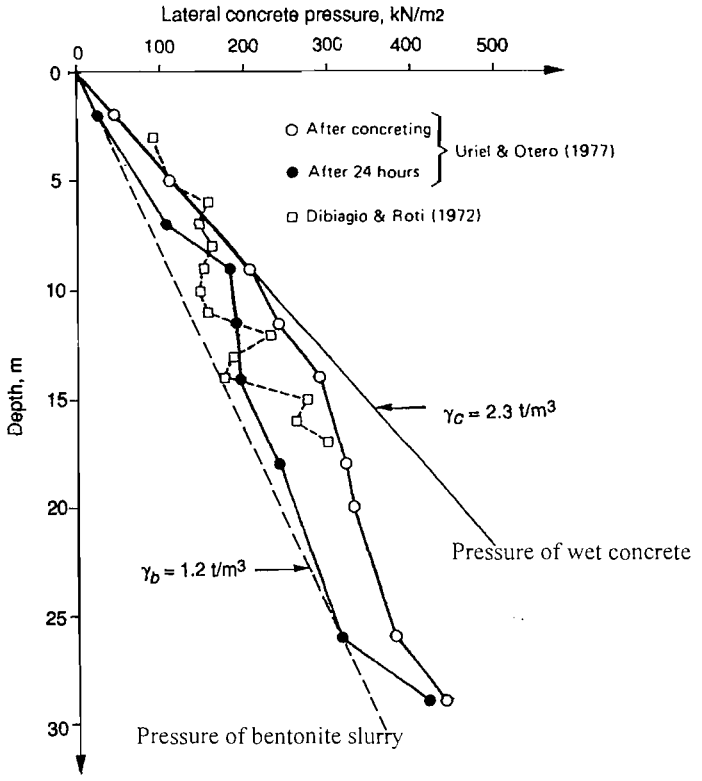

(a) Total horizontal stress measured in diaphragm wall panels (from Clayton & Milititsky, 1983)

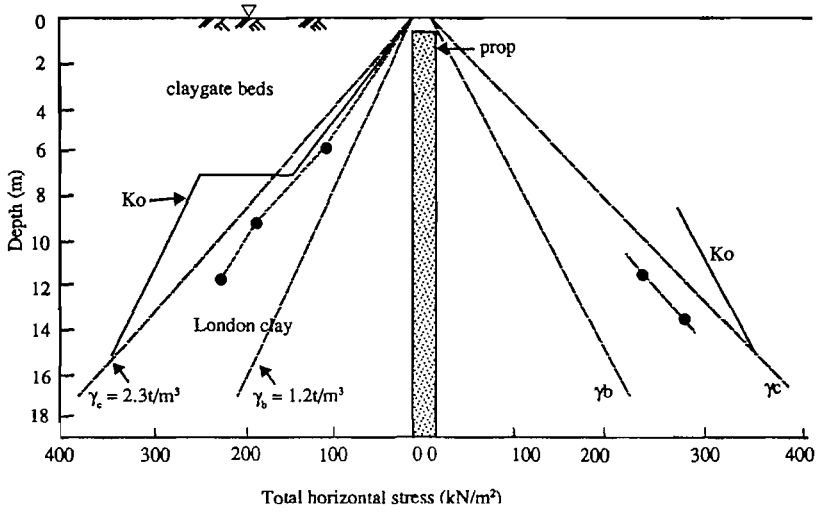

(b) Total horizontal stress measured adjacent to the Bell Common retaining wall (from Tedd *et al.*, 1984)

Figure 2.15 The effects of wall installation

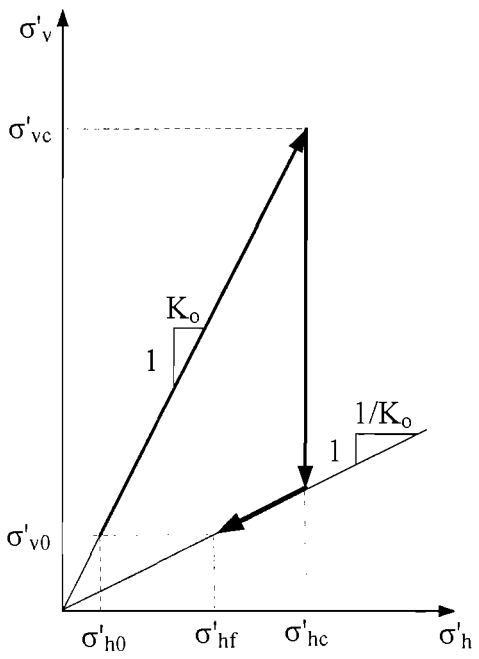

(a) Stress path for shallow soil element

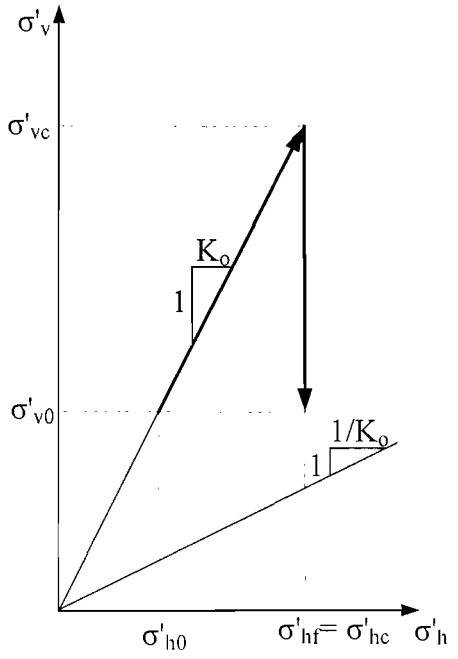

(b) Stress path for deep soil element

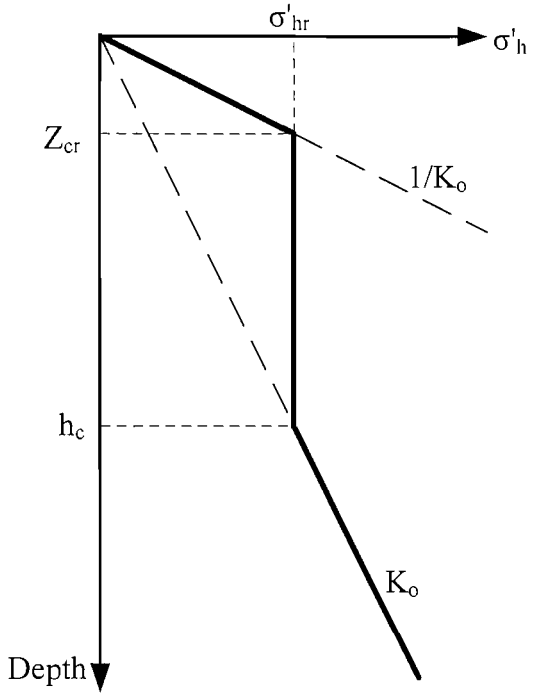

(c) Stress distribution after construction

Figure 2.16 The pressure of compacted granular materials (Broms, 1971)

Chapter 3 Prediction of stress path and cyclic radial strain

For a typical integral abutment with a retained height of 8m, a representative soil element (key soil element) was taken to be at mid retained height, *i.e.* at a depth of 4m below the top of the bridge deck, and at a small distance behind the abutment wall (Figure 3.1a). Although changes in earth pressure coefficient may not be as large at this level as near the surface of the backfill, they are subject to greater vertical stress levels, and the lateral stress changes induced will have a greater effect on the bending moments in a propped wall. In this chapter, estimation will be made about the total stress path and the magnitude of cyclic radial strain that could be imposed on the representative soil element as a result of temperature-induced abutment rotation.

3.1 Prediction of the total stress path

For simplicity (since this avoids the need to introduce principal stress rotations during cycling) the abutment wall was assumed to be smooth, and the friction between the abutment and soil was neglected. For a smooth abutment wall the thermal movements of the deck essentially lead to changes in the horizontal total stresses in the soil behind the wall, whilst the vertical total stresses remain constant, fixed by the weight of overburden. The total vertical stress σ_v can be estimated as:

$$\sigma_v = \gamma z \qquad (3.1)$$

where γ is the soil bulk density and z is the depth of the soil element. The total stress path could be represented as a 135° line in the s-t stress space (Figure 3.1b).

The initial stress state before cyclic loading will be discussed in the test programme for clay and sand respectively in the following chapters (Section 5.4.2 and 6.4.1).

3.2 Prediction of the cyclic radial strain range

The cyclic radial strain in the representative soil element will be estimated from Finite Element analysis first. Comparison will be made with strains derived from a simplified method, the geostructural mechanism, which was initially proposed by Bolton and Powrie (1988).

3.2.1 Finite element analysis

The analyses were carried out using the continuum finite element program CRISP (Britto & Gunn, 1987). The effect of soil stiffness and the magnitude of the cyclic abutment top displacement have been investigated.

For the typical embedded abutment and frame abutment in Figure 1.3, the finite element mesh and the displacement boundary conditions in the FE analysis are shown in Figure 3.2. All deformations are assumed to occur in plane strain. A 3-D analysis could give a more realistic simulation in cases with complicated boundary conditions (Bloodworth, 2002). However, a plane strain assumption still can lead to a satisfactory result in the analysis of regular retaining structures. The idealized geometry is symmetrical about the centreline line, so the mesh represents half the cross-section. The bottom and the far vertical boundaries are placed sufficiently remote from the abutment for changes in stress and strain there to be negligible. Smaller elements are placed in regions around the abutment where the greatest stress or strain gradients are expected. In regions where the changes in stress or strain are expected to be small, larger elements are used with little loss of accuracy.

Both the soil and the abutment are modelled using linear strain quadrilateral elements. To simplify the problem, the bridge deck is modelled as a rigid prop at the abutment crest as indicated in the figures, and the thermal cyclic deck length change is simulated by a cyclic horizontal movement of the prop. Slip elements are used to simulate a smooth vertical interface between the soil and the abutment. For the horizontal interface between the frame abutment base and the soil beneath, a friction angle of 40^{o} is assumed.

The effect of soil stiffness on the cyclic lateral strain range in the representative soil element is investigated. The soil is modelled as linear elastic isotropic material with Young's modulus increasing linearly with depth. Three different Young's moduli over a wide range have been examined, which are E_1=15000+15000z, E_2=5000+5000z and E_3=1500+1500z (kPa), where z (m) is the depth below the abutment top. The soil is assumed to have a Poisson's ratio of 0.25, and a bulk unit weight of 20kN/m^3. The reinforced concrete wall is modelled as linear elastic material with Young's modulus 30GPa, Poisson's ratio 0.15, and unit weight 20kN/m^3.

A total cyclic displacement of 16mm is applied to the crest of the abutment to simulate the annual temperature influence on a 60m long concrete bridge deck. The

annual cyclic lateral strain range experienced by the representative soil element 4m depth behind the abutment, from different soil stiffnesses, are summarized in Table 3.1.

Table 3.1 Annual cyclic lateral strain ranges in the representative soil element (at a depth of 4m, and just behind the abutment) derived from different soil stiffness

Total annual abutment top displacement d (mm)	Young's Modulus of soil (kPa)	Total annual cyclic lateral strain range in the representative soil element (%)	
		Embedded abutment	Frame abutment
16	15000+15000z (m)	0.081	0.093
16	5000+5000z (m)	0.080	0.097
16	1500+1500z (m)	0.076	0.099

It is evident that the change of soil stiffness has only marginal influence on the cyclic lateral strain range. This could be attributed to the geometry of this particular problem. In the region around a stiff integral abutment, the geometry, mainly the shape of the rigid abutment body and the horizontal displacement of the abutment top, has a predominant influence on the horizontal deformation of the soil behind the abutment. Therefore, the magnitude of the cyclic lateral strain range in the soil depends little on the actual soil properties, such as stiffness. A similar observation was made for deep penetration problems, where the Strain Path Method was used (Baligh, 1985).

It is beneficial to note that the purpose of the simulation is to estimate the annual cyclic lateral strain range, which will be used as input in the radial-strain controlled cyclic stress path testing. Realistic change or accumulation of vertical strain, volumetric strain or stresses are not expected to be obtained from this analyses, or other more advanced modelling, because the soil stress-strain behaviour remains unknown (Section 2.3). They will be investigated in the following experimental programme.

For different annual abutment top displacement (or concrete deck length), the annual cyclic lateral strain ranges in the representative soil element are compared in Table 3.2.

Table 3.2 Annual cyclic lateral strain range for different concrete deck lengths

Concrete deck length (m)	Total annual abutment top displacement d (mm)	Total annual cyclic lateral strain range in the representative soil element (%)	
		Embedded abutment	Frame abutment
90	24	0.120	0.144
60	16	0.080	0.097
30	8	0.040	0.048

3.2.2 Comparison with a simplified method

The cyclic radial strain in the representative soil element is also estimated by a method using a geostructural mechanism, which was initially proposed by Bolton and Powrie (1988).

In the geostructural mechanism, a simplified admissible strain field is assumed compatible with a frictionless rigid wall rotating outwards by a small angle about the base (Figure 3.3a). A line at 45° to the vertical, extending upwards from the toe of the wall, divides the soil into two regions. Inside triangle AOV, the strain increment is approximately uniform, and outside the triangle the soil is assumed undeformed. The horizontal strain increment $\delta\varepsilon_h$ inside AOV can be calculated by the extension $h\delta\theta$ in AV:

$$\delta\varepsilon_h = -\frac{h\delta\theta}{h} = -\delta\theta \qquad (3.2)$$

where h is the length from the pivot to the wall crest. Bolton and Powrie (1988) suggested that inward rotation of the wall simply caused the signs of the strains to reverse, with the absolute value unchanged.

For a rigid propped embedded wall VW rotating about a point O near its toe, six of these deforming triangles may be used to construct an idealized deformation mechanism, as shown in Figure 3.3b. As before, the lateral strain increment in each of the six deforming triangles is assumed to be uniform and equal to the incremental wall rotation $\delta\theta$. Similar principles are used to define the deforming triangles in the soil around a propped rigid wall rotating about the crest.

Bolton and Powrie (1988) validated the geostructural mechanism by comparing the soil displacement computed in this method with those measured during a centrifuge test on an unpropped wall (Figure 3.3c). It can be seen that the two patterns of deformation are in good agreement.

To estimate the lateral strain behind an integral abutment using equation 3.2, it is necessary to determine the position of the pivot. Springman *et al.* (1996) demonstrated in their centrifuge tests that a rigid embedded integral abatement tends to rotate around a point near the bottom of the wall when it is under cyclic displacement on the crest. Bolton and Powrie (1988) also noted that during excavation a rigid unpropped wall rotates around a pivot just above the toe. Therefore, for a typical embedded integral abutment as shown in Figure 1.3a, the wall is assumed to rotate around a pivot point close to the toe and in this case, the length h above this pivot point is assumed to be 18m. However, it should be noted that when h varies from 19m to 16m, the value of $\delta\varepsilon_h = d/h$ increases only by 19%, which is not significant for the purpose of estimation.

For the frame abutment as shown in Figure 1.3b, the wall is assumed to rotate around its base and h=8m. The total annual cyclic lateral strain ranges inside the representative soil element for different cyclic abutment top displacement can be derived using equation 3.2. Comparisons are made with those from FE analysis in Table 3.3.

Table 3.3 Comparison of annual cyclic lateral strain ranges in the representative soil element derived from finite element analysis and the simplified method

Total annual abutment top displacement d (mm)	Total annual cyclic lateral strain range behind an embedded abutment (%)		Total annual cyclic lateral strain range behind a frame abutment (%)	
	From FE analysis	$\delta\varepsilon_h$= d/h	From FE analysis	$\delta\varepsilon_h$= d/h
24	0.120	0.133	0.144	0.3
16	0.080	0.089	0.097	0.2
8	0.040	0.044	0.048	0.1

For the embedded abutment, the FE analysis and the geostructural mechanism give close results. For the frame abutment, the geostructural mechanism overestimates the cyclic lateral strain range, compared with that derived from FE analysis. One reason is that the deformation of the frame abutment involves not only rotation, but also horizontal translation. Thus the assumption in the geostructural mechanism that the wall only rotates around its base imposes a stricter boundary condition that leads to a larger wall rotation and therefore a larger lateral strain in the soil. Furthermore, the geostructural mechanism was originally proposed and validated for long embedded wall (Bolton & Powrie, 1988), the strain behind which may be more suitable to be

estimated using this method. Even so, the geostructural mechanism still gives a reasonably conservative estimation of the cyclic lateral strain. An advantage of the geostructural mechanism is its flexibility, and instant judgement can be made about the radial strain change when the geometry of the problem changes.

During the experimental program, soil specimens will be subjected to different cyclic radial strain ranges, which will cover the magnitudes obtained from the FE analysis and geostructural mechanism (as listed in Tables 3.2 and 3.3).

3.3 Summary

In this chapter, the total stress path and cyclic radial strain range have been estimated for the representative soil elements behind integral abutments. It can be seen that the idealized total stress path is a 135^{o} line in the *s-t* space, which is different from a normal 45^{o} stress path. Furthermore, the cyclic radial strain range is small (at the level of 0.1% for typical abutments). In Chapter 4, the development of an automatic triaxial cyclic loading system will be described, which is capable to carry out small radial strain-controlled cyclic testing following the required stress path.

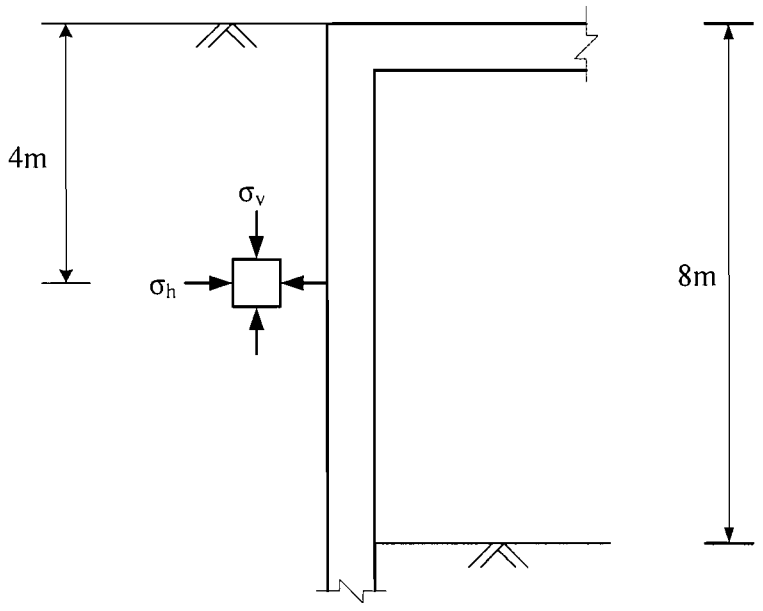

(a) The location of the representative soil element, which will be tested in the laboratory

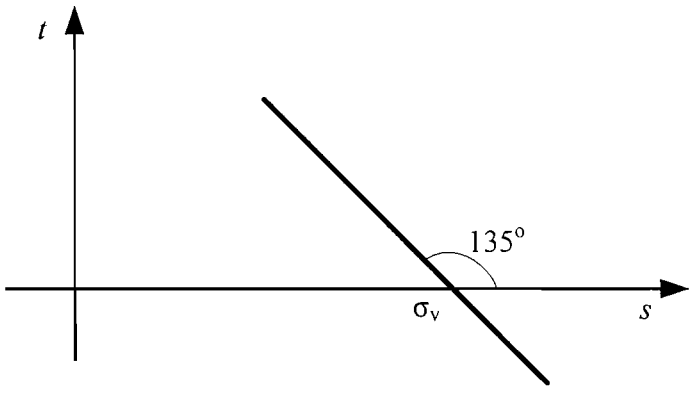

(b) The idealized total stress path in *s*-*t* stress space for the representative soil element

Figure 3.1 The location and idealized total stress path for the representative soil element

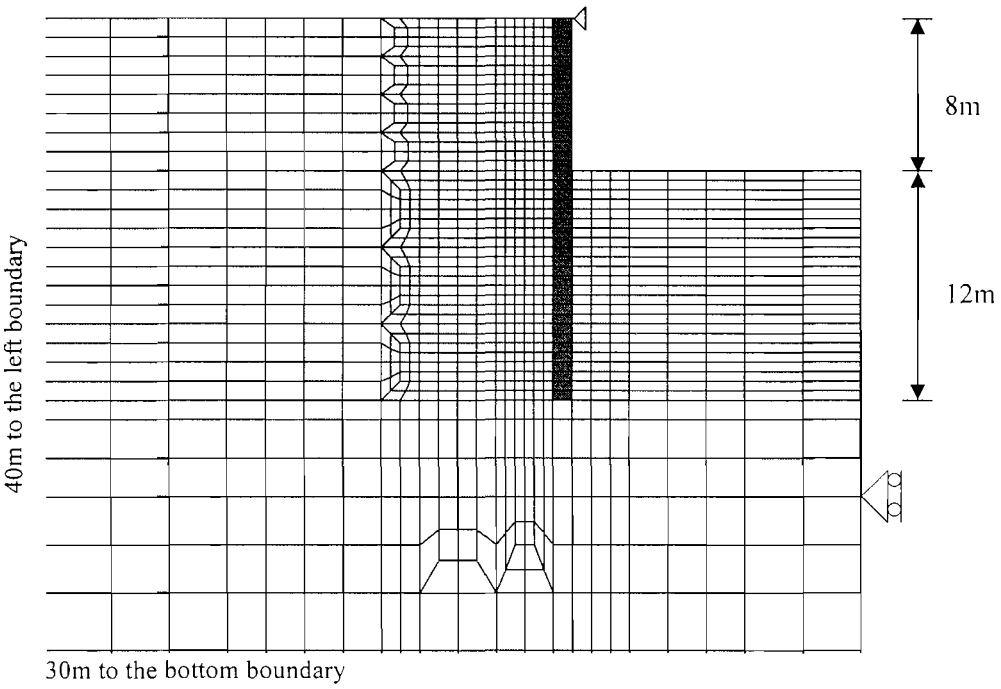

(a) embedded integral abutment

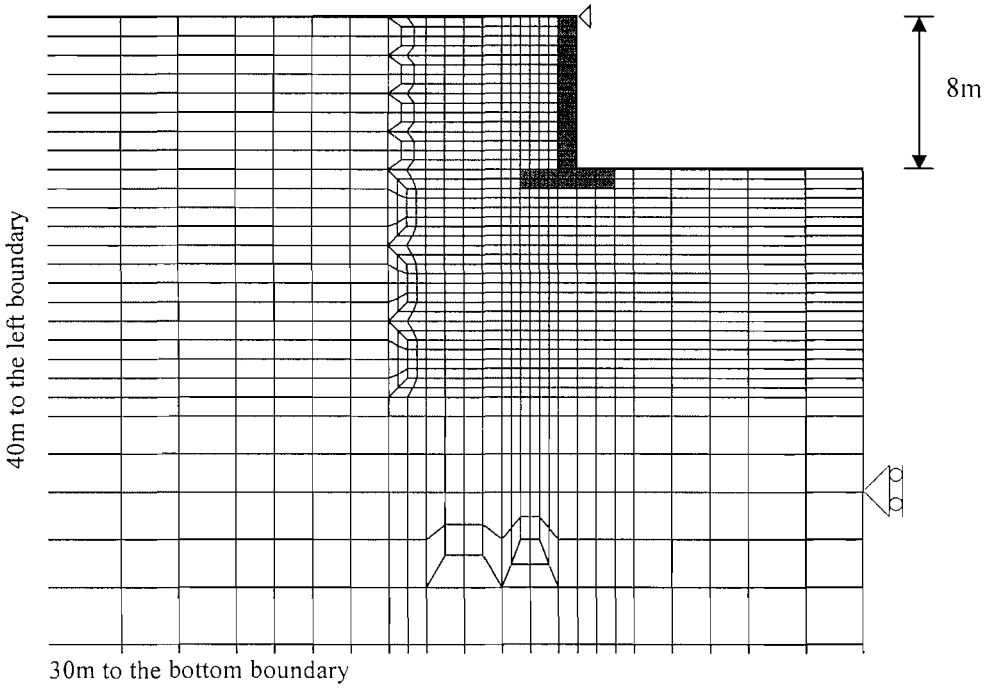

(b) frame integral abutment

Figure 3.2 Mesh for the finite element analysis

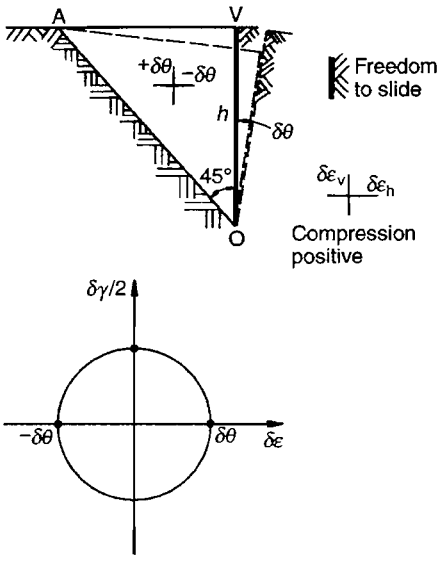

(a) Idealized deformation pattern for a rotating wall and corresponding Mohr cyclic of strain

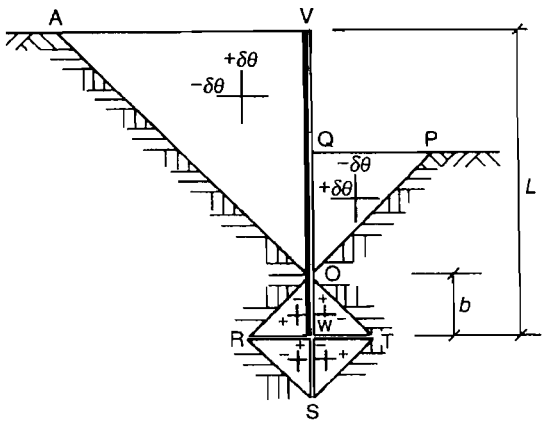

(b) Synthesis of idealized displacement pattern for a stiff unpropped wall, rotating about a point near its toe

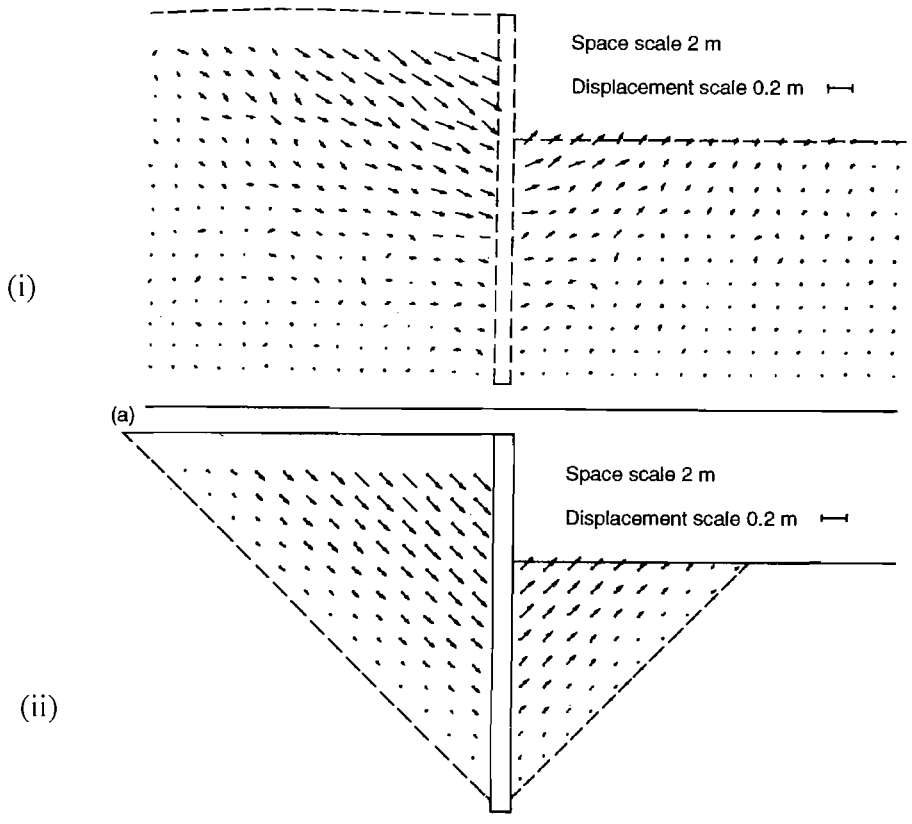

(c) Comparison of (i) measured and (ii) calculated soil movements for an unpropped wall of retained height 10m and embedment 20m

Figure 3.3 The geostructural mechanism proposed by Bolton & Powrie (1988)

Chapter 4 Development of an automated triaxial cyclic loading system

4.1 Introduction

In this research, radial strain-controlled cyclic loading tests were performed with a constant total vertical stress to investigate the behaviour of a representative soil element behind an integral abutment. A long testing period was expected, which might perhaps last for weeks or even months. These requirements could not be achieved by manual control as in a conventional triaxial test. Therefore, an automated triaxial cyclic loading system was developed in this research. The major functions of this system include:

1) to carry out radial strain controlled cyclic loading following a 135° total stress path closely in the *s-t* space, with the stress and strain measured accurately;
2) to be able to allow a rest period after a stress excursion for stress relaxation (or strain creep);
3) to conduct cyclic testing over a long period without attention, detecting and correcting any possible errors automatically in the process;
4) to be flexible for any special requirement emerging during the experimental investigation.

This chapter will first describe the system equipment. Then the instrument and measuring devices will be introduced, as well as the calibration of transducers. The technique for local small strain measurement will be discussed extensively. Finally, the development of the control software will be discussed, which integrates the whole system and conducts the desired cyclic loading automatically.

4.2 System equipment

The experimental system consisted of four major parts, the Bishop & Wesley hydraulic triaxial cell, the pressure control system, the signal conditioning unit, and the computer. A photograph about the system in operation is presented in Figure 4.1 and a general layout is schematically illustrated in Figure 4.2. The whole system was operated in an air-conditioned environment with a constant temperature of 20°C.

4.2.1 The Bishop &Wesley Hydraulic Triaxial Apparatus

The apparatus for controlled stress path testing on 100mm diameter specimens was manufactured by Wykeham Farrance Ltd, based on the design of Bishop and Wesley's hydraulic triaxial apparatus (Bishop and Wesley, 1975).

The cell chamber was manufactured from Perspex and had four circumferential reinforcements to allow a maximum working pressure of 1700 kPa. The cell was held in place by six external tie rods. It had an inside diameter of 166mm, which was marginally larger than the 100mm diameter soil specimen with full instruments setup. Great care and patience was required when closing the cell to avoid disturbing the LVDTs and mid-plane probe.

The apparatus was self-contained and required no loading frame. Axial force was exerted on the test specimen by moving the sample pedestal upwards or downwards. The base pedestal had a diameter of 100mm and was fitted with a high air entry ceramic porous stone. The base pedestal was mounted at the top of a loading ram by six 6mm screws. At the bottom end of the loading ram there was a piston and lower pressure chamber. The lower pressure chamber had an inside diameter of 162 mm and was filled with de-aired water. Two Bellofram rolling seals were used to retain the cell fluid and the lower chamber fluid. The ram travelled up and down in a linear guide comprising a cage of ball bearings housed in a turret joining the cell to the base. Accordingly axial ram friction was very small. The pedestal and loading ram were moved upwards or downwards by pumping the water in or out of the lower pressure chamber. External strain measurement was made by measuring the vertical displacement of the cross-arm arrangement attached to the ram.

Four valves with pressure transducers were fitted to the cell. Three were for the measurement of pore water pressure (the top, the mid-plane and the base). The fourth was for the cell fluid. There was also a valve fitted to the lower chamber with a pressure transducer. All de-airing blocks were oriented with the transducers vertical and the sensing membrane facing upwards, which allowed the air to be expelled through the air bleed plug at the top of the block during flushing. Valves were placed on both sides of each de-airing block, which was particularly useful to allow calibration of the transducers without removing them from the de-airing blocks and to flush the pipe lines during test.

The valve manifold allowed a number of useful tasks to be performed. The water from the de-airing reservoir could be routed to any one of a number of destinations including, the cell chamber, the lower chamber, base pedestal, top cap, mid-plane probe and the three water-filled pressure controllers.

A flat top cap was designed for the tests in which only positive (compressive) deviator stress was desired (Figure 4.3), since traditional top caps with a conical recess would force the top cap to align with the loading ram and cause specimen bending (Baldi *et al.*, 1988). The flat top cap had a diameter of 100mm and a thickness of 30mm. The top cap body was made of Perspex with a stainless steel disc (50mm in diameter and 5mm in thickness) recessed in the centre of top surface. The surface of the steel disc was polished to minimize the friction between the top cap and the hemispherical end of the ram.

In the tests in which negative deviator stress was required, an extension device was used. At first a commercial suction device for 100 mm diameter specimen was adopted, which consisted of a suction cap, a Vylastic sleeve and a top cap. It was soon found that the enlarged suction cap was too bulky, and there was very limited space between the suction cap and the cell chamber. This caused a problem with the suction pipe, which was guided out from the side of the suction cap and was open to the atmosphere on the other end. The suction pipe was found to be pushed firmly against the internal surface of the cell chamber, which introduced considerable horizontal force and vertical friction onto the loadcell. To overcome this problem, a 70mm commercial suction device was used, with the top cap re-designed to adapt the 100mm specimen (Figure 4.4). The purpose-designed top cap was machined from a whole Perspex block to such a shape that it consisted of two cylinders; the upper one with a diameter of 70mm and a height of 10mm, and the lower one with a diameter of 100mm and a height of 25mm. This design was compact and could be installed easily in this cell chamber. Another advantage of this design was that the Vylastic sleeve would not be pushed too low when docking the suction cap, since the lower part of the top cap would stop the movement of the sleeve. In contrast, for a conventional top cap with a shape of a whole cylinder, this might happen and the triaxial cell chamber had to be opened to adjust the position of the sleeve.

4.2.2 The pressure control system

Three digital pressure/volume controllers manufactured by Geotechnical Digital Systems Ltd (GDS) were used for pressure control. The cell pressure and lower chamber pressure were controlled by two advanced controllers (Serial Nos. 000870 and 000872), while the back pressure was controlled by a standard controller (Serial No. 02404). Each controller was filled with de-aired water. The advanced controllers had a fluid storage capacity of 1000 cm^3 while the standard controller had a capacity of 200 cm^3. The controllers operated on the principle of varying the pressure in the cylindrical vessel by the inward and outward movement of a piston connected to a geared stepper motor via a threaded shaft. A feedback loop between a pressure transducer which monitored the pressure in the vessel and the control circuit of the stepper motor ensured that the target pressure was achieved. Pressure changes could be entered using the key pad, or alternatively the command could be made digitally by a computer though an IEEE-488 port (to advanced GDS controllers) or RS-232 port (to standard GDS controller).

4.2.3 The signal conditioning unit

The signal conditioning unit received the output analogue signals from various measurement devices, amplified and converted them to digital form, and then passed this information to the computer. The unit incorporated within the system was an ADU signal conditioning system manufactured by ELE International Ltd. The system consisted of a series of function modules, including two analogue input modules, one analogue to digital converter (ADC) module and one microprocessor module.

Analogue input module

The analogue input module was a general purpose input scanner capable of accepting up to 8 separate signal sources. It also featured a 10V stabilized power supply for transducer excitation. A total of ten channels in two analogue input modules were allocated to monitor signals from ten transducers within the system, which were specified as below:

Channel 1: Axial LVDT-1

Channel 2: Axial LVDT-2

Channel 3: Radial LVDT

Channel 4: Mid-plane pore water pressure

Channel 5: Base pore water pressure

Channel 6: Cell pressure

Channel 7: Load cell reading

Channel 8: External strain-1

Channel 9: External strain-2

Channel 10: Lower chamber pressure

Analogue to digital converter (ADC) module

In the analogue to digital converter (ADC) module, analogue signals from various measurement devices were amplified and offset, before being converted to digital form.

The ADU function *Gain* (that is, amplification) was applied to analogue input channels so that a higher resolution could be achieved from the incoming signal. The amplification range could be varied from Gain 0 (amplify 2^0=1 time) to Gain 10 (amplify 2^{10}=1024 times). Any gain value was allowed as long as the equivalent voltage at the input to the ADC did not exceed ±10V. Higher gain would bring a higher resolution, but also would cause a smaller measurement range, if no offset voltage was applied. To obtain a full stress-strain curve, higher resolution for strain measurement was needed at the small strain level, while a larger measurement range became necessary at medium or large strain level. A method was designed in the control program to achieve this requirement. At the start of each shear stage, a higher gain was allocated. When the output reading became larger and close to the end of the current measurement range, a lower gain was automatically allocated, so that the strain could be measured at a larger range without interruption.

The offset function did not amplify the incoming signal, but it could pull the incoming signal voltage to an optimized range, so that a higher gain could be applied without reducing the measurement range. For example, the pressure transducers always produced a positive output voltage, *e.g.* 0~70mV corresponding to a pressure range of 0~700kPa. If no offset voltage was applied, at most Gain 7 (amplify 2^7=128 times) could be allocated. However, when an offset voltage of -35mV was applied and the output voltage was offset to a range of -35mv~35mV, Gain 8 (amplify 2^8=256 times) could be

allocated while the pressure measurement range was kept the same. The maximum offset voltage provided by the ADU was ±5 V. It is important to understand where the offset voltage was applied. The signal amplifier in the ADC module had two sections. After the signal was amplified by the first amplifier section, the offset voltage generated by the ADU was applied to the output, after which the resulting signal passed to be amplified by the second amplifier section.

Finally, the signal voltages were converted to digital readings, which ranged from 0 to 4096, by the 12-bit analogue to digital converter module. Conversion time for the converter was 25 ms, which was adequate for the slow rate testing carried out during this research.

The microprocessor module

The microprocessor module contained the microprocessor system which controlled the functions of the other modules. It also contained a RS232 interface to enable standard interconnection to the computer.

4.2.4 The computer

A PC was used as the central controller for the whole system. This sent commands to the pressure controllers and signal conditioning unit, while receiving and storing data. A computer program was developed to control the whole system automatically, which will be discussed in section 4.5.

4.3 System instrument and measuring devices

4.3.1 Measurement of load and stress

Load cell

Axial load was measured by an internal submersible load cell manufactured by Thames Side Maywood Limited (Model 4958). Compared with external load measurement, an internal load cell has the advantage that errors from ram friction will not

be introduced in measurement. This is crucial when load changes at small strain levels are to be measured, for example when detecting very small strain stiffness.

Pore water pressure transducers

Four pressure transducers were used to measure cell, mid-plane, lower chamber and back pore water pressure. These were all PDCR 810 transducers manufactured by Druck Ltd, with a maximum pressure range of 1000 kPa. The sensing element was a silicon diaphragm with an integrated silicon strain gauge bridge, giving high performance as reflected in the manufacturer's specification of a combined non-linearity and hysteresis of less than ±0.1% of full scale.

Mid-plane pore pressure probe

Measurement of pore pressure was required for the determination of effective stresses in undrained triaxial tests. Conventionally the pore water pressure is measured at the base. However, non-uniform pore pressures occur during undrained triaxial tests as a result of end constraints. Bishop and Henkel (1962) suggested two possible solutions to the problem. Firstly, run the test at such a slow rate that the pore pressure is uniform throughout the specimen, and measure the pore pressure at the ends of specimens. Alternatively, make internal local measurement of pore pressure at the mid-height of the specimen. Compared with base pore pressure measurement, mid-height pore pressure measurement was made directly on the specimen and the influence of end restraint was small. Therefore, instant and accurate measurement of the change in pore water pressure at relatively fast shear rate can be obtained.

A flushable mid-plane probe was used in the triaxial apparatus (Figure 4.5). The probe was based on the design of Sodha (1974) and consisted of cylindrical high air entry ceramic of 10 mm diameter, glued into a stainless steel casing with 15 mm of the ceramic extending from the casting. Two small-bore stainless steel tubes entered the back of the casing; one entered the back of the probe casing at the centre while the other entered the casing at the edge. The casing was oricntated with the off-centre tube at the top. This was necessary to remove any air during the de-airing process, as de-aired water was forced into the mid-plane probe through the centre tube and exited the probe by the off-centre tube. These two tubes were guided from the cell through one of the plugs in the

cell base. The loose end of the entry tube was connected to a de-airing block with a pressure transducer, while the loose end of the exit tube was connected to a valve to close the system.

The mid-plane pressure probe was always kept in pressured water between two tests. If the probe was left in air for too long, it would be very difficult to fully saturate the ceramic again and the pressure reading would be unstable. The tubes and the cavity behind the porous ceramic could be flushed at any time during the test, but at most once was necessary after the initial cell pressure was applied.

4.3.2 Measurement of local strains

The local strain measurement system in this research consisted of a number of components, namely the LVDT transducer, the transducer amplifier, the brackets for the axial LVDTs or the calliper for the radial LVDT.

LVDT transducer

Three unguided submersible linear variable displacement transducers (LVDTs) were used (type D5/200WRA/131, manufactured by RDP Electronic Ltd); two were for the axial strain measurement and the third was for radial strain. They had a linear range of ±5 mm, a linearity better than 0.1% and a sensitivity of 64mV/V/mm. These transducers were designed to provide high precision measurement in water or oil environments and had been previously proved to be very robust as well as being very accurate (Heymann 1998). The LVDT transducer contained a stainless steel tube, a moving armature and the electrical cable. The moving armature was a separate component from the body and could move freely along the tube over a large range of displacement, which prevented the transducer from damage when the specimen was under large deformation. At electronic zero position the armature extended 26.5 mm from the body, giving a total transducer length of 81.5 mm. The water was free to enter the tube and had no effect on the operation of the sensor.

The transducer had a right-angle connection between the tube and the electrical lead cable. The hermetic seal between the tube and the lead cable consisted of an internal rubber gland and a polyolefin shrink tube which covered the cable and right angle extension of the transducer body. The cable was thick and stiff, which caused difficulties

during the setup. The LVDT transducers were excited by a 5V alternating voltage at a frequency of 5 kHz.

The LVDT transducer amplifier

The S7AC transducer amplifier was also manufactured by RDP Electronic Ltd. It had two main functions: first, it acted as the power supply to the LVDT transducers; secondly, it amplified and provided offset voltage to the output signal from the LVDT transducers. It should be noted that the output signal from a LVDT transducer was amplified twice, first by the S7AC amplifier (pre-amplifier) and then by the ADU amplifier (main amplifier), before it was converted to digital data and logged by the computer.

The S7AC amplifier had both fine and coarse amplification. Coarse amplification adjustment was achieved via an eight position slide switch, which could provide a maximum amplification of 500 times. Fine amplification adjustment was by rotary 20-turn potentiometer, which could provide a 4:1 adjustment of gain. This design allowed initial coarse adjustment of the amplification level using the slide switch and subsequent fine adjustment by the potentiometer. It was found that the exact amplification level of the fine gain potentiometer was not easy to determine. Therefore, if the amplification was changed via the fine gain potentiometer after the system had been calibrated, it was difficult to return the system to the initial amplification level. This disadvantage was overcome by permanently fixing the potentiometer at a certain position and only using the coarse switch to change the amplification level.

The S7AC amplifier also provided offset voltage to the input signal, through *Fine Zero* and *Coarse Zero* adjustment. The coarse zero adjustment was achieved via a 9-position slide switch providing output zero shifts of about 1V per step and a offset voltage of ±4V at most. The fine zero adjustment was achieved via a screwdriver-adjusted, 20-turn potentiometer allowing a largest adjustment of output zero by ±1V. When using coarse and fine zero adjustment together, any output up to 5V could be suppressed. The zero function provided only an offset voltage to the input signal and did not influence the input signal resolution.

The *Fine Zero* and *Coarse Zero* function was particularly useful at the beginning of a shear stage when small strain measurement was needed and a high amplification gain had

to be adopted. At that time the output signal from the transducers always exceeded the small measurement range because of the large deformation in the previous stages, *e.g.* in the consolidation stage, even if great effort and care had been taken to position the armature around the electronic zero point and prediction was made about the possible deformation in the saturation and consolidation stage when installing the LVDTs on the specimen. In such cases, the output signal could be pulled back to the small measurement range by using the coarse and fine zero function, provided the armature had not moved too far from the electronic zero point.

An additional function in the S7AC was the *Zero Input* switch, which allowed the electrical zero position of LVDT to be found. When the switch was pressed, a zero voltage input was supplied to the S7AC amplifier. If the amplifier did not provide a zero output signal, it could be adjusted to zero by using the *Fine Zero* function. Once the output of the amplifier had been zeroed, the switch could be released and the electrical zero position of the LVDTs could then be found by adjusting the armature for a zero output signal.

One major problem found in tests was the influence of electronic noise on the output signals. Electronic noise was inevitable in the laboratory and it came from other electronic sources, *e.g.* the lighting, other transducers and the computer. To reduce the influence of electronic noise, the aluminium case and the cable shields of the S7AC had to be earthed properly. However, this was found to be inadequate for small strain measurement. When a high ADU gain was set to measure small strains, the output reading was found to jump strongly, even making such a measurement impossible. A simple but effective method was developed in this research, in which the gain of the pre-amplifier (S7AC) was set at its highest levels (Gain 7 or 8), while the gain of the main amplifier in the ADU was set at its lowest levels (Gain 1 or 2). As a result, the output voltage from pre-amplifier per micrometer deformation was maximized, so that it could easily exceed the magnitude of environmental electronic noise, which was generally at the level of 1mV. Using this method, the influence of electronic noise was reduced to an acceptable level and the final reading usually did not vary by more than ±1 bits. However, the influence of electronic noise was found to become a little larger when the LVDTs had been in operation continuously for a long period (about 1 year), probably because of the interaction between LVDTs.

The Brackets for the axial LVDTs

It was found difficult to setup the LVDTs using conventional brackets. After the setup of the LVDT, the armature should be at a position around the electronic zero point. This was necessary as the LVDT output could only be zeroed, or the reading could be pulled back to the small measurement range, by the coarse or fine zero function in S7AC amplifier, at a high amplification level if the armature was sufficiently close to the electrical zero point. For the conventional brackets, the armature rested directly on the bottom bracket. To adjust the output of the armature, the LVDT body tube, which was fixed on the top bracket, had to be loosened and moved upwards or downwards by hand. Such an adjustment was very coarse and it was found very difficult to position the armature around the electronic zero point, since the whole measurement range could be as small as about 0.3 mm.

Two new brackets were designed in this research to attach each LVDT to the 100 mm diameter specimen. Different from the design of conventional bracket, there was a pad screwed on the bottom bracket and very slight adjustment of its height could be made easily by hand directly or using a screw driver. Both the top and bottom brackets were made from aluminium and had a thickness of 10 mm. Each LVDT body was held in position by the top bracket and the armature rested on the pad of the bottom bracket.

The brackets were designed to hold the LVDT body close to the specimen (3 mm) in order to minimize possible errors from bracket rotation. Considering that the chamber cell diameter was small, the screw to fix the LVDT body was designed to be on the side of the top bracket to minimise the overall size of the instrument setup. The brackets were fixed on the membrane using impact adhesive (see Section 5.3.2). An example of the setup of an axial LVDT with the purpose designed bracket is shown in Figure 4.6.

The calliper for the radial LVDT

For the tests on stiff clay, radial strain ε_r was calculated as $\varepsilon_r=-\varepsilon_a/2$ for undrained tests; and $\varepsilon_r=(\varepsilon_{vol}-\varepsilon_a)/2$ for drained tests, where ε_{vol} is the external volumetric strain and ε_a is the local axial strain.

However, for coarse sand specimens under drained loading, the effect of membrane penetration can introduce considerable errors to the external volume measurement (Bica,

1991). Therefore it was necessary to measure the radial strain directly and locally on the coarse sand specimen.

A commercial calliper made from Perspex was evaluated at first (Figure 4.7a), which was based on the design by Menzies *et al.* (1977). It was found that the LVDT reading was likely to become "slack" or even "static", especially when there was a stress reversal. This problem became serious in the tests involving small strain cyclic loading. A number of factors were identified as below:

1) There was significant sliding friction in the area of the hinge, where the ends of the two Perspex arms were partially overlapped. Furthermore, the alignment guide plates also introduced considerable sliding friction.
2) The armature easily became jammed inside the LVDT tube during tests. Since the LVDT body and the armature were fixed on the calliper arms, it was very difficult to align the armature with the LVDT tube before tests.
3) The calliper arms were made from Perspex, which was essentially a soft material with a Young's modulus of only about 3GPa. In contrast, aluminium and steel has a Young's modulus of 70GPa and 210GPa respectively. When the specimen was changing in diameter, the frictions stated above might cause the calliper arms to deform, thus introducing errors. Furthermore, Perspex creeps under relatively small loads (Callister, 2000), which means that the arms themselves might creep under the weight of the LVDT and the stiff cable.
4) The two pads were fixed on the two calliper arms and could not rotate, which could introduce stress inside the hinge and the arms during the setup and tests. Furthermore, these two pads had only a small contacting area (10mm×20mm) with the membrane, which caused the calliper to rotate and slip under the weight of the LVDT.

Great effort was put into identifying and solving these problems, which were finally overcome by using a metal calliper, based on the design by Bishop and Henkel (1962) with improvements (Figure 4.7b). The main features were presented as below:

1) The two steel arms were kept in contact with a brass hinge by two springs without any guide plates. The friction in the connection was very small, compared with that in the Perspex calliper.

2) A weak rubber bellows was installed between the armature and the LVDT body, thus the armature was kept slightly touching the smooth vertical surface of an "L" shape steel attachment, which was fixed on the other arm. Therefore any possible jam between the armature and the LDVT tube was avoided.
3) The calliper arms were made from high-stiffness steel and had a width of 20mm, which could be reasonably considered as a rigid body.
4) Each pad could rotate around a pivot on the arm. These pads also had a much larger contacting area of 25mm×25mm. Furthermore, in the setup, a very thin layer of liquid adhesive was used between the pads and the membrane. Therefore, the slippage or rotation of the calliper was avoided.

To minimise any further possible slight friction, aerosol PTFE lubrication was sprayed on the hinge, the pivots and the LVDT armature.

When testing coarse sand specimens, the membrane would be pushed into the voids between particles by the cell pressure. When the cell pressure varied, the membrane penetration would also cause membrane thickness change (Figure 4.8a). This could introduce errors to the deformation detected by the calliper, which was attached on the membrane. A simple solution was adopted, which was originally developed by Bica (1991) and proved to be effective. Two pads (30mm × 30mm) were cut from an aluminium sheet (0.8 mm thick). These pads were bent, so that the curvature matched the sides of the specimen. These pads were glued inside the membrane, just beneath the calliper pads. As a result, the membrane was separated from the sand at the area under the calliper pads and could not penetrate into the voids during tests (Figure 4.8b).

4.3.3 Measurement of external strains

External axial strain measurement

The external axial deformation of the sample was measured using a direct current linear gauge manufactured by Measurements Group, Inc. The gauge was spring loaded and had a measurement range of 25 mm. It operated on the principle of two parallel metal plates forced apart by the armature, resulting in bending of the plates. Bonded strain gauges, configured in a full Wheatstone bridge arrangement, sensed the strains in the plates and by calibration a relationship between displacement and output was established. As

contact occurs between the armature and the plates, these transducers can be expected to suffer from hysteresis and mechanical wear (Heymann, 1998).

Volume change measurement

External volume change of the saturated soil specimen in drained tests was made by the back pressure GDS standard controller, which had a volume change gauge resolving to 1 mm^3. Great care was taken to check the connections and ensure that there was no liquid leakage before tests by keeping the controller under a constant high pressure over a few days while monitoring the volume reading change. Furthermore, to fulfil the assumption made in the external volume measurement that water is incompressible, the system was fully de-aired using water from a Nold Deaerator, and the specimen was completely saturated with a back pressure of at least 500kPa.

4.4 Calibration of transducers

4.4.1 Calibration methodology

All the measurement transducers were calibrated to evaluate the accuracy and precision of the transducers. A consistent calibration methodology (Heymann, 1998) was adopted which consisted of the following steps:

1. The whole transducer system, including the transducers and signal conditioning unit, was calibrated against a suitably accurate reference. A minimum of 12 calibration points were used over the calibration range of each transducer.
2. A least squares linear transfer function was derived to describe the relationship between the digital output (in bits) and the true value (engineering units).
3. The error was calculated for each calibration point as the difference between the true value (engineering units) and the measured value (output converted to engineering units using the transfer function).
4. The errors were plotted against the true value for instant visual assessment of the maximum error, non-linearity and hysteresis of the instrument.
5. The accuracy of the transducer system was calculated as ±2 times the standard deviation of the errors. Assuming a Gaussian distribution of the errors, this gave

a confidence level of 95% that the difference between a measured value and the true value would be within the specified accuracy.

All transducers were calibrated at the beginning of the experimental programme. Thereafter, quick calibration was performed after each major test to detect any deviations from the initial calibration results. It was found that the performance of each transducer was very stable and calibrations at different times gave almost identical results. The calibration results of all transducers are summarized in Table 4.1.

4.4.2 Dead-weight calibration system

A 580-series hydraulic dead-weight tester manufactured by DH Budenberg Ltd. was used to calibrate the pressure transducers and the loadcell. The system operated on the principle of pressure balance between a piston loaded by dead weights and the pressure at the outlet port. Friction in the system was minimized by machining the pistons to such high tolerances as to not require seals. The slow leakage of oil past the pistons provided lubrication. Both pistons were continuously rotated during calibration for further reduction of friction. All the test weights and piston areas were calibrated against weights and pistons traceable to the National Physical Laboratory. The certificate of accuracy (certificate number 99T26735, 20 September 1999) stated that the accuracy of reading of the pressure measured at 20°C, subjected to a gravitational acceleration of 9.80665 m/s^2, was 0.03% over a pressure range of 100 to 1200 kPa and 0.02% over a pressure range of 1200 to 12000kPa. The accuracy of the dead-weight calibration system further depends on the calibration of the weight set and the correct operation procedures. The calibration of weight set had been carried out at 06/11/2002 against a standard weight set traceable to the National Physical Laboratory through NAMAS certificate No. T25321 Lab Ref. 0134.

4.4.3 Pressure transducer calibration

Pressure transducers were calibrated within their positions in the triaxial apparatus. The pressure outlet from the dead weight calibration system was connected to the de-aired block of corresponding pressure transducer with the valve on the other side of the de-aired block closed. Zero was taken as atmospheric pressure. The calibration

procedure consisted of a load and unload component with typically a minimum of twelve equally spaced pressure increments (50 kPa per increment) for each component. A typical pressure transducer calibration result is shown in Figure 4.9.

4.4.4 Load cell calibration

For compressive load range, the load cell was calibrated against the dead-weight calibration system, which was done by following a similar procedure as that for pressure transducer calibration. For tensile load range, the load cell was calibrated by suspending standard dead weights under a hooker fitted at the bottom of the load cell. A typical load cell calibration result is shown in Figure 4.10.

4.4.5 LVDT calibration

The submersible LVDTs, which were used for the local measurement of axial and radial strain, were calibrated against a micrometer (Mitutoyo series 152-348), which has a range of 25mm and a quoted accuracy of ±1μm. A purpose-built frame was used to position and align both the LCDT and micrometer. Each LVDT were calibrated in at least two measurement ranges. This is because that a higher resolution was needed to measure the small strain stiffness, while a larger measurement range (a lower resolution) became necessary at large soil deformation.

It should be noted that the calibration of LVDTs involved only a monotonic movement of the armature, rather than a movement upwards following by one downwards. This was necessary because during the direction reversal the rotary thimble of the micrometer might become slack, which would introduce errors to the calibration result. During the calibration process, great care was taken not to overshoot the rotary thimble at each reading point. Otherwise the current operation had to be abandoned and the calibration had to be conducted again.

A typical LVDT calibration result is shown in Figure 4.11.

4.4.6 External axial strain gauge calibration

The external axial strain gauges were calibrated using a similar device as that was used for calibrating the LVDTs. A full measurement range of 25mm was calibrated, since the

reading of external axial strain gauges was mainly used at large deformation stage when the local axial LVDTs became out of range. A typical calibration result is shown in Figure 4.12.

4.5 Development of the control software

4.5.1 Introduction

The automated cyclic system was controlled by the control program, which was developed gradually in this research. The program was written in Quick-BASIC language and is attached in Appendix. The control software could fulfill the following functions automatically:

1) Tests could be performed cyclically along a specified stress path, with high accuracy.
2) After the target strain (or stress) was reached, the target strain (or stress) could be held for a specified period for stress relaxation (or creep).
3) Data could be logged from the transducers with the logging rate being changed automatically according to the strain level.
4) Tests could be performed over a long time without attention, with the ability to detect and correct any possible errors.
5) Additionally, a K_o loading could be performed, in which the radial strain is kept constant.

To achieve these functions automatically, the software was designed in a framework to form an information and command "loop", which connected the computer, the pressure control system, the signal conditioning unit and the Bishop & Wesley hydraulic cell, as shown in Figure 4.13.

Basically, in each loop, the signal conditioning unit logged the data from all transducers and transferred them to the computer, and a judgment about the *current state* of the soil specimen, *e.g.* the stresses and strains, was made. The *current state* was then compared with a *target state*, which was set by the computer program, and the *difference*

was found. Based on this comparison, a command was produced and sent to the pressure control system, so that the situation of the soil specimen could be adjusted and the *difference* could be reduced. In short, the system "feels" first, then "acts".

Such a loop was repeated in the whole experiment process to achieve different functions, such as stress path control, holding the strain or stress, or K_o loading, which will be discussed in the following sections. When one function was completed, the program was automatically set to achieve the next pre-designed function. For example, in a radial strain-controlled cyclic test, the system conducted the following stages in sequence: a compressive stress path excursion, the first rest period, an extensive stress path excursion, and the second rest period. The general flowchart showing the layout of the program is illustrated in Figure 4.14.

4.5.2 Stress path control

In the radial strain-controlled cyclic loading tests, a 135° total stress path in the *s-t* space was desired, in which the total vertical stress had to be kept constant. Compared with the 45° total stress path in a conventional triaxial test, it was much more difficult to achieve the desired stress path, since the deviator stress and the cell pressure had to be adjusted simultaneously. Furthermore, to measure the small strain stiffness accurately, it was important to follow the stress path closely without large errors.

Pressure control method

To achieve a stress path with a constant total vertical stress in the Bishop & Wesley hydraulic cell, one method was to directly control the pressure increment in both cell and lower chamber controllers. The axial stress σ_a and radial stress σ_r could be controlled in such a way by changing the cell pressure σ_r and the lower chamber pressure p, which were applied by two GDS advanced controllers respectively. The value of σ_a was dependent on both σ_r and p. By considering the equilibrium of the loading ram, the following relationship is obtained:

$$\sigma_a = p\frac{a}{A} + \sigma_r\left(1 - \frac{a}{A}\right) - \frac{W}{A} \qquad (3.1)$$

or the equation could be written in terms of stress change:

$$\Delta\sigma_a = \Delta p \frac{a}{A} + \Delta\sigma_r \left(1 - \frac{a}{A}\right) \qquad (3.2)$$

where A is the sample area at relevant stage of the test, a is the area of the Bellofram rolling diaphragm, and W is the weight of the loading ram.

According to *Equations 3.2*, $\Delta\sigma_r$ and Δp could be calculated for a certain stress path, and commands *RAMP PRESSURE* would be sent to the cell and lower chamber pressure controllers to achieve these two pressure changes. To realize a smooth stress path, these two pressure changes should be applied simultaneously and a constant ratio must be maintained between them. However, the pressure resolution of a GDS controller was 1 kPa and there was a deadband of ±1 kPa, which means that the controller allowed the pressure to drift by ±1kPa before it took corrective action, even at its *High Precision* module. Furthermore, intense interaction was observed between the two controllers, since both controllers were under pressure control, while the loading ram had to be kept equilibrium at any time. In the best case, the stress state points deviated from the specified stress path by about ±2.5kPa, with clear steps in the deviator stress. Obviously, the direct pressure control method was too coarse, especially when small stain stiffness measurement was needed.

Volume control method

In this research, a volume control method was developed to achieve the required pressure accurately by controlling directly the volume of water inward or outward of the controllers. The resolution of GDS advanced controllers for water volume change was 1 mm^3, which made very fine adjustment to the water pressure possible. The Druck pressure transducers outside the controller were used to monitor the pressure changes, rather than the pressure transducers inside the controllers. An accurate stress path in the triaxial space could be achieved in a procedure specified as below.

At the start of a stress path excursion, a judgment was made first about the desired stress path direction (compressive or extensive). Based on this a *Ramp Volume* command was sent to the lower chamber pressure controller and the loading ram began to move at a constant rate upwards or downwards. Then the process entered a closed loop, which was based on the framework in Section 4.5.1. In any loop, the data was logged first and the target cell pressure was calculated, according to the pre-designed relationship between

the deviator stress and cell pressure. For a stress path in which the total vertical stress need to be kept constant, the target cell pressure σ_{rT} can be derived as

$$\sigma_{rT}=\sigma_v - q \qquad (3.3)$$

where σ_v is the desired constant total vertical stress, and q is the current measured deviator stress.

The *current* measured cell pressure σ_r was compared with the *target* cell pressure σ_{rT}. If σ_r was higher than σ_{rT}, a command would be produced to move a certain volume of water into the cell pressure controller to reduce the cell pressure. If σ_r was lower than σ_{rT}, a certain volume of water would be move out of the cell pressure controller to increase the cell pressure. The volume of the water needing to be moved into or out of the controller depended on the current cell pressure level and the difference between the current cell pressure and target cell pressure, and it can be estimated by trial before test.

The time period for each loop was designed to be about 1 second. This had two benefits: any pressure change could be monitored and responded to in time, while the controller was able to drive the stepper motor to complete one operation. By repeating the loop, the cell pressure was adjusted continuously to keep up with the deviator stress change along the stress path test.

When the target radial strain (or the target deviator stress) was reached, the control software would automatically change the module to hold the target strain (or stress), avoiding any overshoot at the end of a stress path excursion.

Using the volume control method, a stress path could be followed with a variation of only ±0.3kPa from the 135° line, which was at the same level of the sum of the cell pressure resolution plus the deviator pressure resolution, as shown in Figure 4.15. The program had the ability to achieve a more accurate stress path, if the pressure transducers could provide a higher resolution. Other general stress paths could also be easily achieved using the same program and the only necessary update would be *Equation (3.3)*, the relationship between the deviator stress and the cell pressure. The volume control method proved to be highly flexible and had also been used to hold the strain (or stress) and perform K_o loading, as discussed in the following sections.

4.5.3 Holding the target strain or stress

In the strain-controlled tests, a rest period was introduced between each shear excursion, in which the target strain was held constant to reduce the effects of stress relaxation to an acceptable level. This was necessary. If uncontrolled, the large stress relaxation rate would influence the stiffness behaviour in the next excursion, especially at small strain levels, and give misleading results. In this research, the deviator stress relaxation rate was reduced to less than 1% of deviator stress increase rate at the beginning of the next shear excursion. This ratio was considered to be sufficiently small to ensure that stress relaxation induced by previous load excursion did not significantly influence the measured stiffness.

In a rest period in which the radial strain was to be held constant, a similar loop was introduced as that used in the stress path control. The difference was that two targets was set and compared in one loop. One was the target radial strain and the other was the target cell pressure. In each loop, the current radial strain was compared with the target radial strain first. Any difference beyond the tolerance range (0.0002%) would be reduced by compressing or extending the specimen slightly. This was achieved by moving certain amount of water (typically 1 to 3 mm^3 each loop) into or out of the lower chamber controller.

Then the current measured cell pressure was compared with the target cell pressure, which was redefined in each loop, based on the current measured deviator stress (*Equation 3.3*). Any difference would be reduced by moving water into or out of the cell pressure controller. When the cell pressure controller (or the lower chamber controller) was operating, the other one was set to hold its volume to avoid any possible interaction between these two controllers. Such a loop was repeated until the next stress path excursion began.

Figure 4.16 presents an example of a rest period, in which the radial strain was held constant for deviator stress relaxation.

Alternatively, the target cell pressure and deviator stress could be held constant in a rest period for strain creep. In this case, the current cell pressure and deviator stress was compared with target values respectively in each loop and any difference was reduced by volume control. A typical rest period is shown in Figure 4.17, in which the deviator stress and cell pressure were held constant.

4.5.4 K_o loading

The program for the K_o loading was developed in a very similar way as that used for stress path control (Section 4.5.2), using a similar loop principle and volume control method. The only difference was that the radial strain was judged in each loop, instead of the cell pressure. At the start of K_o loading, an initial reading of the local radial LVDT was taken as a reference for any subsequent change in specimen diameter. Then the loading ram began to ramp at a constant rate (2% per day) and the reading of the local radial LVDT was monitored. When there was any change in the radial LVDT reading, the cell pressure would be adjusted by moving a certain volume of water into or out of the cell pressure controller until the radial LVDT returned to its original reference reading. Using this method, the specimen diameter change could be kept within ±0.4μm, which is of the same magnitude as the resolution of the radial LVDT. This procedure was continued until the maximum vertical effective stress specified by the operator was reached.

4.5.5 Data logging and error correction

Data logging was one of the basic functions of the control program. It had two important purposes: 1) to log and record the data to the result file in the hard disk; 2) to provide feedback information to the control software for further operation.

All the raw data were logged and recorded in an unprocessed bit format. This had the advantage of avoiding any distortion of the raw data and providing a reliable original record for later processing and examination. All the data were written to the computer hard disk immediately after logging. However, both bit values and engineering units were shown on the computer screen, so that the operator could judge the current state instantly.

The logging rate could be changed automatically according to the strain level, or by hand through the keyboard. At small strain levels, the data was logged every second so that enough information could be obtained to study the swiftly changed soil behaviour. When the strain became larger and the stiffness change was not as quick as at the beginning, the logging rate was reduced step by step to avoid the data file sizes becoming overwhelming.

For long experiments, which could last for several months, errors inevitably happened during the communication process between the computer and the ADU signal conditioning unit, which were connected through an RS232 port.

The most serious and frequent error was found to be *Timeout*. Usually, after a command was sent out, the computer would be asked to wait to read the feedback data from the ADU before following commands could be processed. However, the command might be lost on the way to the ADU, or the feedback data might be lost on the way to the computer. In either condition, the computer would receive no response and the program process stopped. A possible reason is believed to be electronic noise on the interface.

Some commercial programs adopt very complicated algorithms to detect the timeout but this can be time consuming and inefficient. A simple method was developed in this research, based on the fact that after the command was sent to ADU, any returned data would be stored in the computer buffer before it could be read out. Each time after the command was sent to the ADU, the computer was not asked to read the feedback in the next step. Alternatively, a short period (about 10 ms) was allocated for waiting and then the number of characters in the buffer was counted. This was achieved by using the function *"LOC"* in the BASIC language. If the number was less than expected, a timeout error was believed to have happened and the computer would re-send the command to the ADU. If the number satisfied the requirement, all characters would be read out and the buffer became empty. This method proved to be highly effective in long-period tests, in which the timeout error happened almost everyday. The program could correct it every time.

Other errors also happen, which have been identified as *Bad command received by the ADU* and *Errors with the computer buffer*. These two errors are relatively easy to deal with and more details can be found in Xu (2004).

4.6 Summary

An automated triaxial cyclic loading system was developed in this research, so that small lateral strain controlled cyclic loading tests could be performed with a constant total vertical stress and the behaviour of the representative soil element behind an integral abutment could be examined.

The system was designed based on a Bishop & Welsey hydraulic triaxial apparatus, with pressure controllers, a signal conditioning unit and a computer. Both strains and pore water pressures were measured locally, with great attention being paid to the measurement of small strain stiffness.

The whole system was controlled by the control software, which was designed on a "loop" framework and utilised a volume control method. This software proved to be highly effective in cyclic stress path testing.

The system could achieve the following major functions:

1) to carry out radial strain-controlled cyclic loading along a 135^{o} total stress path in the *s-t* space, with stress and strain measured accurately;
2) to be able to allow a rest period between two stress excursions for stress relaxation (or strain creep);
3) to conduct long-period tests without attention, detecting and correcting any possible errors automatically;
4) to be flexible for any special requirement emerged during the research.

With the successful development of this system, a pre-designed experimental plan could be achieved automatically and accurately, which was essential for further laboratory testing on different soils in this research.

Transducer	Measurement	Company	Serial No.	Design range	Calibration range	Resolution	Accuracy	Accuracy / Calib. range (%)
Load cell	Axial load (internal)	MIL	0184819	4kN	0 to 4kN -2kN to 0	0.951 N 0.951N	±2.032N ±0.569N	±0.05 ±0.03
Pressure transducer	Lower chamber pressure	Druck	1448698	1000kPa	700kPa	0.192kPa	±0.653kPa	±0.09
Pressure transducer	Cell pressure	Druck	1521891	1000kPa	700kPa	0.192kPa	±0.668kPa	±0.09
Pressure transducer	Mid plan pressure	Druck	1239783	1000kPa	700kPa	0.192kPa	±0.417kPa	±0.06
Pressure transducer	Base pore pressure	Druck	1239782	1000kPa	700kPa	0.192kPa	±0.553kPa	±0.08
LVDT	Axial displacement (local)	RDP	28563	10mm	0.6mm 5.5mm	0.153μm 1.417μm	±0.602μm ±5.506μm	±0.10 ±0.10
LVDT	Axial displacement (local)	RDP	28564	10mm	0.6mm 5.5mm	0.156μm 1.451μm	±0.349μm ±2.863μm	±0.06 ±0.05
LVDT	Radial deformation (local)	RDP	28561	10mm	1.2mm	0.309μm	±0.475μm	±0.04
Linear Displacement Sensor	Axial displacement (external)	MM	MG0167	25mm	25mm	7.433μm	±29.74μm	±0.12
Linear Displacement Sensor	Axial displacement (external)	MM	MG0163	25mm	25mm	7.376μm	±36.963μm	±0.14

Table 4.1 Calibration results for transducers

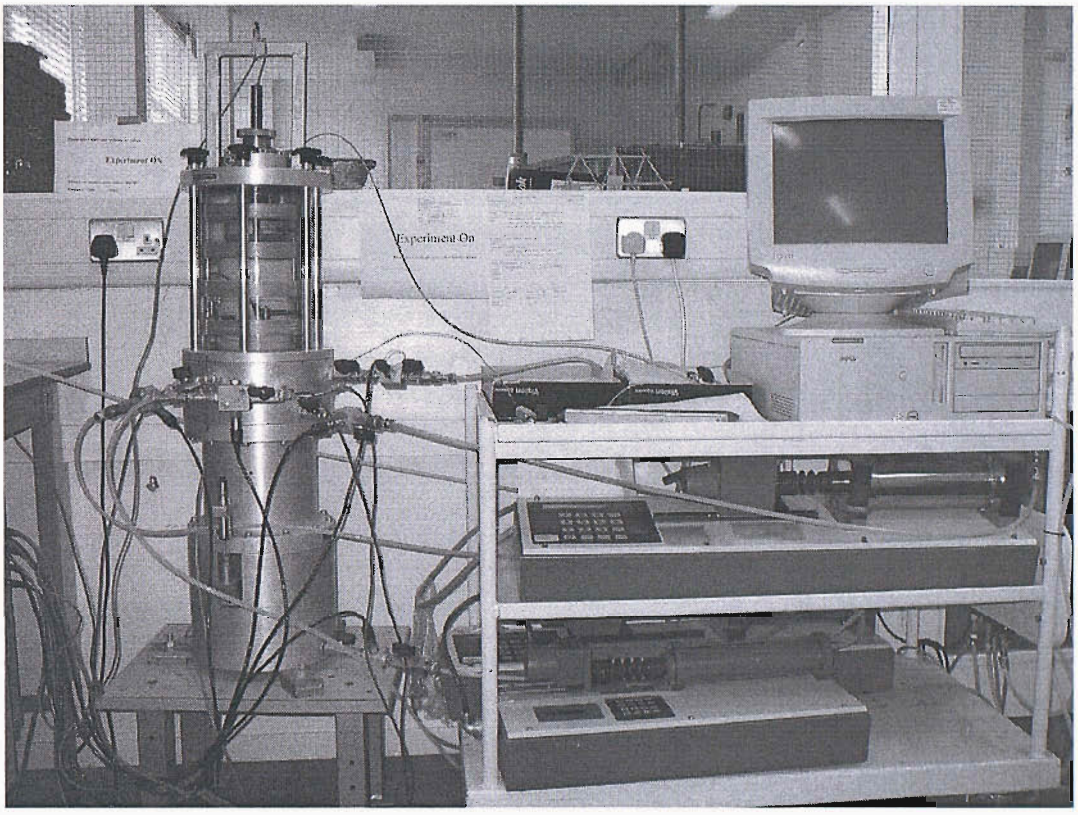

Fig 4.1 Photograph of the automated triaxial cyclic loading system

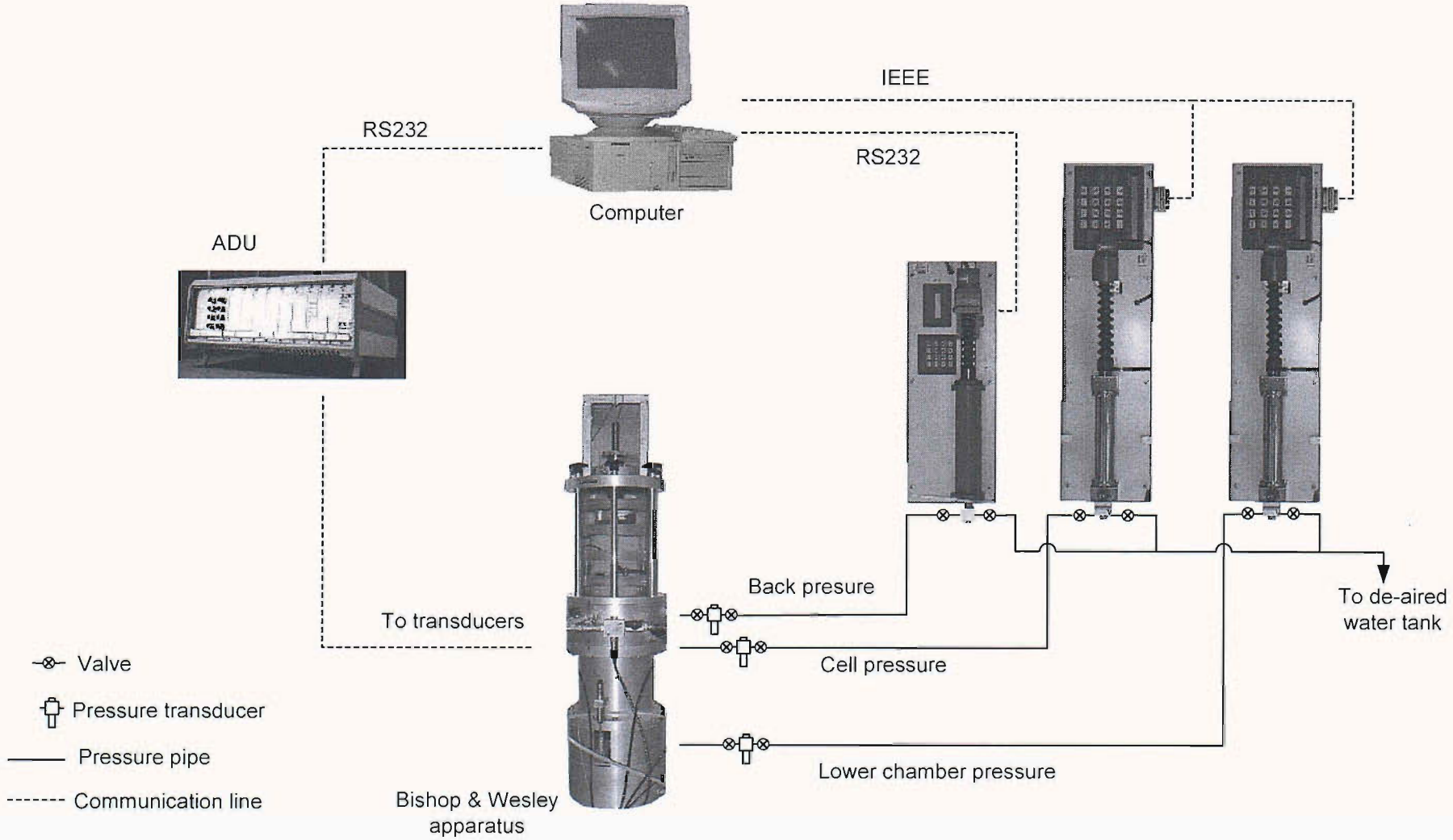

Figure 4.2 Schematic diagram of the automatic triaxial cyclic loading system

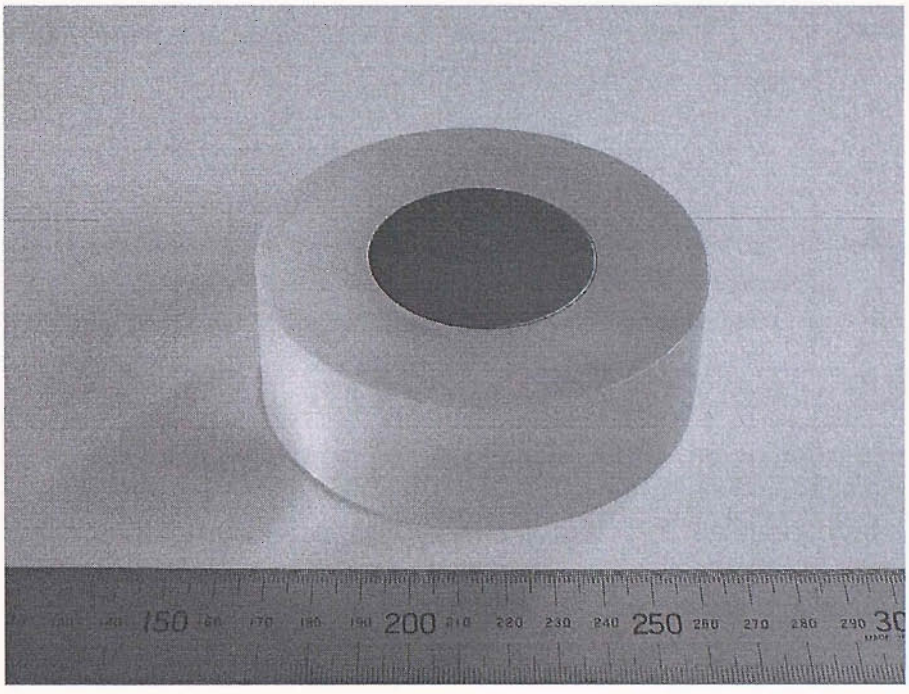

Figure 4.3 The flat top cap

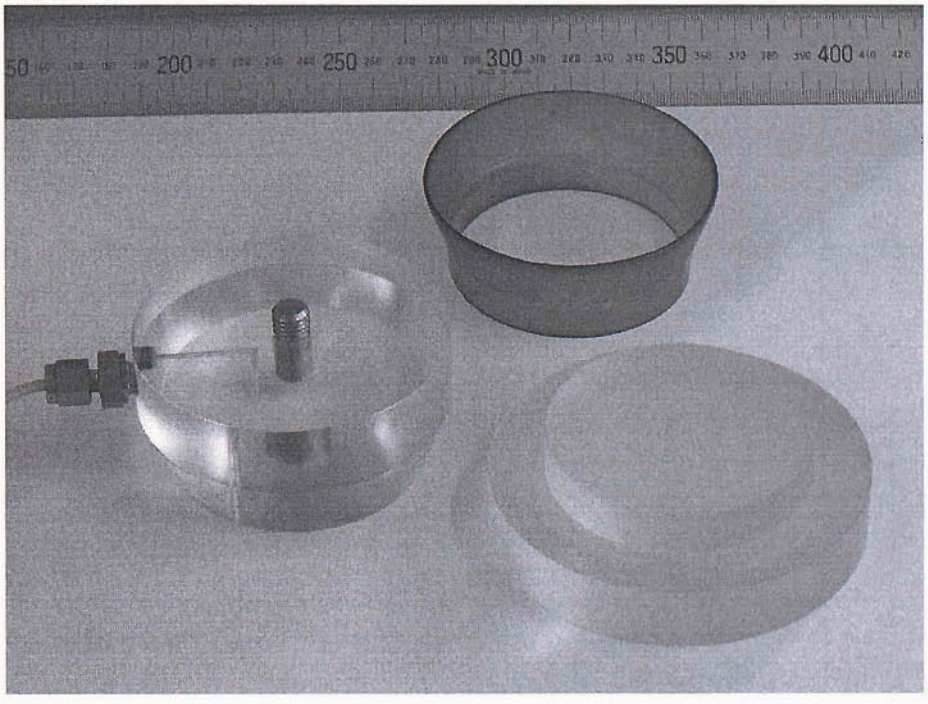

Figure 4.4 The extension device, including a suction cap, a sleeve and a top cap

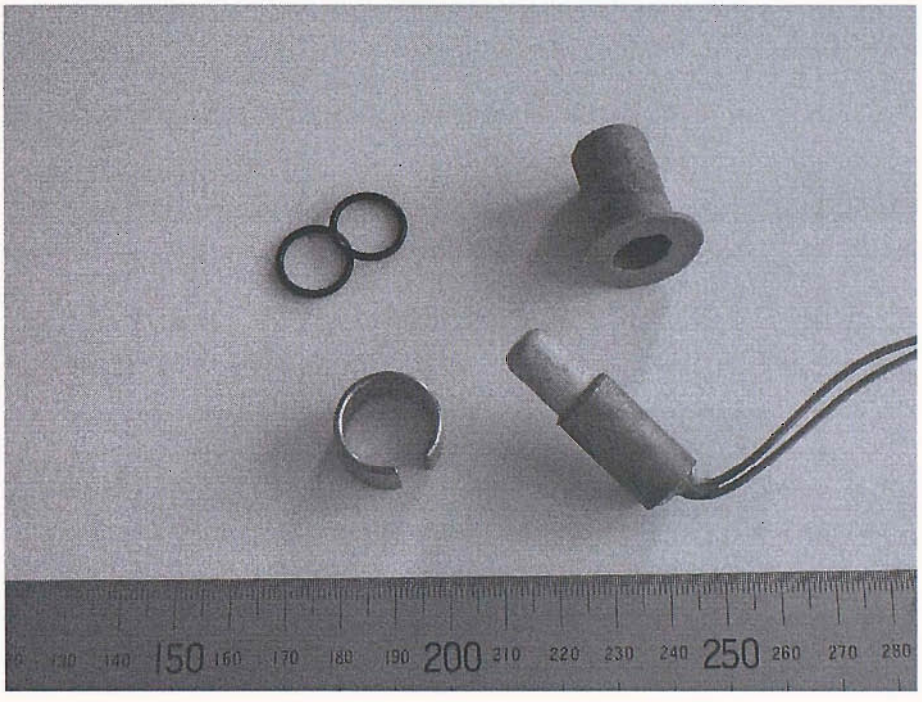

Figure 4.5 The mid plane probe, latex grommet, O-rings and the O-ring stretcher

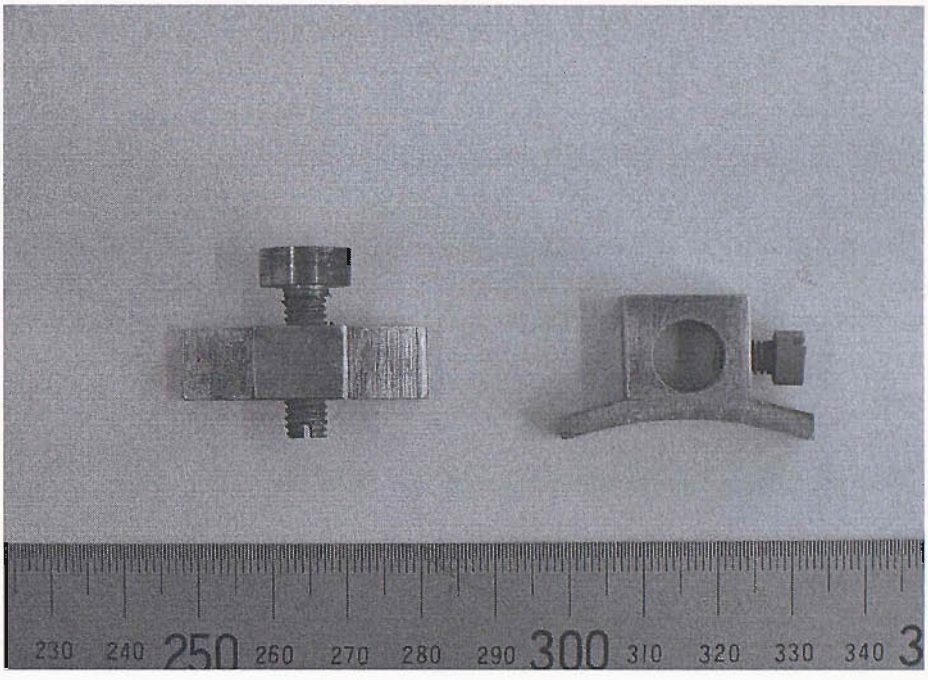

(a) The brackets for axial LVDT

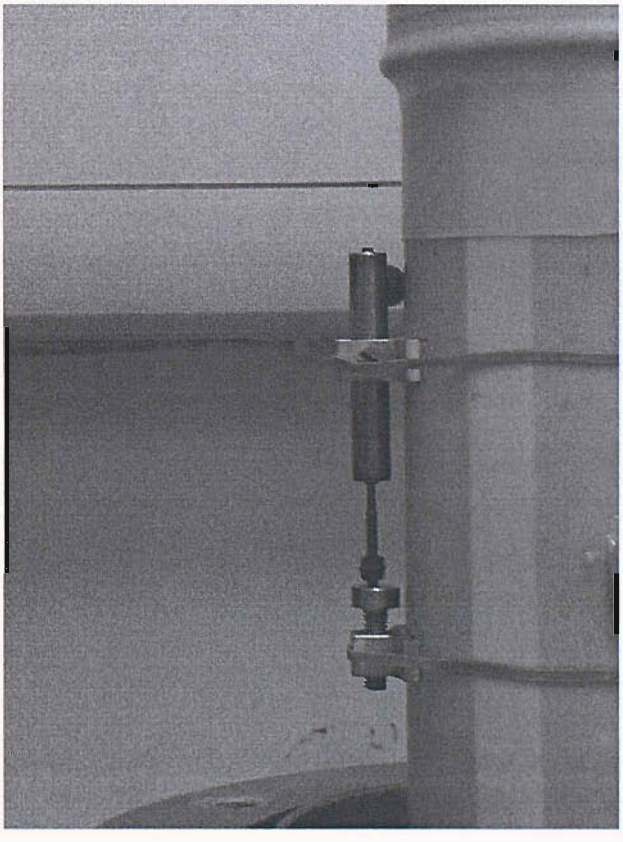

(b) The setup of LVDT with the new designed brackets

Figure 4.6 The brackets for axial LVDT

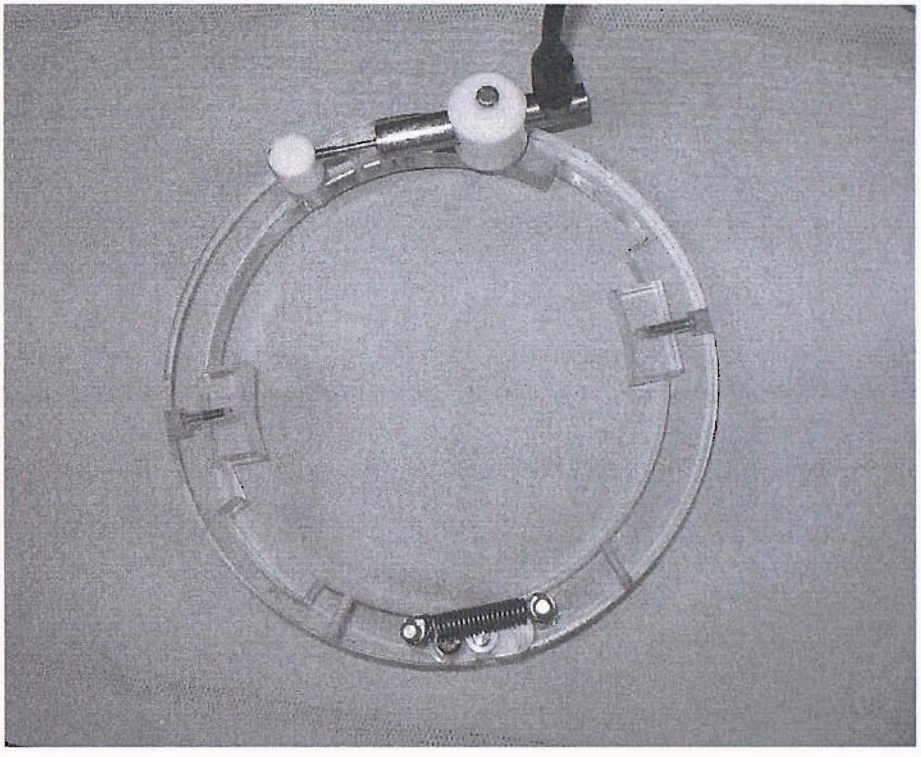

(a) The Perspex calliper

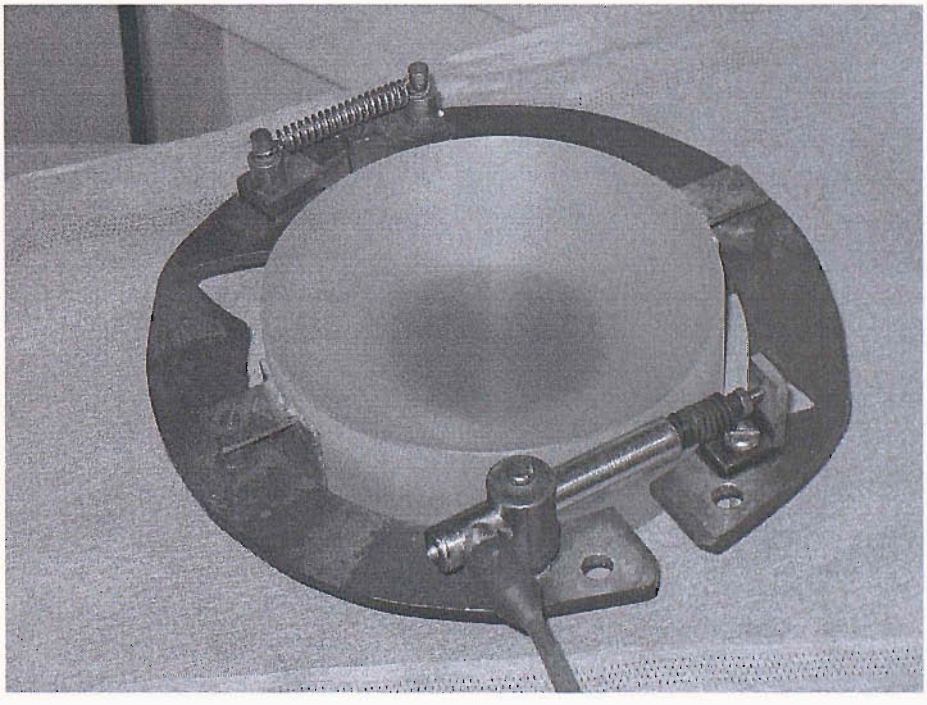

(b) The metal calliper used in this research

Figure 4.7 The calliper for radial strain measurement

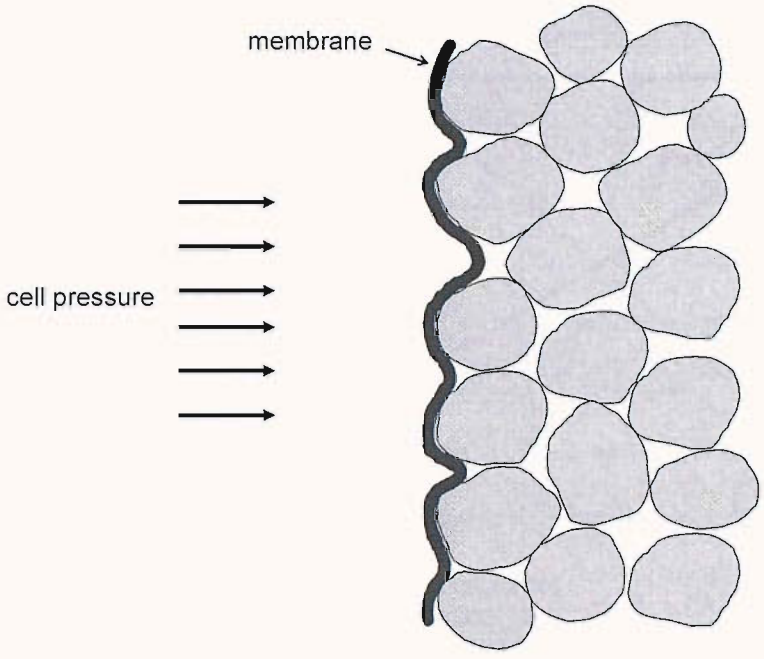

(a) The effect of membrane penetration

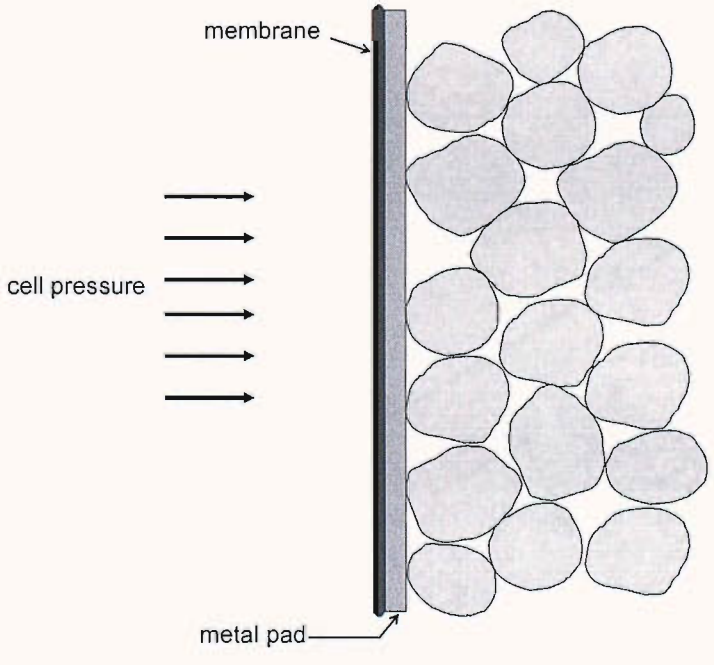

(b) The metal pad

Figure 4.8 The use of metal pads to prevent the effect of membrane penetration on the thickness of membrane

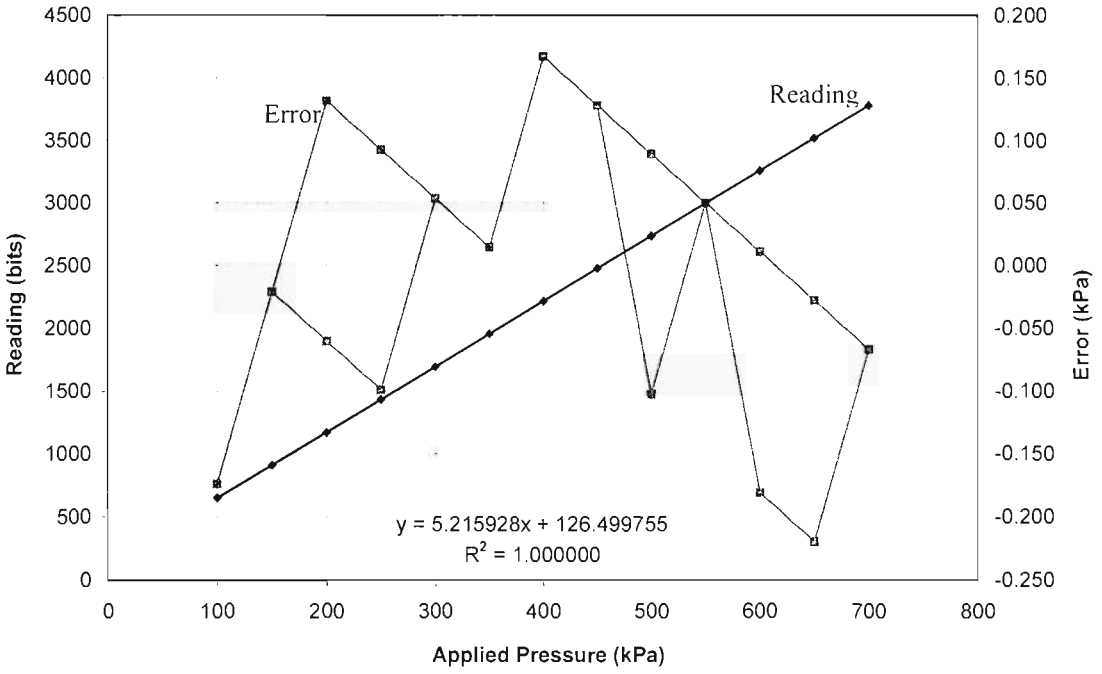

Figure 4.9 Typical calibration result of a pressure transducer

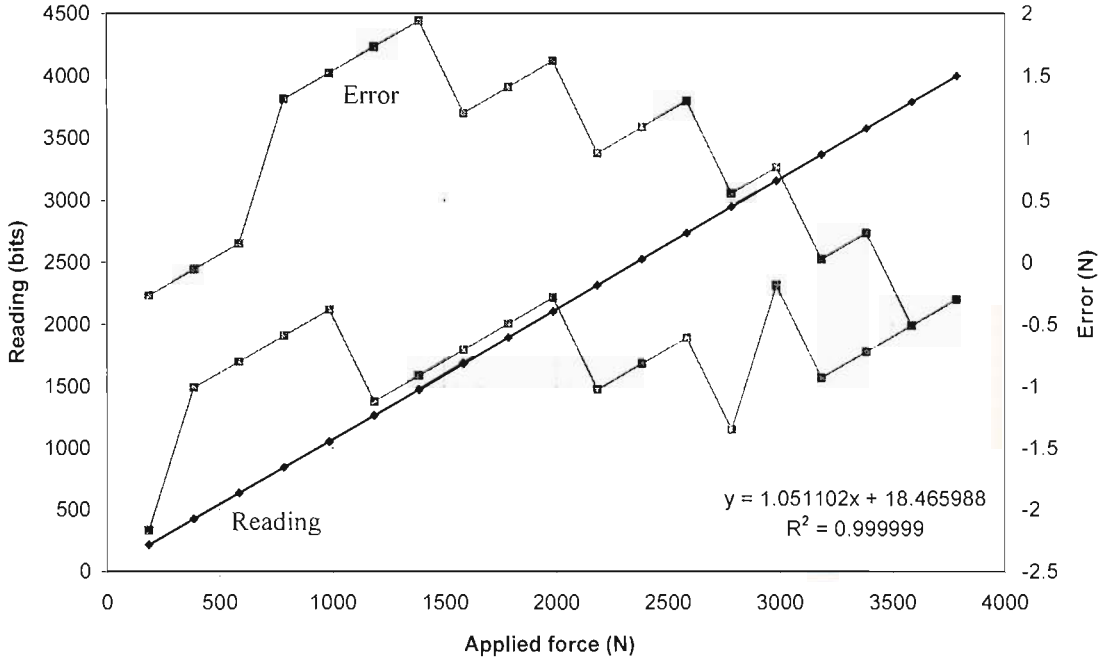

Figure 4.10 Typical calibration result of the axial load cell

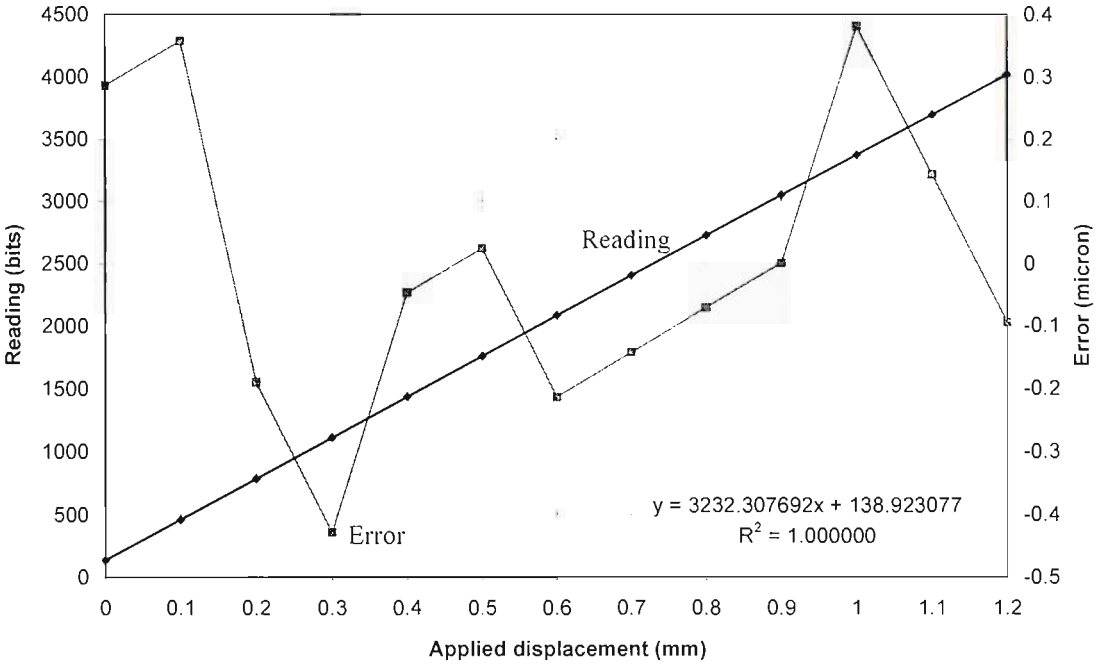

Figure 4.11 Typical calibration result of a LVDT

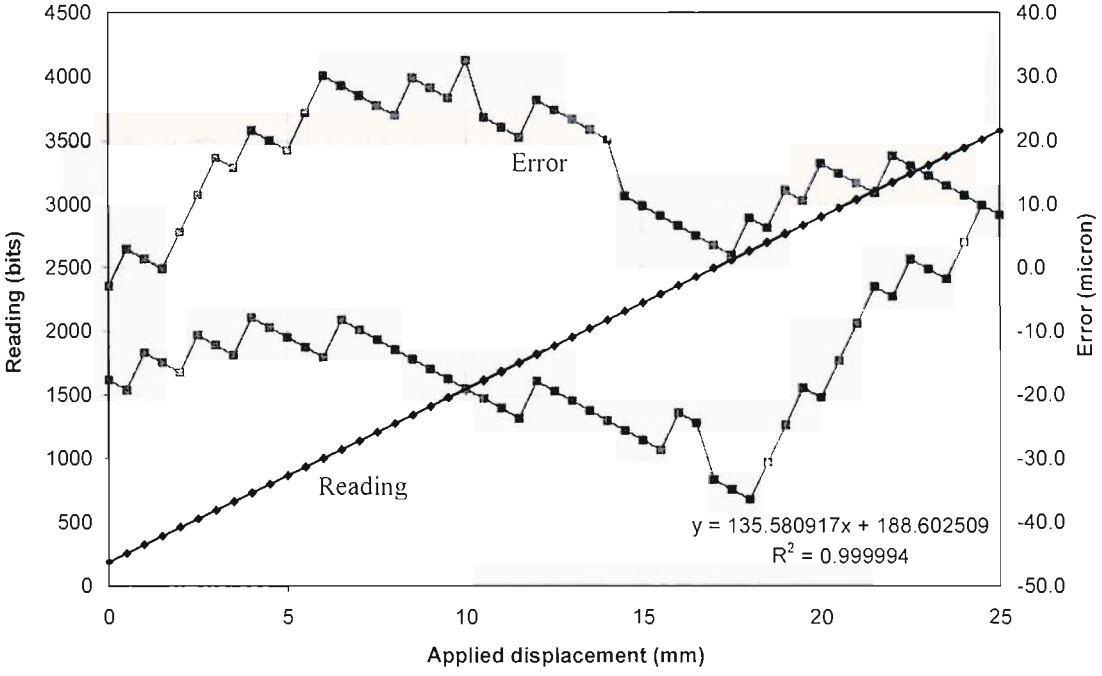

Figure 4.12 Typical calibration result of an external strain gauge

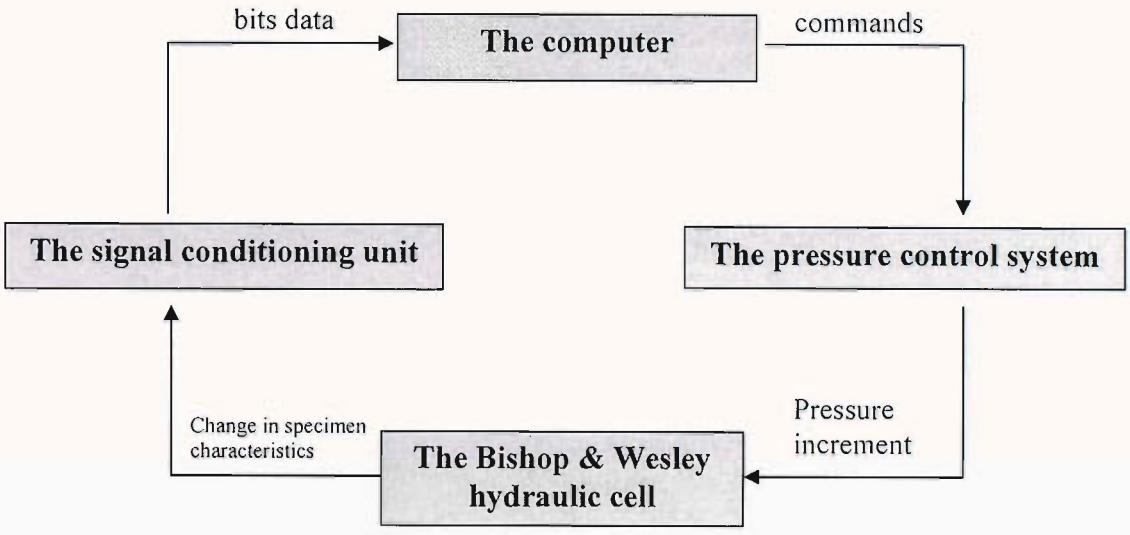

Figure 4.13 The "loop" framework for the control software

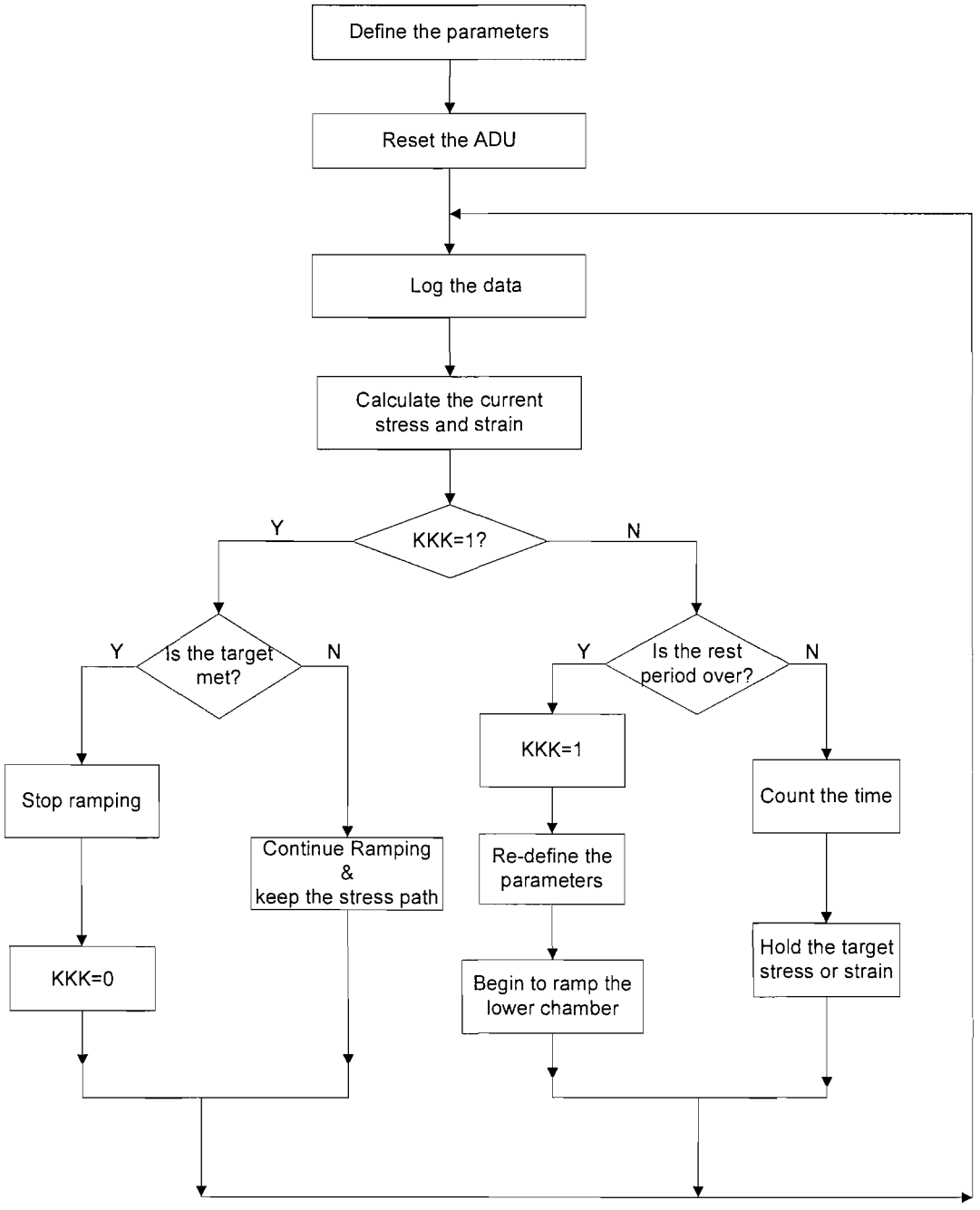

Figure 4.14 The main flowchart of the control programme

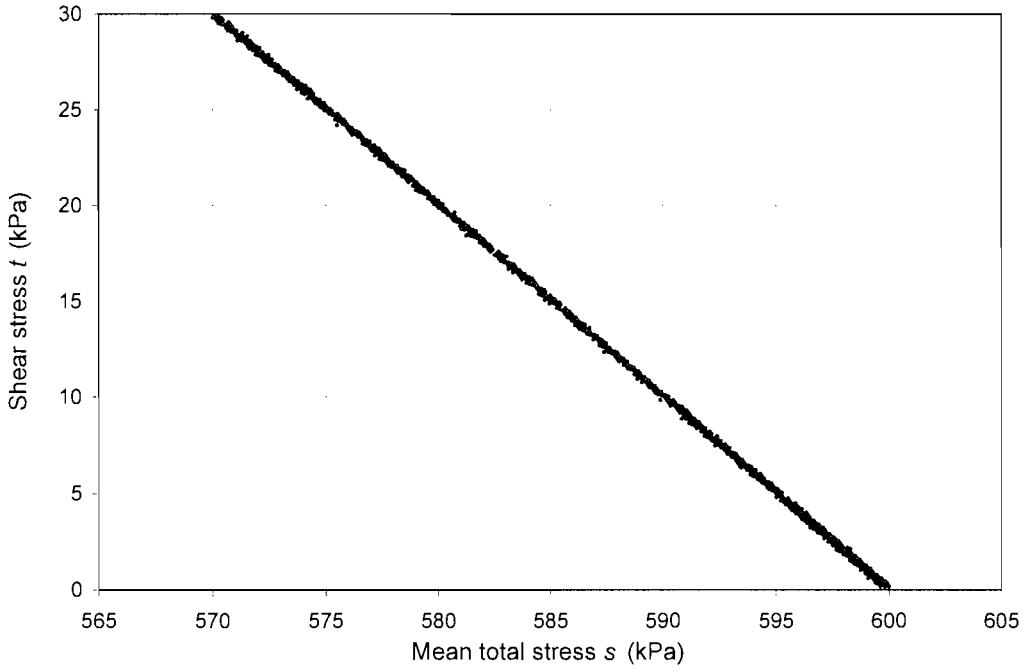

(a) the stress path in the *s*-*t* space

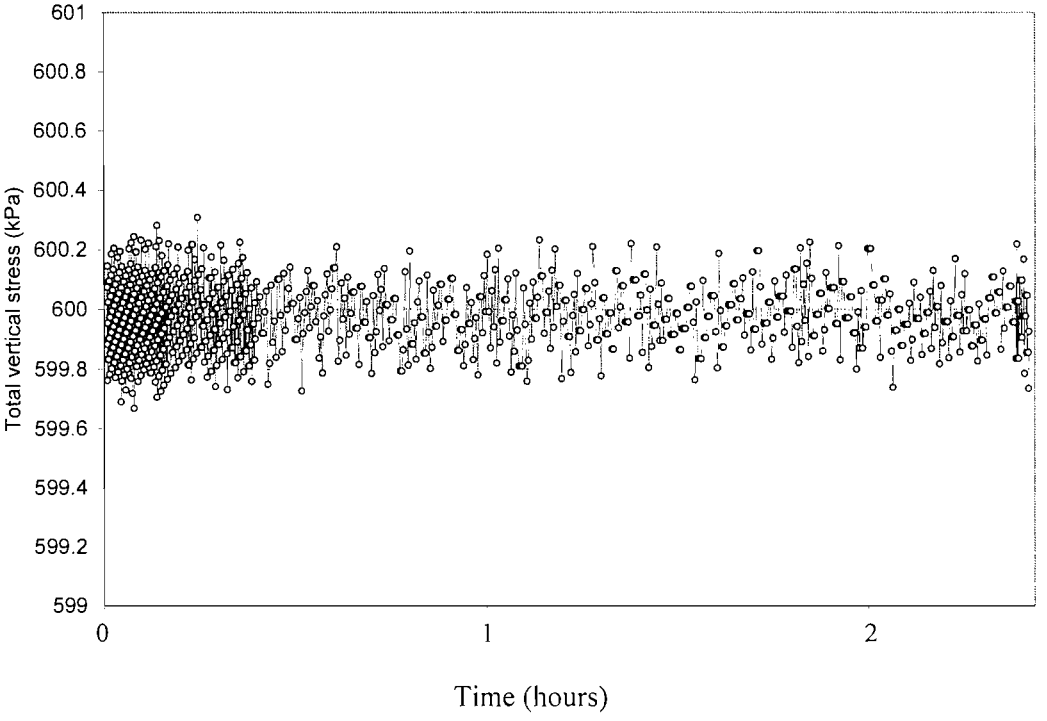

(b) the total vertical stress variation during the stress path excursion
(the data logging rate was changed automatically from once every second at the beginning to once every 15seconds)

Figure 4.15 A typical stress path excursion

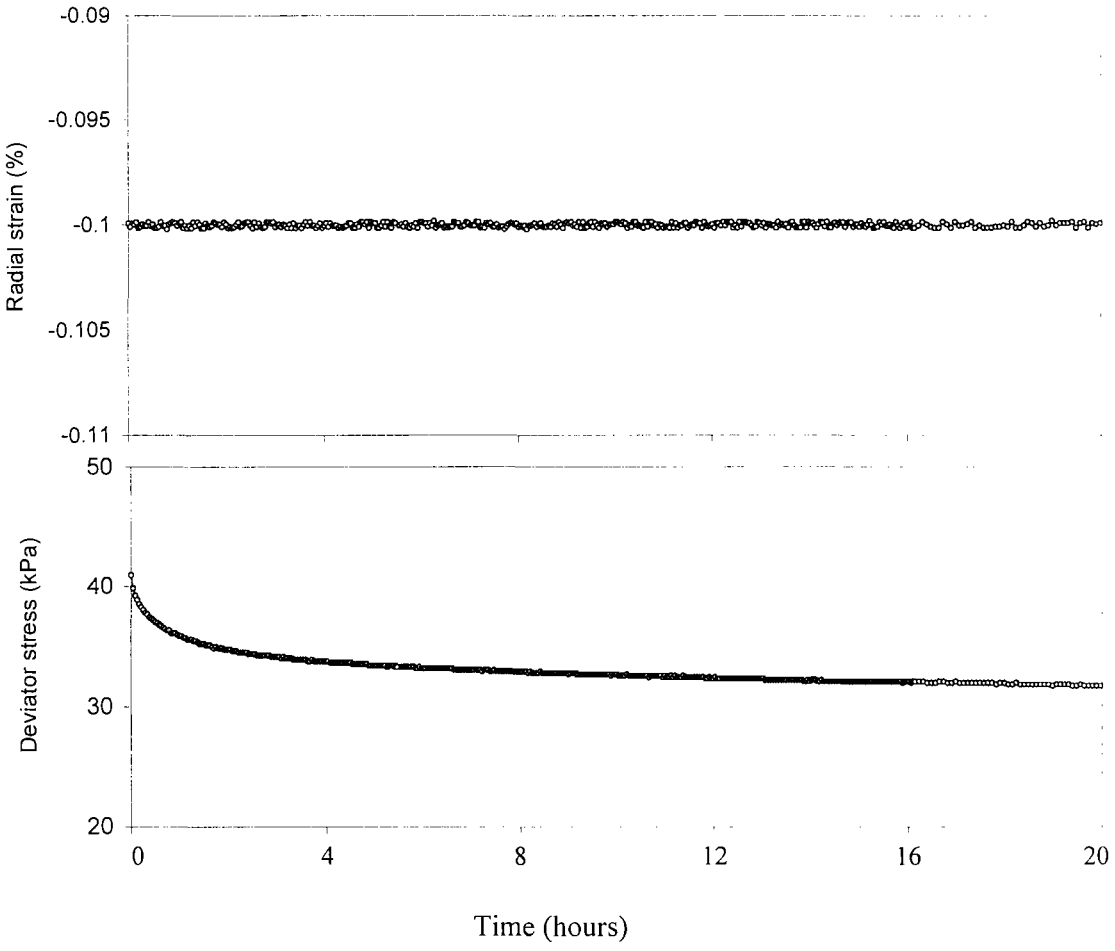

Figure 4.16 A typical rest period, in which the target strain was held constant for stress relaxation

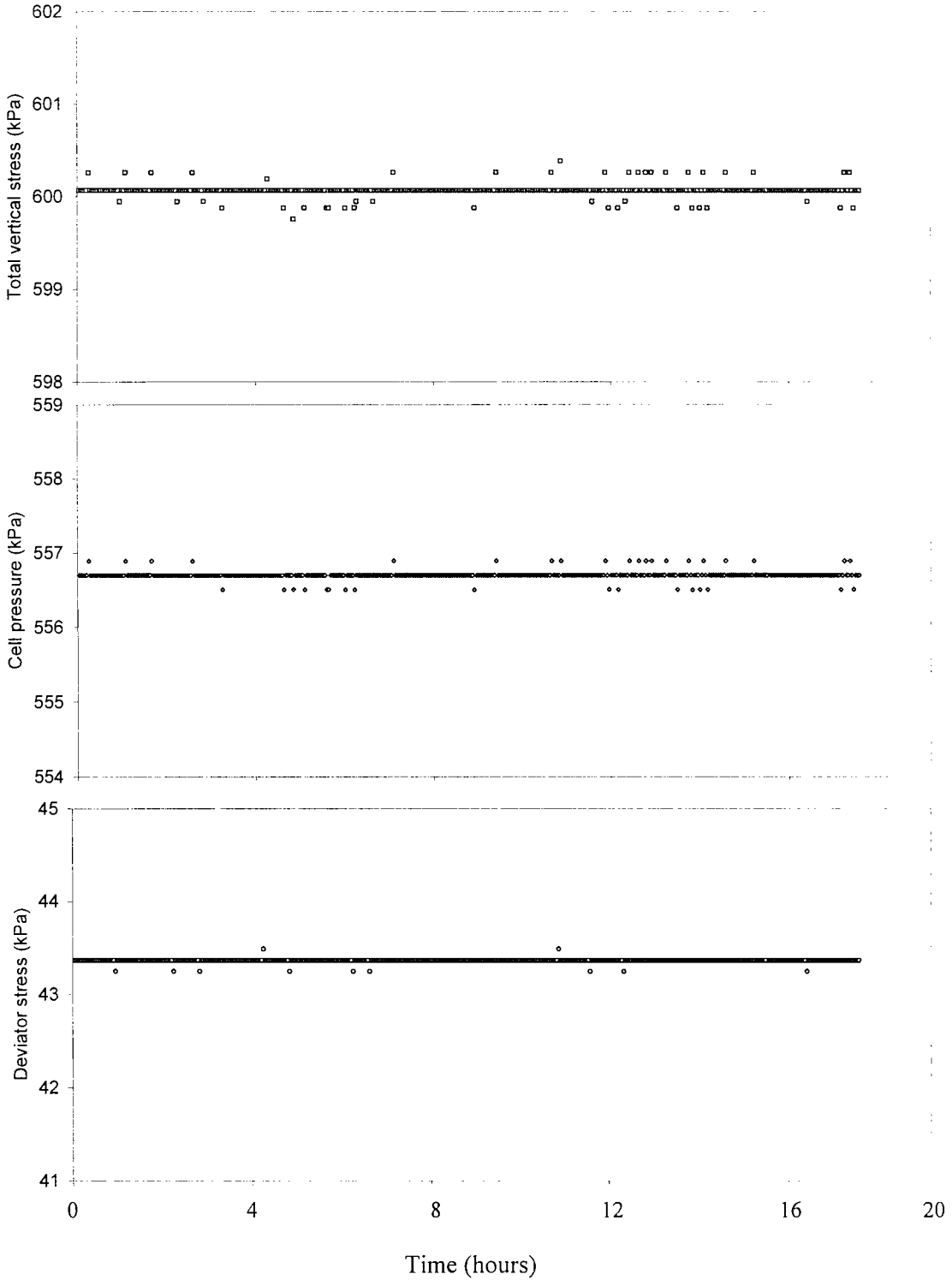

Figure 4.17 A typical rest period, in which the deviator stress and cell pressure were held constant for strain creep

Chapter 5 Laboratory testing on stiff clay

5.1 Introduction

In this research, the behaviour of a representative element behind an embedded integral abutment constructed in stiff clay was investigated by carrying out radial strain-controlled cyclic stress path testing on Atherfield I Clay, which is a heavily overconsolidated stiff clay. Three undisturbed 100mm diameter specimens were tested in the automated cyclic stress path system. This chapter will describe the experimental programme and present the major findings.

5.2 Description of Atherfield I Clay

Three Atherfield I Clay specimens (AC1, AC2 and AC3) were used. They were obtained from the construction site of a propped retaining wall forming part of a cut-and-cover tunnel on the Channel Tunnel Rail Link (CTRL) at Ashford, Kent, where extensive field monitoring was being carried out (Clark *et al.*, 2004). This area is underlain by strata belonging to the Lower Cretaceous system of Mesozoic Age and typically consists of Weald Clay, overlain by Atherfield I Clay, Atherfield II Clay and Hythe Beds (Figure 5.1).

Atherfield Clay is a stiff to very stiff, closely fissured clay and consists of two distinct materials according to its plasticity behaviour (Clark *et al.*, 2004). The upper layer (Atherfield II Clay) is grey, about 8m thick at the field monitoring site and is generally of relatively high plasticity, with a plasticity index of 50%. The lower layer (Atherfield I Clay) is chocolate brown, about 4.5m thick at this location and has a plasticity index of 20-30%.

Atherfield I clay was investigated in this experimental programme. Samples AC1 and AC3 were obtained from the construction site of the nadir sump at a depth of 15m below the original ground surface, with no ground water being observed. AC2 was obtained from the instrument section at a depth of 17m, which is 600m to the nadir sump, and a pore water pressure of about 80 kPa was measured.

Different sampling techniques were used in the field. AC1 and AC2 were borehole samples with a diameter of 104 mm. AC1 was obtained by open-drive sampler, while AC2 was taken by the wireline drilling technique. AC3 was a block sample with a size of about $30\times30\times30cm^3$, obtained using the method described by Clayton *et al.*,

1995. The wireline drilling technique and block sampling are believed to be capable of obtaining high quality overconsolidated clay samples with less disturbances (Clayton *et al.*, 1995).

Scanning electron micrographs were taken to examine the microstructure of Atherfield I Clay (Figure 5.2). The micrograph sample preparation technique followed the procedure of air dry – fracture – mount – peel – gold palladium coat (Barden & Sides, 1971). The very dense fabric of the clay is evident.

5.3 Specimen preparation and setup

After being taken in the field, all samples were carefully sealed and stored in an air-conditioned environment. In the process of specimen preparation and setup, great attention and care was paid to avoiding any disturbance and minimising moisture loss.

5.3.1 Atherfield I Clay specimen preparation

After extracting the sample of Atherfield I Clay from the tube (for AC1 and AC2) or from the wood box (AC3), the clingfilm and foil were removed and the sample was inspected for any evidence of disturbance. Usually there were some small fissures at the ends of the tube samples or at the edges of the block sample, but the major part was always in good condition and the length was carefully selected for coarse cutting. The additional length of the tube sample was removed by cutting pieces off each end by means of a knife. The size of block specimen was reduced first by a hand held bow saw, and then a knife was used to cut the sample into a cylinder that was slightly larger than the required specimen size.

The sample was then fixed in a two-part metal mould to reduce the length to 200mm and trim the ends. Particular attention was given to trim the ends of the specimen, as it was recognized that the specimen had to be a right cylinder to ensure axi-symmetrical load application in the triaxial apparatus (Clayton & Heymann, 2001). The ends of the two-part mould were carefully measured before specimen preparation to ensure that the end surfaces were flat and parallel to each other. For the first specimen the ends were trimmed using a steel ruler. This method was slow. A new purpose-designed trimming scraper was manufactured, which was a high stiffness steel bar with a sharp edge. It was 250mm long and had a cross section of 20×5mm. This scraper proved to be very effective. It took less than 10 minutes to trim one sample end into a flat and smooth surface. When trimming one end, the other end

was covered with at least three layers of clingfilm, in order to minimize moisture loss and prevent fissures developing.

After the completion of trimming both ends, the sample was removed to a soil lathe to smooth the side surface. Two pieces of damp filter paper were placed on the ends of the sample to protect the flat surfaces. At first a tensioned wire was used to smooth the side surface. This method was found to be very slow. Both hands had to hold the tensioned wire in operation. When the soil sample needed to be turned around, the operation had to be stopped as the wheel needed to be turned by hand. Furthermore, the tensioned wire itself was not effective and the soil surface had to be trimmed many times. The total time on the lathe was more than one hour and the risk of loss of moisture to the air increased. As an alternative, the high stiffness steel scraper for the end trimming was used for side surface smoothing (Figure 5.3). This method proved to be very effective as only one hand was needed to hold the scraper horizontally in operation while the other hand could turn the wheel at the same time. The total time could be reduced to about 30 minutes. Great care was taken in the smoothing process to avoid removing too large soil pieces and causing damage. Occasional sand particles on the side surface were carefully removed and the small holes were replaced by soft remoulded clay.

Three sub-samples were selected for moisture content measurement using the soil pieces scraped from the top, middle and the bottom part. These samples were weighted immediately and then put inside an oven for at least 24 hours to dry. Once the preparation was completed, the specimen was weighed and the geometry was measured. The diameter was record at six positions (top, middle and bottom, each in two orthogonal directions), while the height was measured at four positions. The average bulk unit weight of the samples was derived as 21 kN/m^3.

5.3.2 Atherfield I Clay specimen set-up

Due to the very low permeability of such a heavily overconsolidated clay, side drainage was used in the tests to facilitate consolidation or swelling. Six vertical filter paper strips (20mm wide) were used to enhance drainage. The filter paper strips were first soaked in de-aired water and then carefully placed on the soil vertical surface. Enough space between strips was allowed for the installation of the LVDTs. At the location of the mid-plane pore pressure probe, the filter paper strip was cut into two

pieces, both with a clear distance of at least 25mm to the mid plane probe to avoid a "short circuit" between the back pressure line and mid-plane probe. 100mm diameter round filter paper sheets were placed at the top and bottom with their edges touching the side filter paper strips. This was necessary as the 70mm diameter porous stone was embedded inside the base pedestal and there was a clear distance of 15mm between the porous stone and the side filter paper strips. Without the round filter paper at the bottom, it could take more than 1 month to achieve full consolidation or swelling, as observed in the swelling stage of the test on specimen AC2.

The latex membrane was carefully checked for defects before the test, and was then soaked in de-aired water for at least 24 hours. After drying both the inside and outside using paper towels, the membrane was placed over the specimen with filter paper strips. Then the specimen was laid down horizontally on a cradle to measure and mark the positions of the LVDTs. One part of a 100mm diameter three-part mould was used as the cradle; the other one was used as a ruler to mark the vertical and horizontal lines on the specimen (Figure 5.4). The part used as ruler was carefully measured before test to ensure that the end edges were exactly perpendicular to the side edges and the inside surface was smooth. This method proved to be much better than the conventional way, in which the positions for the LVDTs were marked after the specimen was placed on the pedestal. It was found difficult to mark vertical and horizontal lines by hand on a vertical cylinder specimen using a standard ruler.

A small positive pressure was applied to the back pressure line until a thin layer of water was visible on the bottom high air entry ceramic, before carefully sliding the specimen onto the base pedestal. The sliding action minimized the risk of trapping air between the sample and ceramic. Two O-rings were used to seal the bottom of the membrane. Next, the top cap was placed in position. Before two O-rings were placed on the top of the membrane, as much air as possible was removed from between the sample and membrane by stroking upwards with the fingers.

The two pairs of brackets for the LVDTs were fixed on the pre-marked positions on the membrane using impact adhesive. The brackets were held in position by hand for at least 3 minutes immediately after they were glued onto the membrane, to allow the impact adhesive to gain its initial strength. More time was required for the adhesive to achieve its full strength. Two elastic bands were put over the top and bottom brackets to facilitate the growth of adhesive strength. The next step was to install the mid plane probe, leaving the brackets to rest before installation of the LVDTs.

A small hole (2 to 3 mm diameter) was cut carefully into the membrane at the mid height. Then the hole was stretched so that the flange of the latex grommet could be sandwiched between the membrane and the specimen. After that a slightly oversized hole was drilled by hand to accept the 11.7mm diameter probe, using a steel drill head. Before the probe was inserted, some soft remoulded clay was placed into the hole, in order to avoid cavities between the high air entry ceramic and the stiff clay. Two small-bore stainless steel tubes enter the back of the probe casing; one at the centre and the other at the edge. The probe was carefully orientated with the off-centre tube at the top. During the flushing process, de-aired water was pumped into the probe through the centre tube and any possible air was forced to exit through the top tube. Two small O-rings were placed over the stretched membrane and grommet to seal the specimen from the cell water, using a small steel stretcher specially designed for the purpose. In addition, as a precaution, silicone sealant was spread around the end of the probe to reinforce the seal before closing the cell. Under high water pressure, the silicone sealant would spread and solidify at the end of the probe, thus enhancing the seal.

Each axial LVDT was clamped vertically to the top bracket, with great care taken to position the armature around the electrical zero. Additionally, some allowance was made for the axial deformation during the consolidation or swelling stage, based on the experience from previous tests. The aim was to have the LVDTs as close as possible to the electrical zero point once the sample reached the target initial effective stress. This was necessary to ensure the LVDTs could be zeroed at high amplification. The specially designed bottom brackets proved to be very successful, enabling slight adjustment of the armature. A photograph of the specimen after set-up is presented in Figure 5.5.

Before closing the cell, the internal load cell was raised to its highest position to leave enough height for the specimen. A crane was used to lift the cell chamber. Since the inside diameter of the cell chamber was only 168mm, great care had to be paid to avoid disturbing the LVDTs. This task was difficult as the crane could not lower the cell chamber exactly vertically, and its position had to be adjusted during the process. As experience grew, the process became easier.

5.3.3 Saturation, swelling and consolidation

System saturation

In the tests on stiff clay, full system saturation was achieved by increasing the cell pressures while keeping the back pressure line closed. Therefore no water was allowed to enter or leave the specimen. Immediately after filling the triaxial cell, a cell pressure of 400 kPa was applied to the specimen under undrained conditions and the response of the mid-plane probe was monitored. If the mid-plane probe response was sluggish or slower than that of the base pore pressure measurement, the probe was flushed with de-aired water to remove any trapped air. This was done by applying a pressure in the probe cavity from the centre steel tube, which was about 10 kPa larger than the measured mid-plane pressure. The valve of the off-centre steel tube was open to allow air to move out. Once the probe was de-aired, the valve was closed and enough time was allowed for all the pressures to reach equilibrium.

The cell pressure was then raised in increments ($\Delta\sigma_c$) of 50 kPa or 100 kPa. Enough time was allowed between increments for the pore pressure to reach a steady value, and its change Δu was recorded. The B-value (pore pressure coefficient) was calculated from:

$$B=\Delta u/\Delta\sigma_c$$

For soft clay the B-value is expected to be close to 1.0 at full saturation. But for stiff clay, such as the Atherfield I Clay, the B-value can be significant less than 1.0 even at 100% saturation. A B-value of 0.90~0.95 was considered as the criteria for full saturation (Head, 1986). In this research, a satisfactory B-value was typically achieved when the cell pressure reached 600 to 650 kPa. Furthermore, full saturation was ensured during the following rest period to allow for creep (before the stress excursion), which lasted at least 10 days with a high pore pressure (larger than 500kPa).

During the sampling of soil from the field, storage and specimen preparation, there was some disturbance of the soil (Hight, 1986). Possible causes are shearing during sampling, total stress relief and moisture loss. One method to evaluate the extent of the disturbance is to compare the initial mean effective stress p'_o after saturation with the estimated *in situ* mean effective stress (Heymann, 1998).

Table 5.1 Comparison of p'_o after saturation for different specimens

Specimen name	Location in the field	p'_o after saturation (kPa)	p'_o estimated in the field (kPa)	Moisture content w_i (%)
AC1	Nadir sump	361	315*	20.0
AC2	Instrumented section	285	277	20.0
AC3	Nadir sump	307	315*	19.2

Note: * with the assumption of u=0.

The value of p'_o of each specimen in the field was estimated from the field monitoring by Clark (2005). The bulk unit weight of Atherfield I Clay is 21kN/m^3. The value of K_o, the *in situ* pressure coefficient, was quoted as being unity at the depth of sampling on the basis of pressuremeter measurement (Geotechnical Design Basic Report, 1997). Samples AC1 and AC3 were obtained from the nadir sump site at a depth of 15m below the original ground surface, with no ground water being observed. For simplicity, u=0 was assumed for the sampling depth at the nadir sump site. Sample AC2 was obtained from the instrument section, at a depth of 17m below the ground surface, and a pore water pressure of about 80 kPa was measured.

From Table 5.1, it can be seen that the value of p'_o of each specimen was reasonably close to the estimated *in situ* mean effective stress. This appears to imply that the disturbance was not significant for these specimens.

Swelling and consolidation

After full saturation was achieved, specimens AC2 and AC3 were brought to the desired effective stress of about 74kPa (see Section 5.4.2) by isotropic swelling. This was done by applying a constant back pressure from the standard controller while keeping the cell pressure constant. During the swelling stage, the volume change, mid-plane pore pressure and the local axial strain were monitored continuously. For stiff clay with low permeability, satisfactory swelling was deemed to have occurred after 95% of the excess pore pressure had dissipated (Head, 1986), which usually took about one week with both end and side drainage employed in this research. However, for AC2, no filter paper was placed at the bottom. The clear distance between the porous stone and the side filter strips led to an extremely slow swelling process, which took more than one month.

After full swelling was achieved, the back pressure line was closed and enough time was left for the creep rate to reduce to an acceptable level. In this research, the local axial strain creep rate was reduced to less than 0.02% per day (1% of the machine shearing rate, 2% per day) before the next loading excursion began.

For specimen AC3, tests were also carried out at other effective stress levels (115kPa and 230kPa). This was achieved by consolidation, which followed a similar procedure as that for swelling.

Connection of the suction device

For specimen AC3, a suction device was used to apply a negative deviator stress. The suction cap was connected with the top cap immediately after the swelling stage. Traditionally, after docking the suction cap in the Vylastic sleeve, the valve of the suction pipe would then be opened directly to the atmosphere and a rigid connection could be expected because of the pressure difference across the sleeve. However, in the trial tests, it was found that in the process of turning the valve open by hand (even very slowly), the pressure inside the sleeve dropped suddenly and the effective stress of the specimen changed dramatically. This would cause considerable disturbance to the specimen, which was not acceptable.

In this research, a new method was developed for the connection process by reducing the pressure inside the sleeve in small steps. A GDS standard pressure controller was used to connect the outlet of the suction pipe. The suction cap was lowered onto the top cap until a small positive deviator stress was reached, *e.g.* 3~5kPa, while the cell pressure controller was set to hold the current cell pressure constant. Then the pressure inside the sleeve was reduced using the pressure controller slowly and in steps. During the first few steps (3kPa per step), the deviator stress of the specimen reduced and water continued to move out of the sleeve before the suction controller reached the target pressure. Enough time was allowed for all pressures to reach equilibrium and the deviator stress was returned to the original small positive value, before the next small pressure decrease was applied through the suction controller. Typically, once the pressure provided by the suction controller was 30kPa lower than the cell pressure, any further pressure decrease would not cause the deviator stress to change and no more water would move out, at which time the connection process was thought to be successful. Then the pressure could be reduced in much larger steps (*e.g.* 20 kPa to 50kPa) before the suction pipe was disconnected from the suction controller and opened to the air. Using this method, disturbance to

the specimen was minimized. It was found that there was negligible change in the effective stress of the specimen after connection.

After the connection, the specimen was left for rest under an isotropic pressure condition. However, the restraint provided by the fixed rigid suction device would introduce undesirable deviator stress as the creep strain increased. This problem was avoided by using the function of holding target stress in the control programme (see Section 4.5.3). The target deviator stress was set to be zero while the target cell pressure was set to be the desired value.

5.4 Test procedure for Atherfield I Clay

5.4.1 General

The behaviour of the representative stiff clay element behind an embedded integral abutment was investigated by conducting radial strain-controlled cyclic loading on Atherfield I Clay specimens. The following factors, which were thought could have an influence on the stress-strain behaviour and stiffness behaviour of stiff clay, were examined.

- the magnitude of cyclic radial strain range
- the number of cycles applied
- the initial stress state before cyclic loading
- undrained or drained conditions

Furthermore, undrained monotonic shearing was performed to study the strength behaviour. A summary of all tests is given in Tables 5.2 to 5.4.

The test on specimen AC1 applied an undrained unconsolidated monotonic shearing. After the specimen was fully saturated, the specimen was sheared to failure with a constant cell pressure.

The tests on specimen AC2 and AC3 provided the majority of the data. Due to the limited number of high-quality undisturbed samples, a number of stages were conducted on each specimen.

For specimen AC2, undrained radial strain-controlled cyclic loading was carried out first. Then, an undrained monotonic shearing was carried out until an axial strain

of 2.4% was reached. Specimen AC2 was not brought to failure, but was then used to test the new purpose-designed extension device described in Section 4.2.1.

The test on specimen AC3 consisted of four stages. First, undrained radial strain-controlled cyclic loading was performed. This was followed by drained radial strain-controlled cyclic loading. In the third stage, the specimen was consolidated to an isotropic initial mean effective stress of 115kPa, after which an undrained loading-unloading loop was carried out under a radial strain range of 0.05%. Finally, the specimen was consolidated to an isotropic initial mean effective stress of 230kPa, after which the specimen was sheared undrained to failure with a constant cell pressure.

All the tests were performed along a 135° total stress path in the *s-t* space (a constant total vertical stress), as shown in Figure 3.1, except for the undrained monotonic shearing stages of AC1 and AC3, in which the specimens were compressed to failure with a constant cell pressure.

In the following sections, the detailed testing procedure will be described according to the testing types, namely undrained radial strain-controlled cyclic loading (Section 5.4.2), drained radial strain-controlled cyclic loading (Section 5.4.3) and undrained monotonic shearing (Section 5.4.4).

5.4.2 Undrained radial strain-controlled cyclic loading

Atherfield I Clay is a heavily overconsolidated stiff clay, with a very low permeability. The representative stiff clay element behind an embedded integral abutment is likely to experience some temperature-induced cyclic loading under undrained conditions. Therefore, the behaviour of stiff clay under undrained radial strain-controlled cyclic loading was investigated extensively on specimens AC2 and AC3 (Table 5.3).

The choice of initial stress state before cyclic loading

The initial stress state before cyclic loading on specimen AC2 and AC3 was carefully chosen. The representative soil element was located at 4m below the ground surface, with a ground water level of 3m depth assumed. Although the *in situ* earth pressure coefficient K_o in heavily overconsolidated clay is usually high, especially at shallow depth (Skempton, 1961), the effects of wall installation can significantly reduce the lateral earth pressure, with the value of K dropping to a magnitude of

around unity (Clayton & Milititsky, 1983; Tedd *et al.*, 1984), as discussed in section 2.7.1.

The excavation in front of the embedded abutment will further reduce the lateral earth pressure behind the wall. The reduction extent is difficult to predict, since it depends on the detailed construction sequence and technique. However, the stress reduction and associated strain change are believed not to be significant. Jardine *et al.* (1986) demonstrate that typical shear strain levels behind a retaining wall are less than 0.1%. In cases when retaining structures are well propped, or in stiff ground, typical strain levels could be even less, and perhaps as low as 0.01%.

Therefore, the earth pressure coefficient is expected to drop to approximately unity, mainly because of the effects of wall installation. To take account of uncertainties, different initial stress states were designed for specimen AC2 and AC3 before cyclic loading.

After saturation, specimen AC2 was first swelled (see Section 5.3.3) to an isotropic effective stress of about 80kPa, which replicated the stress condition inside the representative soil element after the installation of the diagram wall in stiff clay. Then the excavation in front of the wall was simulated by reducing the lateral stress under undrained conditions with a constant total vertical stress until an axial strain of 0.1% was reached. The cyclic loading was started from this stress state. For specimen AC3, a well propped wall was assumed, which is expected to result in a negligible change in the lateral earth pressure, compared with that due to the effects of wall installation. Therefore, the cyclic loading was designed to begin from an isotropic stress state ($\sigma_h'=\sigma_v'=$ 76kPa).

The first strain excursion at each cyclic radial strain range was designed to be radial extension (the abutment moving away from the soil), to reflect the slight outwards movement introduced by the shrinkage and creep of the concrete deck after casting (Barker & Carder, 2001). In the beginning of the undrained cyclic test on AC2 under a cyclic radial strain range of 0.04%, the specimen was subjected to radial compression (q decreasing) first by a radial strain of 0.02%, which was then followed by 0.04% radial strain cycles. No obvious influence was found in the following stress-strain behaviour during cyclic loading, as shown in Figure 5.6.

Testing procedure

The soil behind the bridge abutment experiences cyclic loading of different magnitudes due to daily and annual variation in effective bridge temperature.

Therefore, different cyclic radial strain ranges were applied (Table 5.3). For a 60m long concrete deck, the total annual radial strain range was estimated as 0.08%, as discussed in Section 3.2.

Small cyclic radial strain ranges were tested first. This meant that the maximum amount of data could be obtained before there was a possibility of the specimen becoming damaged or destructured.

Between two strain excursions, a rest period was induced for stress relaxation under constant radial strain. This is necessary for investigating the small strain stiffness of stiff clay (see Section 2.6.5). In the tests on stiff clay, the deviator stress relaxation rate was reduced to less than 1% of the deviator stress change rate at the beginning of the next loading excursion. The rest period lasted from a few hours to a few days, depending on the magnitude of the cyclic radial strain range (see Table 5.3). Its length was determined during the first rest period under a new cyclic radial strain range. The rest periods took considerable time, making the whole test period very long.

The cyclic loading under a particular radial strain range would continue until it became evident that the soil had entered a "resilient state", in which the soil stress-strain relationship was no longer changed with cycling. The cyclic radial strain range was then raised to a larger magnitude.

The shearing rate was chosen to be 2% axial strain per day, which was slow enough for the pore water pressure to equilibrate inside the soil specimen under an undrained condition (Bishop & Henkel, 1962).

5.4.3 Drained radial strain-controlled cyclic loading

The behaviour of stiff clay subjected to radial strain-controlled cyclic loading under drained conditions was also investigated in this research, to check whether drainage would lead to build-up of lateral stress.

After undrained radial strain-controlled cyclic loading, specimen AC3 was found to be still in good condition, as there is no obvious reduction in the small strain stiffness and no signs of destructuring or damage to the specimen. Therefore AC3 was then used for drained cyclic loading under three cyclic radial strain ranges (0.05%, 0.1% and 0.15%).

Atherfield I Clay is a heavily overconsolidated stiff clay with low permeability. Oedometer test results suggest a coefficient of consolidation c_v= 2.2 m^2/year for

design purpose (Geotechnical Design Basis Repost, 1997). Because drained loading could only be achieved extremely slowly on the 100mm diameter stiff clay specimen, even with both ends and side drainage, only one cycle was performed at each radial strain level (Table 5.4).

The suitable shearing rate for drained loading was decided by carrying out trials with different shearing rates. At first, a shearing rate of 0.2% axial strain per day was applied; it was found that the response was similar to an undrained loading with significant accumulation of mid-plane excess pore water pressure. Then, much slower shearing rates were tried. It was found that when the shearing rate was reduced from 0.03% to 0.015% axial strain per day, the drainage performance of the soil had not been improved significantly. Even with a shearing rate as low as 0.015% axial strain per day, where it took more than 8 days for one cycle of 0.05% radial strain range, there was still some excess pore water pressure (about ±5kPa). Any further lower shearing rate would become impractical. Therefore, the shearing rate was selected as 0.03% axial strain per day.

Although 100% drainage was not achieved in each stress excursion, the excess pore water pressure was left to dissipate in the following rest period. Thus the whole cycle is more representative of an idealized case in field, in which the bridge deck length is changed over a relatively shorter period and then kept constant for a period for full drainage in the soil behind.

5.4.4 Undrained monotonic shearing

Undrained monotonic shearing on specimens AC1, AC2 and AC3 were conducted at different initial mean effective stresses (p_o'), as shown in Table 5.2. These tests aimed to investigate the strength behaviour of Atherfield I Clay. All the shearing rates were set as a constant external axial strain rate of 2% per day, the same as that for the undrained cyclic loading.

5.5 Results and discussion

In this section, the major findings from the experimental programme will be presented, including the stress-strain behaviour of Atherfield I Clay under radial strain-controlled cyclic stress path testing (Section 5.5.1), as well as the undrained stiffness behaviour (Section 5.5.2) and the undrained strength behaviour (Section 5.5.3).

5.5.1 Stress-strain behaviour under cyclic loading

For integral abutment design, a major concern is whether there will be a build-up of lateral earth pressure with temperature-induced cyclic loading. Therefore, the stress-strain behaviour of stiff clay under radial strain-controlled cyclic loading is of practical importance. The major findings on the stress-strain behaviour of Atherfield I Clay specimens (AC2 and AC3) will be presented here.

Stress-strain behaviour under undrained cyclic loading

On each specimen, different cyclic radial strain ranges were applied under undrained conditions (Table 5.3). The initial stress states for specimens AC2 and AC3 were different, as discussed in Section 5.4.1. For specimen AC2, all the undrained cyclic loading was carried out above the isotropic line. For specimen AC3, the undrained cyclic loading started around the isotropic state and was performed crossing the isotropic line.

Figure 5.6~Figure 5.9 presents the test results from specimen AC2 (under radial strain ranges of 0.04% and 0.075%) and specimen AC3 (under radial strain ranges of 0.05% and 0.1%). These radial strain ranges correspond to the strain variation inside the representative soil element caused by the annual length change of a medium bridge deck (30~60m), as discussed in Section 3.2.

For both specimens under different cyclic radial strain ranges, the deviator stress-radial strain behaviour exhibited a very similar pattern (Figures 5.6~5.9). Each strain excursion led to a change of horizontal stress, the magnitude of which depended on the cyclic radial strain range. The high non-linearity of the stress-strain behaviour during each stress excursion is evident. During the first strain excursion at each radial strain level, a slightly stiffer soil behaviour was observed as the previous radial strain level was being exceeded. However, in the subsequent strain excursions, such a pattern was not maintained, but instead the soil returned to follow the trend defined by the previous strain range. After the first cycle, the soil stress-strain relationship became identical and repeatable for each cycle. The soil was then believed to have entered a "resilient" state. There was no perceptible accumulation of deviator stress after a number of cycles. The maximum total lateral stress in each cycle was unchanged and not influenced with the increasing number of cycles (Table 5.5 and 5.6).

Typical effective stress paths for specimen AC2 (under a radial strain ranges of 0.075%) and specimen AC3 (under a radial strain ranges of 0.1%) are presented in Figure 5.10a & b respectively, derived from the mid plane pore pressure measurement. The total stress path is 135° in the *s-t* space. Some observations can be made.

First, the effective stress paths of each cycle followed an approximately vertical direction. There was no sign of yielding, which implies the soil exhibits pre-failure behaviour. For specimen AC2, no obvious difference was found between each stress excursion, though there was a slight variation in the mid plane pore water pressure (Figure 5.10a). For specimen AC3, a small difference between compression and extension paths was found in the mid part of the effective stress paths. The effective stress paths towards compression tended to bend to the left, while those moving towards extension tended to bend to the right (Figure 5.10b).

Secondly, the effective stress path of each cycle formed a closed loop. After each cycle, the effective stress returned to its original value, with no obvious changes in deviator stress or mean effective stress. In the resilient state, the effective stress path loop in one cycle was a repetition of the previous one. There was no shift of the effective stress path with cycles. This is consistent with the observation in the deviator stress-radial strain relationship.

Stress-strain behaviour under drained cyclic loading

Because of the very slow rate of loading required, only a single cycle of drained loading under three different cyclic radial strain ranges (0.05%, 0.1% and 0.15%) was carried out on specimen AC3, to check whether drainage would lead to build-up of lateral stress (Table 5.4).

The deviator stress-radial strain curve of specimen AC3 under a drained cyclic radial strain range of 0.15% is presented in Figure 5.11. Similar to the results of the undrained cyclic tests, the drained stress-strain curves also formed a closed loop. There was no obvious accumulation of deviator stress (or total lateral stress) after a full cycle.

The effective stress paths are presented in Figure 5.12a, based on the mid plane pore pressure measurement. An idealized effective stress path under 100% drainage condition is superimposed, which is a 135° straight line parallel to the total stress path. In contrast, a fully undrained effective stress path follows an approximately vertical direction, as observed in the previous undrained tests. It can be seen that even though

a rate of radial strain change as low as 0.03% per day was used, full drainage was not achieved at the mid-plane of the specimen.

The effective stress path in a whole cycle formed a closed loop around the 135° line in the *s'-t* stress space. At the end of each cycle, the effective stress state returned to its initial position. It was noted that the mid plane pore water pressure varied significantly during the test.

The volumetric strain is plotted against radial strain in Figure 5.12b. The volume increased when the deviator stress increased, since the mean effective stress decreased at the same time. A Poisson' ratio of 1.5 is evident for drained loading along this 135° stress path. After a whole cycle, there was no obvious accumulation of volumetric strain. This appears to suggest that there would not be significant changes in the density and void ratio of stiff clay even after drained cycles.

In summary, the above evidence shows that for Atherfield I clay under either undrained or drained cyclic loading with different radial strain ranges, the stress-strain behaviour will not change with cycles. The initial stress state has no major influence on the stress-strain behaviour under cyclic loading.

5.5.2 Undrained stiffness behaviour of Atherfield I Clay

It was thought that the stiffness of clay behind an integral abutment may change during the temperature-induced cyclic loading, presenting uncertainty for design. Therefore, the stiffness behaviour of Atherfield I Clay has been investigated extensively in this experimental programme. Conventional triaxial testing with external strain measurement generally underestimates the stiffness of natural soil (Section 2.6.2). In this experimental programme, the axial strain of Atherfield I Clay was measured locally using LVDTs, therefore eliminating any possible errors that could be introduced by external strain measurement. Furthermore, the rates of creep or stress relaxation were reduced to a sufficiently low level before the next stress excursion began, so that their influence on stiffness measurement was minimized.

In this section, the method to derive undrained Young's modulus will be introduced first. Then general undrained stiffness behaviour at small strains will be examined. A number of factors will then be investigated, which could have an effect on the stiffness behaviour of Atherfield I Clay under undrained cyclic loading, including:

- strain excursion direction inside one cycle, *e.g.* radial compression or radial extension;
- number of cycles under a particular cyclic strain range;
- previous cyclic radial strain ranges;
- stress path location;

Furthermore, the stiffness anisotropy will be evaluated. At the end of this section, a comparison will be made between local and external axial strain measurement during undrained cyclic loading.

During the first strain excursion (radial extension) at each radial strain range, a stiffer soil behaviour was observed once the previous radial strain level was exceeded. However, such a pattern was only observed for the first strain excursion and was not found during the following strain excursions under each radial strain range. Therefore, it was believed to be a temporary feature when the cyclic radial strain range was being raised to a larger size. For this reason, and for the ease of comparison, the stiffness behaviour during the first strain excursion under each cyclic radial strain range will not be included in the following discussion.

The method to derive undrained Young's modulus

Most natural soil, including overconsolidated stiff clay, exhibit both stiffness and strength anisotropy. This is mainly due to the fact that the particles tend to become aligned with the horizontal plane during deposition (Hight & Leroueil, 2002).

To simplify the problem, stiffness isotropy has been assumed when quoting the horizontal stiffness variation during cyclic loading. However, as might be expected, the Atherfield I Clay is strongly anisotropic. Its extent will be estimated using the method of Graham & Houlsby (1983).

For a stiff clay element behind an embedded integral abutment, the horizontal undrained Young's modulus E_{uh} is of most importance, because the lateral stress changes with cyclic strains while the vertical pressure remains constant. By assuming isotropy, the relationship between strain increase and total stress increase in an undrained triaxial test can be expressed as below, according to Hooke's law:

$$\begin{bmatrix} \Delta\varepsilon_a \\ \Delta\varepsilon_r \\ \Delta\varepsilon_r \end{bmatrix} = \frac{1}{E_{uh}} \begin{bmatrix} 1 & -\nu & -\nu \\ -\nu & 1 & -\nu \\ -\nu & -\nu & 1 \end{bmatrix} \begin{bmatrix} \Delta\sigma_a \\ \Delta\sigma_r \\ \Delta\sigma_r \end{bmatrix} \qquad (5.1)$$

For an undrained triaxial test, $\Delta\varepsilon_v=\Delta\varepsilon_a+2\Delta\varepsilon_r=0$, so that $\Delta\varepsilon_r=-0.5\Delta\varepsilon_a$ and $\nu=0.5$.
For a stiff clay element behind an integral abutment, the total vertical stress remains constant ($\Delta\sigma_a=0$), therefore

$$E_{uh} = \frac{\Delta\sigma_r}{2\Delta\varepsilon_r} \qquad (5.2)$$

Since the total vertical stress remains constant, $\Delta\sigma_r=-\Delta q$, and $\Delta\varepsilon_r=-0.5\Delta\varepsilon_a$, equation (5.2) can also be further expressed as:

$$E_{uh} = \frac{\Delta q}{\Delta\varepsilon_a} \qquad (5.3)$$

Similarly, for a conventional undrained triaxial test with a constant total radial stress ($\Delta\sigma_r=0$), the vertical undrained Young's modulus E_{uv} is of interest, which can also be derived from Hooke's law with an assumption of isotropy as

$$E_{uv} = \frac{\Delta q}{\Delta\varepsilon_a} \qquad (5.4)$$

Although equations (5.3) and (5.4) appear to be identical, it should be noted that equation (5.3) is for the derivation of E_{uh} from undrained radial loading with constant total vertical stress, while equation (5.4) is for E_{uv} from undrained triaxial loading with constant total radial stress.

General undrained stiffness behaviour at small strains

The undrained stiffness behaviour of Atherfield I Clay in all undrained stress excursions exhibited some general patterns, as demonstrated in Figure 5.13. Figure 5.13a presents a typical curve of undrained secant horizontal Young's modulus E_{uh} against radial strain, whilst Figure 5.13b plots a typical curve of undrained secant vertical Young's modulus E_{uv} against axial strain. Two observations can be made, as below.

First, the stiffness appears to be exhibit a plateau at strain levels up to about 0.002%, though there was some variability in the data due to electronic noise and measurement resolution. Such a plateau is indicative of linear stress-strain behaviour, which occurs inside the *Y1* yield surface as proposed by Jardine *et al.* (1991) (also see Section 2.6.3). The limit of the plateau coincides with the experimental results by Clayton and Heymann (2001), who found the limits of the linear stress-strain behaviour of Chalk, London Clay and Bothkennar Clay were all approximately at 0.002% to 0.003% axial strain.

Secondly, the highly non-linear nature of the specimen response is evident. The stiffness decreased sharply over the strain range of 0.01% to 0.1%. Since the strain level in the soil behind a typical integral abutment is also within a similar range (Section 3.2), this implies that the non-linear stress-strain response of soil should be taken into consideration in design or that the stiffness required for calculations has to be derived at an appropriate strain level. These two curves are further normalized by p_o' and compared in Figure 5.18.

Effect of strain excursion direction in one cycle on stiffness

During the radial strain-controlled cyclic loading, each cycle consisted of two strain excursions with different loading directions; one was radial compression and the other was radial extension. The undrained stiffness behaviour of both strain excursions in each cycle was examined.

Figure 5.14a plots a typical pair of compressive and extensive stiffness-strain curves in one cycle for specimen AC2. Although the strain excursion directions were different, no obvious difference was observed in either the value of the maximum stiffness at very small strains or the rate of degradation of stiffness between the two curves.

For specimen AC3 under undrained cyclic loading, a typical comparison is presented in Figure 5.14b. In general, the two curves exhibited a similar pattern. The value of maximum stiffness at very small strains was the same for both the compression and extension excursions. Over the axial strain range of 0.01% to 0.1%, the stiffness in radial extension (q increasing) was found to be marginally lower than that in radial compression (q decreasing). The two stiffness-strain curves converged again near the end of the whole strain range. A reason for this slight difference during the mid strain range could be the small difference between the compressive and extensive effective stress paths in AC3, as shown in Figure 5.10b. In contrast, for specimen AC2, no obvious difference was found between the compressive and extensive effective stress paths (Figure 5.10a).

The above results show that the small strain stiffness is very similar for compression and extension inside one cycle.

Influence of the number of cycles on stiffness

A number of cycles were performed under each cyclic radial strain range. The stiffness behaviour of Atherfield I Clay from different cycles under each cyclic radial strain range was examined and compared.

Typical comparisons between two stiffness-strain curves from different cycles for specimen AC2 and AC3 are made in Figure 5.15a & b respectively. For AC3, the slight difference in the stiffness between the radial compression and radial extension excursions persisted throughout the cycles (Figure 5.14b); therefore only stiffness curves in radial compression were compared here. For both specimens, the stiffness-strain curves from different cycles were very similar, without obvious difference in the maximum stiffness or in the rate of degradation. It is clear that the soil stiffness behaviour remained unchanged throughout the cyclic loading under each cyclic radial strain range.

The above evidence shows that the number of previous cycles has no obvious influence on the soil stiffness-strain characteristic. This observation coincides with the fact that during the resilient state, each stress-strain loop was a repetition of the previous one, without any effect from the number of cycles.

Influence of previous cyclic radial strain ranges on stiffness

In this experimental programme, cyclic loading was performed under a low strain range first before increasing to higher magnitudes. This had the benefit that enough information could be obtained before any possible damage or destructuring happened. The influence of increasing strain level on the stiffness behaviour of Atherfield I Clay is examined by comparing stiffness-strain curves under different cyclic radial strain ranges.

Figure 5.16a compares the typical stiffness-strain curves at radial strain ranges of 0.04% and 0.075% for specimen AC2. The maximum stiffness at very small strains and the rate of degradation were found to be almost identical.

For specimen AC3, typical stiffness-strain curves under radial strain ranges of 0.05%, 0.1% and 0.15% are compared in Figure 5.16b. Although the strain range tripled, the small strain stiffness was unchanged and the rate of degradation was similar. Only near the end of each strain range was a very slight difference found in stiffness. However, it was unlikely that destructuring had happened, since the small strain stiffness remained unchanged. In contrast, destructuring would lead to

significant reduction in small strain stiffness. Hight *et al.* (1997) carried out undrained triaxial tests on Pliopleistocene sand (Crag) with loading-unloading cycles, in which a significant reduction was found in the small strain stiffness with progressive destructuring. Clayton & Heymann (2001) noted that once destructuring occurs, there was a dramatic decrease in the stiffness of Chalk.

The above results show that for Atherfield I Clay under this type of loading, the influence of increasing strain levels had only negligible influence on stiffness behaviour.

Influence of stress path location on stiffness

During the undrained radial strain-controlled cyclic loading, specimen AC2 was loaded above the isotropic line, while specimen AC3 was tested crossing the isotropic line. These Atherfield I specimens were obtained from a single construction site at Ashford, thus the geological history, chemical composition and soil structure can be assumed to be very similar to each other. Although the sampling technique was different for each specimen, the disturbance before testing was found to be insignificant (see Section 5.3.3). Therefore, the influence of stress path location could be examined by comparing the stiffness behaviour from these two specimens.

Since the soil stiffness was found not to be influenced by the strain excursion direction (Figure 5.14), number of cycles (Figure 5.15) or previous cyclic strain ranges (Figure 5.16), a representative stiffness–strain curve for each specimen under undrained cyclic loading can be produced, as presented in Figure 5.17. The stiffness is not normalised in the comparison, as the initial mean effective stresses (p'_o) for specimen AC2 and AC3 under undrained cyclic loading were close to each other. It can be seen that the two specimens exhibited almost identical stiffness characteristics, both for the maximum stiffness at very small strains and the rate of degradation of stiffness. The stress path location (including the initial stress state and principal stress reversal) appears to have had no obvious influence on the stiffness behaviour.

Evaluation of stiffness anisotropy

The stiffness anisotropy of Atherfield I Clay is evaluated using different methods. Figure 5.18a shows vertical undrained secant Young's modulus E_{uv} curves as a function of local axial strain for two specimens of Atherfield Clay loaded vertically (Curve 1 & 2), in an undrained triaxial compression test. Also shown are the

equivalent curves, but at lower effective stress levels, for Atherfield Clay specimens swelled back to the mean effective stress of the representative element, and then loaded horizontally, changing the radial total stress whilst holding the vertical total stress constant. For these curves the horizontal undrained secant Young's modulus E_{uh} is plotted as a function of the horizontal (radial) strain (Curve 3 & 4). The rate of stiffness reduction with increasing strain is similar for the two types of loading. Differences between the curves are highlighted after normalising the data by the initial mean effective stress p_o' at the start of shearing, as shown in Figure 5.18b. It can be seen that E_{uh}/p_o' is in general larger than E_{uv}/p_o'.

Figure 5.19a plots the effective stress paths in q-p' space for specimens AC1, AC2 and AC3 during monotonic shearing at different initial mean effective stresses p_o', while Figure 5.19b normalise the same graph by p_o'. It can be seen that all the three curves are not vertical at the beginning and exhibit initial slopes of about -4. This implies a strong inherent anisotropy, with a Young's modulus in the horizontal direction of about 2 times higher than that in the vertical direction (Graham & Houlsby, 1983).

Figure 5.20 plots the change in mid-plane pore water pressure (Δu) against change in mean total stress (Δp) for specimen AC1 and AC3 during monotonic shearing stage with a constant lateral stress. The initial linear behaviour can be described as $\Delta u = m\Delta p$, and in this case m=2 for both specimens. In contrast, an isotropic sample would lead to $\Delta u = \Delta p$ and m=1. Further evidence emerges from the ratio of volumetric strain against axial strain during the isotropic consolidation stage of specimen AC3 (Figure 5.21). An isotropic material will produce a ratio of 3. However, the ratio for Atherfield I Clay is found to be about 2, which indicates that the horizontal stiffness is about 2 times the vertical stiffness (Graham & Houlsby, 1983).

The above evidence shows that Atherfield I Clay is strongly anisotropic, with a Young's modulus in the horizontal direction of about 2 times that in the vertical direction.

Local and external axial strain measurement during cyclic loading

External axial strain measurement may introduce large errors, such as those identified by Baldi *et al.* (1988), including bedding errors, compliance errors, and alignment errors (see Section 2.6.2). The local axial strain measured by LVDTs was therefore compared with those measured by external strain gauges. It was found that for all the three specimens, the external measurement significantly overestimated the

axial strain during the virgin stress excursion. Figure 5.22a presents a typical comparison of local and external strains in the monotonic shearing stage of specimen AC1.

After a number of cycles, the comparison was made again. Figure 5.22b presents the tests results from the monotonic shearing stage of specimen AC2. It is found that external strain measurement gave a reasonable result after cyclic loading, though the resolution of external strain was coarse and the axial strain was still overestimated. One likely reason is that during cyclic loading the bedding errors and seating errors were reduced. For example, the irregular gaps between the top cap (or the base pedestal) and the ends of the specimen may become closed under cyclic loading. The remaining slight overestimation of axial strain after a number of cycles might be due to the compliance of the equipment, *e.g.* the deformation of Perspex top cap under loading. The extent of compliance errors would not be changed by the cyclic loading. But it appeared to be much smaller in this experiment, compared with the bedding errors or seating errors.

In summary, during undrained radial strain-controlled cyclic loading, the stiffness behaviour of Atherfield I Clay was not influenced significantly by the strain excursion direction inside a single cycle, or by the number of cycles, previous cyclic radial strain ranges, or the stress path location. Strong anisotropy was found in stiffness, with a Young's modulus in the horizontal direction of about two times higher that in the vertical direction.

5.5.3 Undrained strength of Atherfield I Clay

Specimens AC1 and AC3 were sheared to failure under a constant cell pressure (Tests AC1-T1 and AC3-T4, see Table 5.2), enabling the undrained strength behaviour of Atherfield I Clay to be investigated. Specimen AC2 was sheared to an axial strain level of about 2.5% (Test AC2-T2), but was not brought to failure. It was removed for the trial testing of the improved extension device.

Figure 5.23a shows the deviator stress-axial strain characteristics of specimens AC1 and AC3 during the undrained monotonic shearing stages. Both specimens reached their peak strength at approximately the same axial strain level of 4%. After that strain, the strength decreased with indication that a critical state was being approached. The shearing was stopped at an axial strain of about 6%, in order to protect the LVDTs

from being damaged. After each test, the specimen was removed from the triaxial cell and examined. A shear band was evident at the mid part for each specimen.

In order to examine the initial stiff zone at small strains, the strains in Figure 5.23a have been re-plotted to a logarithm scale in Fig 5.23b. It shows that the mobilized strength increases sharply at the small strain level. Only 0.1% deformation was needed in both tests to mobilize 25% of the total soil strength.

The effective stress paths followed by specimens AC1, AC2 and AC3 during undrained shear are presented in Figure 5.24. A failure envelope is imposed, for an effective friction angle $\varphi'=26^{o}$ and an effective cohesion $c'=10$kPa. Although AC2 did not reach its peak shear strength, it is evident that the soil had failed. After reaching the failure envelope, the stress paths of all three specimens began to move along the yield envelope, possibly due to the development of the shear band at the mid part.

5.6 Summary

In this experimental programme, the behaviour of a representative stiff clay element behind an embedded integral abutment was investigated by carrying out radial strain-controlled cyclic stress path testing on Atherfield I Clay.

The undrained test results show that each strain excursion led to a change of horizontal stress, the magnitude of which depended on the cyclic radial strain range. However, the stress-strain behaviour did not change with cycling. The stiff clay entered a resilient state after the first cycle of loading and there was no obvious build-up of maximum horizontal stress. The initial stress state had no obvious influence on the stress-strain behaviour.

Drained cycles were also imposed on Atherfield I Clay specimen. It was found that Atherfield I Clay has a very low permeability. During loading and unloading with drainage, both volumetric and axial strains were recoverable, and there was no evidence of an increase in horizontal stress.

The undrained stiffness behaviour of Atherfield I Clay has been investigated. The stiffness is strain level dependent and exhibits high non-linearity. It can be expected to change significantly over the range of horizontal strains that can be expected behind embedded abutment in stiff clay.

Under cyclic loading, the stiffness behaviour of Atherfield I Clay remained unchanged. The maximum stiffness at small strains and the degradation rate of stiffness was found not to be effected by the strain excursion direction, or by the number of cycles, previous cyclic radial strain range, or the stress path location. Strong anisotropy was found in stiffness of Atherfield I Clay, with a Young's modulus in the horizontal direction of about two times that in the vertical direction.

Local and external axial strain was compared. It was found that the overestimation in the external strain measurement decreased after a number of cycles, probably because the bedding errors and seating errors were reduced by the cyclic loading.

The strength behaviour of Atherfield I Clay was also investigated. It was again shown that only small deformation (0.1%) was needed to mobilized 25% of the full strength.

Table 5.2 Summary of all tests on Atherfield I Clay

Specimen No.	Test No.	p_o' (kPa)	Type of test	Note
AC1	AC1-T1	360	Undrained monotonic shearing*	
AC2	AC2-T1	80	Undrained radial strain-controlled cyclic loading	see Table 5.3
	AC2-T2	80	Undrained monotonic shearing	
AC3	AC3-T1	76	Undrained radial strain-controlled cyclic loading	see Table 5.3
	AC3-T2	76	Drained radial strain-controlled cyclic loading	see Table 5.4
	AC3-T3	115	Undrained loading-unloading	
	AC3-T4	230	Undrained monotonic shearing*	

Note:

* Only AC1-T1 and AC3-T4 followed a 45° stress path in the *s-t* space (a constant radial total stress). All the other tests followed a 135° stress path in the *s-t* space (a constant vertical total stress).

Table 5.3 Summary of undrained radial strain-controlled cyclic tests

(Shearing rate: 2% axial strain per day)

Test No.	Stage No.	Cyclic radial strain range (%)	Initial q before cyclic loading (kPa)	Number of cycles	Length of rest period (hours)
AC2-T1	AC2-U-0.04%	0.04	15.87	5	12
	AC2-U-0.75%	0.075	14.41	3	14
AC3-T1	AC3-U-0.025%	0.025	0.48	6	8
	AC3-U-0.05%	0.05	0.60	6	13
	AC3-U-0.1%	0.1	-3.51	4	22
	AC3-U-0.15%	0.15	-3.75	1	30

Table 5.4 Summary of drained radial strain-controlled cyclic tests

(Shearing rate: 0.03% axial strain per day)

Test No.	Stage No.	Cyclic radial strain range (%)	Initial q before cyclic loading (kPa)	Number of cycles	Length of rest period (days)	Total time for one cycle (days)
AC3-T2	AC3-D-0.05%	0.05	0	1	1.2	5
	AC3-D-0.1%	0.1	-0.12	1	1.5	8
	AC3-D-0.15%	0.15	0.12	1	2	10

Table 5.5 Summary of undrained test results for specimen AC2
(Test AC2-T1)

Specimen.	Radial strain range (%)	Cycle Number	q (kPa)		σ_h (kPa) *	
			at the start of a cycle	at the end of a cycle	at the start of a cycle	at the end of a cycle
AC2	0.04	1	15.87	10.18	68.13	73.82
		2	14.66	9.93	69.34	74.07
		3	14.29	9.93	69.71	74.07
		4	13.93	9.93	70.07	74.07
		5	14.17	10.05	69.83	73.95
	0.075	6	14.41	8.48	69.59	75.52
		7	13.32	8.48	70.68	75.52
		8	12.60	8.36	71.4	75.64

Table 5.6 Summary of undrained test results for specimen AC3
(Test AC3-T1)

Specimen	Radial strain range (%)	Cycle Number	q (kPa)		σ_h (kPa) *	
			at the start of a cycle	at the end of a cycle	at the start of a cycle	at the end of a cycle
AC3	0.05	1	0.60	-10.54	83.40	94.54
		2	-2.78	-10.78	86.78	94.78
		3	-2.18	-10.65	86.18	94.65
		4	-2.54	-10.18	86.54	94.18
		5	-1.33	-9.57	85.33	93.57
		6	-1.87	-9.57	85.87	93.57
	0.1	7	-3.51	-13.93	87.51	97.93
		8	-3.87	-13.69	87.87	97.69
		9	-4.11	-13.32	88.11	97.32
		10	-3.63	-13.32	87.63	97.32
	0.15	11	-3.75	-14.78	87.75	98.78

Note: * σ_h is the corresponding horizontal total stress in the field and is derived as ($\gamma \times z - q$), where γ is the bulk unit weight of soil (21kN/m^3), and z is the depth of the representative soil element (4m).

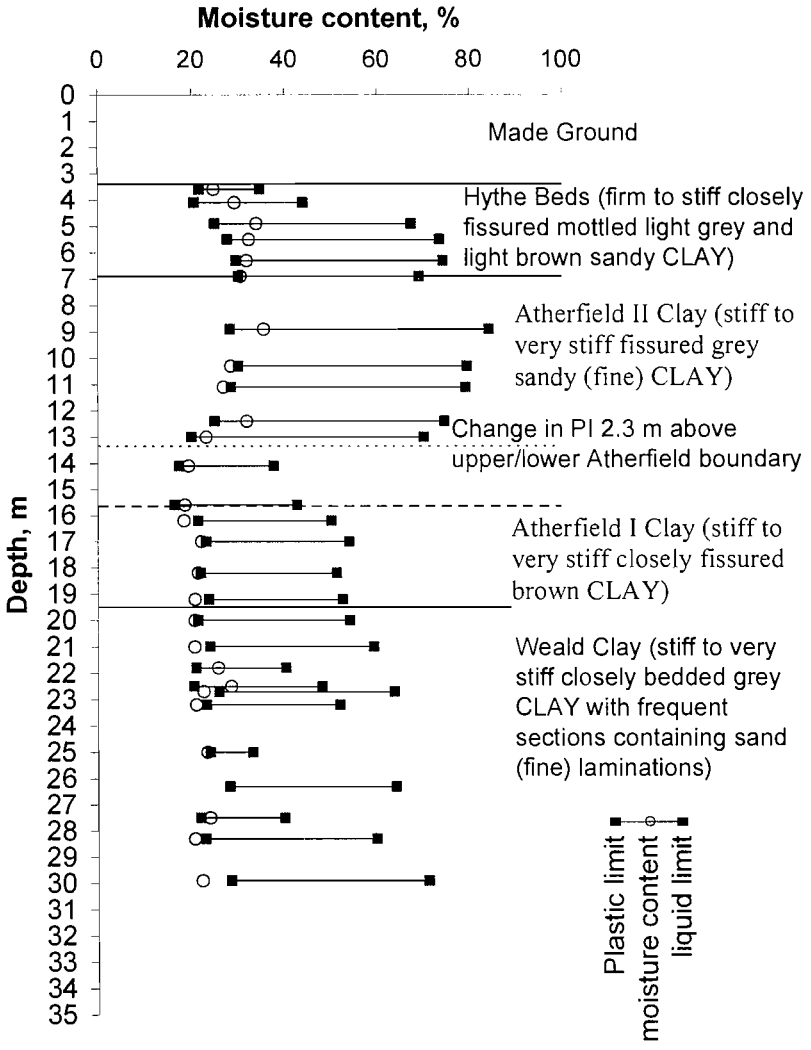

Figure 5.1 Geotechnical profile at the cut-and-cover tunnel (CTRL) at Ashford, Kent, including liquid and plastic limit data (Clark, 2005)

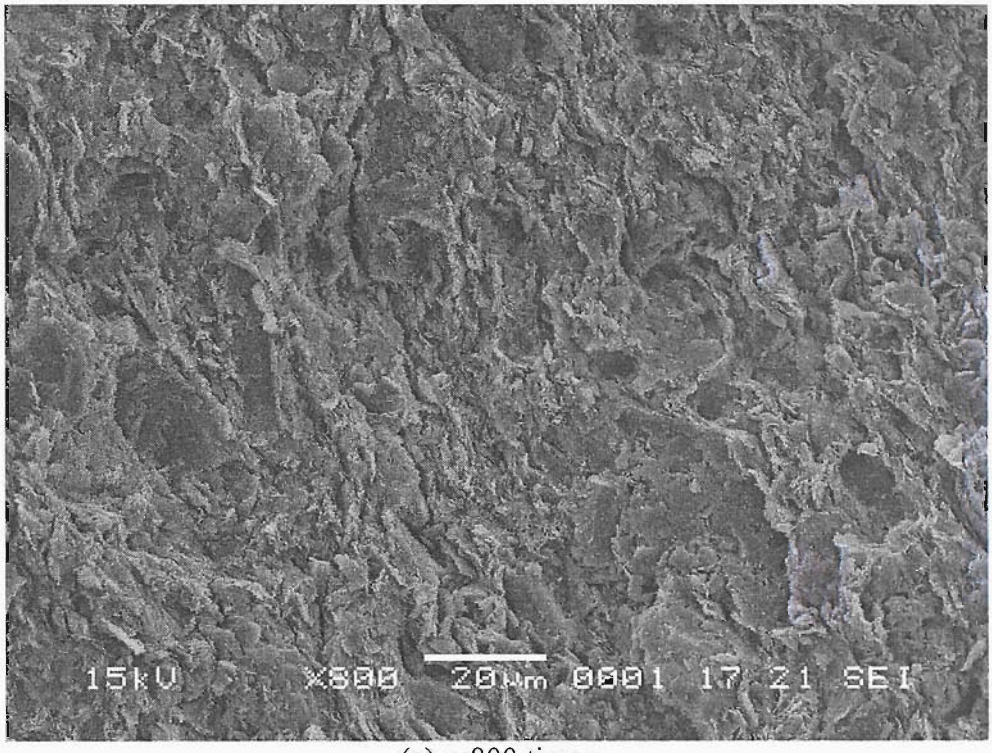

(a) ×800 times

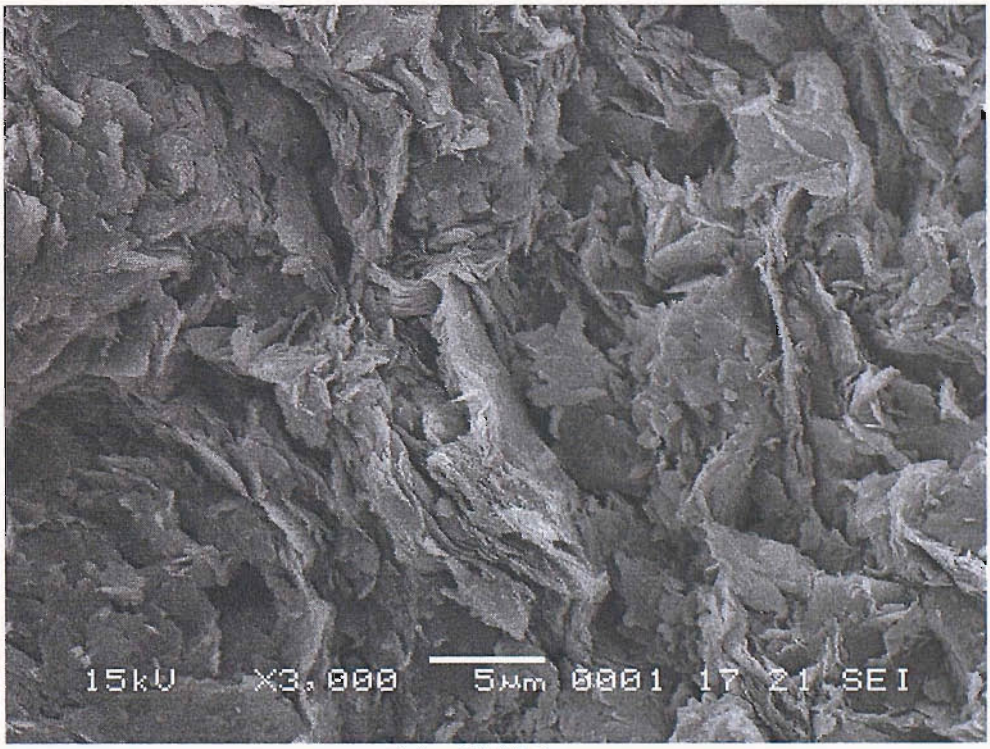

(b) ×3000 times

Figure 5.2 Scanning electron micrographs of Atherfield I Clay

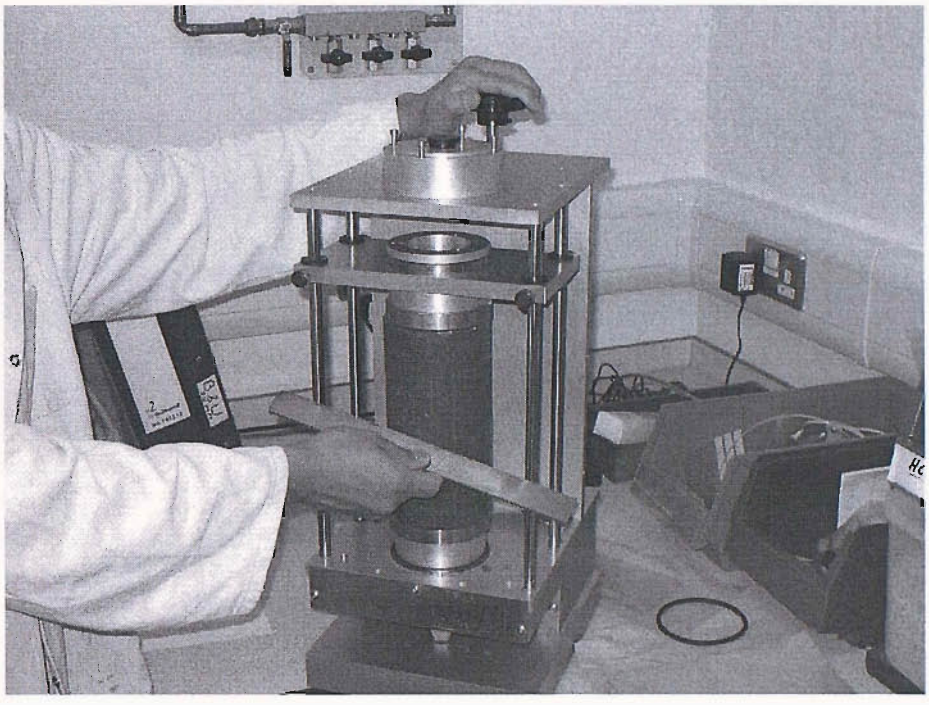

Figure 5.3 The procedure of smoothing the specimen surface in the soil lathe using the steel scraper

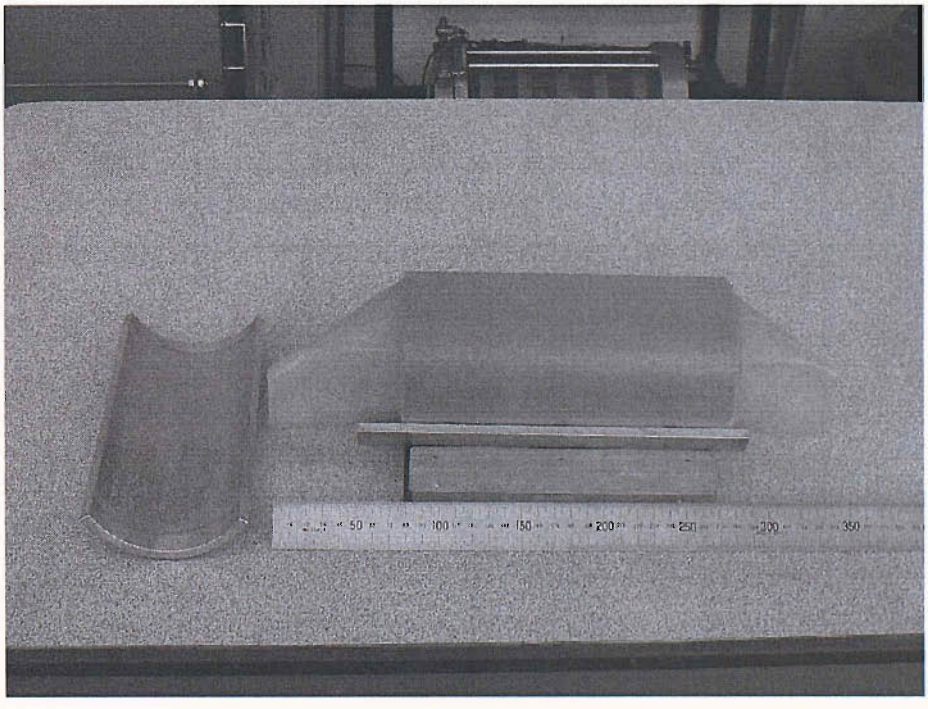

Figure 5.4 Tools used to mark the positions of the LVDTs on the membrane

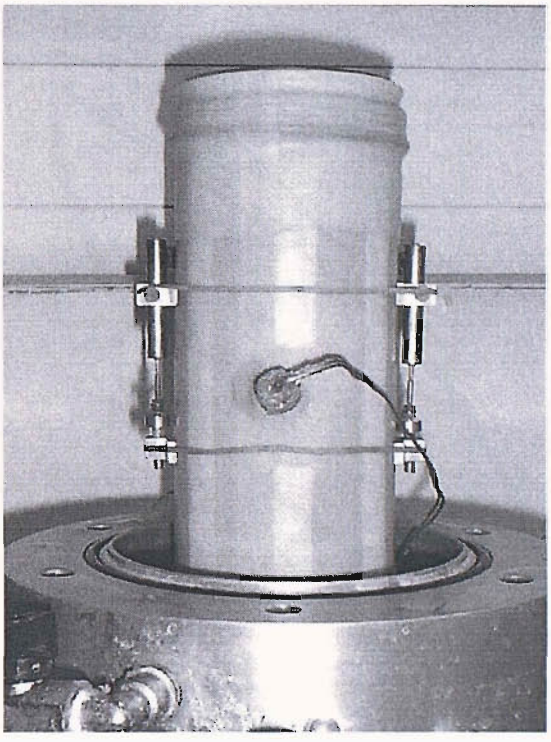

Figure 5.5 The completion of set-up of an Atherfield I Clay specimen

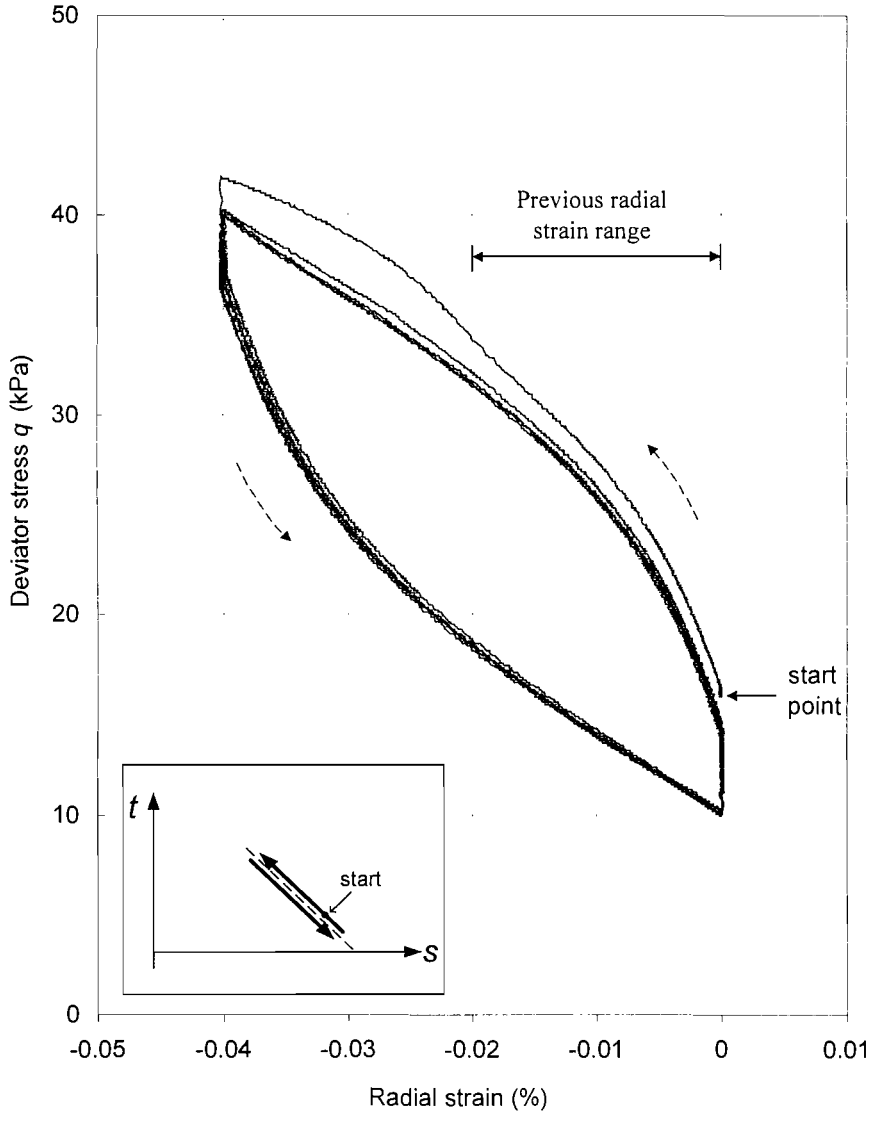

Figure 5.6 Curves of deviator stress against radial strain for specimen AC2 under an undrained cyclic radial strain range of 0.04% (5 cycles)

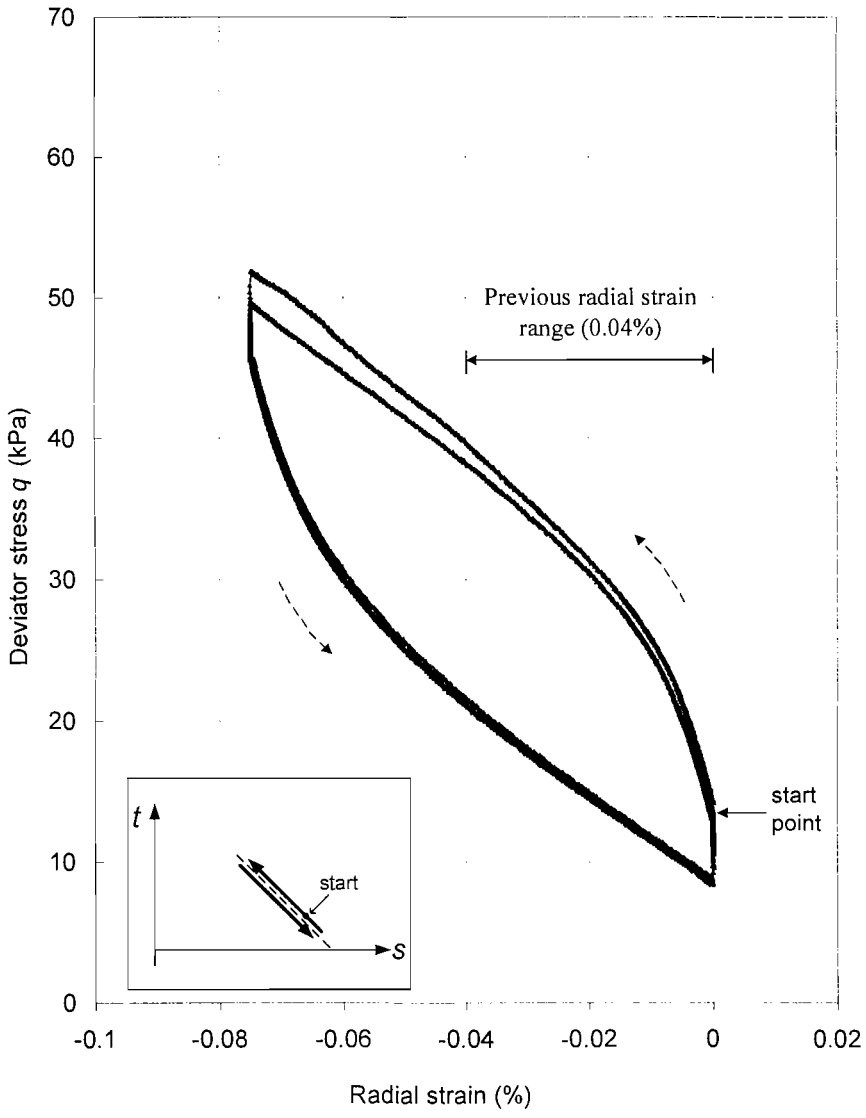

Figure 5.7 Curves of deviator stress against radial strain for specimen AC2 under an undrained cyclic radial strain range of 0.075% (3 cycles)

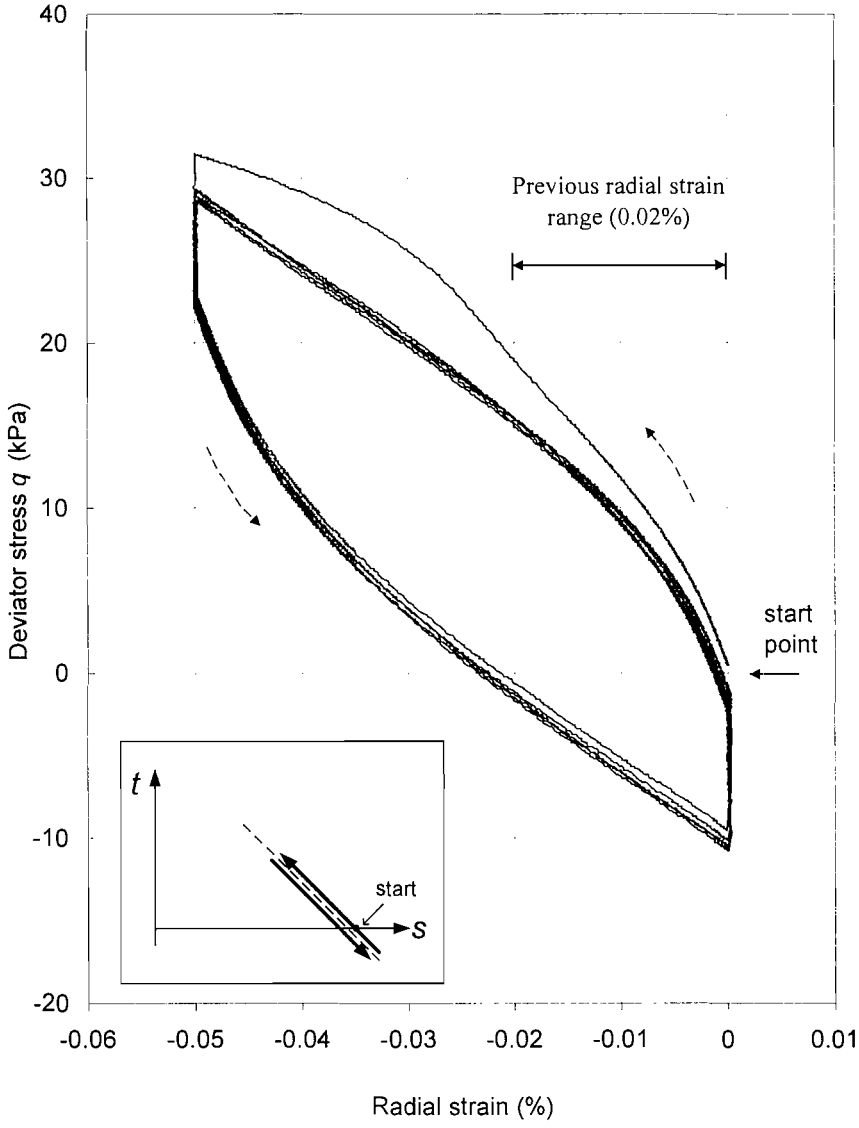

Figure 5.8 Curves of deviator stress against radial strain for specimen AC3 under an undrained cyclic radial strain range of 0.05% (6 cycles)

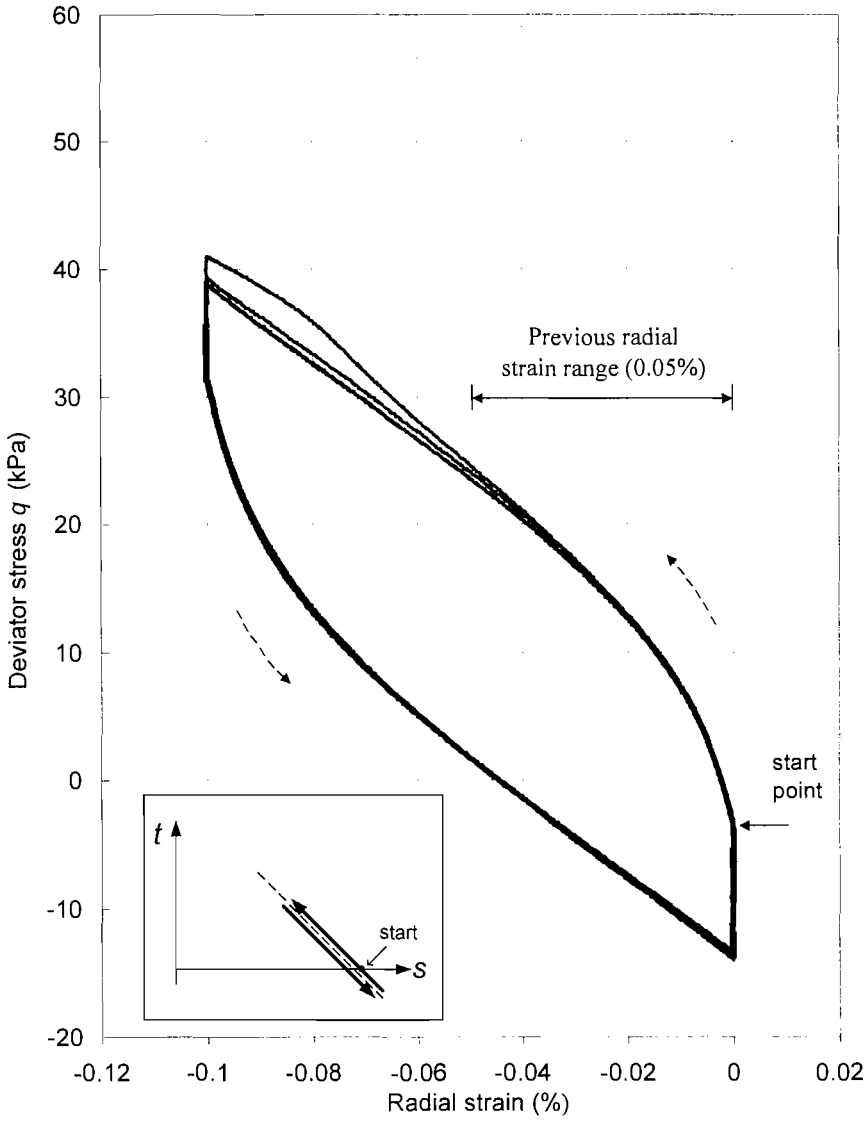

Figure 5.9 Curves of deviator stress against radial strain for specimen AC3 under an undrained cyclic radial strain range of 0.1% (4 cycles)

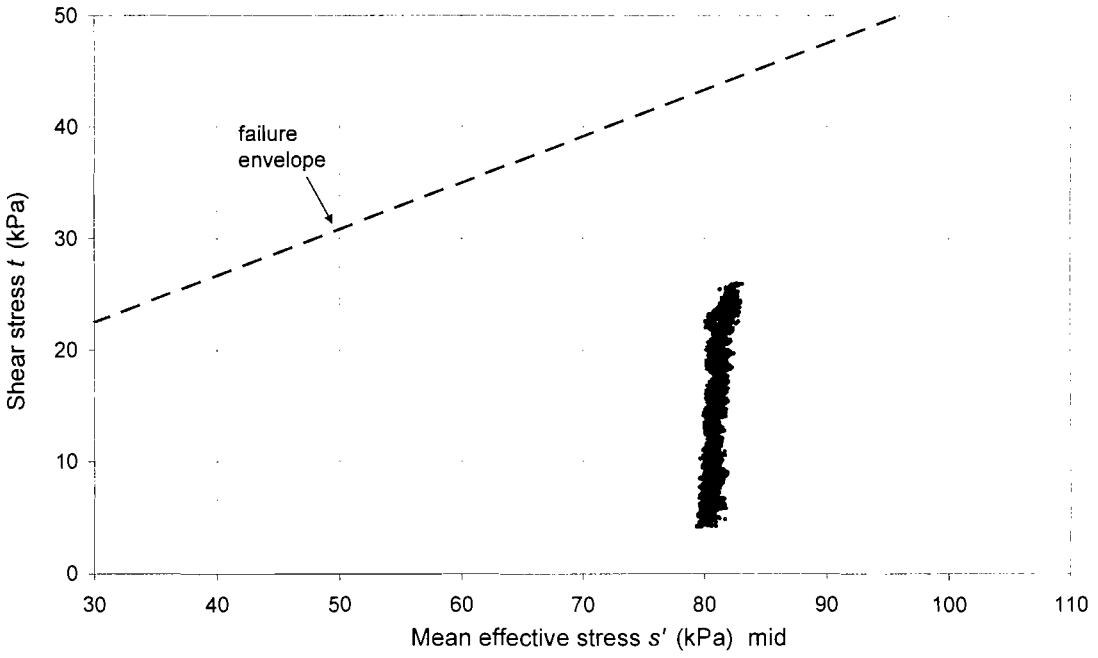

(a) Specimen AC2 under a cyclic radial strain range of 0.075% (3 cycles)

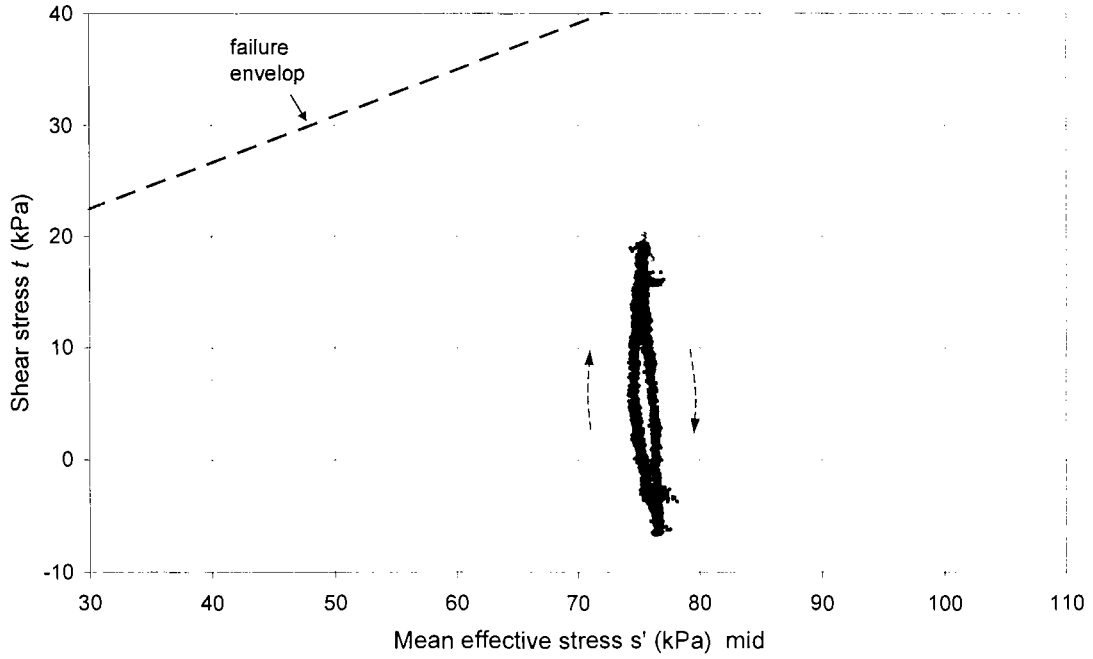

(b) Specimen AC3 under a cyclic radial strain range of 0.1% (4 cycles)

Figure 5.10 Effective stress paths of specimens AC2 and AC3 under undrained cyclic loading (based on the mid plane pore water pressure measurement)

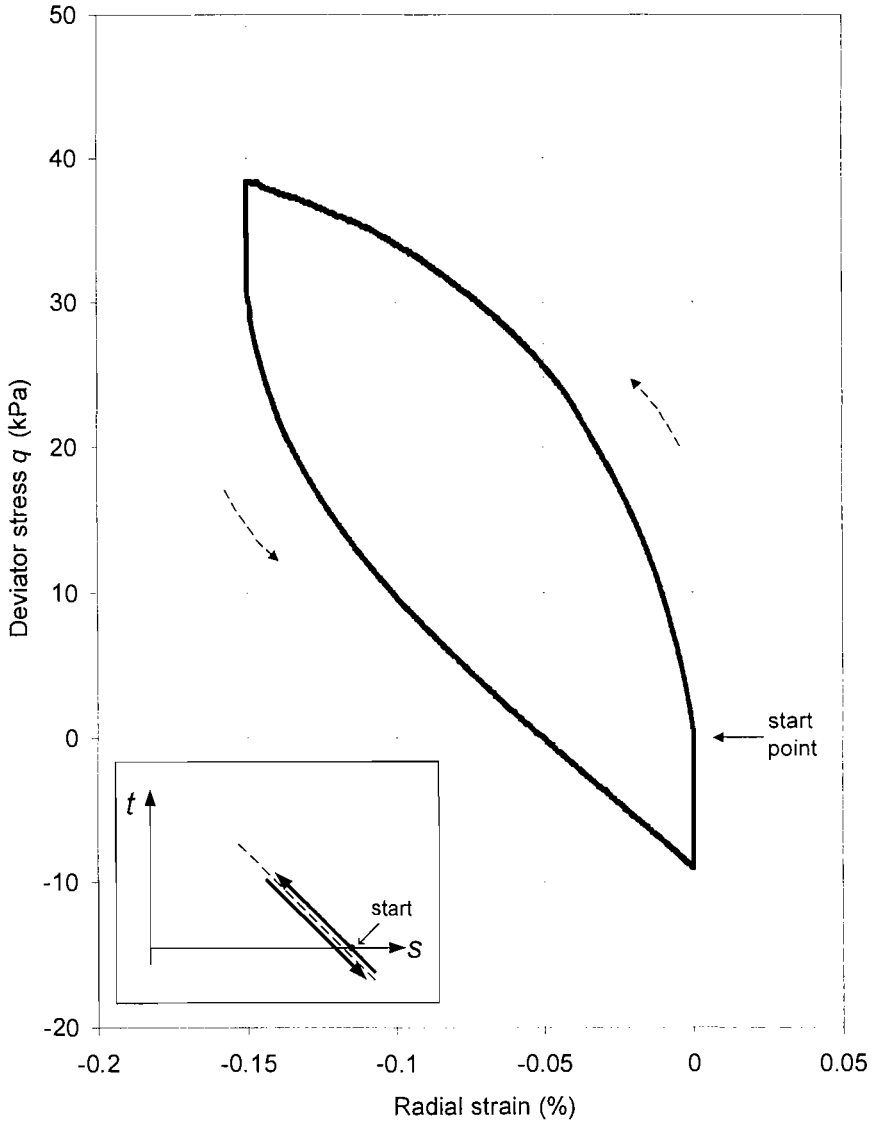

Figure 5.11 Curves of deviator stress against radial strain for specimen AC3 under a drained cyclic radial strain range of 0.15% (1 cycle)

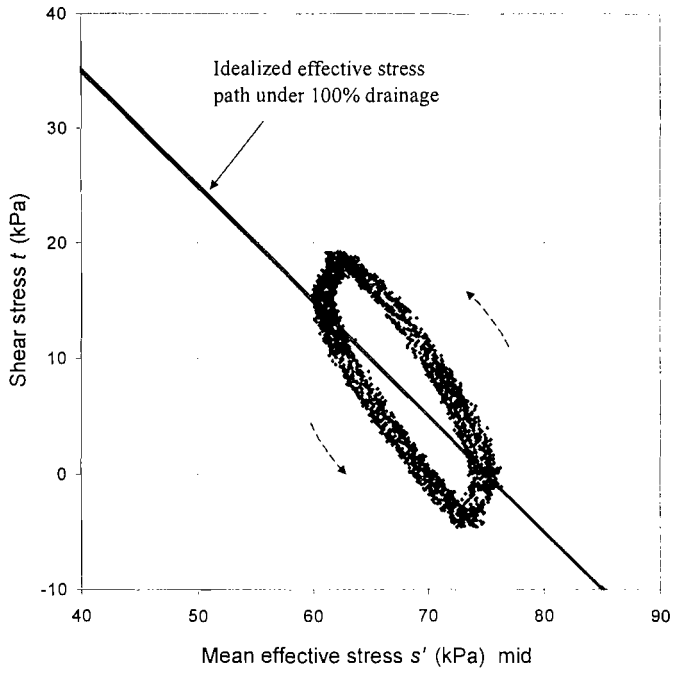

(a) The effective stress path, based on the mid plane pore water pressure measurement

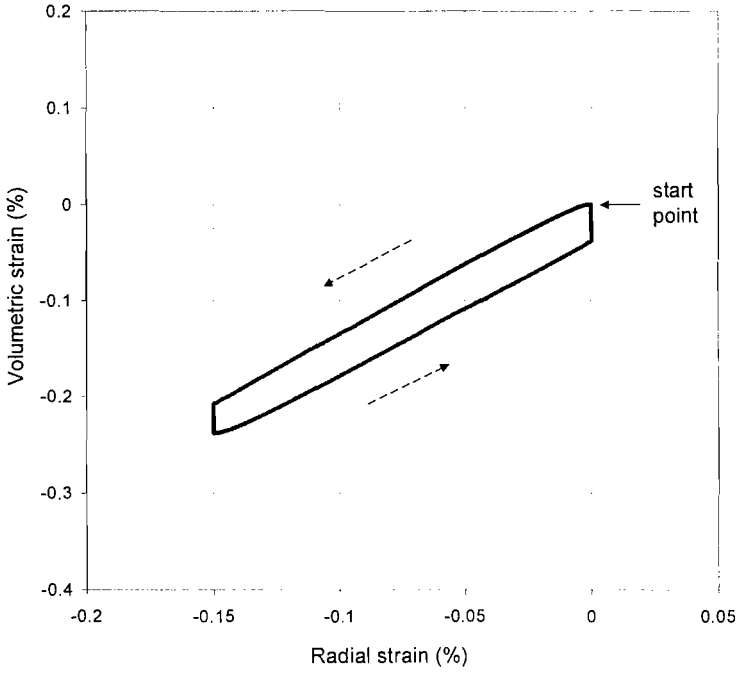

(b) The radial strain-volumetric strain relationship

Figure 5.12 Effective stress path and radial strain-volumetric strain relationship of specimen AC3 under a drained cyclic radial strain range of 0.15% (1 cycle)

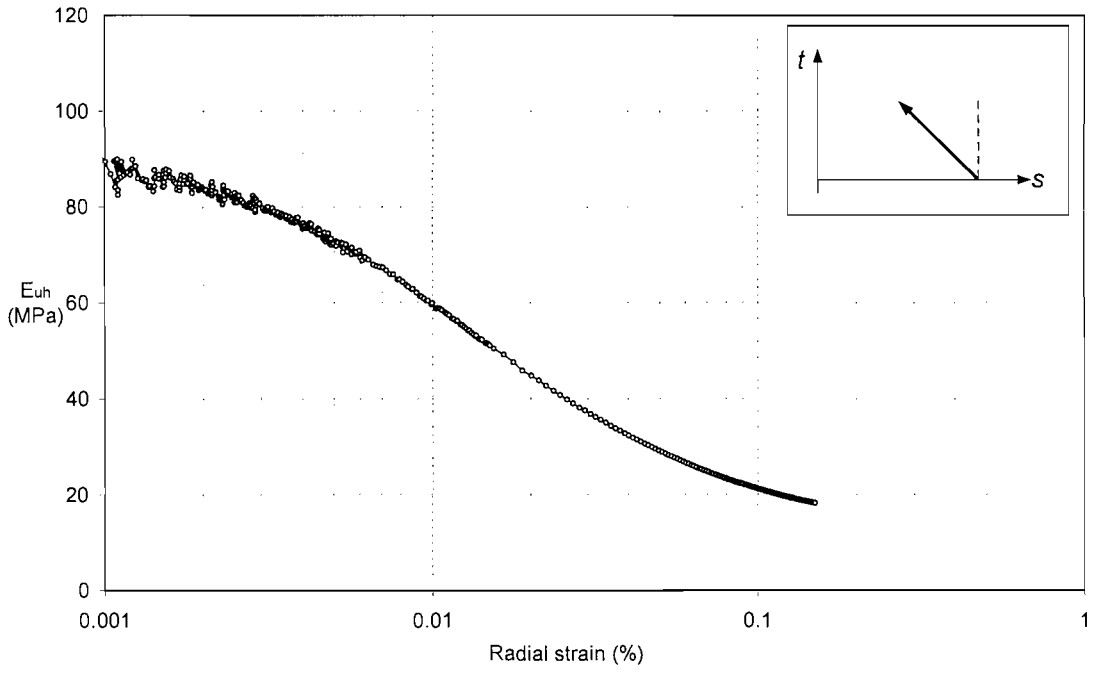

(b) Undrained secant horizontal Young's modulus as a function of radial strain for specimen AC3 (p_o'=76kPa)

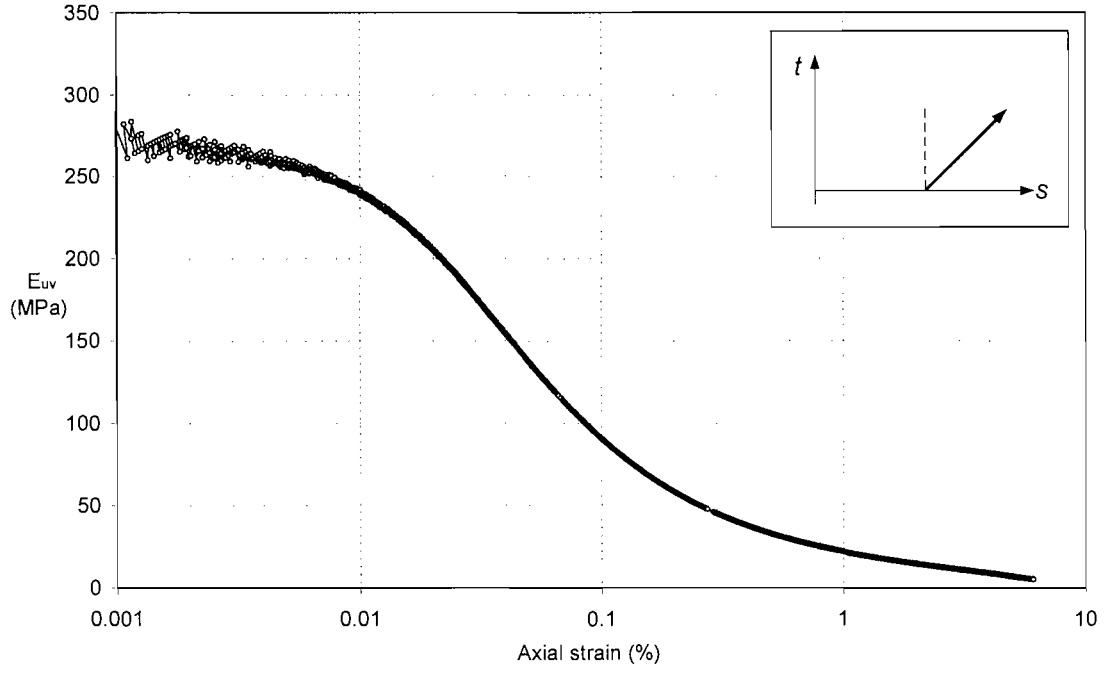

(b) Undrained secant vertical Young's modulus as a function of axial strain for specimen AC1 (p_o'=360kPa)

Figure 5.13 Typical undrained stiffness at small strains

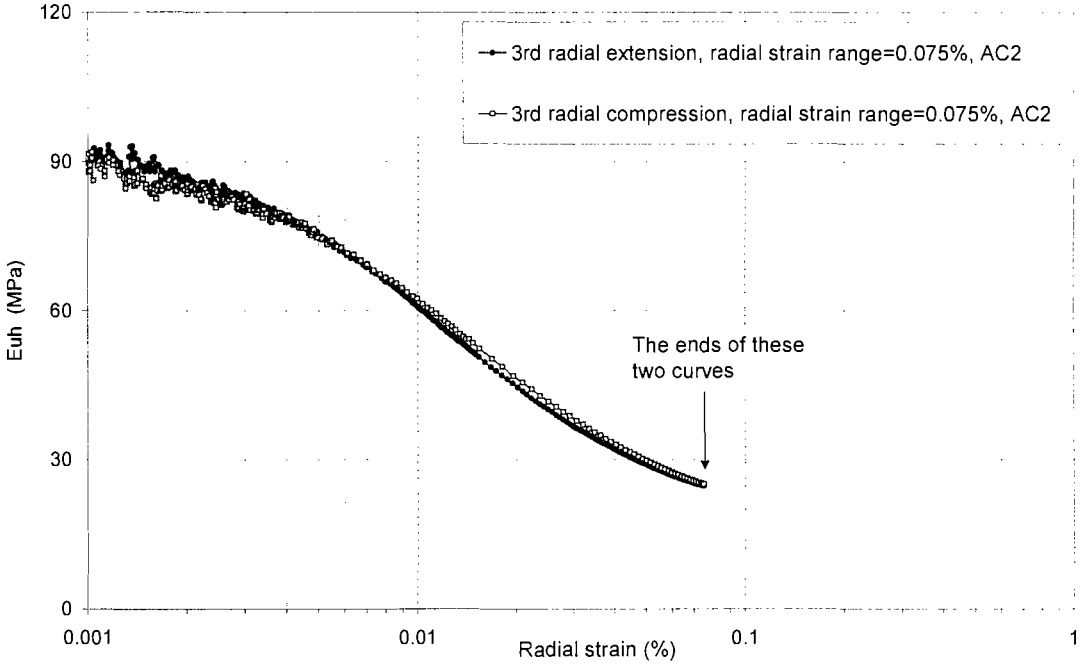

(a) Comparison in one cycle under an undrained cyclic radial strain range of 0.075%, specimen AC2

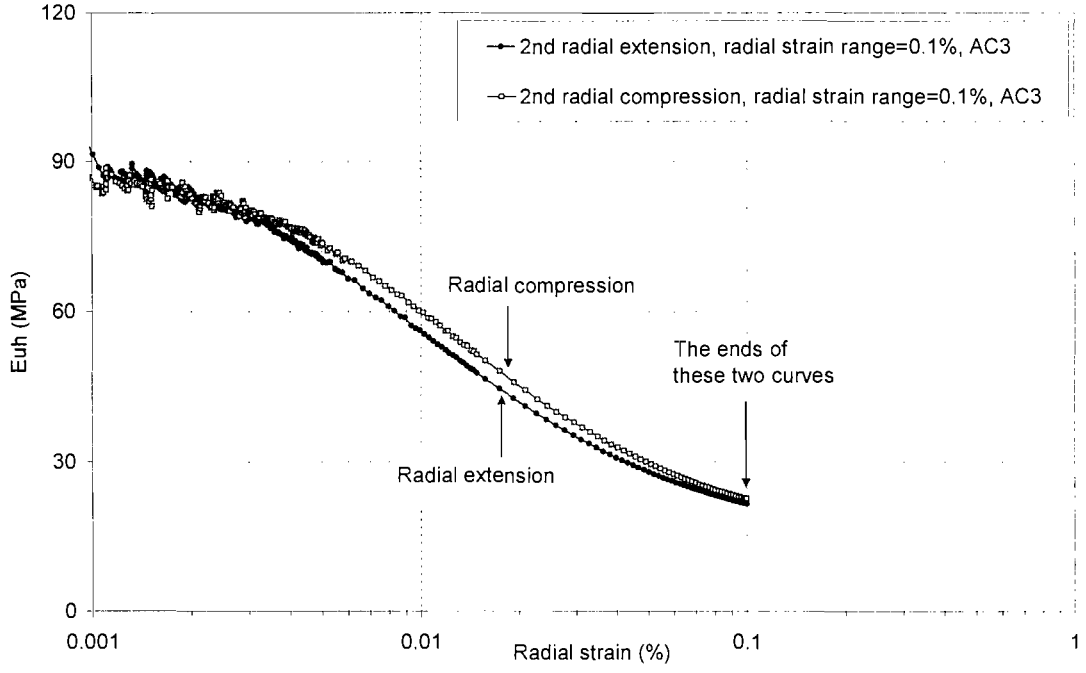

(b) Comparison in one cycle under undrained cyclic radial strain range of 0.1%, specimen AC3

Figure 5.14 Comparison of the stiffness behaviour of radial compression and radial extension in one typical cycle

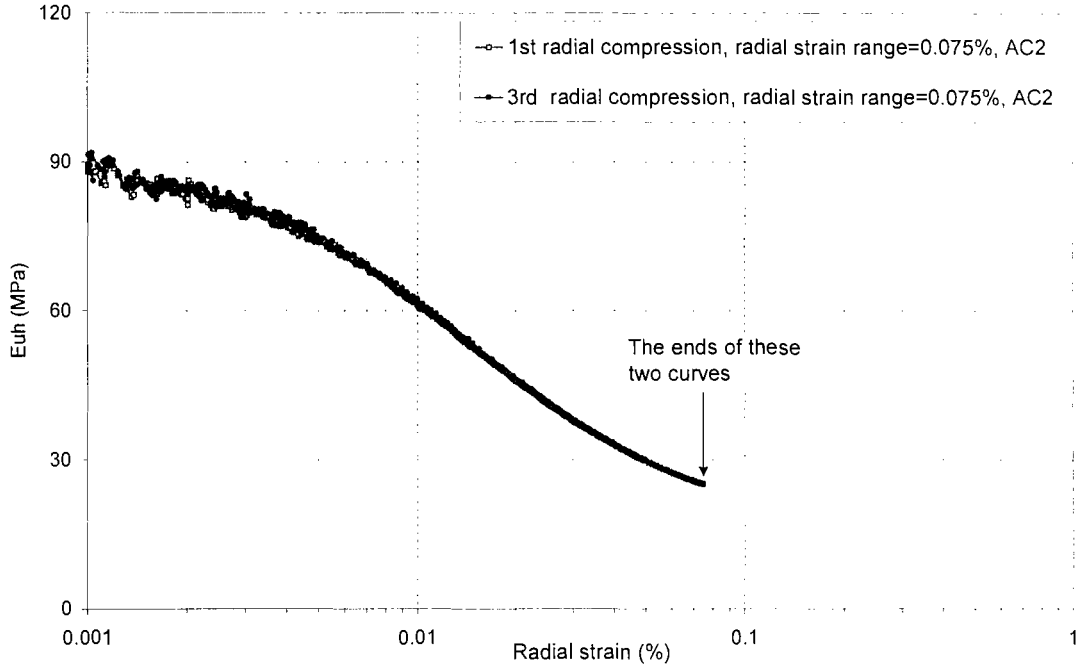

(a) The stiffness of the first and the last radial compression under an undrained cyclic radial strain range of 0.075%, specimen AC2

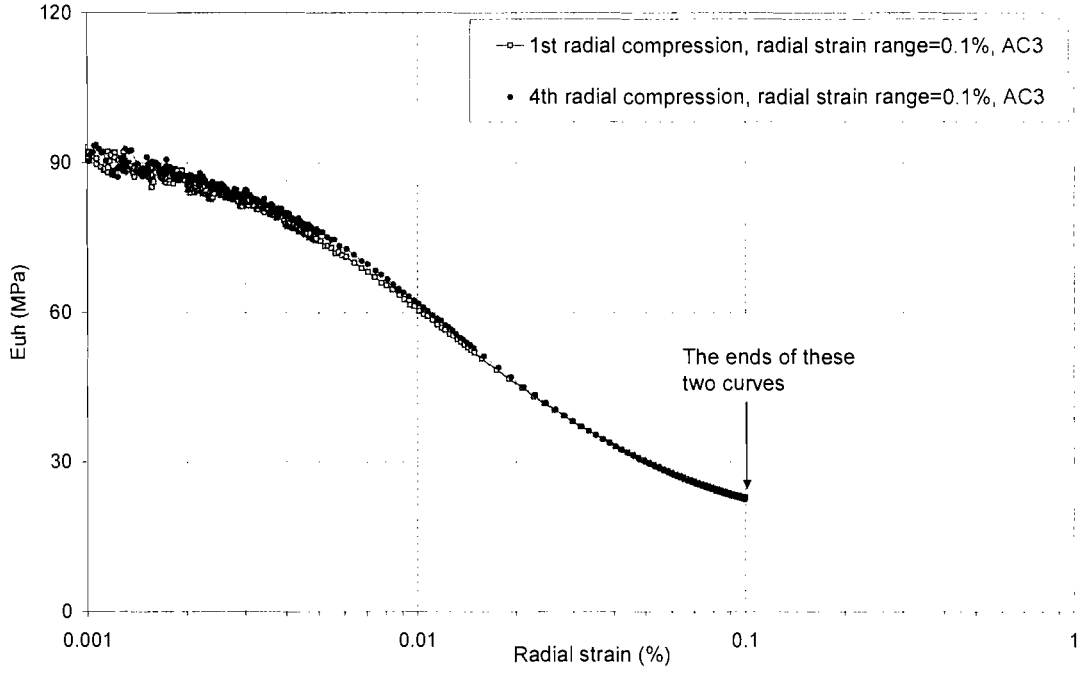

(a) The stiffness of the first and the last radial compression under an undrained cyclic radial strain range of 0.1%, specimen AC3

Figure 5.15 Comparison of stiffness behaviour in different cycles under the same cyclic radial strain range

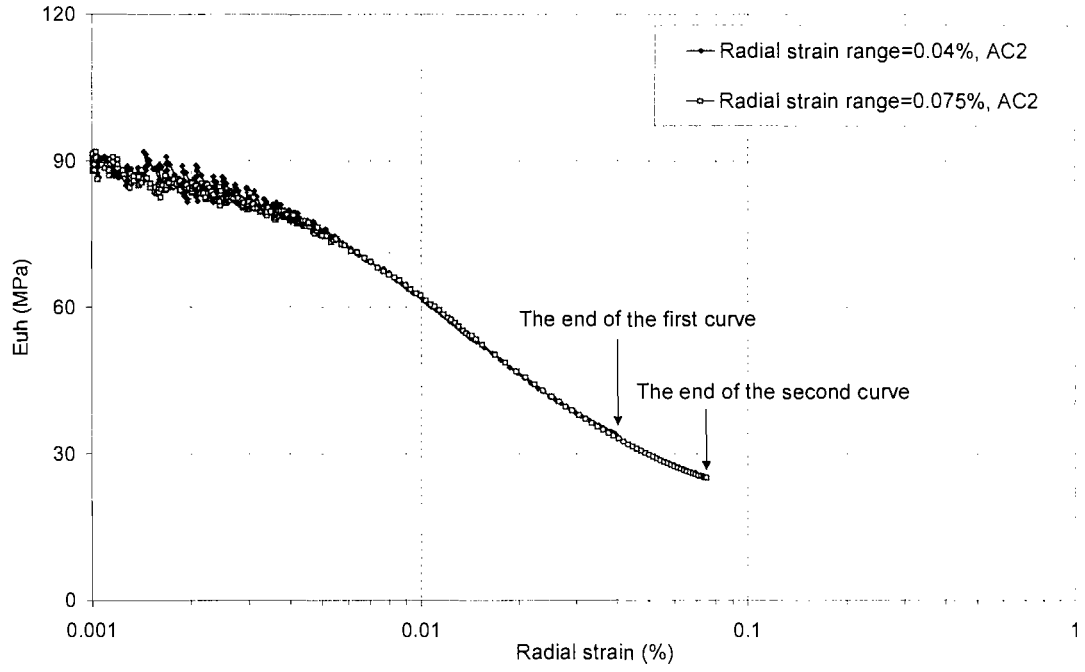

(a) The stiffness of the last radial compression excursion under different undrained cyclic radial strain range for specimen AC2

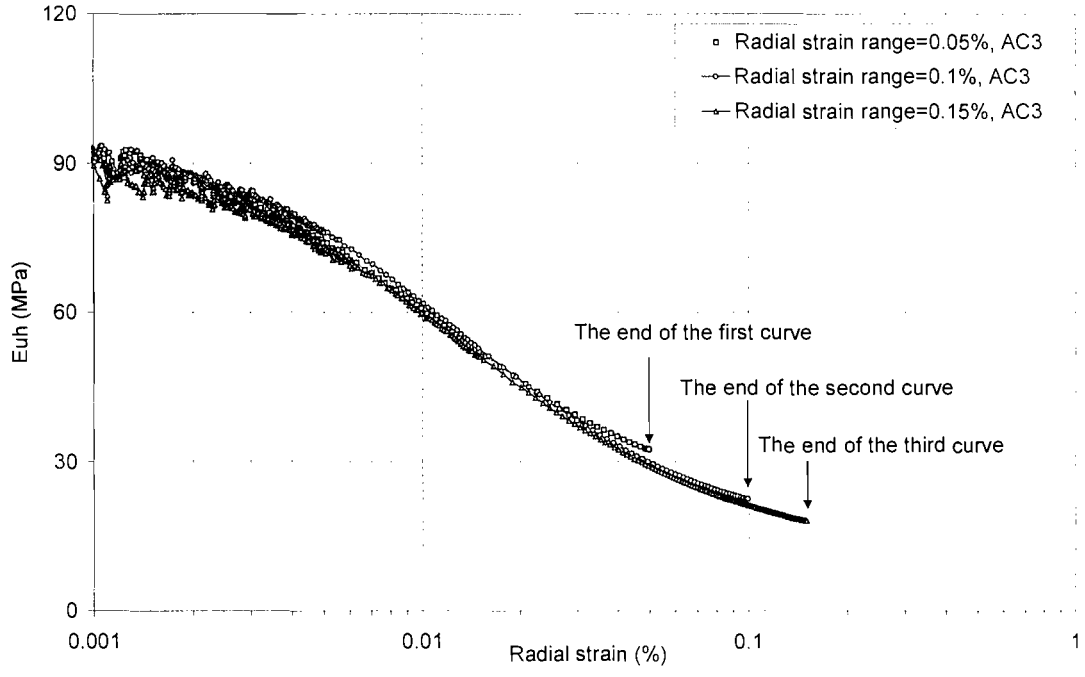

(b) The stiffness of the last radial compression excursion under different undrained cyclic radial strain ranges for specimen AC3

Figure 5.16 Comparison of stiffness under different undrained cyclic radial strain ranges

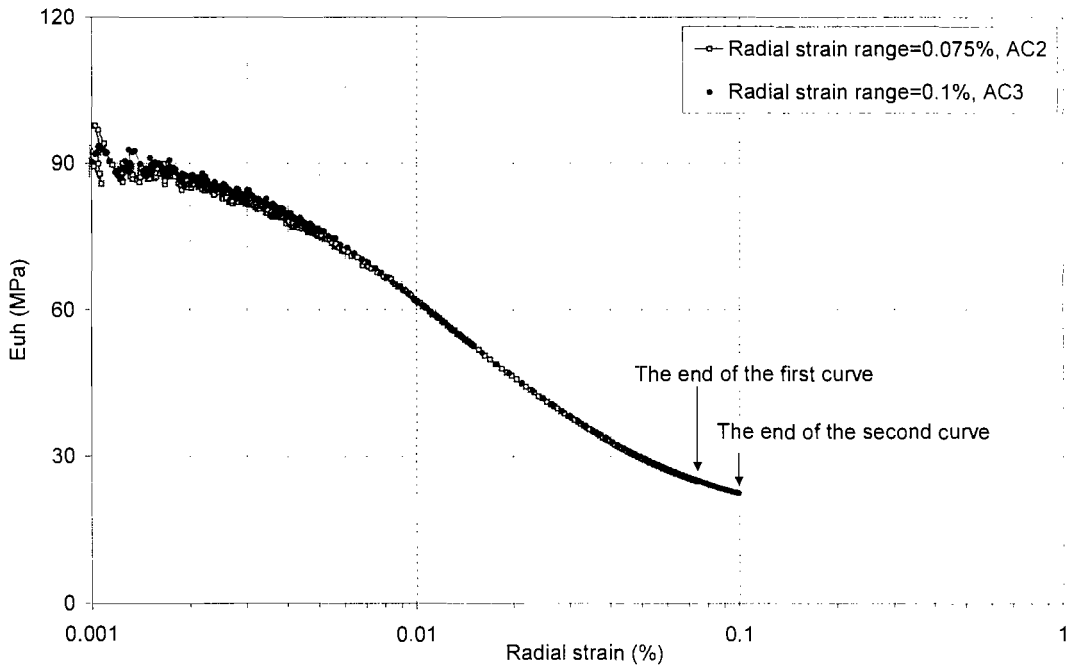

Figure 5.17 Comparison of typical undrained stiffness behaviour of specimens AC2 and AC3

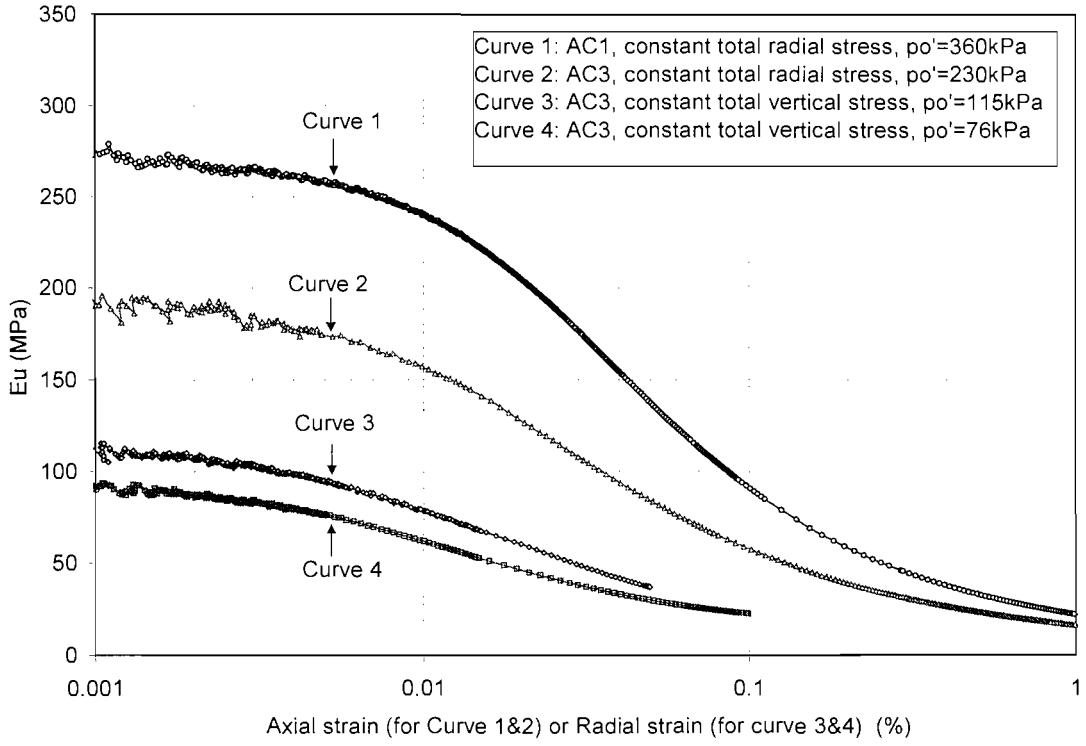

(a) Variation of undrained secant Young's modulus as a function of local axial strain for 2 specimens loaded with a constant total radial stress and two specimens loaded with a constant total vertical stress

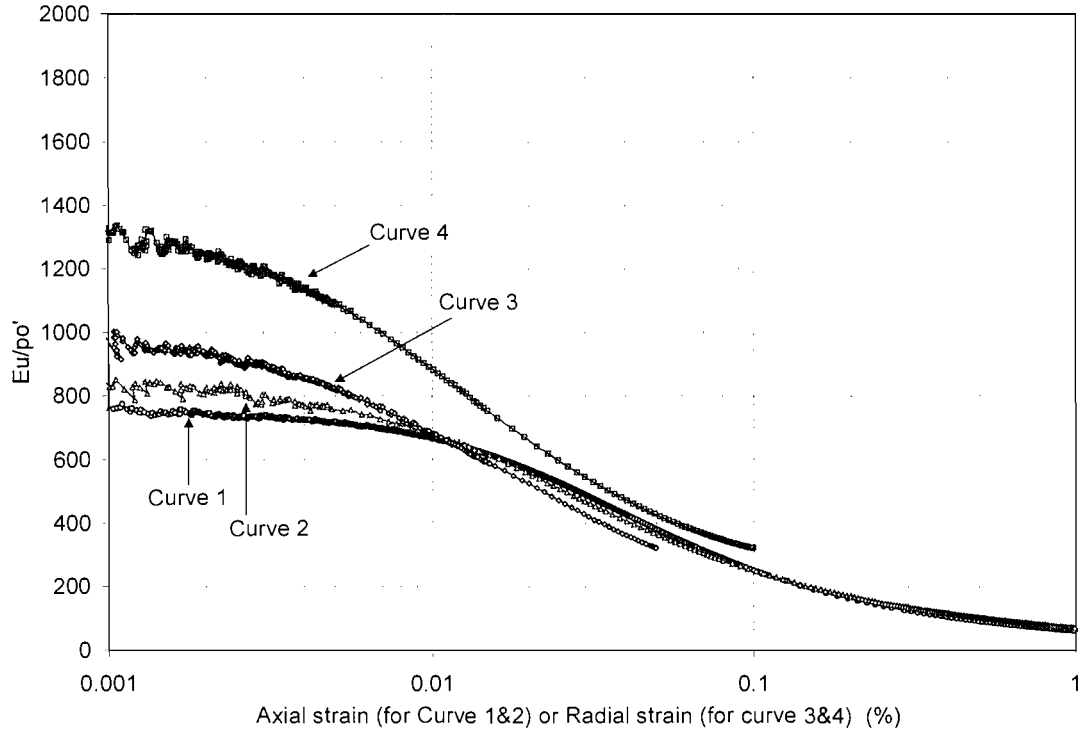

(b) Normalised stiffness E_u / p'_o

Figure 5.18 Comparison of undrained stiffness during different total stress paths

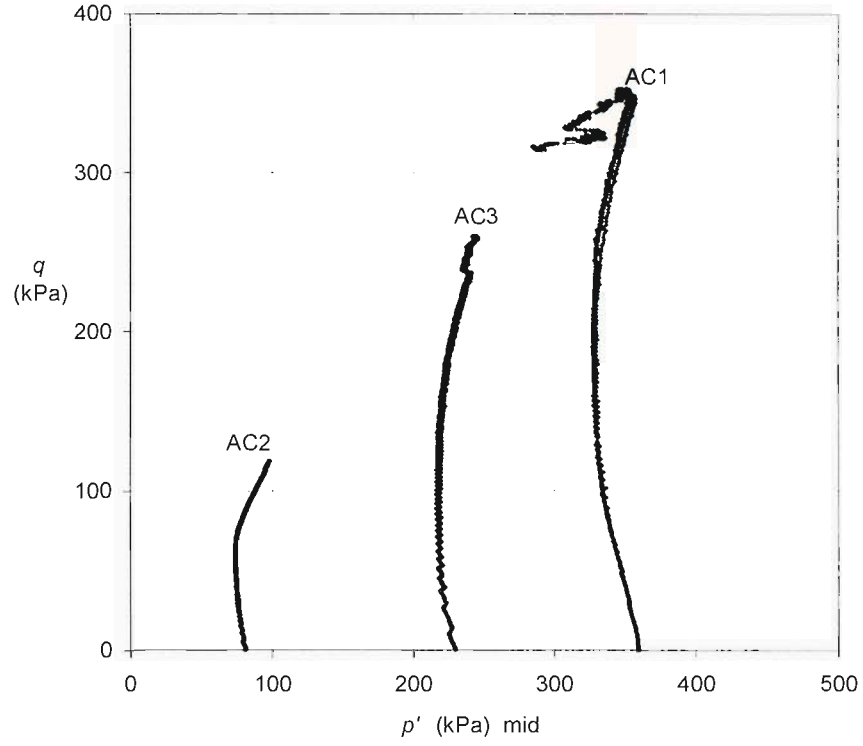

(a) in q-p' space

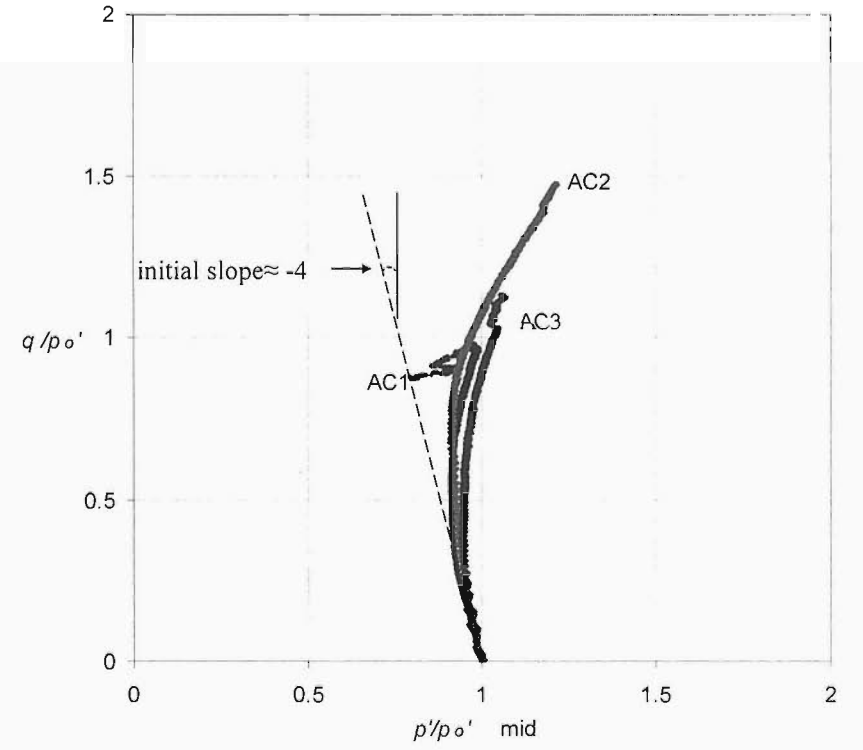

(b) in q/p_o'-p'/p_o' space

Figure 5.19 Effective stress paths for specimens AC1, AC2 and AC3 during undrained monotonic shearing.

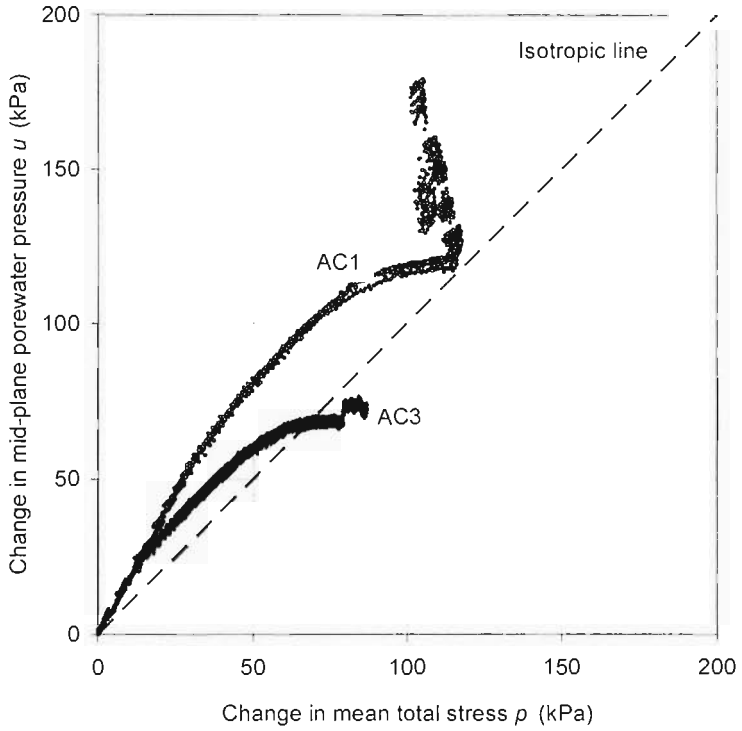

Figure 5.20 Change in pore water pressure against applied total stress change during the undrained monotonic shearing for specimens AC1 and AC3 with a constant cell pressure

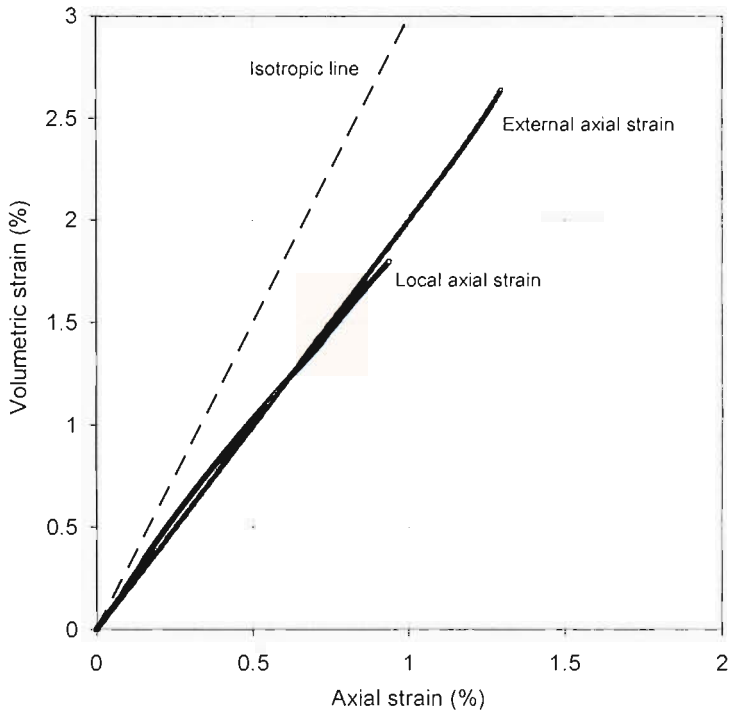

Figure 5.21 Anisotropic strain response during isotropic consolidation stage, specimen AC3

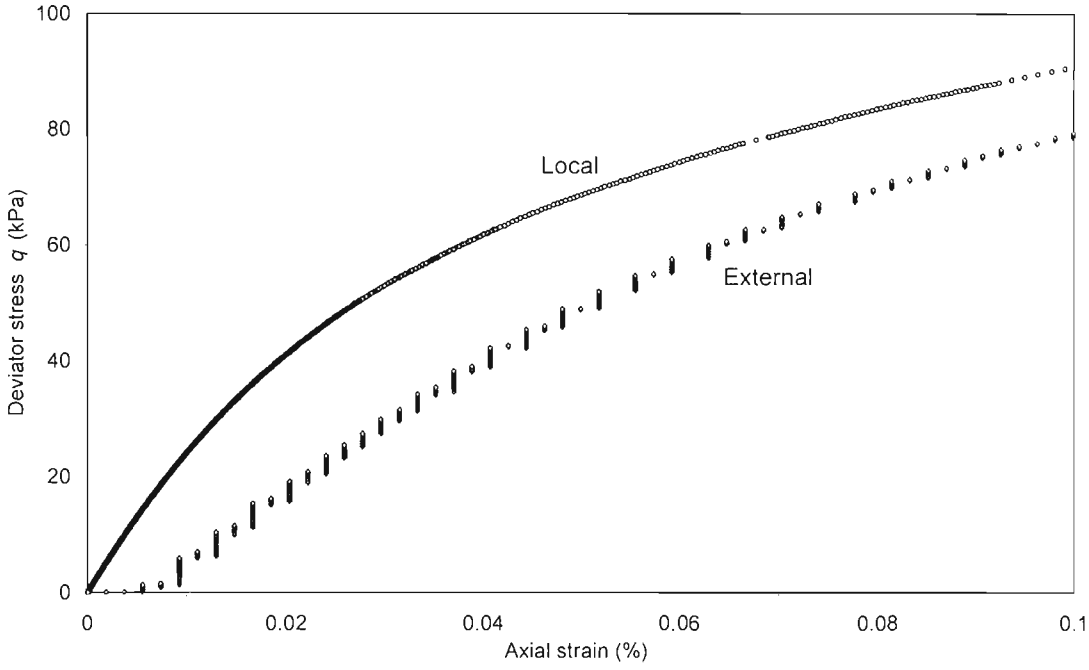

(a) Undrained monotonic shearing stage of specimen AC1 (virgin loading)

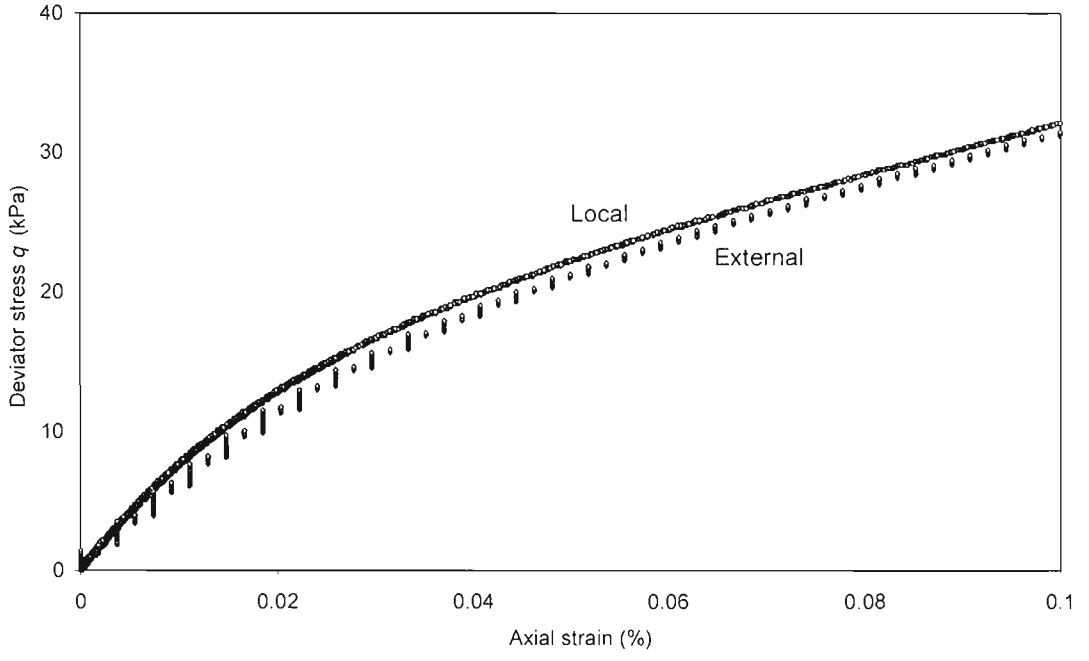

(b) Undrained monotonic shearing stage of specimen AC2 (after a number of loading cycles)

Figure 5.22 Comparison of results from external and local axial strain measurement

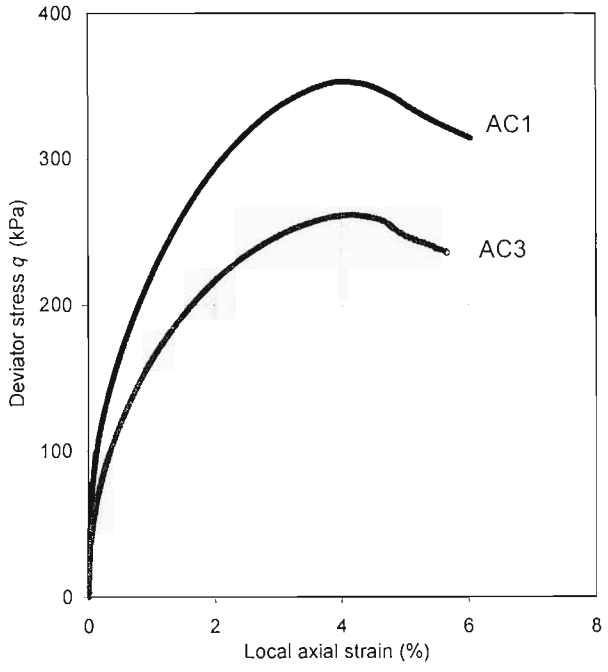

(a) Deviator stress against axial strain

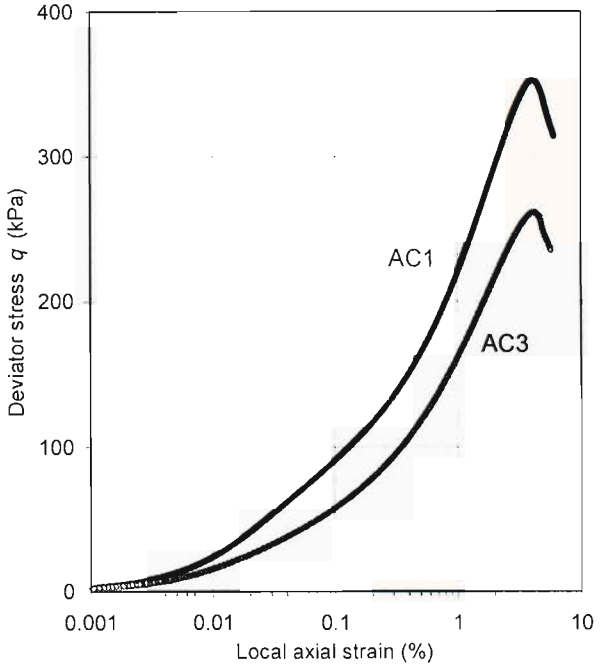

(b) Deviator stress against the logarithm of local axial strain

Figure 5.23 Undrained strength behaviour of specimens AC1 and AC3

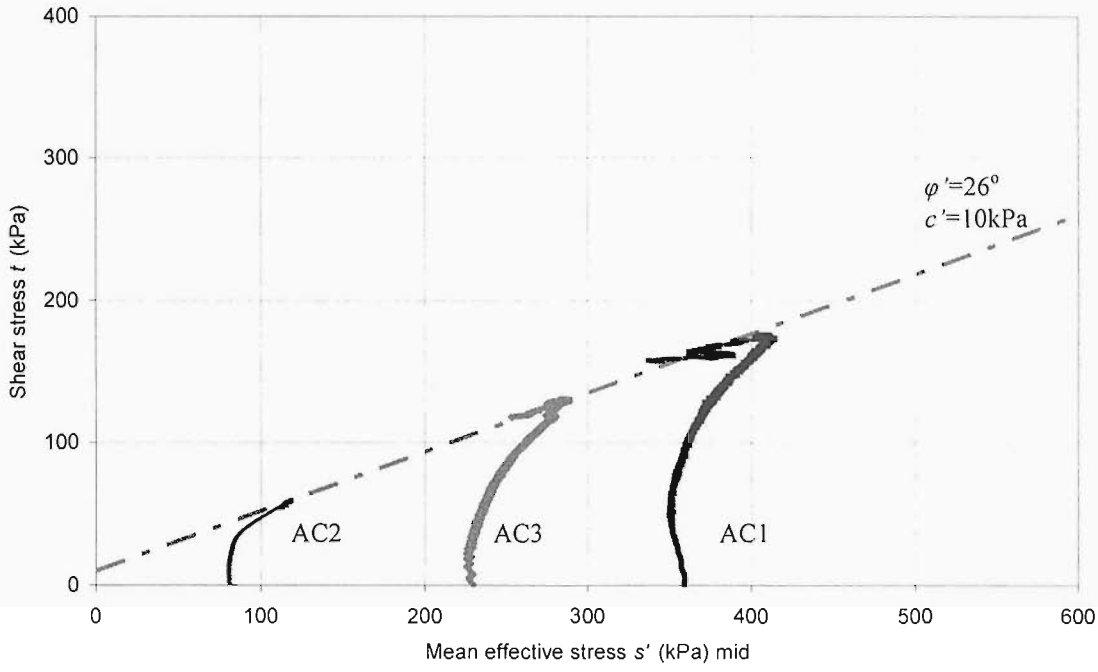

Figure 5.24 Effective stress paths of specimens AC1, AC2 and AC3 during undrained monotonic shearing

Chapter 6 Laboratory testing on granular materials

6.1 Introduction

In this research, the behaviour of a representative soil element of granular materials at mid retained height behind a frame integral abutment was investigated by carrying out radial strain-controlled cyclic stress path testing on Leighton Buzzard B sand specimens and a glass ballotini specimen. This chapter will describe the experimental programme and present the major findings.

6.2 Description of granular materials adopted

A coarse sand, Leighton Buzzard B sand, was investigated in the tests to study the behaviour of granular backfill behind integral abutments. Leighton Buzzard sand is a light brown sub-round, uniform, natural, uncrushed silica sand. It is free from silt, clay or organic matter. It is extracted from part of the Lower Greensand at Leighton Buzzard, Bedfordshire, UK. The sand used in this research was supplied by David Ball Group plc.

Furthermore, 1mm diameter glass ballotini was also studied in a special test to investigate the influence of granular particle shape in this special problem. The glass ballotini was produced from high quality and pure soda-lime glass. It was supplied by Jencons Ltd.

The particle size distribution of Leighton Buzzard B sand and glass ballotini was determined by passing the mass through a series of sieves with diminishing apertures (Clause 9.2, BS1377: Part2: 1990). The results are presented in Figure 6.1, and a mean particle size (D_{50}) of 0.9mm is evident for both materials.

Scanning Electron Microscope (SEM) was used to examine the detailed particle shape of both Leighton Buzzard B sand and glass ballotini, as presented in Figures 6.2 and 6.3 respectively. The particle shape of sand is highly irregular and the length along different axes varies considerably. In contrast, most of the glass ballotini particles have a spherical shape.

Santamarina and Cho (2004) characterise the shape of a single particle using three principal scales: *sphericity* versus platiness, *roundness* versus angularity, and *roughness* versus smoothness. Sphericity is quantified as the diameter ratio between the largest inscribed and the smallest circumscribing sphere. Roundness is quantified

as the average radius of curvature of surface features relative to the radius of the maximum sphere that can be inscribed in the particle. Roughness relates to surface features much smaller than the particle diameter. Sphericity and roundness can be estimated by visual comparison with charts, such as the one shown in Figure 6.4a.

Since a natural sand particle is not perfectly spherical, its apparent orientation can be changed by rotation. The orientation of a sand particle can be described in terms of the inclination of the longest particle axis in the spatial space (Mitchell, 1993), as shown in Figure 6.24b.

The specific gravity (Gs), maximum and minimum densities of both Leighton Buzzard B sand and 1mm diameter glass ballotini were measured in the laboratory and are presented in Table 6.1, as well as the maximum and minimum void ratio.

Table 6.1 Parameters for Leighton Buzzard B sand and 1mm diameter glass ballotini

	Leighton Buzzard B sand	1mm diameter glass ballotini	Method
specific gravity (Gs)	2.65	2.50	Clause 8.2, BS1377:Part2:1990
maximum density (Mg/m^3)	1.755	1.650	Cresswell *et al.* (1999); Clause 4.2, BS1377:Part4:1990
minimum density (Mg/m^3)	1.499	1.494	Clause 4.4, BS1377:Part4:1990
e_{max}	0.768	0.674	
e_{min}	0.510	0.515	

It can be seen that the particle shape has a much larger influence on the maximum void ratio than on the minimum void ratio, as observed by Holubec and D'Appolonia (1973). The difference between maximum and minimum void ratio also increases as particles become angular and non-spherical.

6.3 Specimen preparation and setup

The 100mm diameter sand specimens were prepared by depositing the sand under water. This is because complete saturation is very difficult to achieve if the sample is placed dry and subsequently flooded (Bishop & Henkel, 1962). Before preparing a specimen, the desired amount of dry sand was calculated and weighed. Then the dry sand was poured into a desiccator full of de-aired water and stirred thoroughly. The

mixture was then subjected to a vacuum for at least one night to expel any possible trapped air. This procedure was found to be as efficient as expelling the air by boiling (Khatrush, 1986). At the same time, the latex membrane was also soaked in de-aired water for at least 24 hours after being carefully checked for defects.

After drying both the inside and outside using paper towels, the positions of the two inner pads, as well as the circumference of the specimen bottom end, were marked on the membrane. These inner pads were used to prevent the errors introduced by the membrane penetration, as discussed in Section 4.3.2. The height of the pads was chosen to be around the mid position of the LVDT armature, since the cut on the calliper arm was not large enough for the LVDT tube. Then the two pads were glued on the inner side of the membrane. Care was taken that the periphery of each inner pad was fully sealed to the membrane, otherwise sand particles would come into the gap between the inner pad and the membrane.

The membrane was then slipped over the base pedestal and two O-rings were used to seal the bottom of the membrane. During the preparation, the back pressure line was kept slightly opened and de-aired water continue to flow through the back pressure line to the surface of the base porous stone until the mould was set up and filled with de-aired water. This was done to ensure that the porous stone was kept moist and no air was trapped within the back pressure line.

A three-part split mould was used to retain the shape of the specimen during construction and support the specimen until effective pressure of sufficient magnitude to make the specimen self-supporting was applied. At first the three-part mould was secured by a steel circlip at mid height. However, a small gap was found between two mould parts at the bottom during the preparation of dense sand specimens. Therefore, another steel circlip was used to reinforce the bottom of the mould. Half the height of the mould was initially filled with de-aired water, which pushed the membrane tightly against the inside of the mould and eliminated wrinkles formed in the membrane.

Clingfilm was wrapped around the mould to prevent sand particles from falling into the space around the base pedestal by accident, since this could jam the ram and cause damage. Care was also taken when dismantling the sand specimen after a test. At first, the sand particles that dropped outside the membrane had to be collected by hand. This was found difficult and time-consuming, as the space between the base pedestal and the inner wall surface was deep and narrow. A vacuum cleaner that could be used under moisture condition was modified by adding a small-diameter pipe at the end of

the suction outlet. This proved to be very efficient and any sand particles that dropped outside the membrane could be collected easily.

During construction of a sand specimen, the sand-water mixture was poured in a funnel, which was filled with de-aired water with the lower outlet submerged into the water contained in the membrane. A glass rod was used to control the speed of the flow. The sand-water mixture was then allowed to flow through the water inside the membrane. To achieve different densities, different procedures were followed, as discussed below.

1) To prepare a loose sand specimen, the sand was deposited into the water slowly. Care was taken not to disturb the sand that was already deposited inside the mould.

2) A dense specimen was achieved by tapping the mould at certain intervals using a wooden stick. After each construction layer (approximately 20~30mm), the mould was tapped moderately for 50 times from different directions.

3) To prepare a very dense specimen, each construction layer was tapped first, followed by compaction. A hammer was used, which had a hemisphere ceramic head with a diameter of 40mm. Each time the hammer had to be lifted upwards very slowly, in order to reduce the suction induced. Even so, some disturbance to the surface layer was inevitable. However, the effect of compaction on the deeper sand was not influenced significantly. Using this method, a relative density of higher than 90% could be achieved.

During preparation, the sand was kept submerged in the de-aired water. After the sand level reached the top of the mould, the flow of sand was stopped and the surface of the specimen was flattened gently using a metal ruler.

Next the top cap was placed in position. After ensuring no sand particles were trapped between the top cap and membrane, two O-rings were placed to seal the top of the membrane.

A suction pressure was applied through the back pressure pipe to generate an initial effective stress inside the specimen. Considering that a K_o loading was to be followed to reach a vertical effective stress of only 80 kPa, the initial effective stress had to be as low as possible. For the very dense specimen, a suction pressure of -5 kPa was enough. But for the loose specimen, at least -10 kPa was required to maintain the shape of the specimen and support the attached LVDTs with their stiff cables. The specimen was then left for the pressure inside to equalize, which usually took at least half an hour.

The mould was carefully removed, avoiding disturbing the specimen. The height of the specimen was measured at three different positions. The diameter of the specimen was measured at three positions along the height of the sample with measurements taken in two orthogonal directions at each section.

The radial LVDT calliper was glued on the membrane at the position where the two inner pads were underneath. A very thin layer of Loctite clear adhesive was used between the calliper pads and the membrane to avoid slippage of the calliper. This type of adhesive was different from the impact adhesive used for the axial LVDT brackets, as it had a setting time of at least ten minutes, which allowed adjustment of the calliper pads to be made. Before the adhesive gained its initial strength, the calliper had to be held by hand and care was needed to ensure the calliper remained horizontal. Then the LVDT brackets were glued on the membrane. Before installing the LVDTs, at least one hour was left for the adhesive to gain its strength. Figure 6.5 presents a photograph of a specimen after set-up.

The cell chamber was then closed. Before de-aired water began to flow into the cell, the back pressure pipe was closed. It was considered desirable to keep the effective stress as constant as possible during the process of increasing the cell pressure to the desired value. However, if the specimen was kept in an undrained condition while increasing the cell pressure directly to the target value, increase in the effective stress would be inevitable since the value of B was much less than unity at a low pressure level. A method was developed in this research. The cell pressure was increased in small steps (5~10 kPa), under undrained conditions initially. After each step of increase, the effective stress was brought back to the target value by temporarily opening the back pressure line and adjusting the back pressure. Usually once the pore water pressure reached 300kPa, the B value was found to be very close to unity and any further increase in cell pressure would not change the effective stress significantly. Thus large steps of increase (20~30 kPa) in cell pressure could be then applied until the back pressure reached the target value.

The back pressure for the tests on coarse sand was kept at 520kPa throughout the test. A high magnitude of back pressure has two major benefits: first, it will accelerate the dissolution of any remaining air bubbles into the water; as a result, the water will become essentially incompressible, and the pressure transducers will produce a quick and accurate response to the pore pressure changes during the test.

The suction cap was then connected to the top cap, following the same procedure as described in Section 5.3.3. After connection, the specimen was left in an isotropic

stress state for at least one day. The control software held the target cell pressure and a zero deviator stress automatically. During this period, any trapped air would be dissolved into the de-aired water under high pressure, and the reading of LVDTs would become stable.

The set-up of the glass ballotini specimen in the special test followed the same procedure as that for sand.

6.4 Test programme procedure

The following factors have been investigated in laboratory testing, which might have an influence on the stress-strain behaviour of the representative soil element behind frame integral abutments.

- the initial density of sand
- the range of cyclic radial strain
- the location of the stress path
- the granular particle shape

The whole test programme can be divided into a main test programme and two special tests. The effects of initial density and cyclic radial strain range were investigated in the main test programme, which consisted of tests on three sand specimens (LBS1, LBS2 and LBS3) over a wide range of densities (loose, dense and very dense) subjected to cyclic radial strain ranges (0.05%, 0.1% and 0.2%) similar to those to be expected in a soil element at mid retained height behind a typical frame integral abutment. The influence of the stress path location was investigated in a special test on a coarse sand specimen (LBS4), whilst the influence of particle shape was investigated in a special test on a glass ballotini specimen (G1). All tests are summarized in Table 6.2. The procedure of each test programme will be described in this section.

6.4.1 Main test programme

The main test programme was designed to investigate the influence of initial sand density and cyclic radial strain range on the behaviour of granular materials behind typical frame integral abutments. It consisted of the application of different size of cyclic radial strain ranges to three coarse sand specimens (LBSS1, LBS2 and LBS3) with different densities. Normally, it can be expected that the granular material

behind a frame integral abutment will be in a dense condition, as a result of compaction. However, loose granular backfill has also been recommended behind integral abutments as a means of avoiding high earth lateral pressures, with the adoption of a run-on slab at the same time (Card & Carder, 1993). Therefore, in addition to the dense and very dense sand specimens, a loose sand specimen was also tested in the experimental programme.

On each specimen, K_o loading was performed first to reach the desired vertical effective stress, followed by radial strain controlled cyclic stress path testing.

K_o loading

Before cyclic loading, drained monotonic K_o loading was applied to each sand specimen to set up the initial stress conditions of the representative soil element. Although granular material is usually compacted in thin layers behind a frame bridge abutment, Clayton & Symons (1992) have demonstrated that the depth h_c to which compaction pressures are significant will not exceed 3~4m, below which the horizontal earth pressure coefficient could reasonably be assumed to equal to K_o for rigid walls such as abutments (also see Section 2.7.2).

In this research, the representative soil element selected for investigation is located at a depth of 4m behind a rigid frame integral abutment (see Section 3.1). Therefore, the representative soil element was considered to be below the depth affected by compaction pressures, and (with the exception of special tests on specimen LBS4) the first cyclic loading started from the earth pressure at rest (K_o) state, with σ'_v= 80kPa. A bulk soil density of 20 kN/m^3 and full drainage were assumed.

Ideally, a series of unloading-reloading K_o loading would be more suitable for simulating the whole process of compacting the soil in layers. However, difficulties would be met since the desired vertical effective stress was very low (80kPa). Furthermore, the research aimed to investigate the behaviour of soil under temperature-induced cyclic loading. Monotonic K_o loading was believed to be adequate to simulate the incoming stress path before cyclic loading and to achieve the initial stress condition of the representative soil element.

K_o loading was performed automatically, as described in Section 4.5.4. The specimen was compressed at a rate of 2% per day under a constant back pressure. The reading of the local radial LVDT was monitored. Any deviation in the radial LVDT reading would be corrected by adjusting the cell pressure. This procedure was continued until the desired vertical effective stress (80kPa) was reached.

Radial strain-controlled drained cyclic testing

After K_o compression, cyclic stress path testing was performed. Since the soil behind an integral abutment experiences different size (*e.g.* daily and annual) of temperature-induced cyclic loading, different cyclic radial strain ranges were applied to each specimen. For a 60m long concrete deck, the annual cyclic radial strain range in the representative soil element was estimated as about 0.2%, as discussed in Chapter 3. Therefore, the applied cyclic radial strain ranges were selected as 0.05%, 0.1% and 0.2%. On each specimen, the smallest cyclic strain excursions were applied first, with the expectation of achieving a resilient state. If the maximum lateral effective stress continued to increase towards the passive value and no resilient state was observed, the cyclic radial strain range would be raised to a larger size.

Since granular backfill has a very high permeability and a drainage system is normally installed behind a frame abutment, all the cyclic loading tests were performed under a drained condition with a constant back pressure. The external shearing rate was selected as 6% per day, which was slow enough to prevent excess pore pressures developing.

The backfilling of a bridge abutment might be completed in either the summer or the winter months. Springman *et al.* (1996) has demonstrated that the initial direction of loading has no influence on sand behaviour during subsequent cyclic loading. Furthermore, even if the abutment moves outwards from the soil initially in reality, the sand will move from K_o state to the active state very quickly, during which the effect of previous stress history is expected to become insignificant. Therefore, for the sand specimens, all tests began with the abutment moving into the soil (the stress state moves away from the active state).

During the cyclic loading it was noted that when the deviator stress increased or decreased to a value around -40kPa, the rate of local axial deformation temporarily became much slower than the external shearing rate before these two rates matched each other again. A possible reason might be the compliance between the Perspex suction cap and the embedded steel screw. This led to a slowing of the applied deformation and to some time-dependent creep. However, since both stress and strain were measured locally on the specimen, only slight influence was found on the curves of deviator stress–local axial strain and the curves of deviator stress–local radial strain. Therefore, this problem had no impact.

During the cyclic testing, frequent checks were necessary to ensure that the reading of the axial LVDTs was not out of range, especially for the loose sand specimen.

Once the LVDT reading was near the end of the measurement range, an offset voltage was applied by adjusting the Coarse Zero function in the S7AC amplifier (see section 4.3.2), so that the reading could be pulled back to the middle of the measurement range. The back pressure controller also needed daily inspection, since the water continued to flow out of the loose sand specimen and move into the pressure controller.

Drained monotonic shearing

After the cyclic loading, each specimen was sheared into the active state along the 135° effective stress path to determine the effective friction angle φ'.

6.4.2 Special test on coarse sand

The location of the imposed stress path could influence the stress–strain behaviour of granular materials, for example as a result of 90° principal stress rotations when crossing from triaxial compression to extension, or when approaching either the active or the passive failure states. In such situations, the particulate behaviour of sand particles will change, resulting in a different macromechanical behaviour (see Section 2.6.6). Previous research has demonstrated that during monotonic loading, the granular particles did not transmit the stress equally and that the development of column-like structure was a major feature before failure (Oda *et al.*, 1982; Thornton, 1997). During principal stress reversal, this columnar structure would be destroyed, and the soil would exhibit a much softer behaviour. It was also found that when the sand entered the failure state, rolling of particles, rather than sliding, became a dominant mechanism (Skinner, 1969; Oda *et al.*, 1982).

During the main test programme, all sand specimens had approached the active failure and undergone a 90° principal stress rotation in every cycle of loading. To investigate the influence of the active state and the principal stress reversal separately, a special test was designed (LBS4, Table 6.2), in which much smaller cyclic radial strain ranges were applied to a single loose sand specimen in three stages subsequently (Figure 6.6). During each stage, at most one of these two states was engaged. The test procedure is described as below:

After the initial stress condition was set up by a K_o loading, cyclic loading was performed between the active state and the isotropic state (Stage 1, as shown in Figure 6.6a). This was designed to investigate the behaviour of sand without experiencing

either active failure or principal stress reversal. In this stage, the applied cyclic radial strain range had to be as low as 0.006%, so that the initial cycle could be reasonably distant from both the active state and the isotropic state.

Stage 1 was stopped when a resilient behaviour of deviator stress–radial strain was evident. The deviator stress was then reduced, taking the specimen along the 135° stress path until a value of -30kPa was obtained. Radial strain-controlled cyclic loading was then re-applied, but with an increased strain range of 0.012%, which took the specimen across the isotropic stress line, causing a 90° rotation of the major principal stress, but without reaching the active state (Stage 2, Figure 6.6b).

When a resilient behaviour of deviator stress–radial strain was reached again, the specimen was then loaded to the active state along the 135° stress path. Radial strain controlled cyclic loading was then performed touching only the active state, without reaching the isotropic state initially (Stage 3, Figure 6.6c). The cyclic radial strain range for this stage was 0.012%.

6.4.3 Special test on glass ballotini

As discussed in Section 2.6.6, particle shape could have a significant influence on the engineering properties of granular materials (Terzaghi *et al.*, 1948; Holubec *et al.*, 1973). However, previous research on the influence of particle shape concentrated on monotonic loading. In this research, a special test on 1mm diameter glass ballotini specimen (G1) was performed to investigate the influence of particle shape on the stress-strain behaviour of granular materials subjected to temperature-induced cyclic loading behind integral abutments (Table 6.2).

A dense glass ballotini specimen (G1) was tested with an initial relative density of 76%. To facilitate comparison, the test procedure was designed to be exactly the same as that for coarse sand specimens in the main test programme, as described in Section 6.4.1. After a vertical effective stress of 80kPa was reached by a K_o loading, cyclic stress path loading was applied with a cyclic radial strain range of 0.05%.

6.5 Results and discussion

6.5.1 Stress-strain behaviour of sand in the main test programme

In the main test programme, three coarse sand specimens (LBS1, LBS2 and LBS3) over a wide range of densities have been subjected to cyclic radial strain ranges

similar to those to be expected in a soil element at mid height behind a typical frame integral abutment (0.05%, 0.1% and 0.2%), as summarized in Table 6.2. The major findings from the main test programme will be presented here.

Stress-strain behaviour of the loose sand specimen LBS1

The loose sand specimen LBS1 had an initial relative density of 18%. A total of three cyclic radial strain ranges were applied (0.05%, 0.1% and 0.2%).

Figure 6.7 presents the curves of deviator stress and earth pressure coefficient K ($=\sigma'_h/\sigma'_v$) against radial strain under a cyclic radial strain range of 0.05%. The minimum deviator stress continued to decrease with cycling, which implies increasing lateral stress. During each radial extension excursion (q increasing, equivalent to the integral abutment moving away from the soil), the sand was stiff at first, but its behaviour soon softened, typically at a deviator stress level of about 40kPa, after which the rate of increase of the deviator stress became much slower. There was a progressive accumulation of positive volumetric strain and axial strain with cycling (Figure 6.8).

Under all the three cyclic radial strain ranges (0.05%, 0.1% and 0.2%), a similar tendency was found that the minimum deviator stress continued to decrease while the volumetric strain continued to accumulate with cycling, as demonstrated in Figure 6.9.

Figure 6.10 plots the maximum and minimum values of K (K_{max} and K_{min}) against total cycle number. K_{max} continued to build up towards the passive state, without any signs that a resilient state was expected under all the three cyclic radial strain ranges. K_{min} decreased with a much slower rate. Figure 6.11 plots void ratio and relative density against total cycle number. At the end of cycling, the relative density had risen by an absolute value of almost 30%.

The above results from LBS1 clearly show that for loose sand behind a typical frame integral abutment, the maximum horizontal stress will increase progressively towards the passive state with cycling. At the same time, there will be a significant decrease in the volume. This is comparable with the small scale test results in loose sand of Cosgrove & Lehane (2003), which will be further discussed in Section 7.2.2.

Stress-strain behaviour of the dense sand specimen LBS2

The dense sand specimen (LBS2) had an initial relative density of 70%. A total of three cyclic radial strain ranges (0.05%, 0.1% and 0.2%) were applied. Under each

cyclic radial strain range, both the lateral stress and the volumetric strain were found to accumulate with cycling, similar to the tendency observed for the loose sand specimen (LBS1). Therefore, fewer cycles were performed on the dense specimen.

Figure 6.12 presents the curves of deviator stress and earth pressure coefficient K against radial strain under a cyclic radial strain range of 0.1%. Again, the minimum deviator stress continued to decrease with cycling, while the maximum deviator stress remained relatively constant in each cycle. An accumulation of positive volumetric strain and axial strain is also evident (Figure 6.13)

The deviator stress is plotted against volumetric strain under all the three cyclic radial strain ranges in Figure 6.14. As well as the decreasing trend of the minimum deviator stress, the progressive accumulation of volumetric strain with cycling is evident.

Figure 6.15 shows that K_{max} continued to build up towards the passive state, while K_{min} decreased slightly with cycling. Figure 6.16 plots void ratio and relative density against total cycle number. Again, it is evident that the volume continued to decrease with cycling.

The above results from LBS2 show that for dense sand behind a typical frame integral abutment, the maximum horizontal stress will increase progressively towards the passive state. At the same time, the sand volume will continue to decrease with cycling.

Stress-strain behaviour of the very dense sand specimen LBS3

The very dense sand specimen (LBS3) had an initial relative density of 92%. Two radial strain ranges were applied (0.05% and 0.1%).

Figure 6.17 presents the curves of deviator stress against radial strain under the cyclic radial strain range of 0.1%. The minimum deviator stress continued to decrease with cycling. K_{min} in each cycle was relatively constant and stayed at a value of 0.2. K_{max} in each cycle continued to increase towards the passive state, without any sign that a constant value would be approached. After 250 cycles, K_{max} became very close to the passive value K_p=5, which was estimated by assuming $K_p=1/K_a$, and K_a = 0.2. This passive value corresponds to an effective friction angle (φ') of 42°.

Figure 6.18 plots the curves of volumetric strain against axial strain. It can be seen that during the first 20 cycles, there was still slight accumulation of positive

volumetric strain. However, after the first 20 cycles, the volume began to increase systematically with further cycling, though the rate was very slow.

The deviator stress is plotted against volumetric strain under the same radial strain range (0.1%) in Figure 6.19. Again, it can be seen that the minimum deviator stress continued to decrease, while the volume began to increase after 20 cycles.

The maximum and minimum values of K (K_{max} and K_{min}) are plotted against total cycle number in Figure 6.20. Under both cyclic radial strain ranges of 0.05% and 0.1%, K_{max} continued to build up towards the passive state, while K_{min} decreased slightly at the beginning before becoming stable with cycling. Figure 6.21 plots the void ratio and relative density against total cycle number. It can be seen that the volume still continued to decrease under a cyclic radial strain range of 0.05%, but it began to increase with cycling under a cyclic radial strain range of 0.1%.

The above results from LBS3 show that for very dense sand behind a typical frame integral abutment, the maximum horizontal stress will increase progressively towards the passive state with cycling. However, the sand volume will increase with cycling under a larger cyclic radial strain range (0.1%).

Summary of the main test programme

Two important observations can be made from the main test programme:

1) For all the three coarse sand specimens over a wide range of densities (loose, dense and very dense) subjected to cyclic radial strain ranges similar to those to be expected in a soil element at mid height behind a typical frame integral abutment (0.05%, 0.1% and 0.2%), the maximum horizontal stress continued to build up towards the passive state without any sign that a resilient state would be approached. In contrast, the minimum horizontal stress experienced much smaller change and tended to a magnitude very close to or equal to the active value.
2) For the loose and dense sand specimens, the volume continued to decrease under all the three applied cyclic radial strain ranges. The rate of volume decrease was more significant for the loose sand specimen. However, for the very dense sand specimen under a larger cyclic radial strain range (0.1%), the volume was found to increase systematically with cycling. This implies that densification was not the only factor that could account for the build-up of the maximum horizontal stress.

The final effective friction angle (φ') of each specimen was determined during the monotonic shearing stage after cyclic loading (Table 6.3). It can be seen that all the three specimens exhibited high effective friction angles after cyclic loading. For LBS1, through the final relative density was only 48% after cyclic loading, an effective friction angle of 40° was evident.

6.5.2 Stress-strain behaviour of sand in the special test

A special test was performed on a loose sand specimen (LBS4) to investigate the influence of the location of the stress path (Table 6.2). The test was performed in three stages, as described in Section 6.4.2 and demonstrated in Figure 6.6. The test results will be discussed here, as presented in Figures 6.22 to 6.25.

Stage 1: Cycling between the isotropic state and the active state

When the radial strain-controlled cyclic loading was carried out between the isotropic state and the active state (Figure 6.6a), the coarse sand specimen was found to exhibit a resilient behaviour from the beginning (Figure 6.22). Although the data was affected by the resolution of the instruments, there was a high level of repeatability. There was no obvious deviator stress accumulation. It appears that between the active state and the isotropic state, cyclic loading has little influence on the deviator stress-radial stain behaviour of the coarse sand.

Stage 2: Cycling only across the isotropic state

When the cyclic loading was performed across the isotropic line but without reaching the active state (Figure 6.6b), the curves of deviator stress–radial strain were found to shift upwards with cycling at the beginning (Figure 6.23). After about 60 cycles, the coarse sand specimen entered a resilient state. The 90° principal stress rotation appears to reduce the maximum lateral stress by some extent. Furthermore, during the cyclic loading, the stress-strain curve moved smoothly across the isotropic line and no softer behaviour was observed. This is different from the observation made in monotonic loading by Khatrush (1986).

Stage 3: Cycling only reaching the active state

During Stage 3, the cyclic loading began from the active state without crossing the isotropic line (Figure 6.6c). The minimum deviator stress was found to decrease progressively with cycling, while the maximum deviator stress reached the active state in each compression (Figure 6.24). This appears to have reproduced the major features observed in the main testing program.

In all the three stages, the sand volume continued to decrease with cycling (Figure 6.25), while the maximum horizontal stress exhibited different trends (Figures 6.22~24). This again supports the findings that the build-up of the maximum horizontal stress is not necessarily associated with volumetric strain.

The observations in the tests on specimen LBS4 suggests that the location of the stress path has an important influence on the stress-strain behaviour of sand, and it appears that the progressive increase of maximum horizontal earth pressure is associated with the fact that the sand enters the active state during each cycle. A major feature of failure, such as the active state, is that rolling of particles becomes a dominant mechanism (Skinner, 1969).

6.5.3 Stress-strain behaviour of glass ballotini

The influence of granular particle shape was investigated in a special test (G1), in which cyclic loading was performed on a dense specimen of 1mm diameter glass ballotini under a cyclic radial strain range of 0.05% (Table 6.2). The curves of deviator stress against radial strain are presented in Figure 6.26.

It can be seen that the shape of deviator stress–radial strain curve in each cycle is similar to that observed in the main test programme on the coarse sand specimens. However, after the first cycle of loading, the specimen exhibited a resilient behaviour and no accumulation of deviator stress was observed with cycling.

A number of factors other than particle shape will now be examined that may account for such a major difference between the results for glass ballotini and for coarse sand. These include:

- particle size
- relative density
- cyclic radial strain range
- test procedure

- properties of materials

The particle size distribution of the 1mm diameter glass ballotini was found very close to that of the Leighton Buzzard B sand, as demonstrated in Figure 6.1. Therefore, the difference caused by particle size was insignificant.

In the major test programme on sand, different sand specimens over a wide range of densities (loose, dense and very dense) have been tested under a cyclic radial strain range of 0.05%, the same magnitude as that applied to the glass ballotini specimen. All sand specimens exhibited a progressive accumulation of lateral stress (Figures 6.10, 6.15 and 6.20). Therefore, the difference in results could not be accounted for by density or cyclic radial strain range.

The procedure of the test on glass ballotini specimen was designed to be the same as that for the coarse sand specimens in the main test programme. Therefore, the difference could not be attributed to the test procedure.

The main chemical component of glass is SiO_2, the same as that of the natural silica sand. Furthermore, the specific gravity Gs of glass ballotini is 2.5, which is close to that of the sand. Although the interparticle friction angle φ_μ of dry glass ballotini is low (2°~5°), φ_μ of wet glass ballotini is found to be 27° ~38° (Skinner, 1969), which is fairly close to range usually observed for the coarse sand (Bishop, 1954; Rowe, 1962; Horn, 1969). Therefore, except for the particle shape, most material properties are similar between glass ballotini and natural sand.

The most significant difference between the glass ballotini and the sand particles was found to be the particle shape, as demonstrated in Figure 6.2 and Figure 6.3. The individual sand particle shape is highly irregular and the length of axis is different in different directions. In contrast, most of the glass ballotini particles have a spherical shape. Therefore, it is the particle shape that accounted for the significant difference between the behaviour of sand and glass ballotini during cyclic stress path testing.

This observation may be compared with those found by previous workers on the influence of particle shape. It has long been recognized that besides the particle size, particle size distribution and void ratio, the particle shape could have an important influence on the behaviour of granular materials during monotonic loading.

Koerner (1970) carried out triaxial tests on three types of quartz sand with the same d_{10} value but different sphericity (from angular to subrounded) and showed that sand with angular particles had a much higher strength than that with more spherical

particles. Tests conducted by Holubec and D'Appolonia (1973) on medium to fine sands with varying particle shapes indicated that granular material at a given relative density could have different mechanical behaviour due to angularity. They concluded that the effect of particle shape could be of the same magnitude as that due to the changes in relative density.

Oda *et al.* (1982) investigated the influence of particle shape by carrying out biaxial tests on rod-like particles with oval cross sections cast from polyurethane rubber. The shape of the particles was described by their axial ratio: r_1/r_2, where r_1 and r_2 are the long and short axial radii respectively. For rounded particles with $r_1/r_2 \approx 1.1$, no dependence of peak stress ratio on φ_μ was observed when φ_μ was increased from 26° to 52°. This was consistent with the findings of Skinner (1969) who carried out shear box tests on glass ballotini. On the other hand, for particles with a flatter cross section ($r_1/r_2 \approx 1.4$), the peak stress ratio increased by almost a third when φ_μ was increased from 26° to 52°.

Numerical simulation, such as discrete element method, has become increasingly powerful in detailed studies of the influence of particle shape on the mechanical behaviour of granular materials. Lin and Ng (1997) investigated the behaviour of random arrays of elastic ellipsoidal particles and spherical particles. Mirghasemi *et al.* (2002) reported a series of tests simulations on assemblies of two-dimensional polygon-shaped particles with different particle angularity. Ni (2003) carried out three-dimensional distinct element simulations, in which non-spherical particles were simulated by bonding two spheres together, as discussed in Section 2.6.6. All these investigations suggest that particle shape has a significant influence on the shear strength, deformation behaviour and other engineering properties of granular materials.

The influence of particle shape has been investigated previously only for monotonic loading. In this research, the importance of particle shape during cyclic stress path loading was observed. Taken together the findings of sections 6.5.1~6.5.3, these results strongly suggest that the build-up of horizontal stress observed for the coarse sand specimens was associated with non-spherical particle shape, and the rolling of particles close to or at the active stress state.

6.5.4 Stiffness behaviour of granular materials under cyclic loading

The stiffness behaviour of granular materials under radial strain–controlled cyclic loading will be examined here, including both coarse sand and glass ballotini.

Method to derive stiffness for granular materials

When coarse sand is deposited in water under gravity, the sand particles tend to rest with their longest axis in the horizontal position to attain the lowest potential energy, resulting in the development of inherent fabric anisotropy (Mitchell, 1993).

To simplify the problem, stiffness isotropy has been assumed when quoting the horizontal stiffness variation during cyclic loading. For a coarse sand element behind a frame integral abutment, the effective horizontal Young's modulus E'_h is of most importance, because the lateral stress changes with cyclic strains while the vertical pressure remains constant. By assuming isotropy, the relationship between strain increase and effective stress increase in a drained triaxial test can be expressed as below, according to Hooke's law:

$$\begin{bmatrix} \Delta\varepsilon_a \\ \Delta\varepsilon_r \\ \Delta\varepsilon_r \end{bmatrix} = \frac{1}{E'_h} \begin{bmatrix} 1 & -\nu' & -\nu' \\ -\nu' & 1 & -\nu' \\ -\nu' & -\nu' & 1 \end{bmatrix} \begin{bmatrix} \Delta\sigma'_a \\ \Delta\sigma'_r \\ \Delta\sigma'_r \end{bmatrix} \qquad (6.1)$$

For a coarse sand element behind an integral abutment under drained condition, the effective vertical stress remains constant ($\Delta\sigma'_a$=0), therefore

$$E'_h = \frac{2\Delta\sigma'_r}{2\Delta\varepsilon_r - \Delta\varepsilon_a} \qquad (6.2)$$

Since the test is under drained conditions and effective vertical stress remains constant, $\Delta\sigma'_r = \Delta\sigma_r = -\Delta q$, and equation (6.2) can also be further expressed as:

$$E'_h = \frac{-2\Delta q}{2\Delta\varepsilon_r - \Delta\varepsilon_a} \qquad (6.3)$$

Stiffness behaviour of coarse sand specimens

Figures 6.27~6.29 plot the effective secant horizontal Young's modulus against radial strain for the loose sand specimen LBS1, dense sand specimen LBS2 and very dense sand specimen LBS3 under radial strain-strain controlled cyclic loading. The

corresponding deviator stress–radial strain curves are plotted in Figure 6.7, Figure 6.12 and Figure 6.17 respectively. Several observations can be made.

First, for all sand specimens over a wide range of densities, the secant small strain stiffness of radial extension is much higher than that of radial compression.

Secondly, the secant stiffness during radial extension (the wall moving away from the soil) increased significantly with cycling.

Third, the secant stiffness during radial compression (the wall moving towards the soil) also increased at larger strain level with cycling, but the value remains largely unchanged at very small strains. For all coarse sand specimens radial compression, $E'_{h0.01}$ is found to be around 200MPa. This appears to suggest that when the sand is moving away from the active state, the small strain stiffness is not influenced significantly by the density or packing. Only when the stress state was far below the active state did the secant stiffness begin to increase markedly, resulting in an increasing horizontal stress.

Stiffness behaviour of glass ballotini specimens

Figure 6.30 plots the effective horizontal Young's modulus against radial strain for dense glass ballotini specimen G1 under a cyclic radial strain range of 0.05%. The glass ballotini specimen also exhibited different stiffness behaviour during radial compression and radial extension. However, the stiffness behaviour was found to be uninfluenced by repeated loading, when the specimen entered a resilient state. This is consistent with the fact that no build-up of horizontal stress was observed for glass ballotini specimen (Figure 6.26).

6.7 Summary

In this research, the behaviour of the representative soil element of granular materials behind a frame integral abutment was investigated by carrying out radial strain-controlled cyclic stress path testing on Leighton Buzzard B sand specimens and a glass ballotini specimen.

In the main test programme, for all the three sand specimens over a wide range of densities (loose, dense and very dense) subjected to cyclic radial strain ranges similar to those to be expected in a soil element at mid height behind a typical frame integral abutment (0.05%, 0.1% and 0.2%), the maximum horizontal stress continued to build up towards the passive state without any sign that a resilient state would be

approached. In contrast, the minimum horizontal stress experienced much smaller change and tended to a magnitude very close to or equal to the active value.

In the main test programme, for the loose and dense sand specimens, the volume continued to decrease under all the three applied cyclic radial strain ranges. The rate of volume decrease was more significant for the loose sand specimen. However, for the very dense sand specimen under a larger cyclic radial strain range (0.1%), the volume was found to increase systematically with cycling. This implies that densification was not the only factor that could account for the build up of the maximum horizontal stress.

A special test on loose sand specimen LBS4 again suggests that the build-up of the maximum horizontal stress was not necessarily associated with volumetric strain. The location of imposed stress path was found to have an important influence on the stress-strain behaviour of sand, and it appears that the progressive increase of maximum horizontal earth pressure was associated with the active state, and therefore with rotation of particles.

No obvious accumulation of maximum horizontal stress was observed in the special test on glass ballotini specimen. Taken together, these results suggest that the build-up of horizontal stress observed for the coarse sand specimens was associated with non-spherical particle shape and the rolling of particles close to or at the active stress state.

The coarse sand specimens exhibited markedly different stiffness during radial compression and radial extension. Furthermore, both the stiffness during radial compression and radial extension increased significantly with cycling, though the small strain stiffness immediately after unloaded from the active state was relatively stable. In contrast, for the glass ballotini specimen, the stiffness during radial compression and radial extension did not change obviously with cycling.

Table 6.2 Test programmes on coarse Leighton Buzzard sand and glass ballotini specimens

Specimen	Density	γ_d (Mg/m^3)	e	D_r (%)	K_o	Cyclic radial strain ranges (%)	Number of cycles
LBS1	Loose	1.54	0.72	18	0.5	0.05	120
						0.1	170
						0.2	60
LBS2	Dense	1.67	0.59	70	0.42	0.05	60
						0.1	50
						0.2	30
LBS3	Very dense	1.73	0.53	92	0.32	0.05	52
						0.1	250
LBS4	Loose	1.54	0.72	18	0.5	0.006 [1]	50
						0.012 [2]	100
						0.012 [3]	50
G1	Dense	1.61	0.553	76	0.47	0.05	15

Notes: [1] Stage 1: between active and isotropic state (Figure 6.6a)
[2] Stage 2: only across isotropic state (Figure 6.6b)
[3] Stage 3: only reaching the active state (Figure 6.6c)

Table 6.3 The final effective friction angle φ' for each specimen in the main test programme, determined during the monotonic shearing stage after cyclic loading

Specimen	Initial Dr before cyclic loading (%)	Dr after cyclic loading (%)	Monotonic shearing after cyclic loading	
			K_a	φ'
LBS1	18	48	0.22	40°
LBS2	70	78	0.19	43°
LBS3	92	90	0.19	43°

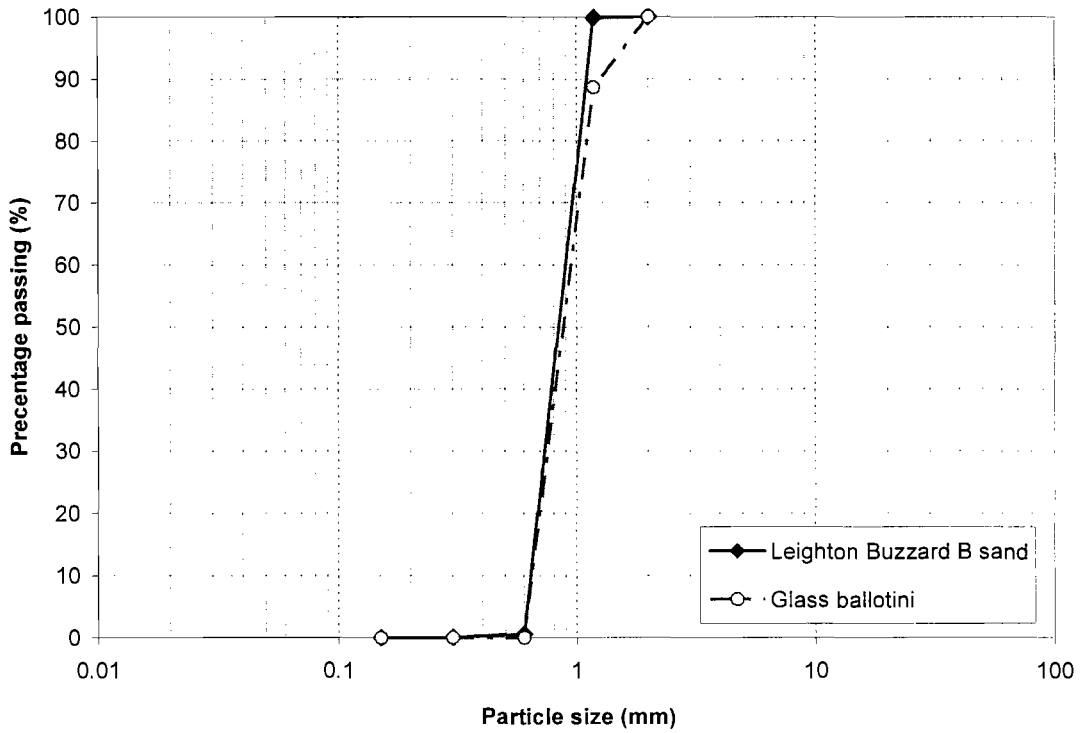

Figure 6.1 Particle size distributions of Leighton Buzzard B sand and glass ballotini

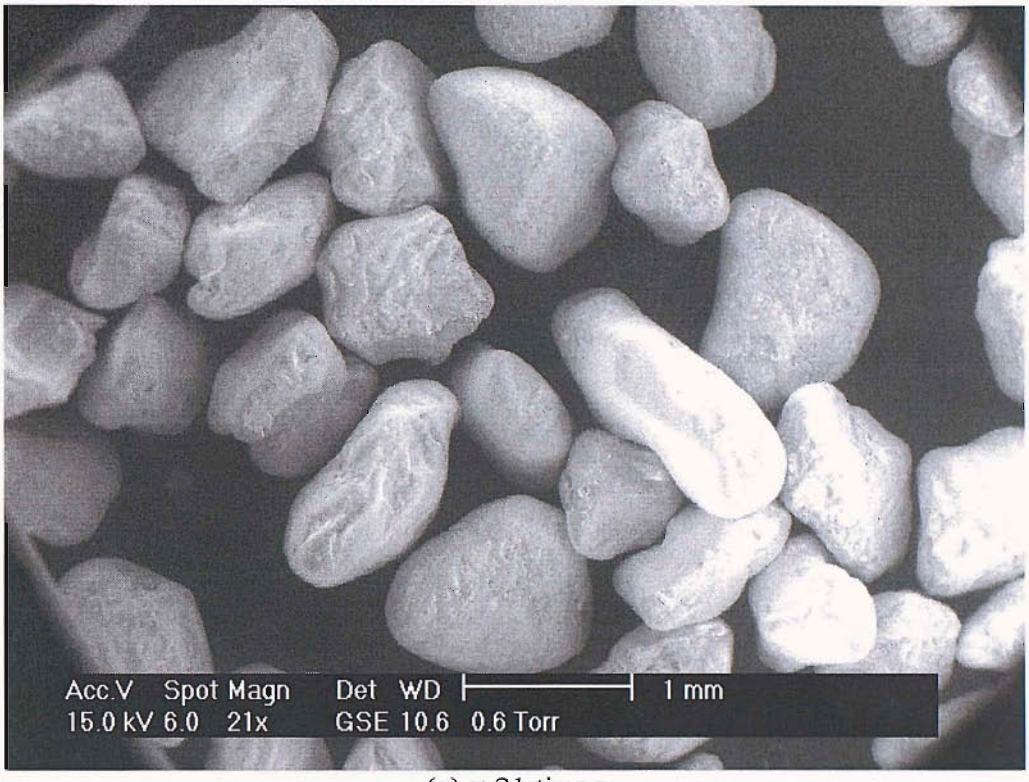

(a) × 21 times

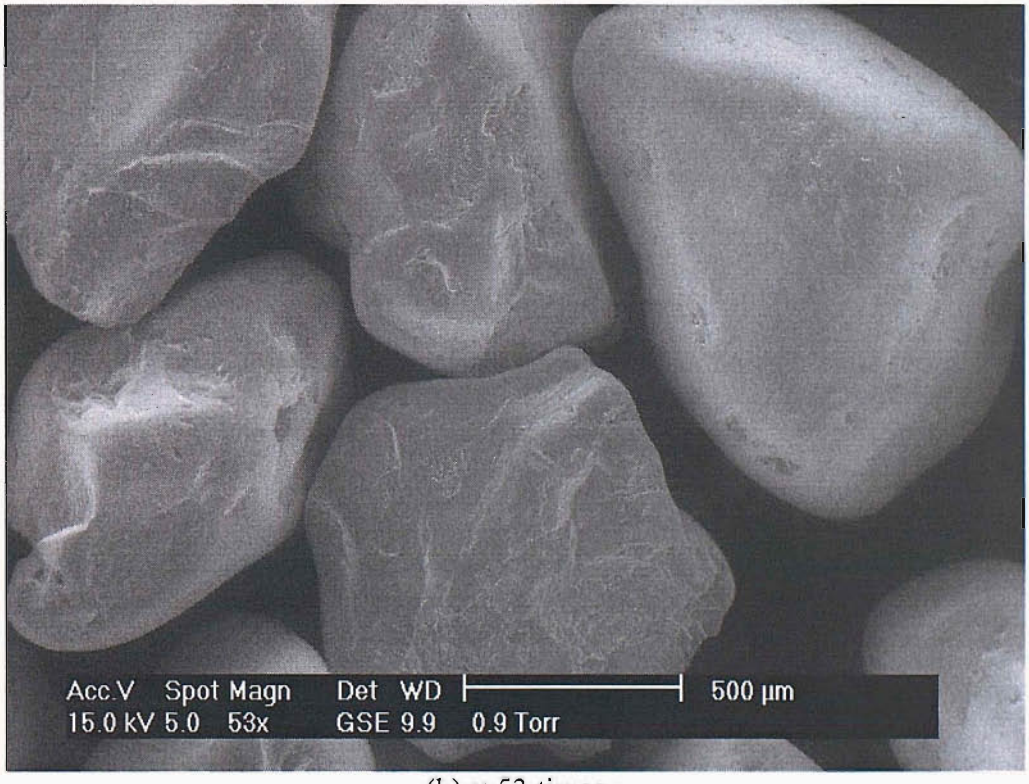

(b) × 53 times

Figure 6.2 Scanning electron micrographs of Leighton Buzzard B sand particles

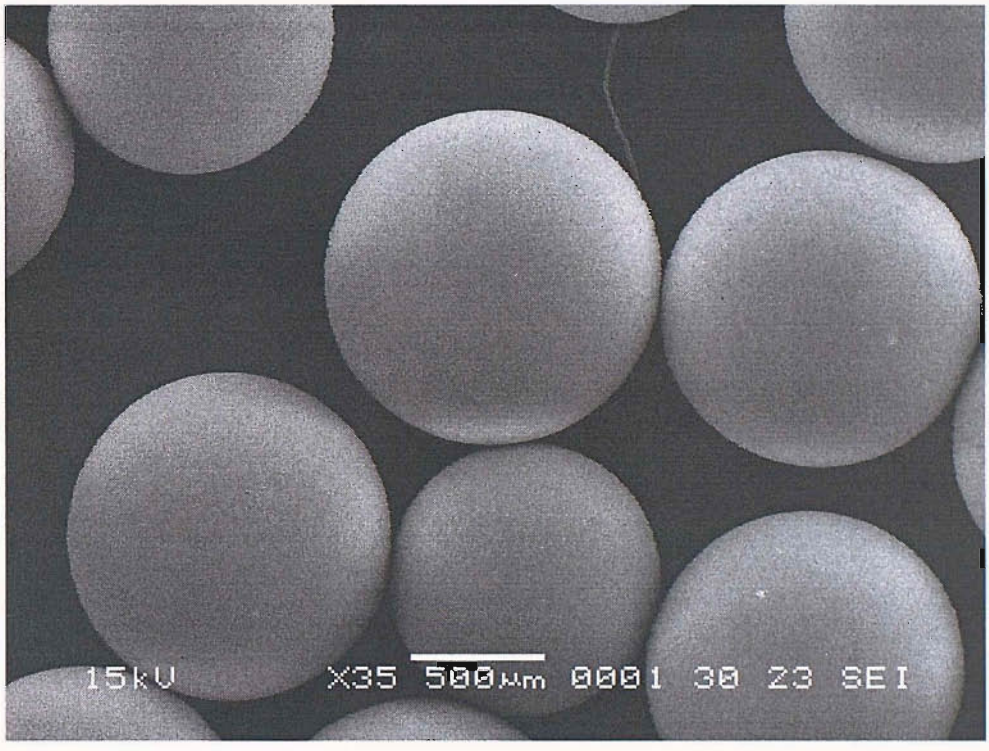

Figure 6.3 Scanning electron micrograph of glass ballotini particles (×35times)

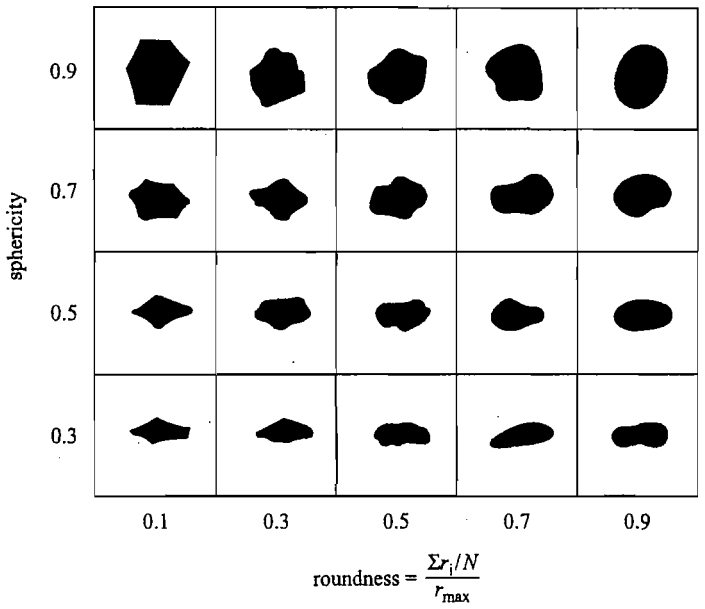

(a) Particle shape description (Santamarina & Cho, 2004)

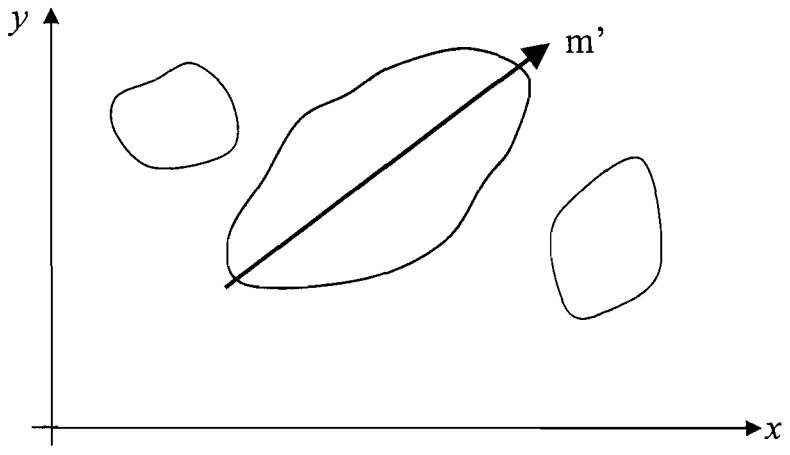

(b) Particle orientation in a 2-D coordination (reproduced from Mitchell, 1993)

Figure 6.4 Description of particle shape and orientation

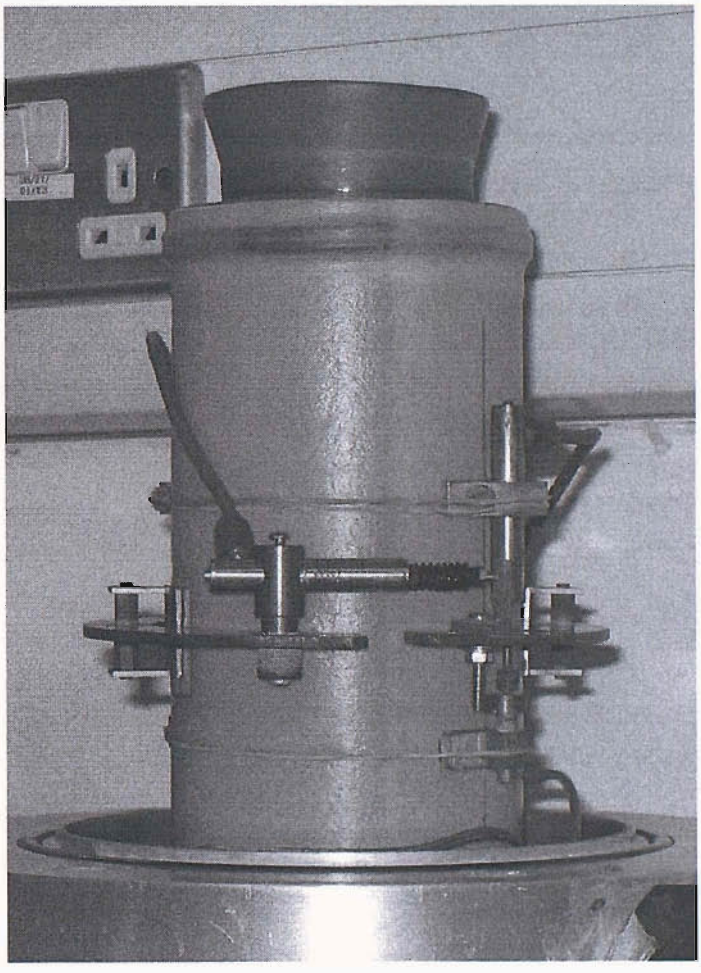

Figure 6.5 The set-up of a coarse sand specimen

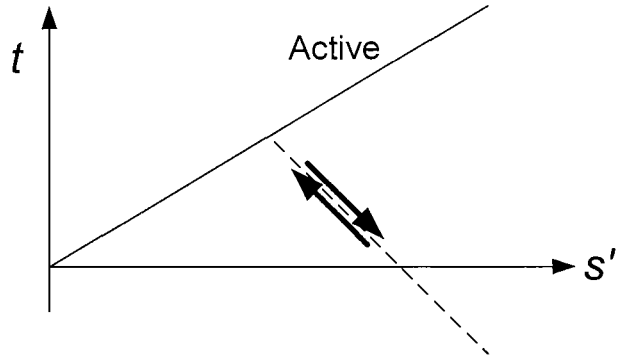

(a) stage 1: cycling between the active state and the isotropic state

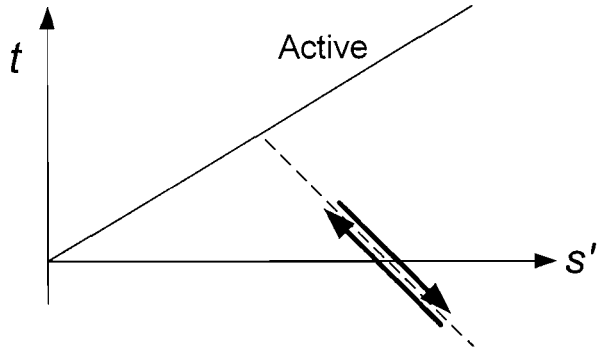

(b) stage 2: cycling across the isotropic state

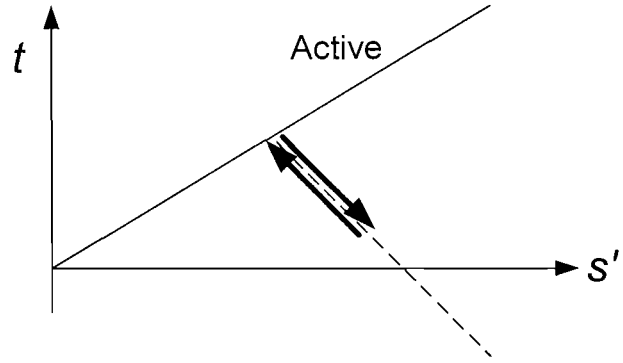

(c) stage 3: cycling reaching the active state

Figure 6.6 Stress paths at different stages during the special test on the loose sand specimen LBS4

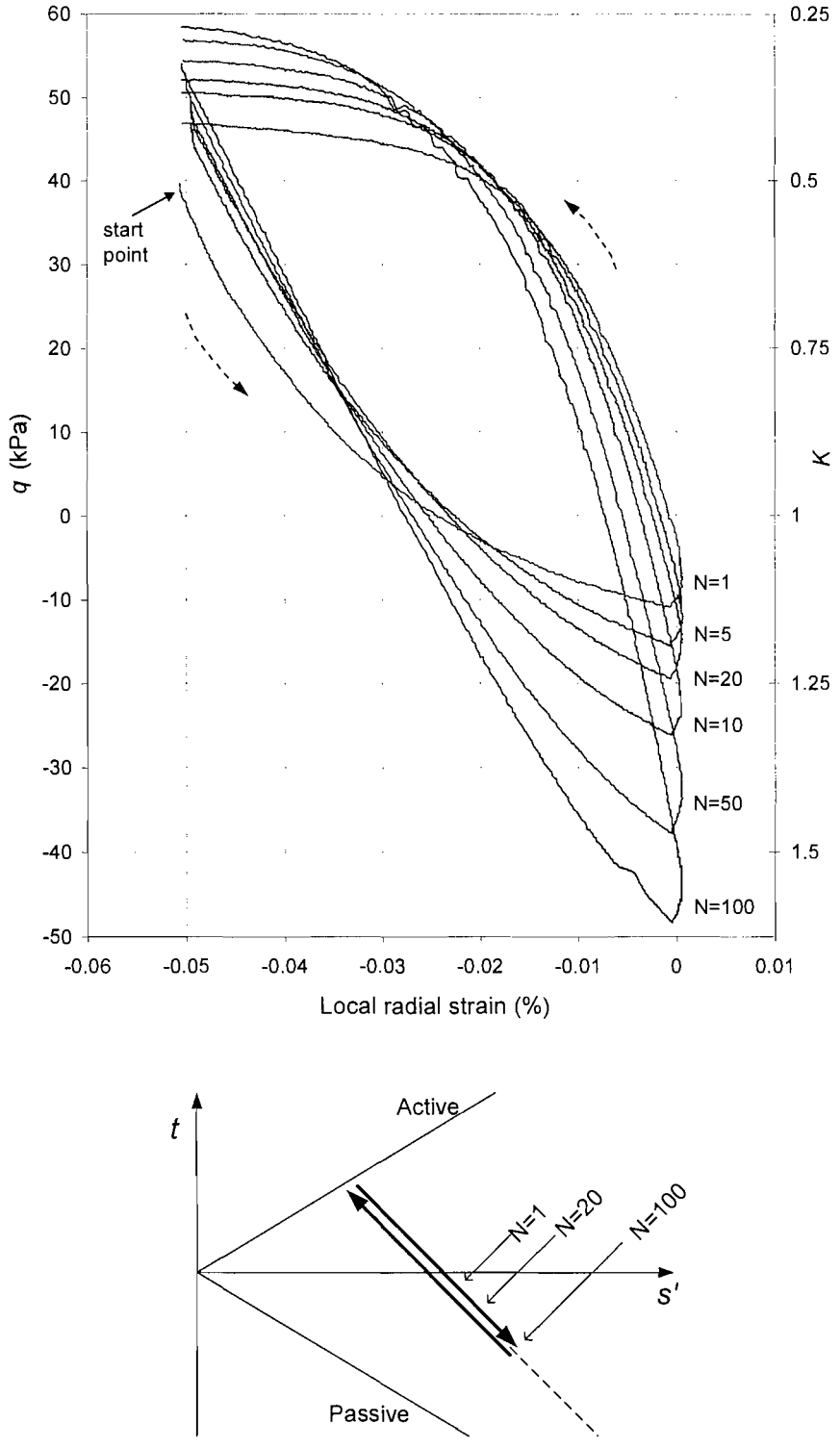

Figure 6.7 Curves of deviator stress and earth pressure coefficient K against local radial strain for the loose sand specimen LBS1 under a cyclic radial strain range of 0.05%

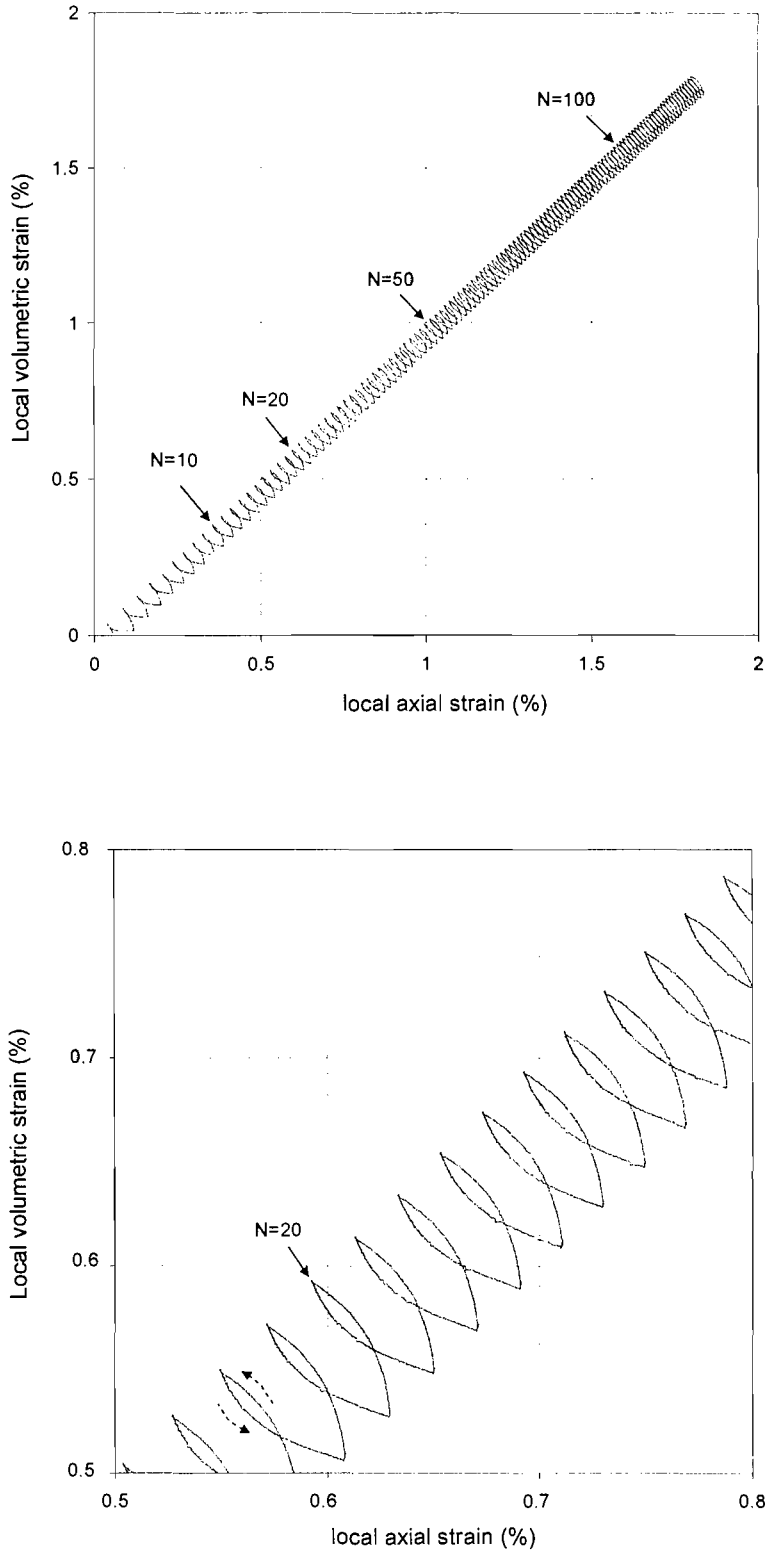

Figure 6.8 Curves of volumetric strain against axial strain for the loose sand specimen LBS1 under a cyclic radial strain range of 0.05%

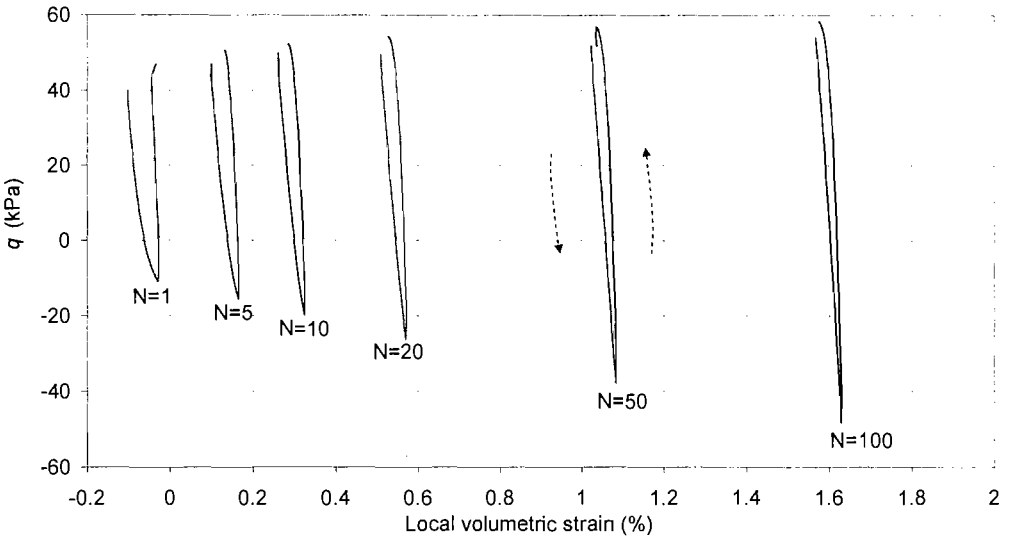

(a) under a cyclic radial strain range of 0.05%

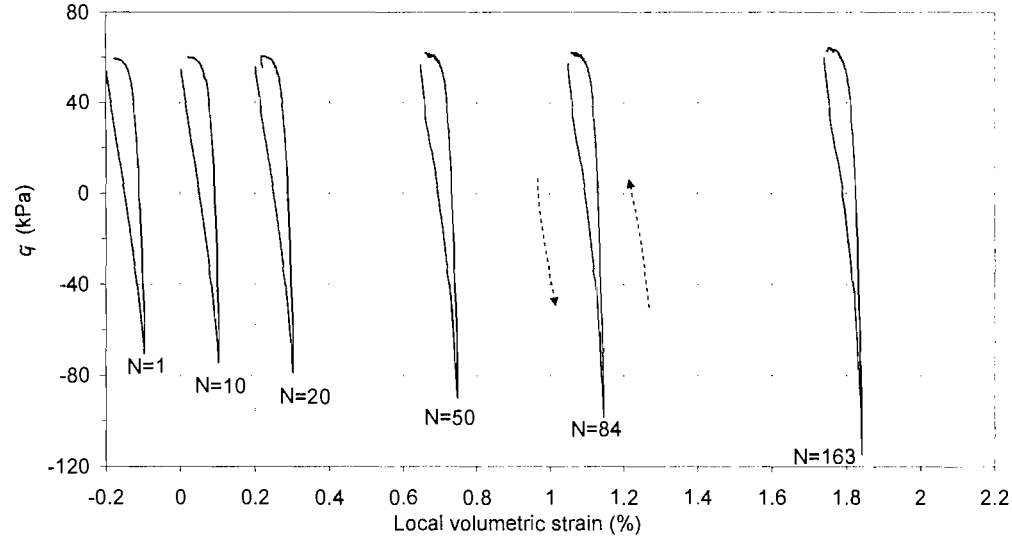

(b) under a cyclic radial strain range of 0.1%

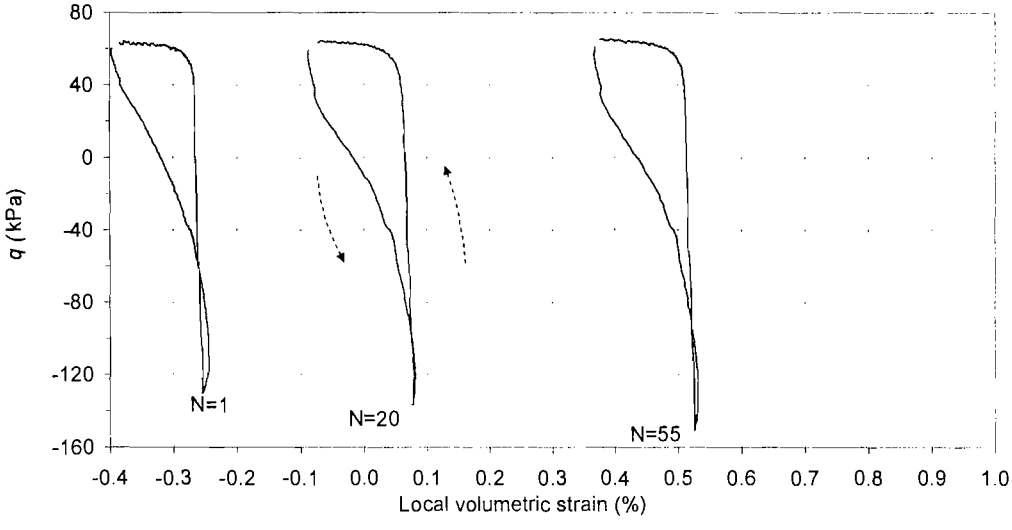

(c) under a cyclic radial strain range of 0.2%

Figure 6.9 Curves of deviator stress against local volumetric strain for the loose sand specimen LBS1 under cyclic radial strain ranges of 0.05%, 0.1% and 0.2%

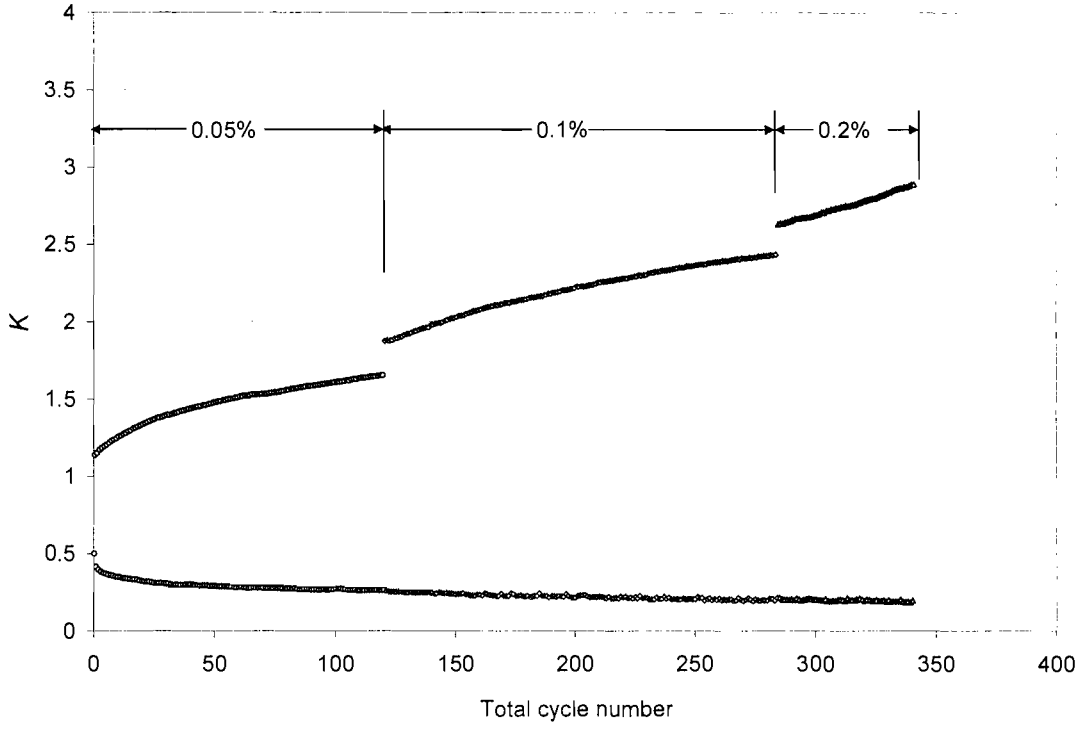

Figure 6.10 Maximum and minimum earth pressure coefficients K against total cycle number for the loose sand specimen LBS1 under cyclic radial strain ranges of 0.05%, 0.1% and 0.2%

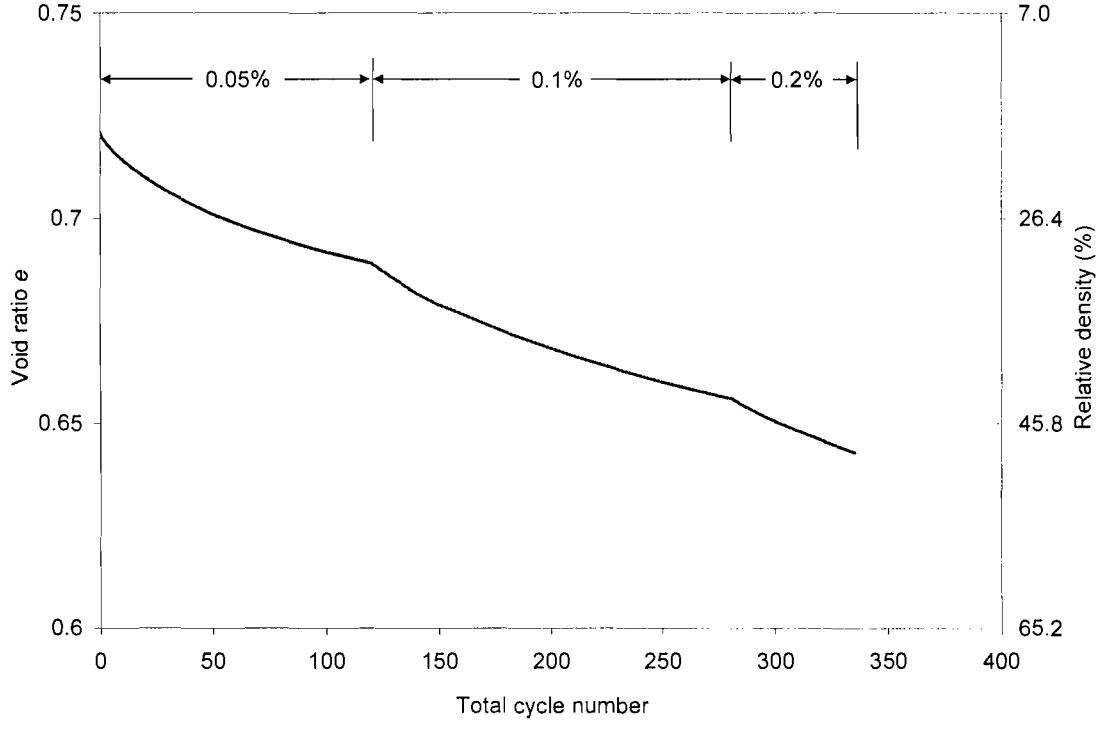

Figure 6.11 Void ratio and relative density change against total cycle number for the loose sand specimen LBS1 under cyclic radial strain ranges of 0.05%, 0.1% and 0.2%

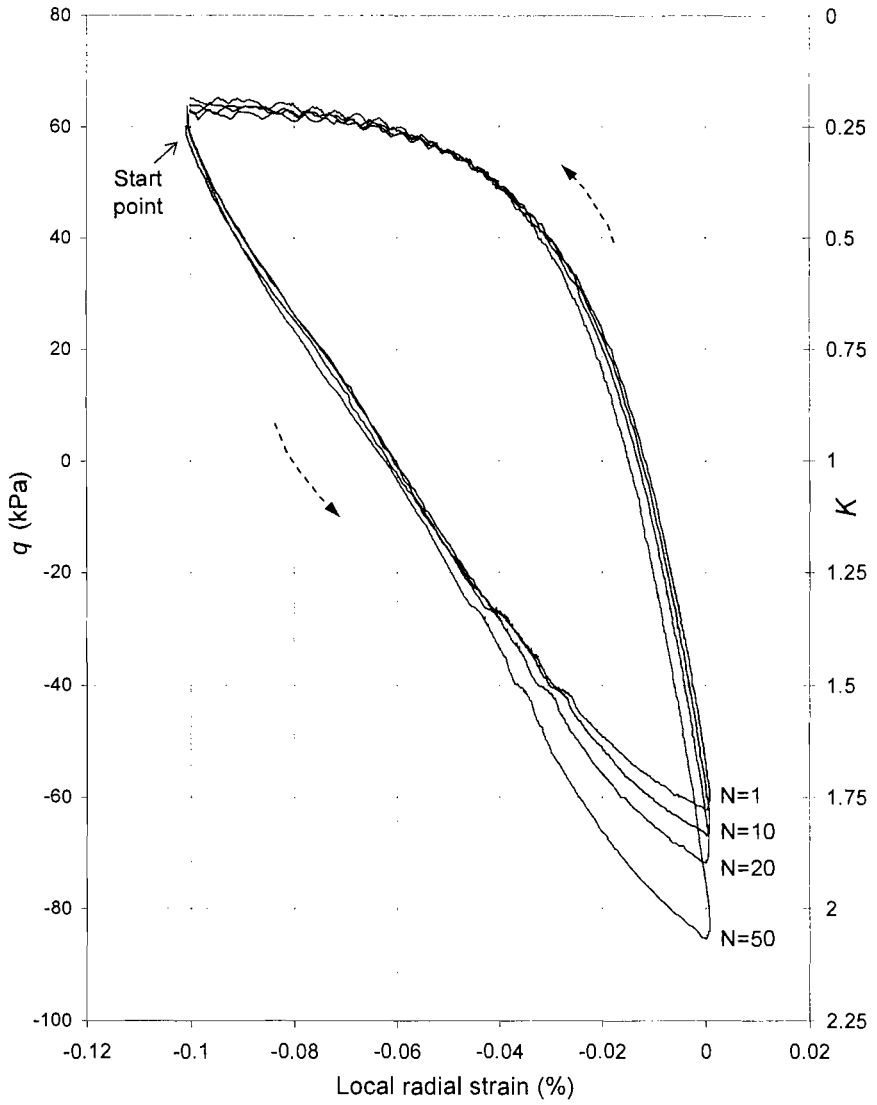

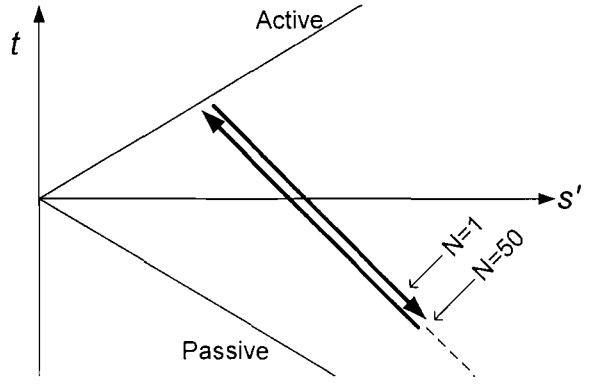

Figure 6.12 Curves of deviator stress and earth pressure coefficient K against local radial strain for the dense sand specimen LBS2 under a cyclic radial strain range of 0.1%

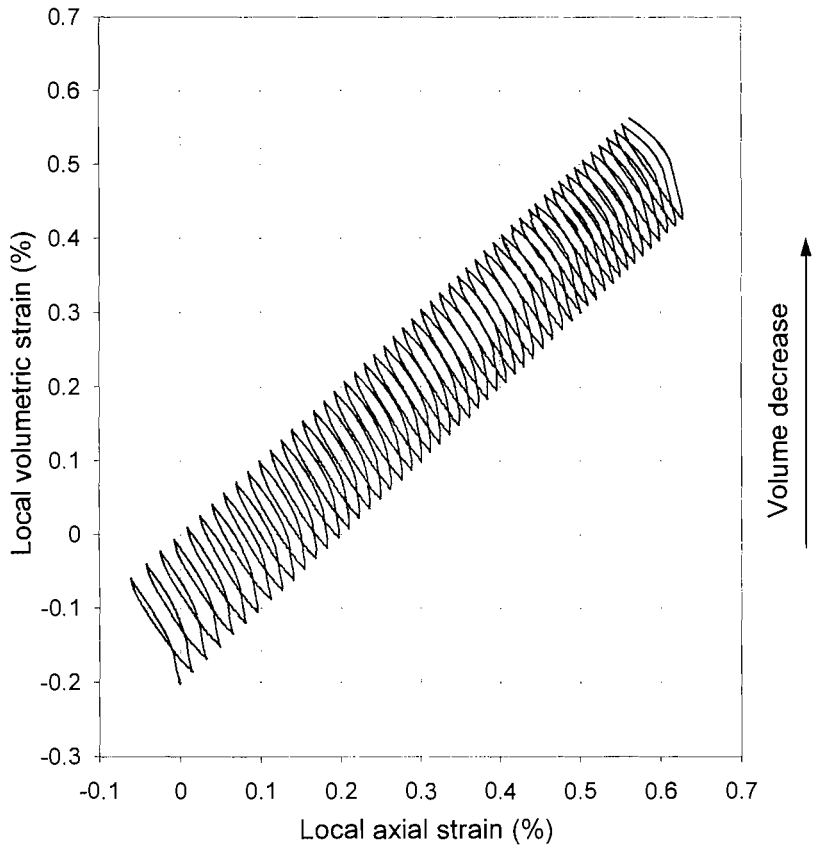

Figure 6.13 Curves of volumetric strain against axial strain for the dense sand specimen LBS2 under a cyclic radial strain range of 0.1%

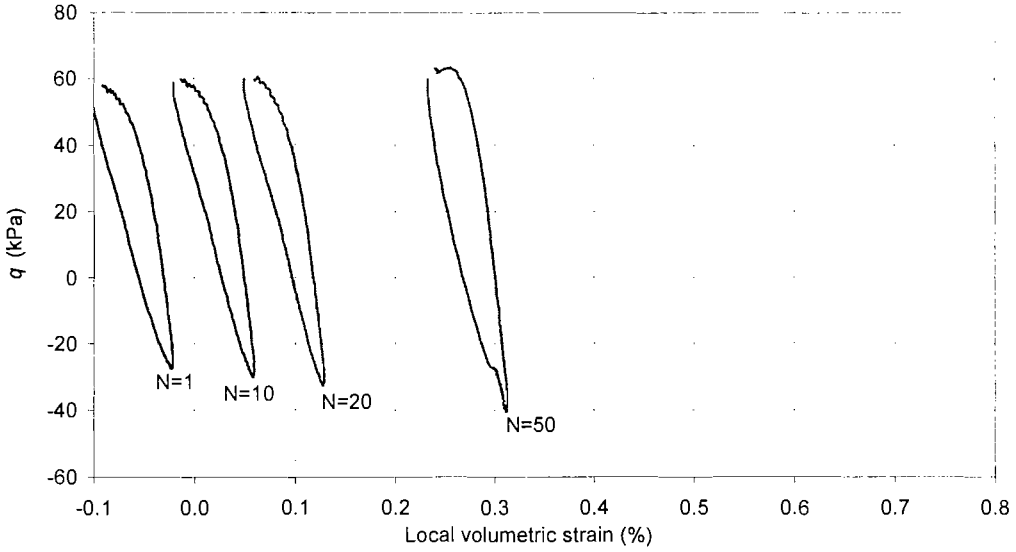

(a) under a cyclic radial strain range of 0.05%

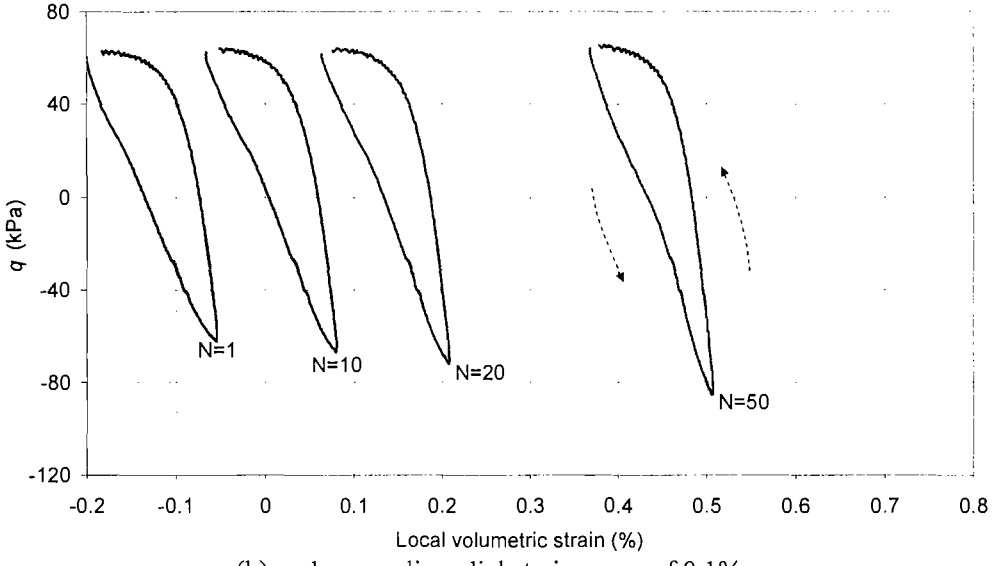

(b) under a cyclic radial strain range of 0.1%

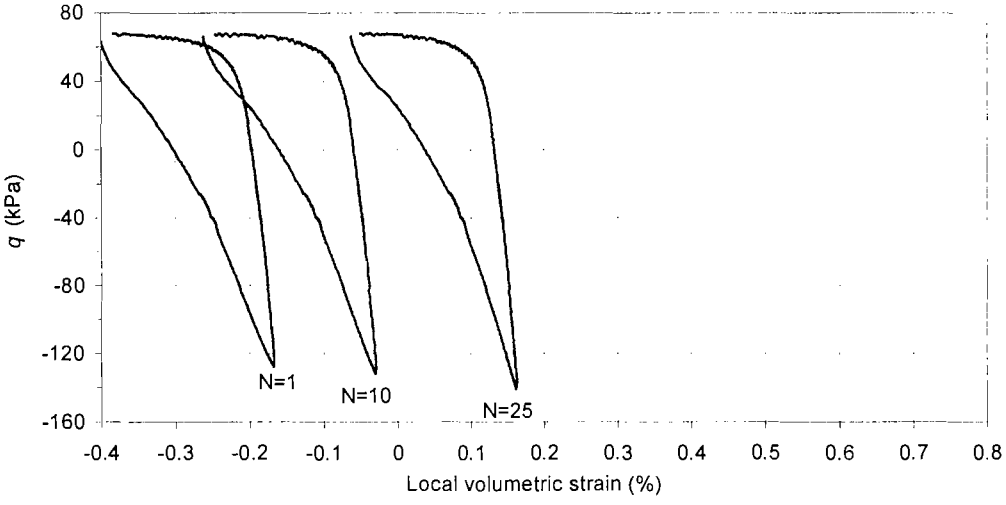

(c) under a cyclic radial strain range of 0.2%

Figure 6.14 Curves of deviator stress against local volumetric strain for the dense sand specimen LBS2 under cyclic radial strain ranges of 0.05%, 0.1% and 0.2%

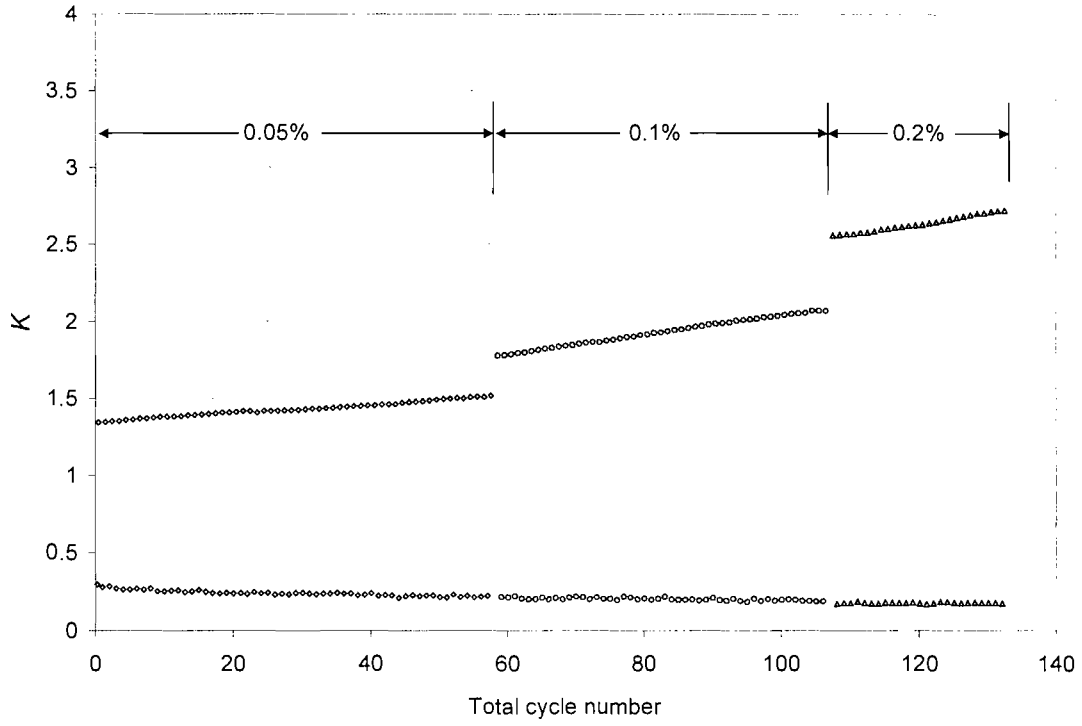

Figure 6.15 Maximum and minimum earth pressure coefficients K against total cycle number for the dense sand specimen LBS2 under cyclic radial strain ranges of 0.05%, 0.1% and 0.2%

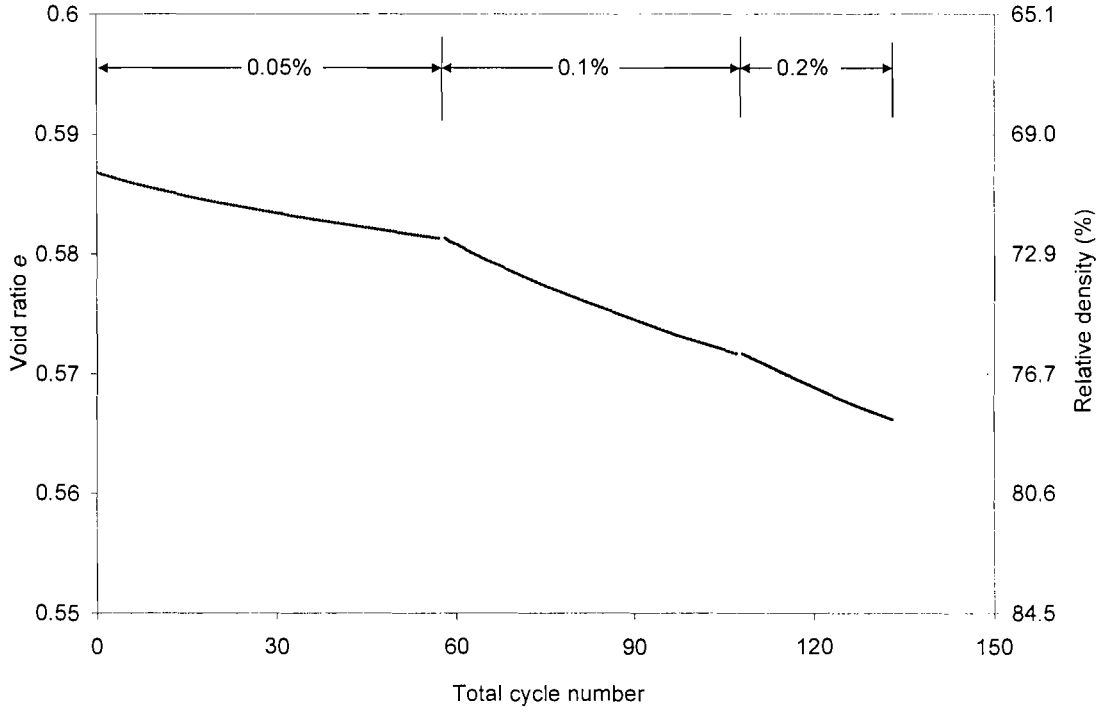

Figure 6.16 Void ratio and relative density change against total cycle number for the dense sand specimen LBS2 under cyclic radial strain ranges of 0.05%, 0.1% and 0.2%

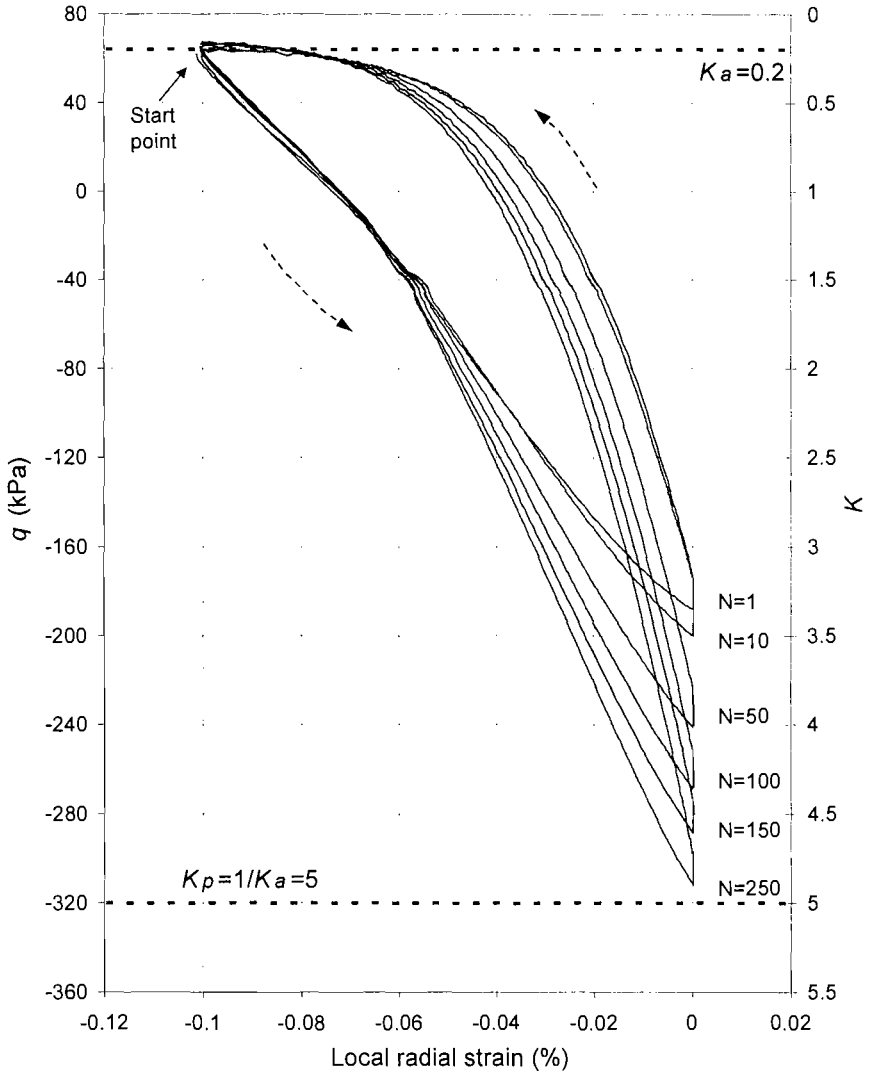

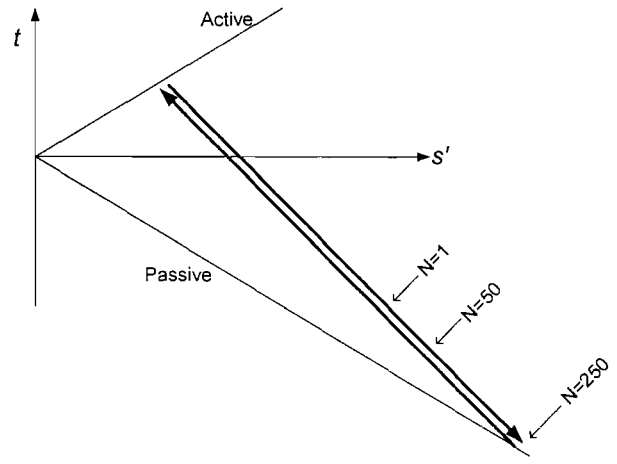

Figure 6.17 Curves of deviator stress and earth pressure coefficient K against local radial strain for the very dense sand specimen LBS3 under a cyclic radial strain range of 0.1%

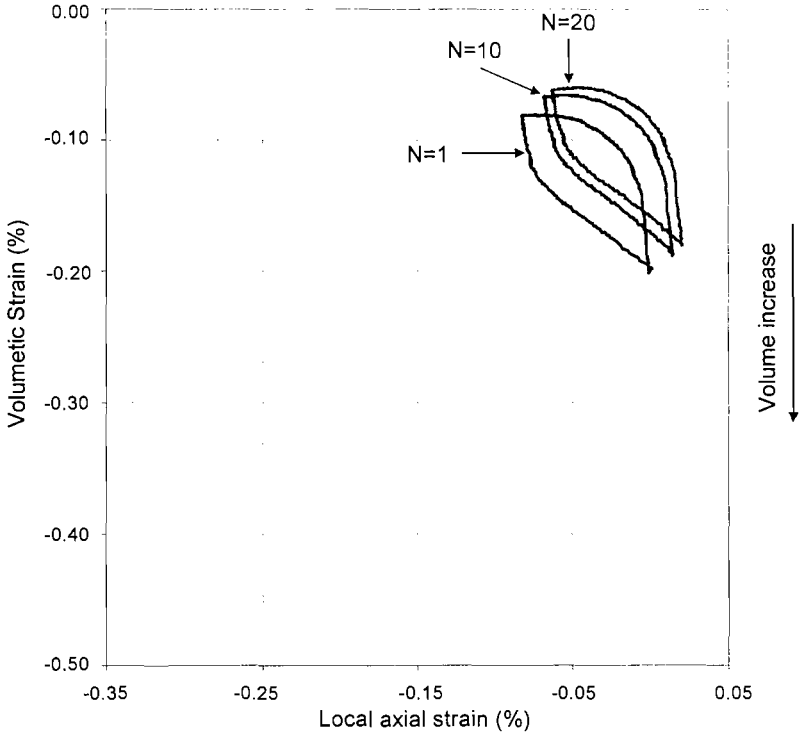

(a) Cycle 1~20

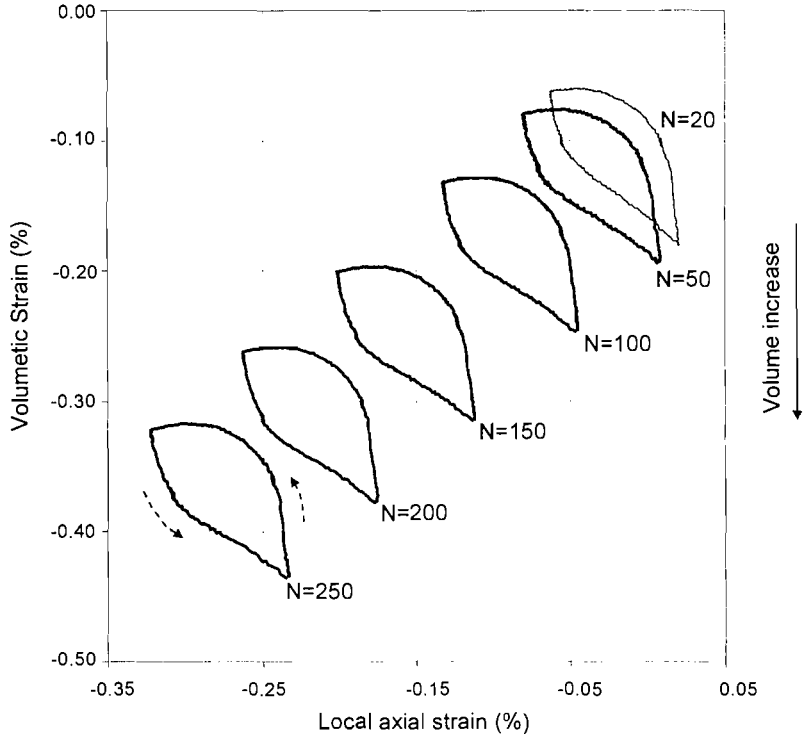

(b) Cycle 20~250

Figure 6.18 Curves of volumetric strain against axial strain for the very dense sand specimen LBS3 under a cyclic radial strain range of 0.1%

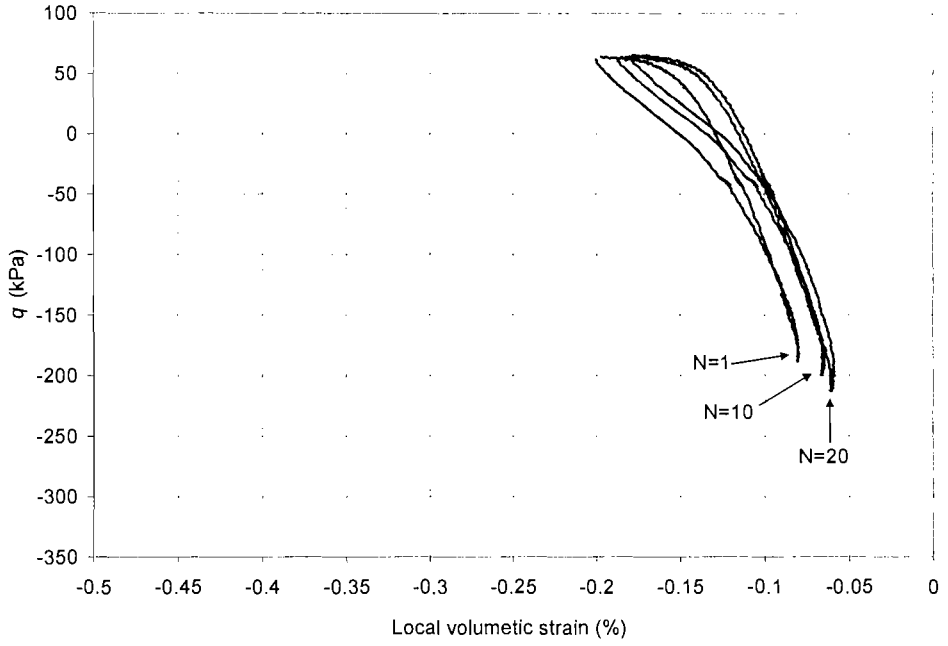

(a) Cycle 1~20

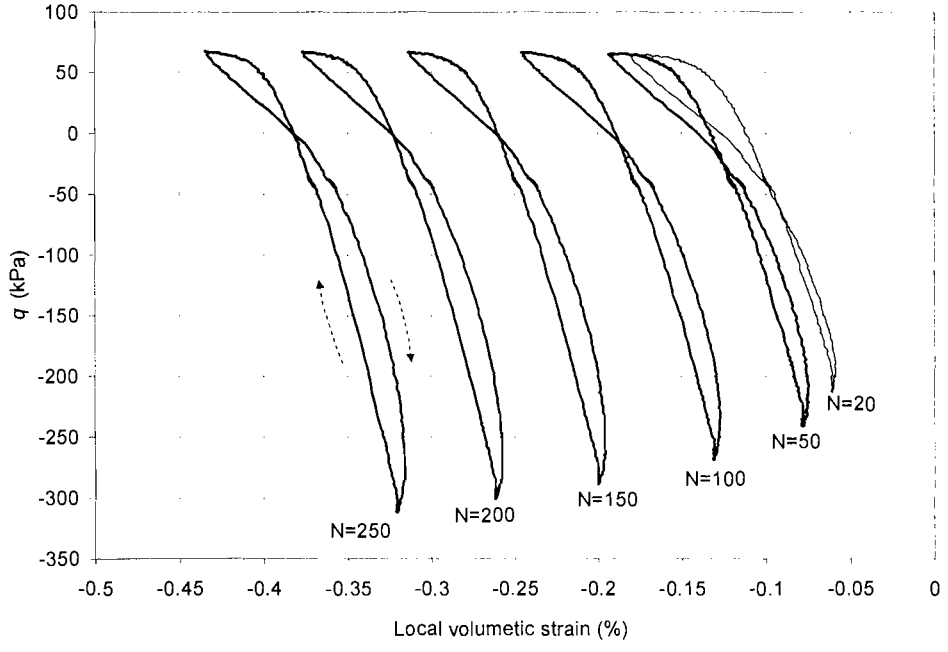

(b) Cycle 20~250

Figure 6.19 Curves of deviator stress against local volumetric strain for the very dense sand specimen LBS3 under a cyclic radial strain range of 0.1%

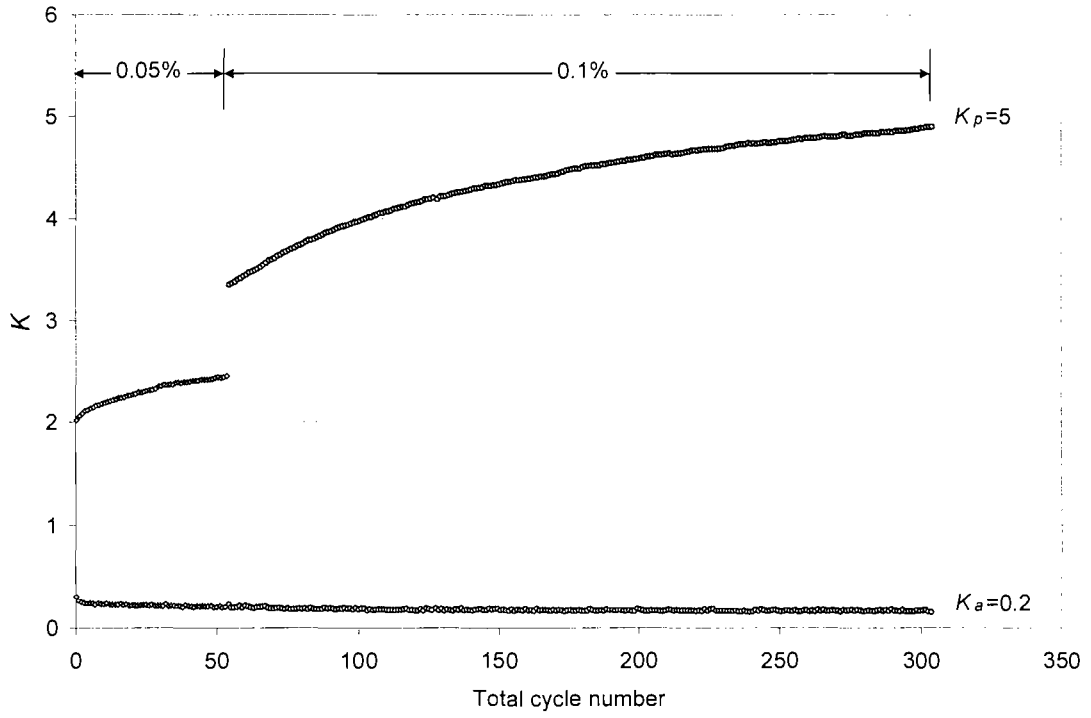

Figure 6.20 Maximum and minimum earth pressure coefficients K against total cycle number for the very dense sand specimen LBS3 under cyclic radial strain ranges of 0.05% and 0.1%

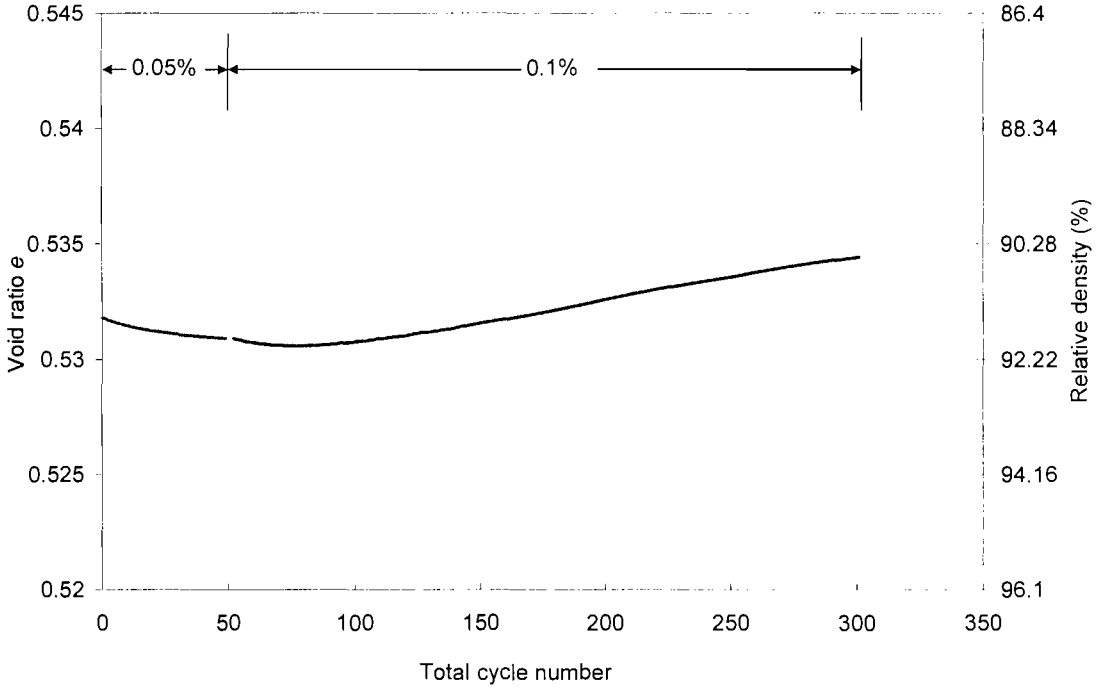

Figure 6.21 Void ratio and relative density change against total cycle number for the very dense sand specimen LBS3 under cyclic radial strain ranges of 0.05% and 0.1%

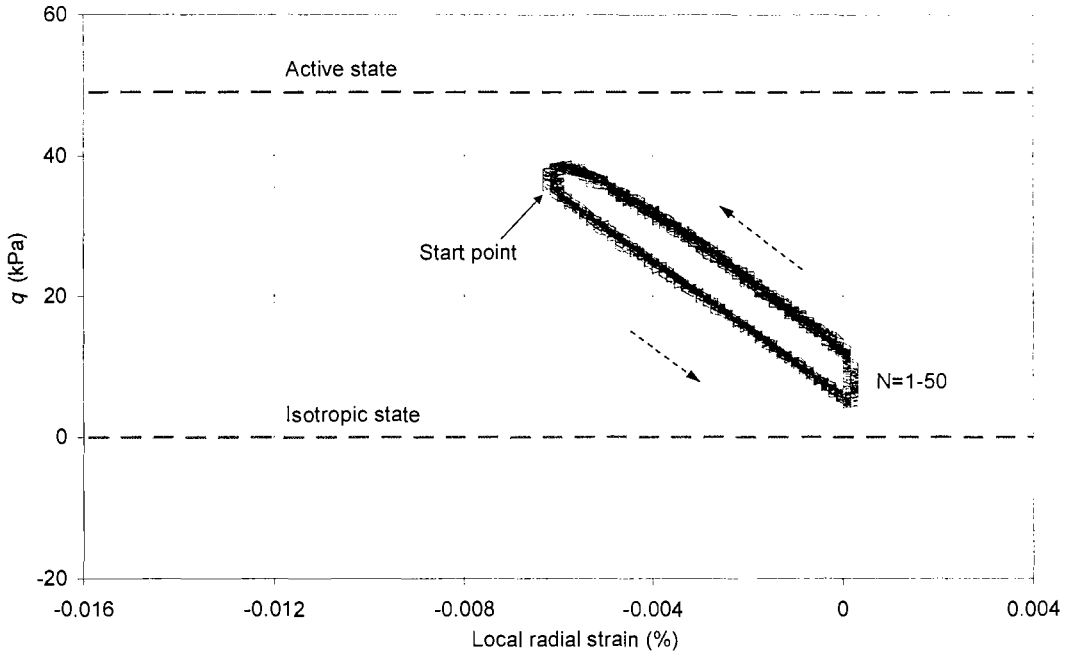

Figure 6.22 Curves of deviator stress against radial strain for the special test on the loose sand specimen LBS4 during Stage 1 (between the active state and the isotropic state, cyclic radial strain range=0.006%)

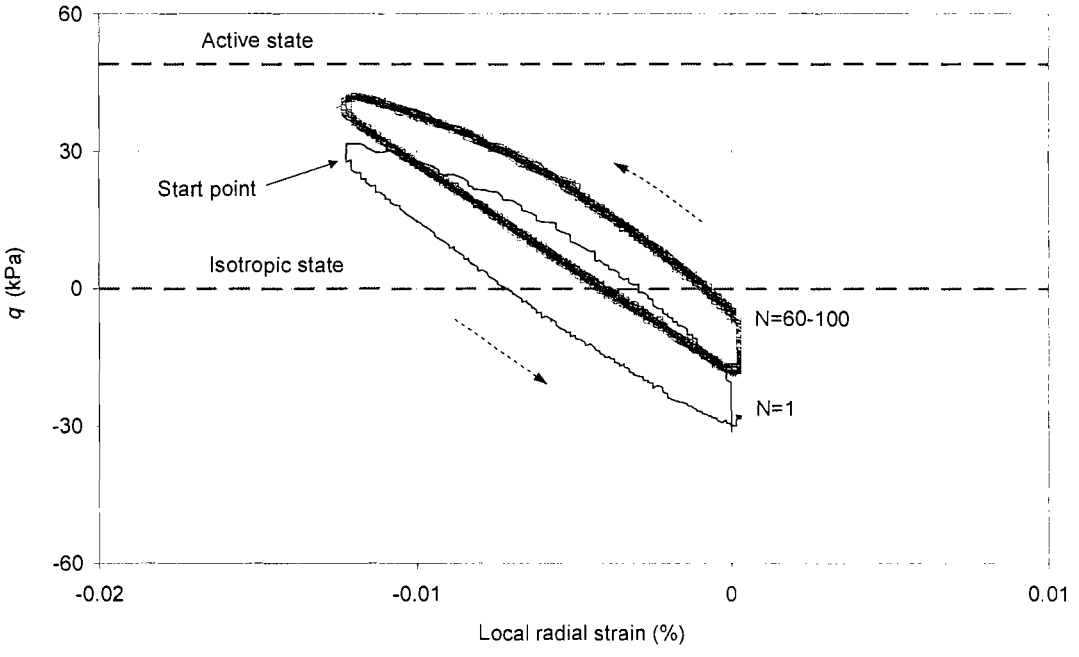

Figure 6.23 Curves of deviator stress against radial strain for the special test on the loose sand specimen LBS4 during Stage 2 (only across the isotropic state, cyclic radial strain range=0.012%)

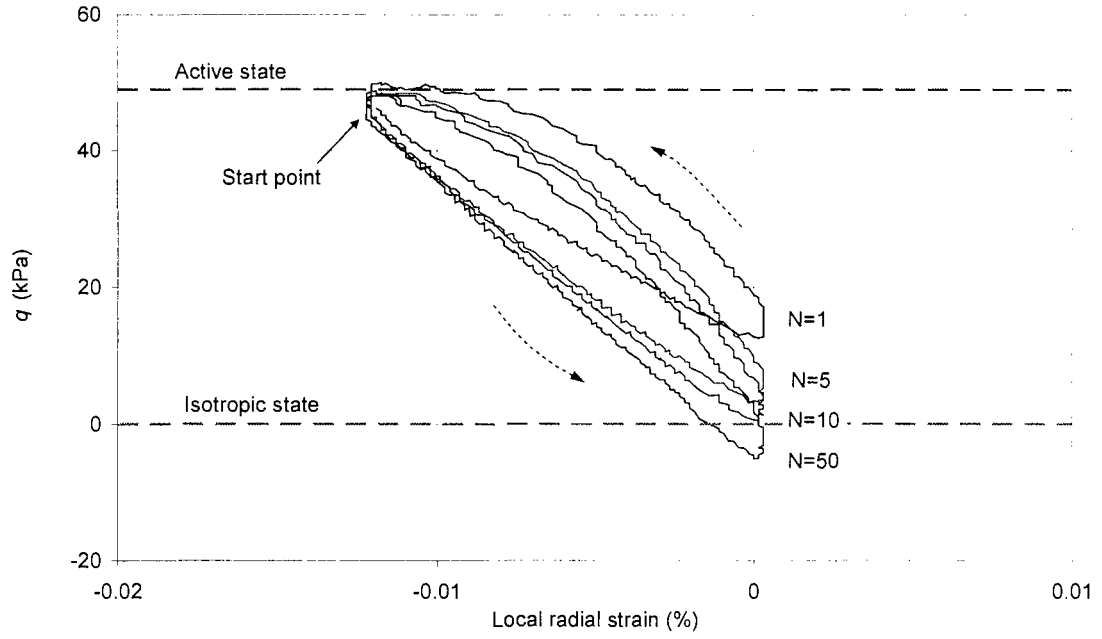

Figure 6.24 Curves of deviator stress against radial strain during the special test on the loose sand specimen LBS4 during Stage 3 (begun from the active state, but above the isotropic state, cyclic radial strain range=0.012%)

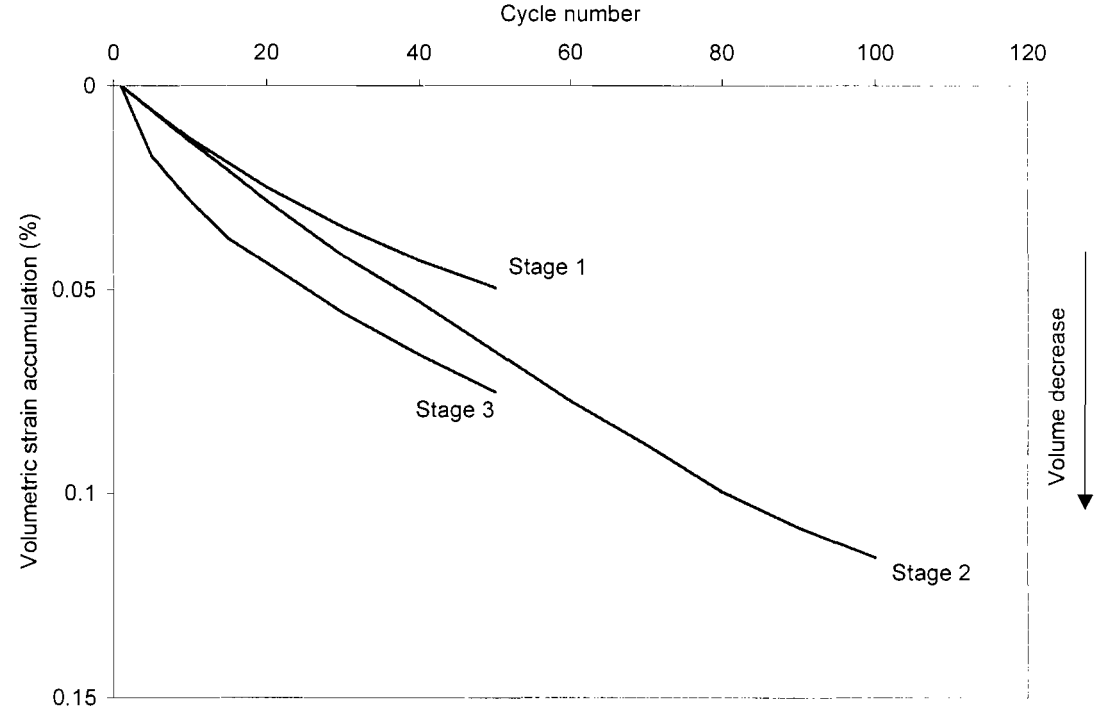

Figure 6.25 Volumetric strain accumulation with cycles at different stages for the special test on the loose sand specimen LBS4

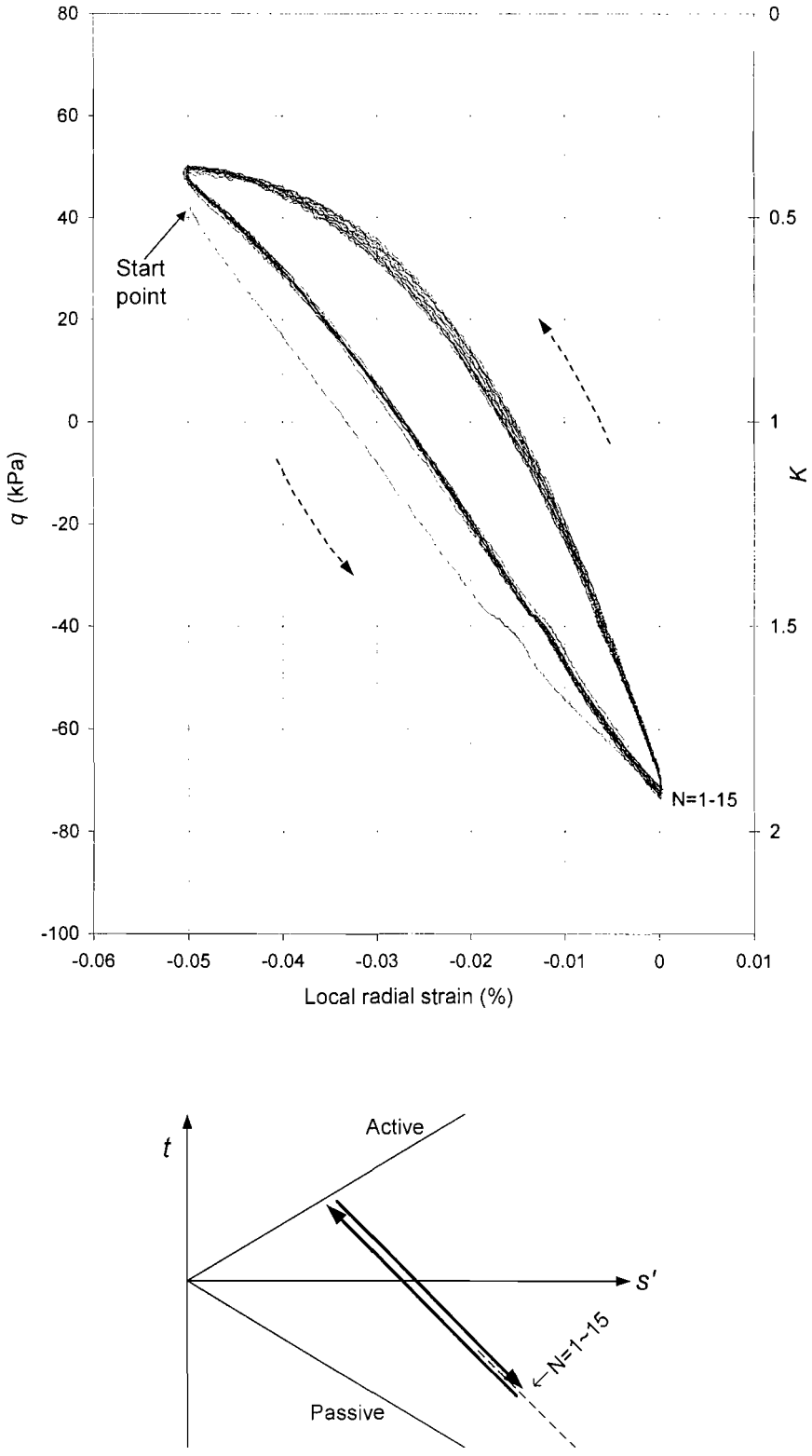

Figure 6.26 Curves of deviator stress against local radial strain for the dense glass ballotini specimen G1 under a cyclic radial strain range of 0.05% (15 cycles)

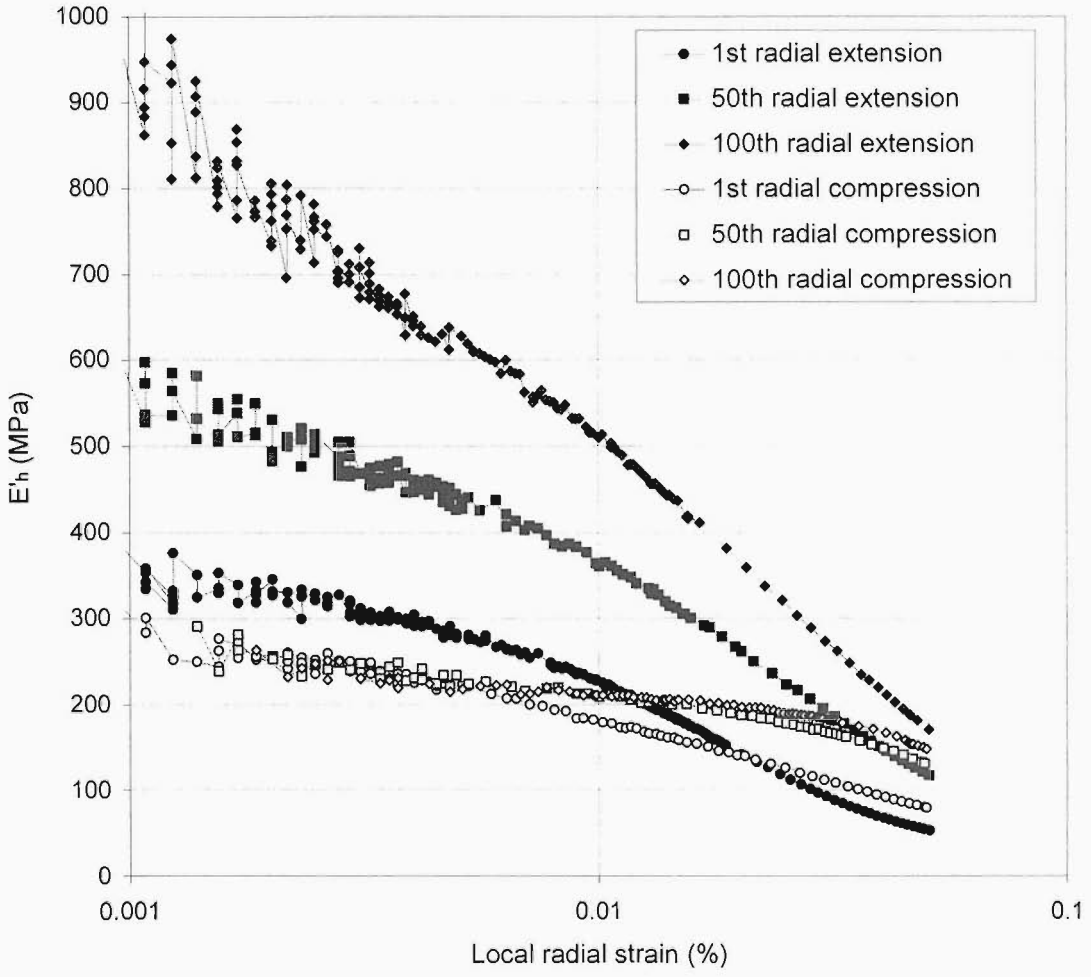

Figure 6.27 Stiffness as a function of local radial strain for the loose sand specimen LBS1 under a cyclic radial strain range of 0.05%

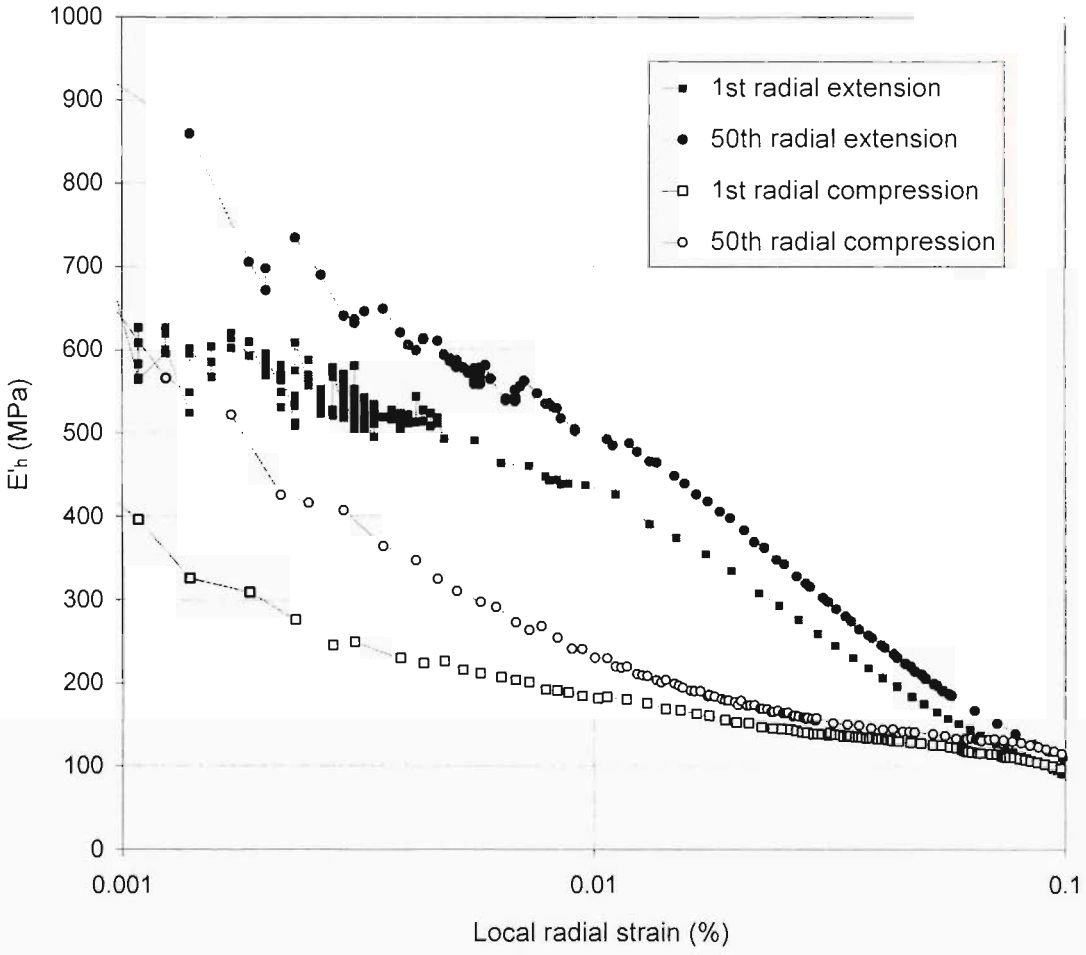

Figure 6.28 Stiffness as a function of local radial strain for the dense sand specimen LBS2 under a cyclic radial strain range of 0.1%

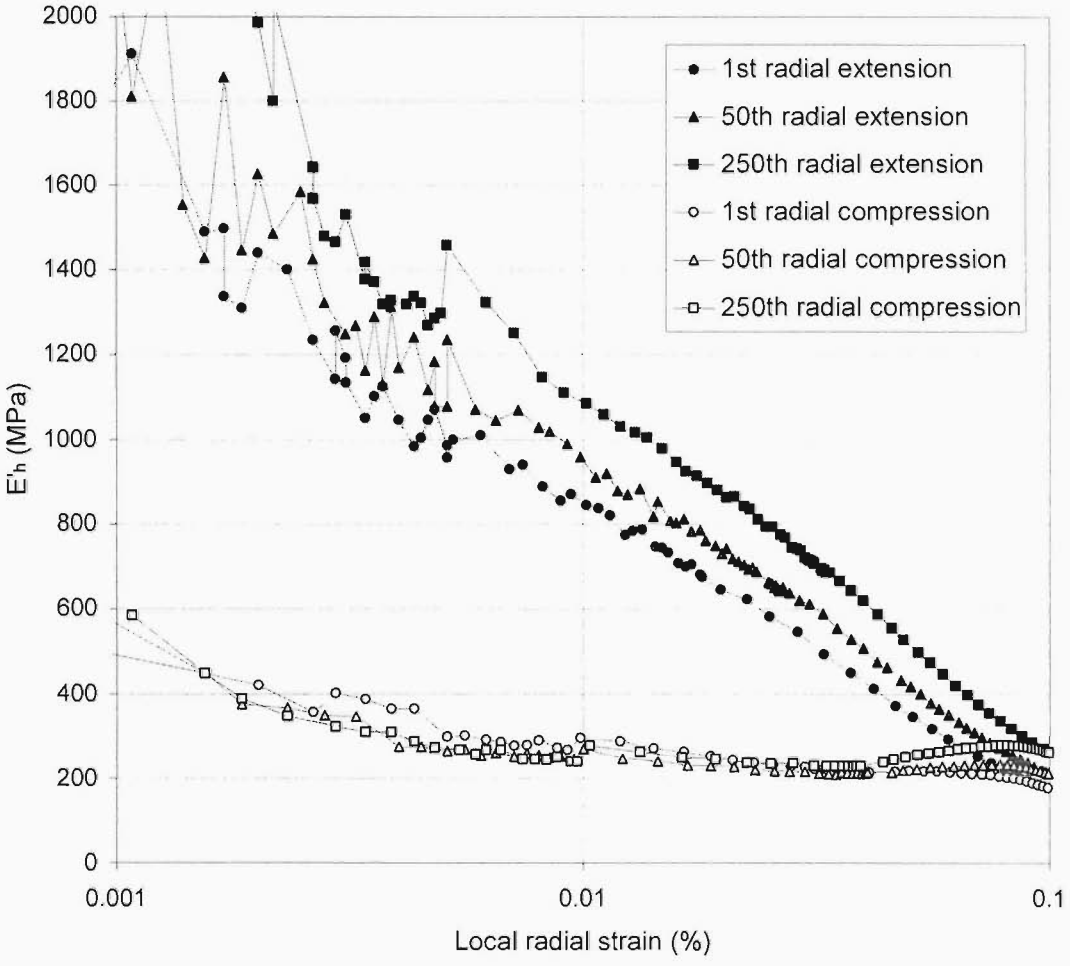

Figure 6.29 Stiffness as a function of local radial strain for the very dense sand specimen LBS3 under a cyclic radial strain range of 0.1%

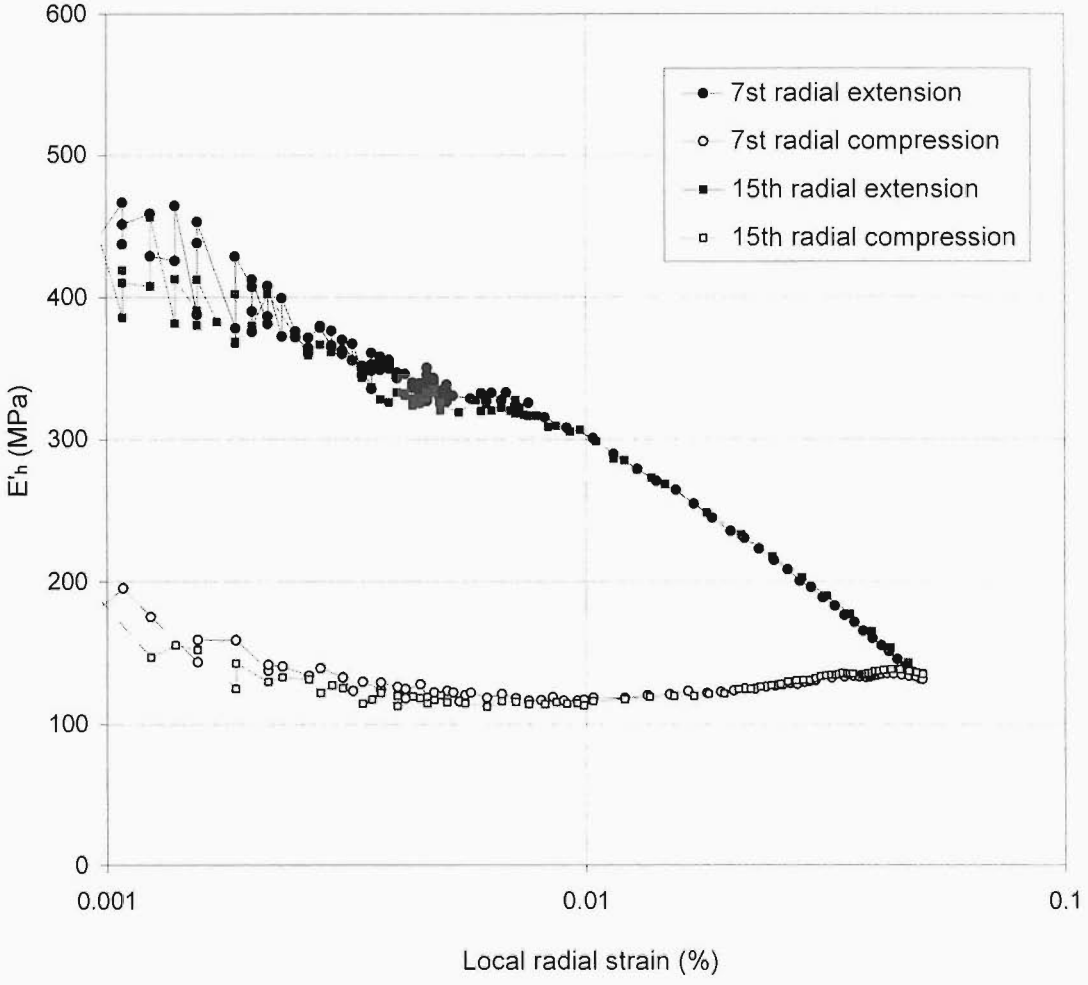

Figure 6.30 Stiffness as a function of local radial strain for the dense glass ballotini specimen G1 under a cyclic radial strain range of 0.05%

Chapter 7 Discussion

In this chapter, the test results for Atherfield I Clay and granular materials (including Leighton Buzzard B sand and glass ballotini) will be compared. Possible reasons will be discussed for the observed differences in behaviour (Section 7.1). Then the findings of this research will be compared with those of previous research on the behaviour of soil behind integral abutments (Section 7.2). Finally, the implications for integral abutment design from this research will be discussed (Section 7.3).

7.1 Comparison of the test results for stiff clay and granular materials

Undisturbed Atherfield I Clay, Leighton Buzzard B sand and glass ballotini have been tested under radial strain-controlled cyclic stress path loading. Significant differences have been found between the results for these materials, which will be highlighted. Possible reasons for these differences will be discussed.

7.1.1 Differences between the test results for stiff clay and granular materials

The two most significant differences were found to be: 1) the stiffness behaviour; 2) the tendency of lateral stress increase under radial strain-controlled cyclic loading.

Stiffness behaviour

Atherfield I Clay, Leighton Buzzard B sand and glass ballotini were tested at similar initial mean effective stress levels. In previous chapters, secant Young's modulus of Atherfield I Clay, Leighton Buzzard B sand and glass ballotini have been examined extensively (sections 5.5.2 and 6.5.4). It will also be beneficial to examine the tangent stiffness, especially for granular materials, which reflects the resistance of soil to stress change during cycling (Figures 7.1 and 7.2).

Marked differences were found in the stiffness behaviour. The small strain stiffness of the coarse sand, even at its loosest packing, was found to be significantly higher than that of the stiff clay (Figure 7.2 vs Figure 7.1, also see Figure 6.27 vs Figure 5.16).

In addition, all granular materials exhibited different stiffness behaviour during radial compression and radial extension (Figure 7.2, Figures 6.27~6.30). In contrast,

for stiff clay specimens, insignificant differences were found between the stiffness behaviour in radial compression and radial extension (Figure7.1 and Figure 5.14).

The stiffness behaviour of stiff clay was found to be unaffected by the cyclic loading (Figure 7.1 and Figures 5.14~16) at all cyclic strain levels. Similar behaviour was observed for the glass ballotini specimen (Figure 7.2b and Figure 6.30). However, for coarse sand, the stiffness during both radial compression and radial extension continued to increase with cycling (Figure 7.2a and Figures 6.27~6.29).

Build-up of maximum lateral stress

For Atherfield I Clay specimens (Figures 5.6~9) and the glass ballotini specimen (Figure 6.26), the stress-strain behaviour entered a resilient state immediately after the first cycle of loading. There was no obvious build-up of lateral stress with cycling. In contrast, no resilient state was observed for the sand. The maximum horizontal stress continued to build-up with radial strain cycling over a wide range of density, and approached the passive state (Figures 6.10, 6.15 and 6.20).

7.1.2 Possible reasons

Possible reasons for the observed differences in stiffness and stress-strain behaviour between stiff clay and granular materials described above will be explored here.

Many researchers attribute clay-like behaviour to the fineness of their particles and physico-chemical effects involving the colloidal activity of their materials (*e.g.* Skempton, 1953). However, Olson and Mesri (1970) investigated the relative importance of mechanical and physico-chemical effects and concluded that for all but the most active of reconstituted clays, mechanical effects were the governing factors in determining compressibility. Therefore, it is believed that the apparent differences in stiffness and stress-strain behaviour of stiff clay and granular materials observed in this research were also caused by mechanical effects.

The microstructure of Atherfield I Clay has been studied using scanning electron microscopy, as presented in Figure 5.2. The clay particles had a sheet-like shape in general. The maximum dimension of clay particle was about 10μm. The clay particles were very thin, and less than 1/100 of the length. Atherfield I Clay exhibited a very dense fabric, with platy particles overlapping each other. The orientation of particles appeared to align with the same direction (presumably the horizontal plane) during deposition.

Leighton Buzzard B sand particles had a diameter of about 1mm, with a sub-rounded particle shape (Figure 6.2). The ratio of the longest to shortest dimension was about 1~2. Glass ballotini particles also had a diameter of about 1mm, with a spherical particle shape (Figure 6.3).

From a mechanical point of view, the deformation of a mass of particles involves three possibilities: 1) deformation of particles, *e.g.* bending, compression or distortion; 2) movement of particles, *e.g.* sliding and rolling; 3) rupture or breakage of particles.

For stiff clay under loading, the strain appears to result from a mechanical bending and compressing of the platy particles. Olson and Mesri (1970) noted that for platy particles, as the diameter-to-height ratio increases, more energy can be stored in the soil by particle bending and the soil exhibits more compressibility. Sliding or rolling of platy particles seems to be unlikely in such a very dense fabric before failure. Rupture of particles may happen in normally consolidated clay with a large void ratio. However, for heavily overconsolidated clay with platy particles parallel to and overlapping each other, which have already experienced large overburden in geological history, the current effective stress level is unlikely to cause significant rupture of particles. Therefore, deformation of platy particles is a major feature for stiff clay under loading, resulting in a relatively low stiffness.

In contrast, for coarse sand and glass ballotini, the strain mainly involves sliding and rotation of the granular particles (Skinner, 1969). The deformation of individual particles is expected to be small, considering the high modulus of the sand quartz or glass and the essentially equidimensional shape, even though the force at contact points may be high. Breakage of particles may become dominant in some crushable soils under high stress level (Cheng *et al.*, 2004). For Leighton Buzzard sand and glass ballotini under a moderate stress level, granular particles are unlikely to be significantly damaged. Therefore, movement of round particles, *i.e.* sliding or rolling, dominates in granular materials under loading, leading to a relatively high stiffness.

In short, it appears that particle shape (and associated dominant response to loading) is the cause of the different stiffnesses of clay and granular materials observed in this research. Previous research has already demonstrated that sand-like behaviour could be transformed into clay-like behaviour by simply adding platy particles to coarse sand. Gilboy (1928) and Mundegar (1997) carried out experiments on mixture of uniform sand and mica of approximately the same grain size, and observed the enormous impact of particle shape on compressibility. Clayton *et al.* (2004) carried out undrained triaxial compression tests with small strain measurement

on mixtures of Leighton Buzzard B sand and fine sand sized mica, which had a particle size of about 0.1mm. The undrained secant Young's modulus decreased significantly with increasing content of mica. It was found that the value of $E_{u0.01}/p_o'$ for specimens with 10%, 15% and 20% mica lay between 500~700, values typically seen in natural stiff clay.

For stiff clay in this research, the deformation of platy particles appears to be fully recoverable or "elastic", as the stiffness behaviour remained unchanged during loading and unloading. As a result, no accumulation of lateral stress was observed with cycling.

To facilitate the explanation about the mechanism for the increasing stiffness and build-up of lateral stress observed for coarse sand, a highly simplified and idealized cartoon is presented (Figure 7.3). Figure 7.3a shows two rows of non-spherical granular particles sliding over each other. The rotation of particles is prevented at this moment by cement. It can be seen that to produce a relative horizontal displacement between the two rows of particles under a constant vertical stress N, horizontal shear stress T is required. Figure 7.3b presents the same mass of particles with the same vertical stress N and the same distance between the two plates. The only difference between Figure 7.3a and Figure 7.3b is the changed orientation of non-spherical particles. Now it is much more difficult to produce a horizontal displacement between the two rows in Figure 7.3b than in Figure 7.3a, due to a greater degree of inter-locking. Therefore, for a mass of non-spherical granular particles, only by changing the orientation of particles can the resistance to deformation be increased significantly. This is not necessarily associated with volumetric strain.

In reality, each sand particle is 3-dimensional with highly irregular surface features, which is much more complicated than the 2-dimensional idealized cartoon. However, the basic principle of the cartoon may be similar to that of the real sands. During the active state in each cycle, rolling becomes dominant. The orientation of particles will be changed, and the extent may be slight. Due to the non-spherical shape and undulate surface, a higher degree of inter-locking may be achieved progressively. When the stress state is well away from the active state (such as the beginning of a radial extension, or the second half of a radial compression), sliding becomes dominant and the changed packing leads to a progressively higher resistance to deformation. As a result, an increasing stiffness and a build-up of lateral stress were observed for coarse sand specimens.

In contrast, the rolling of glass ballotini particles has no influence, as the orientation of a perfectly spherical particle is the same in all directions (Figure 7.1c). As a result, there was no obvious increase in the stiffness or lateral stress for the dense glass ballotini specimen under cycling.

In each cycle, the secant stiffness of granular materials at small strains was found to be relatively low and experienced less increase during radial compression from the active state. This may be the effect of active failure. In the period just after the active state, rolling might be not insignificant. As the rolling resistance is much smaller than sliding, the mass exhibited smaller secant stiffness at small strains. When the strain became large enough, sliding became dominant and a higher stiffness was observed.

In summary, particle shape (platy, sub-round and spherical) is thought to be responsible for the differences in stiffness and stress-strain behaviour of stiff clay, coarse sand and glass ballotini under cycling in this research.

7.2 Comparison with previous research

In this research, radial strain – controlled cyclic stress path tests have been conducted on Atherfield I Clay and Leighton Buzzard B sand specimens, to study the behaviour of stiff clay (behind embedded integral abutments) and granular backfill (behind frame integral abutments). It will be beneficial to compare the findings from this research with those from previous research on the soil behind integral abutments.

7.2.1 Comparison of test results for stiff clay with field monitoring

Before this research, no laboratory investigation had been carried out to study the behaviour of stiff clay behind embedded integral abutments. The only field monitoring on integral abutment embedded in stiff clay was carried out by Barker & Carder (2000). However, lateral pressure was only measured at a depth of 1.5m, where reinforced earth was used. No measurement was made in the deeper stiff clay. Furthermore, the investigation lasted for only about 2 years after construction, and was complicated by the creep and shrinkage of the concrete, as discussed in Section 2.3.2.

Therefore, the main source of information has been from field investigations of the long term behaviour of propped retaining walls embedded in stiff clay. However, during the first few years after construction, measurement may be complicated by the

long term effect of wall installation, excavation in front of the wall and equilibrium of the excess pore water pressure. Even so, useful deductions can still be made.

The propped retaining wall at New Malden

Carder & Darley (1999) reported the field monitoring of an embedded retaining wall propped beneath the carriageway which was constructed in 1975 at New Malden, Surrey. The wall comprised 1.2m diameter contiguous bored piles at 1.2m centres, with a total length of 14.1m and a retained height of 7.4m. A reinforced concrete slab 400mm thick was constructed to prop the wall beneath the carriageway. The slab spanned between the retaining walls across the full 27m width of the underpass, without any hinges incorporated. The geology at the site consisted of stiff London Clay overlain by up to 2m of made ground. The wall was instrumented in 1984 to study its long term behaviour and the lateral earth pressures were measured by push-in spade cells. The results of the first 5 years of monitoring were reported in Carder & Symons (1990), after which the monitoring continued (Carder & Darley, 1999).

As with an integral abutment bridge, seasonal temperature variation caused expansion and contraction of the prop slab located immediately beneath the carriageway. As a result, large fluctuations in the lateral earth pressures and pore water pressures were recorded near the retaining wall, as shown in Figure 7.4a. The lateral pressure just above the toe (SC4) was relatively constant, probably because the wall rotated around a pivot near the toe.

Although no information is available on the magnitude of the retaining wall movement, it can be estimated. Assuming that $\alpha=12\times10^{-6}/^{o}C$ and the annual effective temperature variation range inside the concrete slab to be 43 ^{o}C, the annual movement range of one end of the slab is estimated as 6.9mm. If a further assumption is made that the wall was rigid and rotated about its toe (6.7m below the prop slab), the annual horizontal strain change in the mid part of the retained height can be approximated as ε_h=6.9mm/6.7m≈0.1%. The lateral earth pressures around the mid part of the retained height were found to vary by 30~50kPa annually (SC1 and SC2, at depths of 3.5m and 6.2m respectively). Assuming that London Clay has similar stiffness behaviour as Atherfield I Clay (Xu, 2004), this magnitude is found fairly close to the lateral stress change in the cyclic stress path testing on stiff clay under a cyclic radial strain range of 0.1% (Figure 5.9). There was no obvious tendency for any build-up of lateral pressure after several years, which also agrees with the observations in this thesis.

Figure 7.4b shows the changes in the distributions of total lateral pressure over a period of 8 years. Despite some minor redistributions of stress, there was no significant change in the magnitude or distribution of total lateral stresses. This is supported by the measurement of each spade cell in Figure 7.4a and agrees with the findings in this research that temperature induced cyclic loading does not cause a significant build-up of lateral earth pressure for walls supporting clay.

The cut-and-cover tunnel at CTRL

Clark (2005) reported the results of field monitoring during and after construction of a 12m wide cut-and-cover tunnel at CTRL. The wall comprised 1.05m diameter contiguous bored piles at 1.35m centres. The retained height was 10m and the total length of the wall was 21m. The wall was propped by a permanent reinforced concrete prop at the crest and a base slab at the excavation level. The geology of this site is presented in Figure 7.5a. Construction was completed in March 2001, but the monitoring continued.

Figure 7.5b presents the lateral pressure variation at the mid part of the retained height in Atherfield I Clay (5.3m below the ground surface) after the construction. The lateral pressure varies closely with daily and annual temperature variation. The pressure reaches its maximum value in summer and minimum value in winter. Careful examination of the data showed that the annual lateral pressure variation is about 15kPa.

Temperature gauges were attached to the surfaces of the top concrete prop and an annual temperature range of about 35°C was derived. Assuming $\alpha = 12\times10^{-6}/^{o}C$, the annual movement of the wall crest can be approximated as 2.5mm. The wall was propped at both the crest and the excavation level. If the wall is still assumed to rotate around a pivot 1m above its toe, a lower bound of the annual horizontal strain change in the soil at the mid retained height can be approximated as ε_h=2.5mm/20m≈0.012%. According to the stiffness behaviour of specimens AC2 and AC3 (Figure 5.17), a lateral strain change of 0.012% would cause a lateral stress change of 12kPa, which is fairly close to the field monitoring observations (15kPa). After the first 4 years after construction, no obvious build-up of lateral stress has been observed (Figure 7.5b).

The above evidence supports the findings of this research that daily and annual temperature changes will cause variations of lateral earth pressures in stiff clay behind

integral abutments, the magnitude of which depend largely upon the stiffness of the soil. However, an accumulation of lateral earth pressure with cycling is not expected.

7.2.2 Comparison of test results for sand with previous research

In this section, the findings of this research for coarse sand will be compared with previous research on granular backfill behind integral abutments, including both field monitoring and laboratory testing.

During field monitoring, it was found that the lateral pressure of granular backfill behind an integral abutment drops to an active value in the winter (*e.g.* Darley *et al.*, 1996 and 1998; Barker & Carder, 2000 and 2001; Broms & Ingleson, 1971 and 1972). This is consistent with the findings that only very small strain is needed for the coarse sand to reach the active state.

Most field investigations have not provided clear evidence of the highest values of earth pressure likely to be exerted behind an integral abutment, due to the short periods of monitoring. However, some investigations have found that the peak lateral earth pressure reached a very high value, even approaching the passive state after the first few years. This was observed behind shallow integral abutments at the ends of two bridges by Broms & Ingleson (1971) and Hoppe *et al.* (1996) respectively, as discussed in Section 2.3.3.

Further evidence emerges from Moore (1985), who monitored a conventional spill-through abutment (Figure 7.6a) at the end of a 78 m long concrete deck at Wisley, Surrey, UK. Medium to fine sand was backfilled and compacted behind the abutments, which had a height of about 9m. It is thought that the bearings between the abutment and the deck became damaged and the joints became jammed during the construction stage (Moore, 1985). As a consequence, the abutment became an "integral abutment" in reality and was forced to move along with temperature-induced bridge deck length change. The lateral earth pressure behind the abutment was found to vary closely with seasonal temperature variation. In the first warm summer after the bridge opening, the recorded lateral earth pressure coefficient approached or even exceeded the estimated passive Rankine earth pressure (K_p=3.69, φ=35°) behind the capping beam, which had a height of about 3.3m (Figure 7.6b). The lateral pressures behind the columns were relatively constant. This was expected as there was a gap of about 3.2m between two adjacent columns, so that the soil behind the column had much less restriction for deformation.

Cosgrove & Lehane (2003) also observed a progressive increase of maximum lateral pressure in their small scale test on loose sand. In their test, the ratio of the model wall height to the sand particle size was large, which gave a markedly different finding from previous small scale tests (see Section 2.3.1). The model abutment was 1000mm high, backfilled by dry siliceous sand with a mean particle size (D_{50}) of 0.22mm at an initial relative density of 21%. They noted a progressive increase of K_{max} with cycles, which reached the passive state after 200~500 cycles (Figure 7.7). This is consistent with the observations made in this research that the lateral earth pressure of loose sand behind integral abutments can eventually reach the passive state.

The above evidence demonstrates that the lateral pressure of granular backfill may increase to the passive state behind integral abutments in the field, as observed in this research.

7.3 Implications for integral abutment design

Based on the findings of this research, implications for the design of embedded integral abutment and frame integral abutment will be discussed here.

7.3.1 Design of embedded integral abutment in clay

In this research, radial strain-controlled cyclic stress path tests have been carried out on undisturbed Atherfield I Clay specimens, using stress path and strain levels similar to those to be expected in a soil element at mid retained height behind a full-height embedded abutment.

The test results have shown that daily and annual temperature change will cause significant horizontal stress variations behind embedded integral bridge abutments. The magnitude of these stress changes will depend largely upon the horizontal stiffness of the soil, which depends on strain level, effective stress level and path, and can be expected to change significantly over the range of horizontal strains behind embedded abutments in overconsolidated clay. Evaluation of soil stiffness therefore requires horizontal loading coupled with small-strain stiffness measurement.

However, a build-up of horizontal stress with daily or annual temperature cycles is not expected behind embedded integral abutments in clay. Neither the stress-strain behaviour nor the stiffness behaviour of stiff clay in this research was found to be obviously influenced by the cyclic loading over a wide range of strain levels.

A simplified method is proposed to estimate the horizontal stress change behind embedded integral abutments for the purpose of preliminary approximation, which is attached in Appendix B.

7.3.2 Design of frame integral abutment retained granular materials

Radial strain-controlled cyclic stress path tests have been carried out on coarse sand specimens (Leighton Buzzard B sand), and on glass ballotini, using stress path and strain levels similar to those to be expected in a soil element at mid height behind a full-height frame integral abutment.

Build-up of maximum horizontal stress with horizontal strain cycling has been observed for specimens of Leighton Buzzard Sand over a wide range of density. Once initiated, maximum stresses rose continuously, and approached the passive state.

Loose backfill is not recommended, as it will not change the tendency that the passive pressures will be approached eventually. In addition, loose backfill will undergo large settlement and bring serviceability problems.

The current design standard, BA 42, which connects the design value of K with the abutment movement magnitude, significantly underestimates the largest lateral earth pressure that a backfilled frame integral abutment may experience over a bridge life-time.

This research suggests that horizontal pressure accumulation appears to be associated with irregular, but relatively rotund particle shape, and the rolling of particles close to or at the active stress state. Neither natural cohesive soil nor perfectly spherical glass ballotini showed significant signs of stress increase, for the wide range of strain ranges that were imposed. Therefore, one possible method to prevent the build-up of horizontal stress behind frame abutments might be to prevent the rolling of the backfill granular particles, *e.g.* by using soil cement. Further research is required to investigate this possible solution.

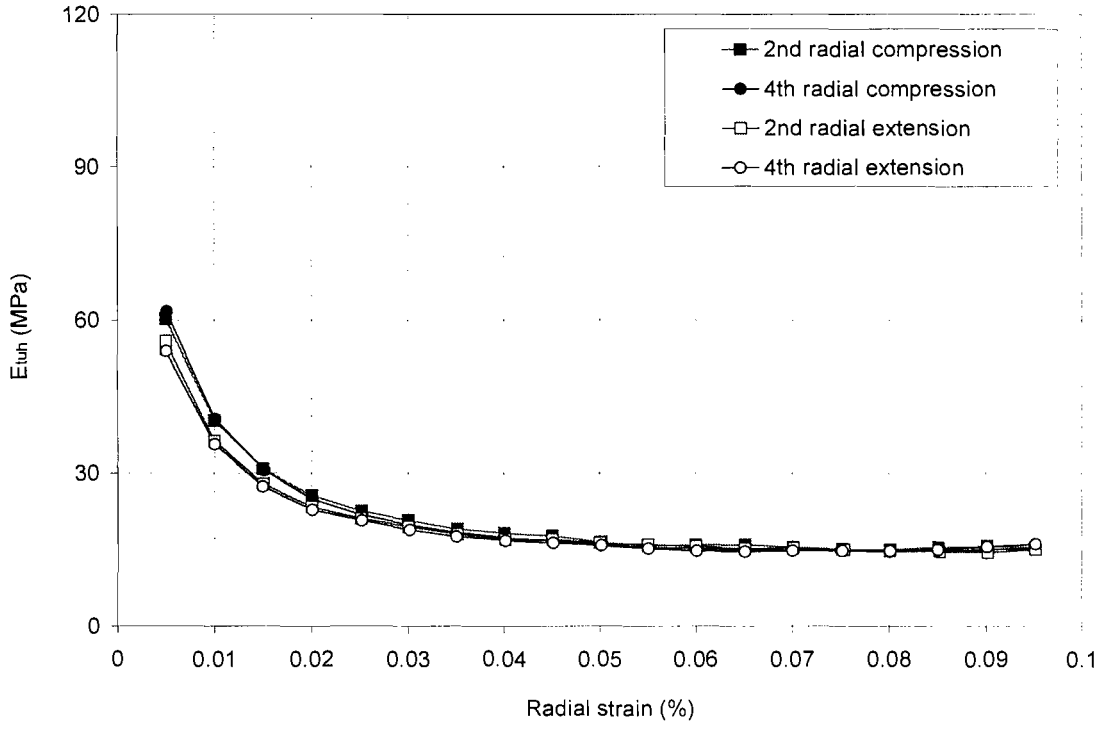

Figure 7.1 Undrained tangent horizontal Young's modulus for Atherfield I Clay specimen AC3 under a cyclic radial strain range of 0.1%

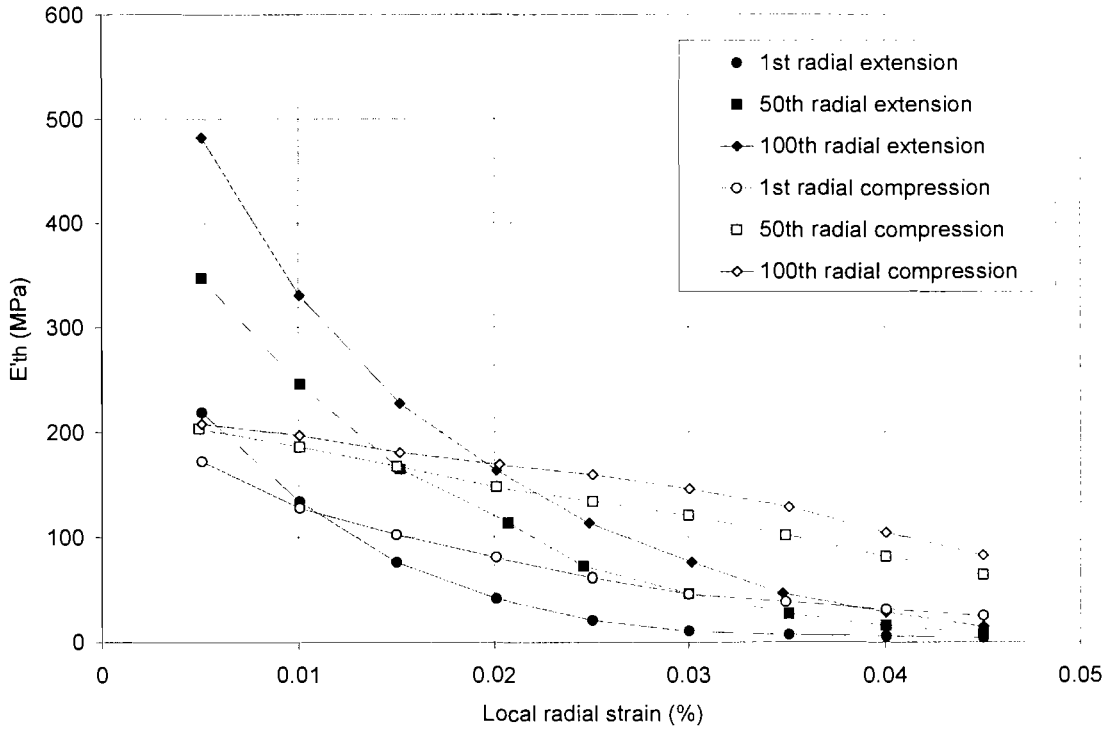

(a) Coarse sand specimen LBS1 under a cyclic radial strain range of 0.05%

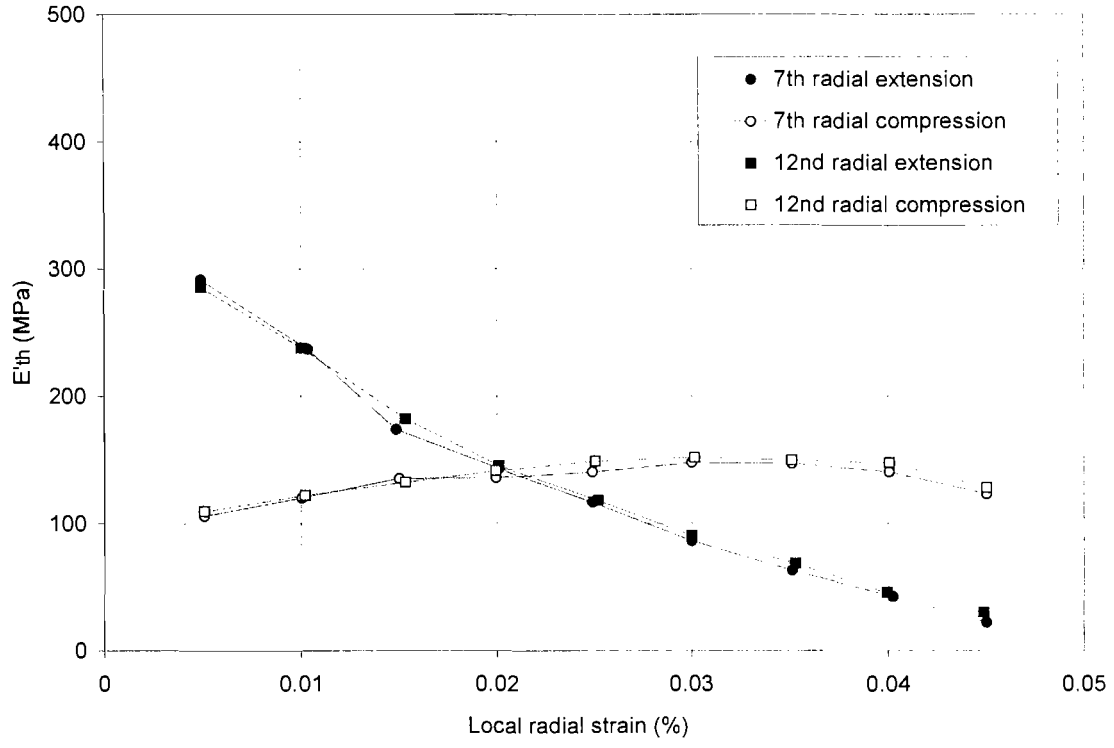

(b) Glass ballotini specimen G1 under a cyclic radial strain range of 0.05%

Figure 7.2 Drained tangent horizontal Young's modulus of granular materials

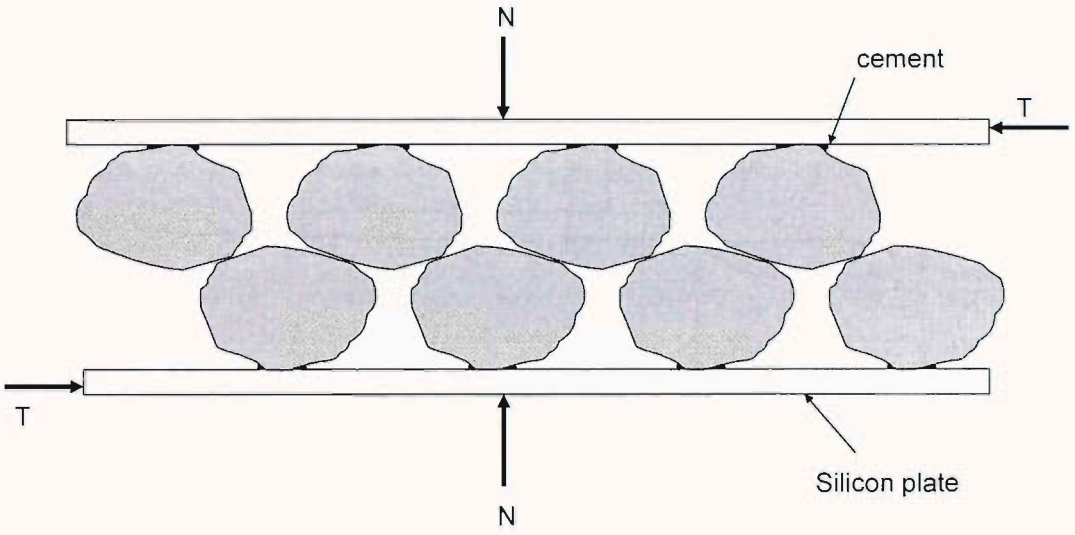

(a)

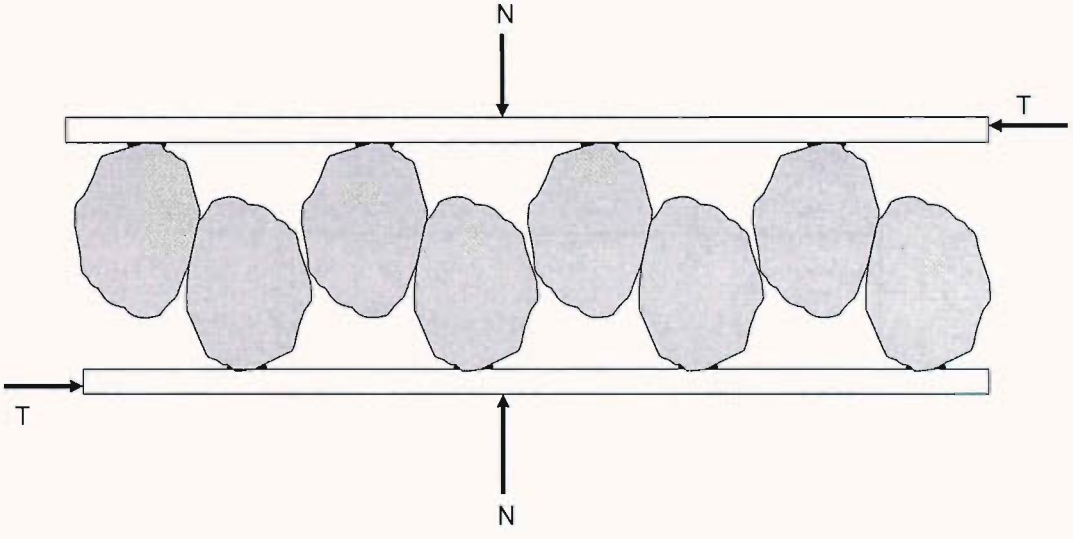

(b)

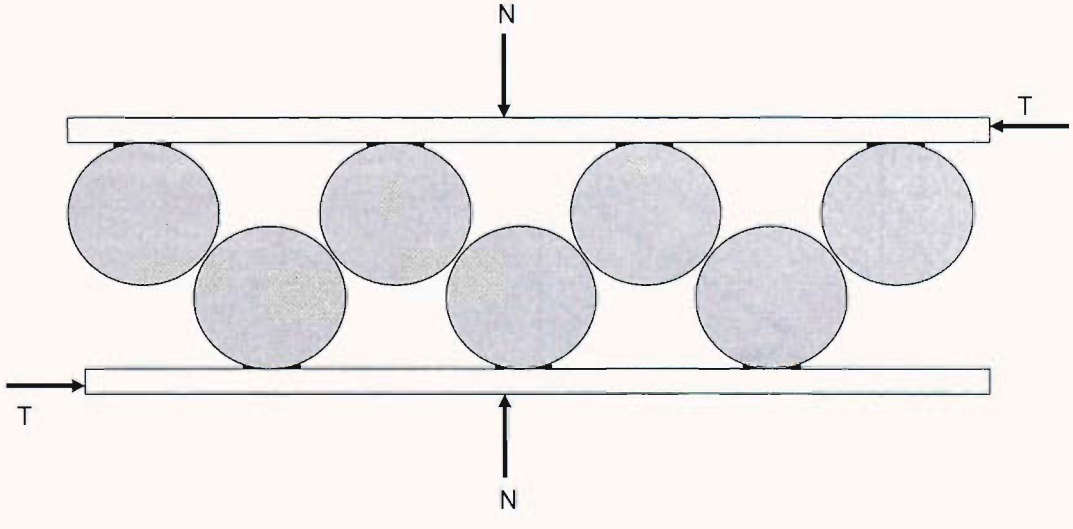

(c)

Figure 7.3 The influence of granular particle shape

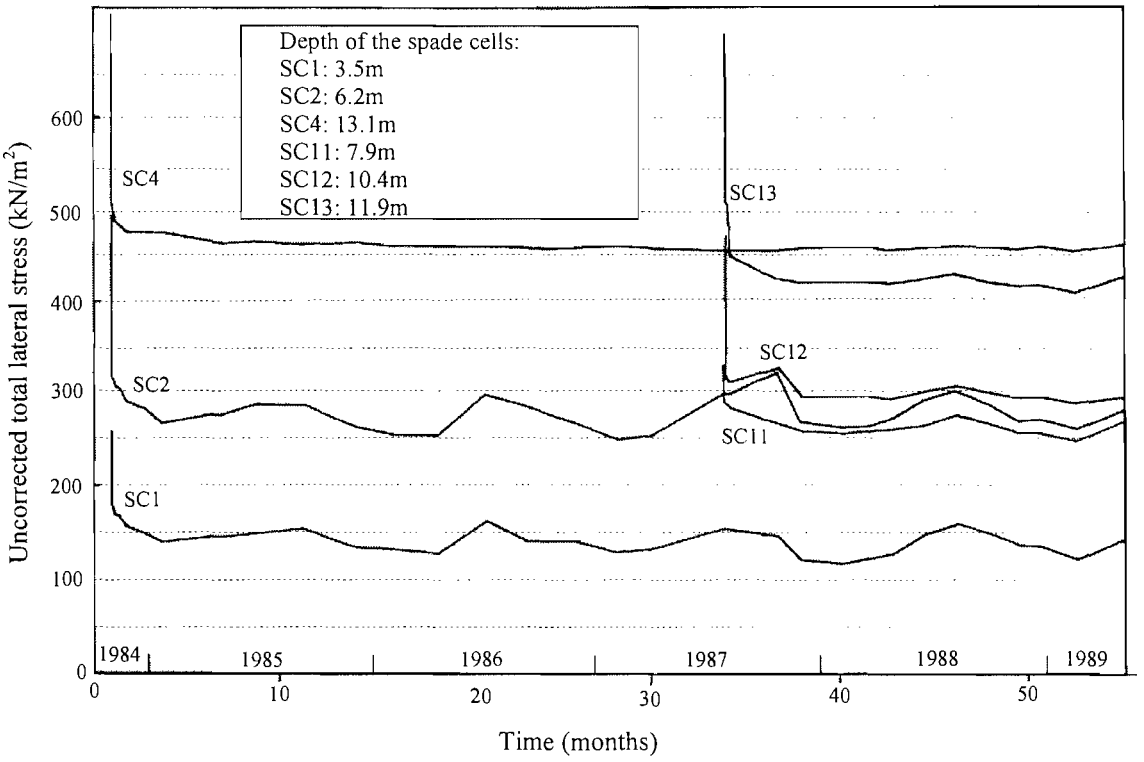

(a) Variation of spade cell readings at 1.5m behind the wall (Carder & Symons, 1990)

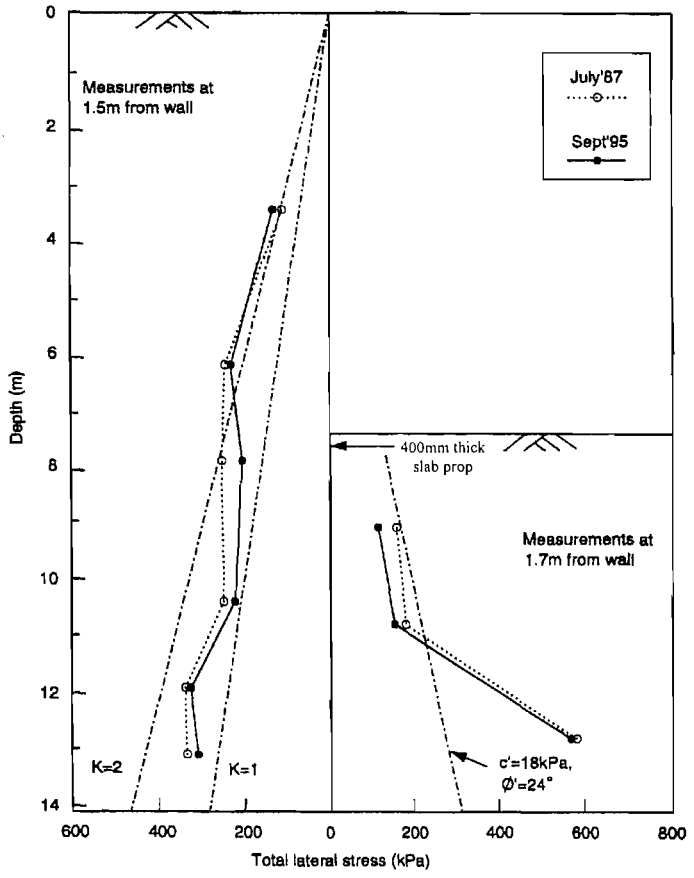

(b) Change in lateral stress distributions over 8 years (Carder & Darley, 1999)

Figure 7.4 The long term field monitoring on a propped retaining wall at New Malden

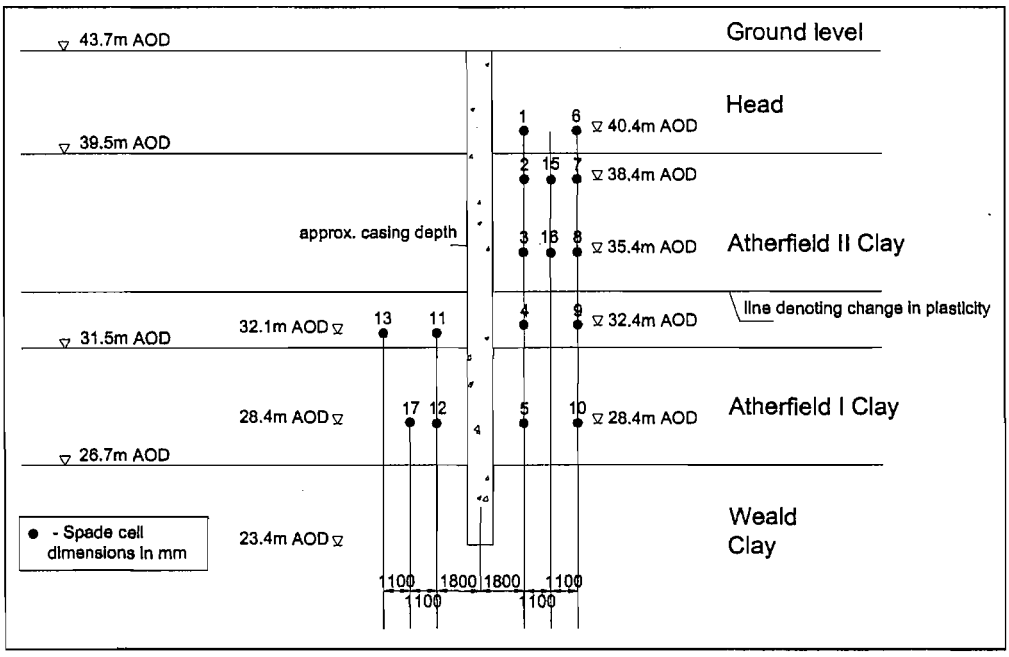

(a) Elevation showing the geology and spade cell locations

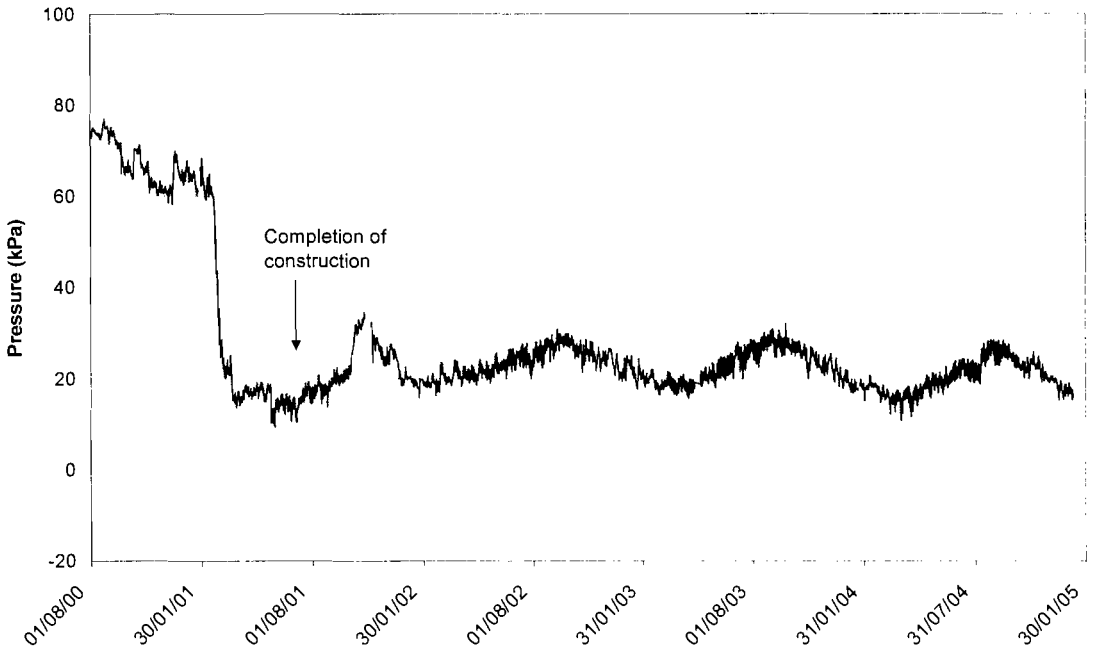

(b) The lateral earth pressure variation at the mid retained height (spade cell 2)

Figure 7.5 Field monitoring from the cut-and-cover tunnel (reproduced from Clark, 2005)

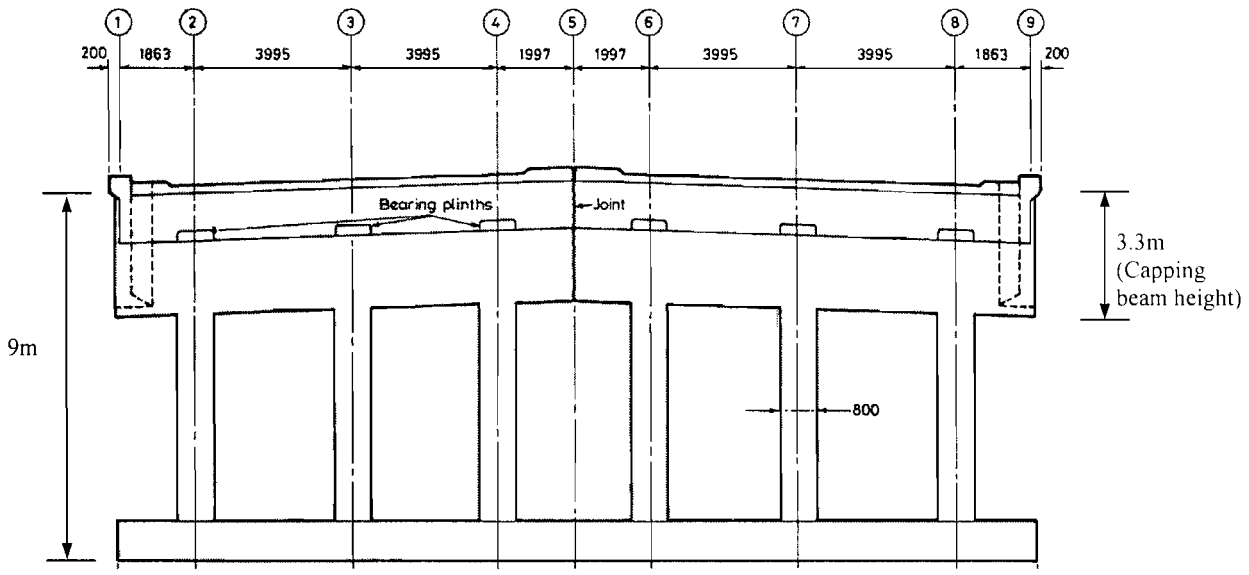

(a) Elevation of the spillthrough abutment

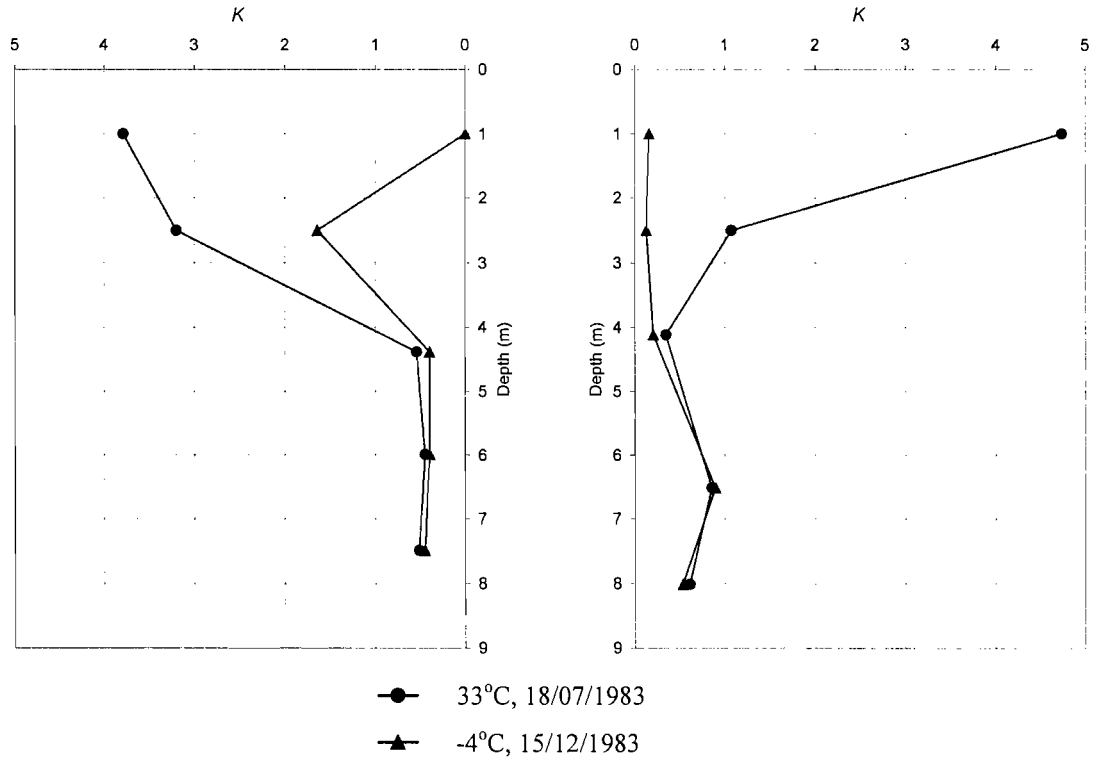

(b) Variation of the lateral earth pressure coefficient behind the abutments
(left: the south abutment E3; right: the north abutment A3)

Figure 7.6 Lateral earth pressures behind spillthrough abutments during summer and winter (reproduced from Moore, 1985)

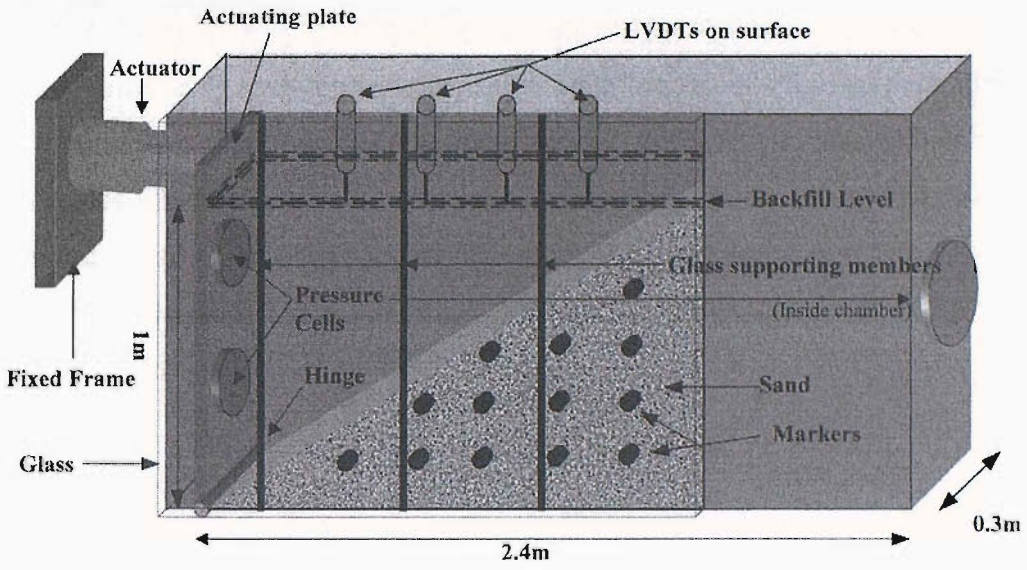

(a) The experiment apparatus (loose sand, D_r=21±2%)

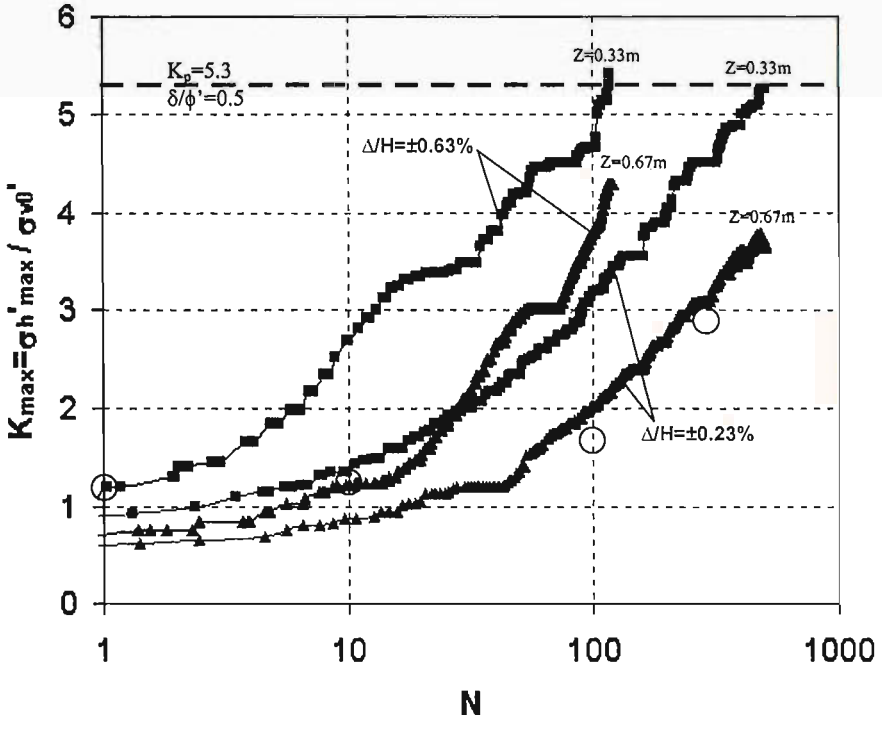

(b) Variation of maximum earth pressure coefficient with cycles
(z—the depth of pressure cell; Δ/H—the rotation the model wall;
O—the K_{max} value from the test on the loose sand specimen LBS1, Figure 6.10)

Figure 7.7 The small scale experiment by Cosgrove & Lehane (2003)

Chapter 8 Conclusions and recommendations

The main aim of this research is to investigate the behaviour of a representative soil element at mid retained height under temperature-induced cyclic loading behind two typical types of full-height integral abutments. One is an embedded abutment constructed in *in situ* stiff clayey ground, and the other is a frame abutment backfilled with granular materials. The major conclusions are presented here, following by recommendations for further work.

8.1 Conclusions

8.1.1 Integral abutments

Compared with conventional bridges, integral bridges have no bearings or joints between the decks and abutments, thus they can significantly reduce maintenance requirements and costs over the bridge life-time. The use of integral bridges has been encouraged over the past decade in the UK. However, because of the integral connection between the superstructure and the abutments, the integral abutments are forced to move with the deck length change caused by daily and annual variations in the effective bridge temperature. As a consequence, the soil behind the abutment is subjected to temperature-induced cyclic loading from the abutment, and uncertainties have arisen about the ultimate magnitude of the lateral earth pressure behind the integral abutments. To predict the lateral earth pressure behind integral abutments, a thorough understanding of the soil behaviour is required.

Previous research on the soil behaviour behind integral bridge abutments has mainly taken three forms: laboratory experiments (centrifuge tests or small scale model tests under normal gravity); field monitoring or numerical modelling. However, because of the complexity of the problem and limitations of previous research, the behaviour of soil behind integral abutments still remains unclear, imposing a major uncertainty on engineers. The current UK design standard, BA42 *The Design of Integral Bridges*, is widely believed to be unsatisfactory such that more research is needed. Furthermore, no research has been carried out on the magnitude of earth pressure behind integral abutments embedded in clayey ground, especially overconsolidated stiff clay, which is a typical ground condition in the UK.

8.1.2 Research methodology

Compared with other research methods, geotechnical laboratory stress path testing has been identified as a promising technique to investigate the fundamental behaviour of soil behind an integral abutment. For a given deformation or strain level, realistic stress changes will not be estimated unless appropriate stress paths are followed. External strain measurement will induce large errors at small strain levels, which can be overcome by local strain measurement. Time-dependent behaviour of soil (creep and stress relaxation) can influence the small strain stiffness measurement in the following stress excursion.

The total stress path of soil behind a smooth integral abutment can be idealized as a 135° stress path in the *s-t* space. The results from finite element analysis show that the change of soil stiffness had only marginal influence on the cyclic lateral strain range in the representative soil element. A simplified method based on a geostructural mechanism (Bolton & Powrie, 1988) was also used to estimate the cyclic lateral strain range, and the results were found to be similar to those from finite element analysis, especially for the embedded abutment.

An automated triaxial cyclic loading system has been developed based on a Bishop & Welsey hydraulic triaxial apparatus, with local strain and stress measurement. It was capable of performing radial strain-controlled cyclic loading tests on 100mm diameter specimen along a 135° stress path in the *s-t* space over a long period, detecting and correcting any possible errors automatically. The whole system was controlled by the control software, which was designed on a "loop" framework and utilised a volume control method.

8.1.3 Conclusions from tests on stiff clay

The behaviour of a representative stiff clay element behind an embedded integral abutment was investigated by carrying out radial strain-controlled cyclic stress path testing on undisturbed Atherfield I Clay specimens.

Undrained cyclic test results show that each strain excursion led to a change of horizontal stress. However, the stress-strain behaviour did not change with cycling. The stiff clay entered a resilient state after the first cycle of loading and there was no obvious build-up of maximum horizontal stress. The initial stress state had no obvious influence on the stress-strain behaviour.

The undrained stiffness of Atherfield I Clay was found to be strain level dependent and to exhibit high non-linearity. It can be expected to change significantly over the range of horizontal strains that can be expected behind typical embedded abutments in stiff clay. Under cyclic loading, the stiffness behaviour of Atherfield I Clay in each strain excursion remained unchanged. The maximum stiffness at small strains and the degradation rate of stiffness was found not to be affected significantly by the strain excursion direction, or by the number of cycles, previous cyclic radial strain range, or the stress path location. Strong anisotropy was found in stiffness of Atherfield I Clay, with a Young's modulus in the horizontal direction of about two times that in the vertical direction.

Drained cycles were also applied to an Atherfield I Clay specimen, which had a very low permeability. During loading and unloading with drainage, both volumetric and axial strains were recoverable, and there was no evidence of an increase in horizontal stress with cycling.

8.1.4 Conclusions from tests on granular materials

The behaviour of a representative soil element of granular materials behind a frame integral abutment was investigated by carrying out radial strain-controlled cyclic stress path testing on Leighton Buzzard B sand specimens and a glass ballotini specimen.

In the main test programme, for coarse sand over a wide range of densities (loose, dense and very dense) subjected to cyclic radial strain ranges similar to those to be expected in a soil element at mid height behind a typical frame integral abutment (0.05%, 0.1% and 0.2%), the maximum horizontal stress continued to build up towards the passive state without any sign that a resilient state would be reached. In contrast, the minimum horizontal stress experienced much smaller change and tended to a magnitude very close to or equal to the active value. The volume of loose sand and dense sand continued to decrease under all the three applied cyclic radial strain ranges. The rate of volume decrease was more significant for the loose sand. However, for the very dense sand under a larger cyclic radial strain range (0.1%), the volume was found to increase systematically with cycling. This implies that the build-up of the maximum horizontal stress is not necessarily associated with volumetric strain.

The location of imposed stress path was found to have an important influence on the stress-strain behaviour of sand, and it appears that the progressive increase of

maximum horizontal earth pressure was associated with the active state, and therefore with rotation of particles. During a special test on a glass ballotini specimen, no obvious accumulation of maximum horizontal stress was observed. Taken together, these results suggest that the build-up of horizontal stress in coarse sand was associated with non-spherical particle shape and the rolling of particles close to or at the active stress state.

The stiffness of coarse sand and glass ballotini was different during radial compression and radial extension. The stiffness of coarse sand increased significantly with cycling, though the small strain stiffness was found to be relatively stable immediately after being unloaded from the active state. In contrast, the stiffness behaviour of glass ballotini did not change obviously with cycling.

8.1.5 Conclusions from discussion

Particle shape (platy, sub-round and spherical) is thought to be responsible for the differences in stiffness and stress-strain behaviour of stiff clay, coarse sand and glass ballotini under cycling in this research. Elastic deformation of platy particles (*e.g.* bending or compressing) is thought to be a major feature for stiff clay under loading, resulting in a relatively low stiffness and no build-up of lateral stress. Movement (sliding or rolling) of particles dominates in granular materials under loading, leading to a relatively high stiffness. Furthermore, for coarse sand, the rolling of non-spherical particles during the active state changes the orientation of the particles, which may lead to a greater degree of inter-locking progressively, resulting in an increasing stiffness and a build-up of lateral stress.

The findings of this research were found to be supported by the results of long-term field monitoring on propped retained walls embedded in stiff clay (Carder & Symons, 1990; Carder & Darley, 1999; Clark, 2005), field monitoring on spillthrough abutments backfilled by granular materials (Moore, 1985) and small scale model tests (Cosgrove & Lehane, 2003).

Implication for integral abutment design has been discussed in this thesis. For embedded integral abutment in stiff clay, knowledge of the soil stiffness is of primary importance for prediction of the lateral earth pressure change due to temperature-induced straining. Evaluation of soil stiffness in the laboratory requires horizontal loading coupled with small-strain stiffness measurement.

For frame integral abutments, the possibility of a passive earth pressure in the long-term has to be taken into consideration. Loose backfill is not recommended, as it will not change the tendency that the passive pressures will be approached eventually. In addition, loose backfill will undergo large settlement and bring serviceability problems.

8.2 Recommendations for further work

This research has revealed that the stress-strain and stiffness behaviour of stiff clay will not change with cycling. Finite element analysis can be used to examine the interaction between stiff clay, embedded integral abutments and a bridge deck, and to study the detailed magnitude and distribution of lateral earth pressure behind an integral abutment. Three-dimensional effects may become important in soil-structure interaction (Bloodworth, 2002) and need to be considered. The soil model should be capable of simulating the small strain stiffness and its non-linearity in stiff clay.

The findings suggest that the build-up of horizontal stress observed for coarse sand was associated with non-spherical particle shape and the rolling of particles close to or at the active stress state. Therefore, one possible method to prevent the build-up of maximum lateral earth pressure in the granular backfill is to use soil cement, which can suppress the rolling of particles in theory. Radial strain-controlled stress path testing can be used to study the effectiveness of this technique, and to decide the suitable cement and the best content. The influence of cement content on the soil small strain stiffness can also be investigated.

The Discrete Element Method (DEM) is a powerful tool in detailed studies of the influence of particle shape on the mechanical behaviour of granular materials. Previous research in this area has concentrated in monotonic loading. Three-dimensional simulation is recommended to examine the particulate behaviour of granular materials during cycling that was observed in this research. DEM can also be used in theory to study the interaction between the granular backfill and the integral abutment at a whole system level, but the computing power required would be large.

Reference

Andersen, K. and Lauritzsen, R. (1988). Bearing capacity for foundation with cyclic loads, *Journal of Geotechnical Engineering*, ASCE, 114(5), 540-555.

Andersen, K., Pool, J.H., Brown, S.F. and Rosenbrand, W.F. (1980). Cyclic and static laboratory tests on Drammen clay, *Journal of Geotechnical Engineering*, ASCE, 106(GT5), 499-530.

Arsoy, S., Barker, R.M., and Duncan, J.M. (2002). *Experimental and analytical investigations of the piles and abutments of integral bridges*, Virginia Transportation Research Council, Final Report 02-CR6.

Atkinson, J.H., Richardson, D., Stallebrass, S.E. (1990). Effect of recent stress history on the stiffness of overconsolidated soil, *Géotechnique*, 47(2), 235-253.

Baldi, G., Hight, D.W., and Thomas, G.E. (1988). A re-evaluation of conventional triaxial test methods, *Advanced Triaxial Testing of Soil and Rock*, ASTM STP 9777.

Baligh, M.M. (1985). Strain path method, *Journal of Geotechnical Engineering*, ASCE, 111(9), 1108-1136.

Barden, L. and Sides, G. (1971). Sample disturbance in the investigation of clay structure, *Géotechnique*, 21(3), 211-222.

Barker, K.J. and Carder, D.R. (2000). *Performance of the two integral bridges forming the A62 Manchester road overbridge*, TRL report 436, Transport Research Laboratory, Crowthorne, Berks.

Barker, K.J. and Carder, D.R. (2001). *Performance of an integral bridge over the M1-A1 Link Road at Bramham Crossroads*, TRL report 521, Transport Research Laboratory, Crowthorne, Berks.

Bica, A. V. D. (1991). *A study of free embedded cantilever walls in granular soil*, PhD thesis, University of Surrey, Guildford.

Biddle, A.R., Iles, D.C. and Yandzio, E.D. (1997). *Integral steel bridges: Design guidance*, Steel Construction Institute, Ascot, Berkshire, Publication number: P163.

Bishop, A. W. (1954). Correspondence on shear characteristics of a saturated silt, measured in triaxial compression, *Géotechnique*, 4(1), 43-45.

Bishop, A.W. (1966). The strength of soils as engineering materials, *Géotechnique*, 16 (2), 89-130.

Bishop, A.W., and Henkel, D.J. (1962). *The Measurement of Soil Properties in the Triaxial Test,* second edition, Edward Arnold, London.

Bishop, A.W. and Lovenbury, H.T. (1969). Creep characteristics of two undisturbed clays, *Proceedings of the Seventh International Conference on Soil Mechanics and Foundation Engineering*, Mexico City, Vol.1, 29-37.

Bishop, A.W. and Wesley, L.D. (1975). A hydraulic triaxial apparatus for controlled stress path testing, *Géotechnique*, 25(4), 657-670.

Bjerrum, L. (1973) Geotechnical problem involved in foundations of structures in the North Sea, *Géotechnique*, 23(3), 319-358.

Bloodworth, A.G. (2002). *Three-dimensional analysis of tunnelling effects on structures to develop design methods*, PhD thesis, University of Oxford.

Bolton, M.D. and Powrie, W. (1988). Behaviour of diaphragm walls in clay prior to collapse, *Géotechnique*, 38(2), 167-189.

Britto, A.M. and Gunn, M.J. (1987). *Critical state soil mechanics via finite elements*,

Chichester: Ellis Horwood.

Broms, B.B.(1971). Lateral pressure due to compaction of cohesionless soils, *Proceedings of the Fourth Budapest Conference on Soil Mechanics and Foundation Engineering*, Budapest, 373-384.

Broms, B.B. and Ingleson, I. (1971). Earth pressure against the abutments of a rigid frame bridge, *Géotechnique*, 21(1), 15-28.

Broms, B.B. and Ingleson, I. (1972). Lateral earth pressure on a bridge abutment, *Proceedings of the Fifth European Conference on Soil Mechanics and Foundation Engineering*, Madrid, Vol. 1, 117-123.

Brown, S.F. (1996). Soil mechanics in pavement engineering, *Géotechnique*, 46(3), 383-425.

Brown, S.F., Loach, S.C. and O'Reilly, M.P. (1987). *Repeated loading of fine grained soils*, TRRL Contractor Report 72.

Brown, S.F. & Selig, E.T. (1991). The design of pavement and rail track foundations, in *Cyclic loading of soils: from theory to design*, Blackie and Son, Glasgow, 249-305.

BS 1377 (1990). *British Standard Methods of test for soils for civil engineering purposes,* British Standard Institution, London.

Burland, J. B. (1989). Small is beautiful—the stiffness of soils at small strains, *Canadian Geotechnical Journal*, Vol. 26, 499-516.

Burland, J.B. and Hancock, R.J.R. (1977). Underground car park at the House of Commons, London: Geotechnical aspects, *The Structural Engineer*, 55(2), 87-100.

Burland, J.B., Simpson, B. and St. John, H.D. (1979). Movements around excavations in

London Clay, *Proceedings of the Seventh European Conference on Soil Mechanics and Foundation Engineering*, Brighton, Vol. 1, 13-29.

Burland, J.B. and Symes, M. (1982). A simple axial displacement gauge for use in the triaxial apparatus, *Géotechnique*, 32(1), 62-65.

Burke, M.P., Jr., and Gloyd, C.S. (1997). Emergence of semi-integral bridges, *Transportation Research Record*, 179-186.

Callister, W.D. (2000). *Materials Science and Engineering: An Introduction*, John Wiley & Sons.

Card, G.B. and Carder, D.R. (1993). *A literature review of the geotechnical aspects of integral bridge abutments,* TRL Project Report 52, Transport Research Laboratory, Crowthorne, Berks.

Carder, D.R. and Card, G.B. (1997). *Innovative structural backfills to integral bridge abutments*, TRL Report 290, Transport Research Laboratory, Crowthorne, Berks.

Carder, D.R. and Darley, P. (1999). *The long term performance of embedded retaining walls*, TRL Report RP381, Transport Research Laboratory, Crowthorne, Berks.

Carder, D.R. and Symons, I.F. (1990). *Long term performance of a propped retaining wall embedded in stiff clay*, TRL Report RP273, Transport Research Laboratory, Crowthorne, Berks.

Cheng, Y.P., Bolton, M.D. and Nakata, Y. (2004). Crushing and plastic deformation of soils simulated using DEM, *Géotechnique*, 54(2), 131-141.

Clark, J. (2005). *Lateral stresses on in situ retaining walls in overconsolidated deposits*, forthcoming PhD thesis, University of Southampton.

Clark, J., Richards, D.J. and Powrie, W. (2004). Wall installation effects - preliminary findings from a field study at the CTRL, Ashford, *Advances in geotechnical engineering: The Skempton Conference*, Thomas Telford, London. Vol. 2, 691-699.

Clayton, C.R.I., Edwards, A. and Webb, D.L. (1991). Displacements in London clay during construction, *Proceedings of the Tenth European Conference on Soil Mechanics and Foundation Engineering*, Florence, Vol. 2, Balkema, Rotterdam, 791-796.

Clayton, C.R.I. and Heymann, G. (2001). The stiffness of geomaterials at very small strains, *Géotechnique*, 51(3), 245-256.

Clayton, C.R.I. and Khatrush, S.A. (1986). A new device for measuring local axial strains on triaxial specimens, *Géotechnique*, 36(4), 593-597.

Clayton, C.R.I., Mathews, M.C. and Simons, N.E. (1995). *Site Investigation*, second edition, Blackwell.

Clayton, C. R. I. and Milititsky, J. (1983). Installation effects and the performance of bored piles in stiff clay, *Ground Engineering*, 17-22.

Clayton, C.R.I., Milititsky, J., and Woods, R.I. (1993). *Earth Pressure and Earth-Retaining Structures*, second edition, Blackie Academic & Professional.

Clayton, C.R.I. and Symons, I.F. (1992). The pressure of compacted fill on retaing walls, *Géotechnique*, 42(1), 127-130.

Clayton, C.R.I., Theron, M. and Vermeulen, N.J. (2004). The effect of particle shape on the behaviour of gold tailing, *Advances in Geotechnical engineering: the Skempton Conference,* Thomas Telford, London, Vol. 1, 393~404.

Cole, K.W. and Burland, J.B. (1972). Observations of retaining wall movements associated with a large excavation, *Proceedings of the Fifth European Conference on Soil Mechanics and Foundation Engineering*, Madrid, Vol. 1, 445-453.

Cosgrove, E.F. and Lehane, B.H. (2003). Cyclic loading of loose backfill placed adjacent to integral bridge abutments, *International Journal of Physical Modelling in Geotechnique*, Vol. 3, 9-16.

Cosgrove E., Lehane B.M. and Ng C W.W. (2001). Sand tested under cyclic triaxial conditions with constant radial stress, *Proceedings of the Fifteenth International Conference on Soil Mechanics and Foundation Engineering*, Istanbul, Vol. 1, 63-66.

Cresswell, A., Barton, M.E. and Brown, R. (1999). Determining the maximum density of sands by pluviation, *Geotechnical Testing Journal*, 22(4), 324-28.

Cuccovillo, T., and Coop, M. R. (1997). The measurement of local axial strains in triaxial tests using LVDTs, *Géotechnique*, 47(1), 167–171.

Darley, P., Carder, D.R. and Alderman, G.H. (1996). *Seasonal thermal effects on the shallow abutment of an integral bridge in Glasgow*, TRL report 178, Transport Research Laboratory, Crowthorne, Berks.

Darley, P., Carder, D.R. and Barker, K.J. (1998). *Seasonal thermal effects over three years on the shallow abutment of an integral bridge in Glasgow*, TRL report 344, Transport Research Laboratory, Crowthorne, Berks.

Darley, P. and Carder, D.R. (1998). *Consultation document on suitability tests for stress absorbing layers behind integral bridge abutments,* TRL report 328, Transport Research Laboratory, Crowthorne, Berks.

Davies, T.G. (1991) Machine foundations, in *Cyclic loading of soils: from theory to design*, Blackie and Son, Glasgow, 367-410.

Emerson, M. (1973). *The calculation of the distribution of temperature in bridges*, TRRL Report 561, Transport Research Laboratory, Crowthorne, Berks.

Emerson, M. (1976). *Bridge temperatures estimated from the shade temperature*, TRRL Report LR696, Transport Research Laboratory, Crowthorne, Berks.

England, G.L., Tsang, C.M. and Bush, D. (2000). *Integral Bridges - A Fundamental Approach to the Time Temperature Loading Problem,* Thomas Telford, London.

England, G.L. and Tsang, C.M.(2001). *Towards the Design of Soil Loading for Integral Bridges*, Invited Keynote Address, Annual Conference of the Concrete Bridge Development Group, Magdalene College, Cambridge, 29 March, 2001.

Gaba, A.R., Simpson, B., Powrie, W. and Beadman, D.R. (2003). *Embedded retaining walls—guidance for economic design*, CIRIA Report C580.

Geotechnical Design Basis Report (1997). *Channel Tunnel Rail Link Technical Report*, No. 440-RUP-LCEEH-00043-AA.

Gilboy, G. (1928). The compressibility of sand-mica mixtures, *Proceeding of A.S.C.E.*, Part 1, 555~568.

Goh, D. (2001). *The behavior of shallow abutments of integral bridges*, Ph.D thesis, University of Birmingham.

Goto, S., Tatsuoka, F., Shibuya, S., Kim, Y.S. and Sato, K. (1991). A simple gauge for local small strain measurements in the laboratory, *Soils and Foundations*, 31(1), 169-180.

Graham, J. and Houlsby, G.T. (1983). Elastic anisotropy of a natural clay, *Géotechnique*, 33(2), 165-180.

Green, P.A. (1972). Some aspects of the foundation design for the Commercial Union Building, *Proceedings of Symposium on Interaction of Structure and Foundation*, Birmingham, 118-130.

Head, K.H. (1986). *Manual of soil laboratory testing, Volume 3: Effective stress tests*, Pentech Press, London.

Heymann, G. (1998). *The stiffness of soils and weak rocks at very small strains*, PhD thesis, University of Surrey, Guildford.

Hight, D. (1986) Laboratory testing: assessing BS 5930, *Geological Society, Engineering Geology Special Publication*, No.2, 43-58.

Hight, D. W., Bennell, J. D., Chana, B., Davis, P. D., Jardine, R. J. and Porovic, E. (1997). Wave velocity and stiffness measurements of the Crag and Lower London tertiaries at Sizewell, *Géotechnique*, 47(3), 451-474.

Hight, D. W., Gens, A. and Symes, M. J. (1983). The development of a new hollow cylinder apparatus for investigating the effects of principal stress rotation in soils, *Géotechnique*, 33(4), 355-383.

Hight, D.W. and Leroueil, S. (2002). Characterisation of soils for engineering purposes, *Proceedings of the Conference on Characterisation and Engineering Properties of Nature Soils*, Singapore, Vol. 1, 29-254, Balkema, Lisse.

Highway Agency (1995). BD 57 *Design for durability*, DMRB 1.3, HMSO, London.

Highway Agency (1996). BA 42 *The design of integral bridges*, DMRB 1.3, HMSO, London.

Highway Agency (2001). BD 37 *Loads for highway bridges,* DMRB 1.3, HMSO, London.

Hird, C.C. and Young P.C.Y. (1989). The use of proximity transducers for local strain measurements in triaxial tests, *Geotechnical Testing Journal*, 12(4), 292-296.

Hird, C. C. and Pierpoint, N. D. (1997). Stiffness determination and deformation analysis for a trial excavation in Oxford Clay, *Géotechnique*,47(3), 665-692.

Hooper, J.A. (1974). Observation on the behaviour of a piled-raft foundation on London Clay, *Proceedings of the Institute of Civil Engineers, Geotechnical Engineering*, 55(2), 547-552.

Hoppe, E. J. and Gomez, J.P. (1996). *Field study of an integral backwall bridge*, Virginia Transportation Research Council Final Report 1996.

Holubec, I. and D'Appolonia, E. (1973). Effect of particle shape on the engineering properties of granular soils. *ASTM STP523*, 304-318.

Horn, M.R. (1969). The behaviour of an assembly of round, rigid cohesiveless particles, *Proceedings of the Royal Society*, Vol. 310 of A, 21-34

Ingold, T. S. (1979). The effects of compaction on retaining walls, *Géotechnique,* 29(3), 265-283.

Ishihara, K. (1993). Liquefaction and flow failure during earthquakes, *Géotechnique*, 43(3), 351-415.

Iwashita, K. and Oda, M. (1998). Rolling resistance at contacts in the simulation of shear band development by DEM, *Journal of Engineering Mechanics*, ASCE Vol. 124, 285–292.

Jardine, R.J. (1991). The cyclic behaviour of offshore piles, in *Cyclic loading of soils: from theory to design*, Blackie and Son, Glasgow, 1-18.

Jardine, R.J. (1992). Some observations on the kinematic nature of soil stiffness, *Soils and Foundations*, 32(2), 111–124.

Jardine, R.J., Symes M J. and Burland, J.B. (1984). The measurement of soil stiffness in the triaxial apparatus, *Géotechnique*, 34(3), 323-340.

Jardine, R.J., Fourie, A.B., Maswoswse, J. and Burland, J.B. (1985). Field and laboratory measurements of soil stiffness, *Proceedings of the Eleventh International Conference on Soil Mechanism and Foundation Engineering*, San Francisco, Vol. 2, 511-514.

Jardine, R.J., Potts, D.M., Fourie, A.B. and Burland, J.B. (1986). Studies of the influence of non-linear characteristics in soil-structure interaction, *Géotechnique*, 36(3), 377-396.

Jardine, R.J., Potts, D.M., St John, H.D. and Hight, D.W. (1991). Some practical applications of a non-linear ground model, *Proceedings of the tenth European Conference on Soil Mechanics and Foundation Engineering*, Florence, Vol. 1, 223-228.

Khatrush S.A. (1986). *Yielding of a fine sand in triaxial stress space*, PhD thesis, University of Surrey.

Koerner, R.M. (1970). Effect of particle characteristics on soil strength, *Journal of Soil Mechnics and Foundation Division,* ASCE, 96(SM4):1221-1234.

Lade, P.V. and Duncan, J.M. (1975). Stress-path dependent behaviour of cohesionless soil, *Journal of the Geotechnical Engineering Division*, ASCE, 51-68

Lambe, T.W. (1967). Stress path method, *Journal of soil mechanics and foundation division*, ASCE, 93(SM6), 309-331.

Lambe, T.W. and Marr, W. A. (1979). Stress path method: second edition, *Journal of geotechnical engineering*, ASCE, 105(GT6), 727–738.

Lambe, T.W. and Whitman R.V. (1979). *Soil Mechanics*, SI Version, John Wiley & Sons.

Lehane, B.M. (1999). Predicting the restraint provided to integral bridge deck expansion, *Proceeding of the Twelfth European Conference on Soil Mechanics and Geotechnical Engineering*, Amsterdam, Vol. 2, 797-802.

Lekarp, F., Isacsson, U. and Dawson, A.R. (2000). State of the art II: Permanent strain response of unbound aggregates, *Journal of the Transportation Engineering Division*, ASCE, Vol. 126(1), 76-84.

Lin, X. and Ng, T.T. (1997). A three-dimensional discrete element model using arrays of Ellipsoids, *Géotechnique*, 47(2), 319~329.

Mair, R. J. (1993). Developments in geotechnical engineering research: applications to tunnels and deep excavations, Unwin Memorial Lecture 1992, *Proceedings of the Institute of Civil Engineers, Civil Engineering*, 3, 27~41.

Marr, W.A. and Christian, J.T. (1981). Permanent displacements due to cyclic wave loading, *Journal of the Geotechnical Engineering Division*, ASCE, 107(GT8), 1129-1149.

Menzies, B.K., Sutton, H. and Davies, R.E. (1977). A new system for automatically simulating K_o consolidation and K_o swelling in the conventional triaxial cell, *Géotechnique*, 27(4), 593-596.

Mirghasemi, A., Rothenburg, L. and Matyas, E. (2002). Influence of particle shape on engineering properties of assemblies of two-dimensional polygon-shaped particles, *Géotechnique*, 52(3), 209-217.

Mitchell, J.K. (1993). *Fundamentals of soil behaviour*, second edition, John Wiley & Sons.

Moore, S.R. (1985). *Earth pressures on spillthrough abutments*, PhD thesis, University of Surrey.

Mundegar, A.K. (1997) *An investigation into the effects of platy mica particles on the behaviour of sand*, M.Sc Dissertation, Imperial College, London.

Newland, P.L. and Allely, B.H. (1957). Volume changes in drained triaxial tests on granular materials, *Géotechnique*, 7(1), 17–34.

Ni, Q. (2003). *Effects of particle properties and boundary conditions on soil shear behaviour 3-D numerical simulations*, PhD thesis, University of Southampton.

Nicholson, B.A. (1997). *Integral bridges—report of a study tour to North America*,

Concrete Bridge Development Group, Crowthorne, Berkshire.

Oda, M., Konishi, J., and Nemat-Nasser, S. (1982). Experimental micromechanical evaluation of strength of granular materials: effect of particle rolling, *Mechanics of Granular Materials*, Vol. 1, 269–283.

Olson, R.E. and Mesri, G. (1970). Mechanisms controlling the compressibility of clay, *Journal of the Soil Mechanics and Foundations Division, ASCE*, **96**(SM6): 1863–1878.

Padfield, C. J. and Mair, R. J. (1984). *Design of retaining walls embedded in stiff clay*, CIRIA Report 104.

Powrie, W. (1985). Discussion on Fifth Geotechnique Symposium: The performance of propped and cantilevered rigid walls, *Géotechnique*, 45(4), 546-548.

Richardson, D. (1988) *Investigations of threshold effects in soil deformations*, PhD thesis, City University, London.

Rowe, P.W. (1962). The stress-dilatancy relation for static equilibrium of an assembly of particles in contact, *Proceedings of the Royal Society*, Vol. 269 of A, 500-527.

Santamarina, J.C. and Cho, G.C. (2004). Soil behavior: the role of particle shape, *Advances in geotechnical engineering: The Skempton Conference*, Thomas Telford, London, Vol. 1, 604-617.

Santamarina, J.C. and Cascante, G. (1998). Effect of surface roughness on wave propagation parameters, *Géotechnique*, 48(1), 129-137.

Santamarina, J.C., Klein, K.A. and Fam, M.A. (2001). *Soils and Waves: Particulate Materials Behavior, Characterization and Process Monitoring*, John Wiley & Sons.

Shaw, P. (1980). *Stress-strain relationships for granular materials under repeated loading*, PhD thesis, University of Nottingham

Singh, A. and Mitchell, J.K. (1968). General stress-strain-time function for soils, *Journal of soil mechanics and foundation division*, ASCE, 102(GT4), 187-301.

Simpson, B. (1992a). Retaining structures: displacement and design, *Géotechnique*, 42(4), 541-576.

Simpson, B. (1992b). Development and application of a new soil model for prediction of ground movements, *Proceedings of Worth Memorial Symposium*, Oxford. 628-643.

Smith, P. R., Jardine, R. J. and Hight, D. W. (1992). The yielding of Bothkennar clay, *Géotechnique*, 42(2), 257-274.

Skinner, A. (1969). A note on the influence of interparticle friction on the shearing strength of a random assembly of spherical particles, *Géotechnique*, 19(1), 150-157.

Skempton, A.W. (1953). The colloidal "activity" of clays, *Proceedings of the Third International Conference on Soil Mechanism and Foundation Engineering*, Vol. 1, 57-61.

Skempton, A.W. (1961). Effective stress in soils, concrete and rocks, *Pore Pressure and Suction in Soils*, Butterworths, London.

Sodha, V. (1974). *The stability of embankment dam fills of plastic clays*, MPhil thesis, Imperial College, University of London

Springman, S. M., Norrish, A. and Ng, C.W.W. (1996). *Cyclic loading of sand behind integral bridge abutments*, Transport Research Laboratory Project Report 146.

Stallebrass, S. (1990). *The effect of recent stress history on the deformation of overconsolidated soils*, PhD thesis, City University, London

Stallebrass, S.E. and Taylor, R.N. (1997). Development and evaluation of a constitutive model for the prediction of ground movements in overconsolidated soils, *Géotechnique*, 47(2), 235-253.

Symons, I. F. and Clayton, C. R. I. (1991). Earth pressures on backfilled retaining walls, *Ground Engineering*, 25(3), 26-34.

Tapper L. and Lehane B.M. (2004). Lateral stress development on integral bridge abutments, *Proceedings of the Eighteenth Australasian Conference on Mechanics of Structures and Materials*, Perth.

Tedd P., Chard B.M., Charles J.A. and Symons 1.F. (1984). Behavior of a propped embedded retaining wall in stiff clay at Bell Common Tunnel, *Géotechnique*, 34(4), 513-532.

Terzaghi, K., and Ralph, B. Peck (1948). *Soil Mechanics in Engineering Practice*, John Wiley and Sons, New York.

Thornton, C. (1997). Force transmission in granular media, *KONA Powder and Particle*, Vol. 15, 81–90.

Wallbank, J., (1989). *The performance of concrete in bridges: a survey of 200 highway bridges*, HMSO, London.

Way, J.A. and Yandzio, E. (1997). *Integral steel bridges: design of a single-span bridge - worked example*, Steel Construction Institute P180.

Wong, R.T. and Authur, J.R.F. (1986). Sand sheared by stresses with cyclic variations in direction, *Géotechnique*, 36(2), 215-226.

Wood, D.M. and Nash, D. (2000). Earth pressures on an integral bridge abutment: a numerical case study, *Soils and Foundations*, 40(6), 23-38.

XU, M. (2004). *The soil behaviour behind an embedded integral abutment*, Transfer Report, University of Southampton.

Vucetic, M. (1995). Cyclic threshold shear strains in soils, *Journal of Geotechnical Engineering*, ASCE, 130(1), 58-70.

Vucetic, M. and Dobry, R. (1991). Effect of soil plasticity on cyclic response, *Journal of Geotechnical Engineering*, ASCE, 117(1), 89-107.

Appendix A

Computer Program for Radial Strain-Controlled Cyclic Stress Path testing

```
'-------------------------------------------------------------------------------------------------
'---                                                                                           ---
'---    RADIAL STRAIN CONTROLLED CYCLIC STRESS PATH TESTING                                    ---
'---                                                                                           ---
'-------------------------------------------------------------------------------------------------

'$INCLUDE: 'DECL.BAS'

10      'SET THE SCREEN COLOR
        SCREEN 0
        COLOR 1, 7
        CLS

20      'SET THE OUTPUT DATA FILE NAME AND WRITING THE HEADING
        LOCATE 5, 30
        INPUT "ENTER FILENAME: ", filename$

        'DAT file for raw bits data
        DIR$ = "C:\data\" + filename$ + ".DAT"
        OPEN DIR$ FOR APPEND AS #11
        WRITE #11, "Date", "Time", "Local axial strain 1", "Gain 1", "Local axial strain 2", "Gain 2",
"Radial strain", "Gain 3", "Mid-plane pwp", "Base pwp", "Cell pwp", "Loadcell", "External strain 1",
"External strain 2", "Lower chamber pwp", "LVDT1",  "LVDT2", "LVDT3", "VOLUME"
        CLOSE #11

        'OUT file for engineering reading
        DEN$ = "C:\data\" + filename$ + ".OUT"
        OPEN DEN$ FOR APPEND AS #13
        WRITE #13, "Date", "Time", "Local axial strain 1", "Local axial strain 2", "Radial strain",
"Mid-plane pwp", "Base pwp", "Cell pwp", "Loadcell", "External strain 1", "External strain 2", "Lower
chamber pwp"
        CLOSE #13

        'SUM file for summary of the cyclic testing
        DSM$ = "C:\data\" + filename$ + ".SUM"
        OPEN DSM$ FOR APPEND AS #15
        WRITE #15, "RAMP BEGAN", DATE$, TIME$
        CLOSE #15

        'Set the screen format
        GOSUB 11000 'SUB SET-UP SCREEN

        LOCATE 2, 1
        PRINT "BEGIN:", TIME$, DATE$
        LOCATE 1, 42
        PRINT "FILENAME:", filename$

30      'SET VARIABLES FOR THE 10 CHANNELS OF THE ADU

        'Set logging interval variables (in seconds)
        INTERVAL(1) = 1
        INTERVAL(2) = 3
        INTERVAL(3) = 6
        INTERVAL(4) = 20
        INTERVAL(5) = 30
        INTERVAL(6) = 60
        INTERVAL(7) = 150
        INTERVAL(8) = 300
        INTERVAL(9) = 600

        'Set gain variables for channel 1~10
        GAIN(1) = 2
        GAIN(2) = 2
```

```
GAIN(3) = 2
GAIN(4) = 8
GAIN(5) = 8
GAIN(6) = 8
GAIN(7) = 10
GAIN(8) = 8
GAIN(9) = 8
GAIN(10) = 8

'Set offset variables for channel 1~10
'0— -5V, 2048—0V, 4096— +5V
OFFSET(1) = 2048
OFFSET(2) = 2048
OFFSET(3) = 2048
OFFSET(4) = 1100
OFFSET(5) = 1100
OFFSET(6) = 4000
OFFSET(7) = 2048
OFFSET(8) = 3000
OFFSET(9) = 3000
OFFSET(10) = 3050

'Set calibration gradient for channel 1~10
CALM(1) = 1
CALM(2) = 1
CALM(3) = 1
CALM(4) = 5.215928
CALM(5) = 5.22266
CALM(6) = -5.222499
CALM(7) = -1.051102
CALM(8) = -134.536205#
CALM(9) = -135.580917#
CALM(10) = -5.21478

'Set calibration interception for channel 1~10
CALC(1) = 0
CALC(2) = 0
CALC(3) = 0
CALC(4) = 126.499755#
CALC(5) = 183.207741#
CALC(6) = 5930.169525#
CALC(7) = 2100
CALC(8) = 4017.002536#
CALC(9) = 3907.397491#
CALC(10) = 3927.1754#

 LIN = 1
 T# = 0!

40      'SET UP PARAMETERS FOR CYCLIC STRESS PATH TESTING

LIRD = 2100     'The loadcell reading at a deviator stress of 0 kPa
PV = 600        'The value of the constant total vertical stress
DFC = 12.5      'Difference between the cell pressure transducer and the GDS controller
JJJ = 1         '1—cyclic stress path testing, 0—only take reading
KKK = 1
TTT = 3

RAMPDIR = 1     '1 for compression, -1 for extension
PASSPORT = 1    'safety measures when there is a re-start of the computer
RESTCOUNT = 0           'the count of the rest period
NMC = 0         'Excursion number
RESTL = 900     'Rest period length
```

```
        LV1 = 2205      'the initial reading of LVDT1
        LV2 = 2938      'the initial reading of LVDT2
        LV3 = 2973      'the initial reading of LVDT3
        RS1 = .1565386  'the resolution of LVDT1
        RS2 = .1532632  'the resolution of LVDT2
        RS3 = .309376   'the resolution of LVDT3

        VOL0 = 86032    'the initial volume reading of the back GDS controller
        SRT = -.5       'the target radial stain

45      'SET HOT KEYS

        'F10—Stop the test
        ON KEY(10) GOSUB 8500
        KEY(10) ON

        'F1 or F2 –decrease or increase the logging interval
        ON KEY(1) GOSUB 6000 'SUB DECREASE LOGGING INTERVAL
        ON KEY(2) GOSUB 7000 'SUB INCREASE LOGGING INTERVAL
        KEY(1) ON
        KEY(2) ON

        'F5 or F6 –decrease or increase the resting period
        ON KEY(5) GOSUB 14000
        KEY(5) ON
        ON KEY(6) GOSUB 14500
        KEY(6) ON

50      ' OPEN RS323 COMMUNICATIONS WITH THE ELE ADU
        OPEN "COM1:9600,N,8,1,CS0,DS0,CD0" FOR RANDOM AS #12

60      'OPEN RS323 COMMUNICATIONS WITH THE BACK PWP GDS CONTROLLER
        'OPEN "COM2:4800,N,8,2,CD0,CS0,DS0,OP0,TB2048,RB2048" FOR RANDOM AS #14

        'SET THE BACK PWP GDS CONTROLLER PRESSURE
        BP = 520
        PRINT #14, "C" + CHR$(4) + RIGHT$(STR$(BP), (LEN(STR$(BP)) - 1)) + CHR$(255);

        FOR q = 1 TO 5000
          LOCATE 4, 1
          PRINT "Q=", q
        NEXT q

        RT = 0   'Restart times of the computer
        A = 0    'Error types detected by the trap

100     'SET A TRAP FOR ANY COMPUTER ERRORS
        ON ERROR GOTO 10000

200     'RESET ELE ADU, CLEAR MEMORY AND PREVIOUS COMMANDS

        RT = RT + 1
        IF RT = 10 OR A = 57 THEN
          CLOSE #12
          CLOSE #14
          GOTO 50
        END IF

        LOCATE 5, 1
        PRINT "RESET TIMES:", RT, TIME$, DATE$

        PRINT #12, "RESET"
```

```
        FOR q = 1 TO 100000
          LOCATE 4, 1
          PRINT "Q=", q
        NEXT q

        IF LOC(12) > 1 THEN
          LOCATE 4, 30
          PRINT "LOC(12) IS:", LOC(12)
          INPUT #12, ECO$
        ELSE
          LOCATE 21, 1
          PRINT "TIMEOUT", TIME$
          GOTO 200
        END IF

        LOCATE 1, 5
        PRINT ECO$

300     'ASK THE LOWER CAHMBER TO RAMP
        IF PASSPORT = 1 THEN
          NMC = NMC + 1
          LOCATE 20, 20
          PRINT LV1, LV2, NMC, RAMPDIR, TIME$
          GOSUB 12000
        END IF
        PASSPORT = 0

350     'TAKE THE READING FROM ADU AND KEEP THE STRESS PATH
        V1 = TIMER
        FLAG = 1!
        WHILE FLAG = 1!
           KEY(1) STOP
           KEY(2) STOP
           KEY(5) STOP
           KEY(6) STOP

500        FOR CHAN = 1 TO 10
                cmnd$ = "AD" + STR$(CHAN) + STR$(GAIN(CHAN)) + STR$(OFFSET(CHAN))
                PRINT #12, cmnd$

                FOR q = 1 TO 1600
                   LOCATE 4, 1
                   PRINT "Q=", q
                NEXT q

                IF LOC(12) > 1 THEN
                    LOCATE 4, 30
                    PRINT "LOC(12) IS:", LOC(12)
                    INPUT #12, RAD
                ELSE
                    LOCATE 21, 1
                    PRINT "TIMEOUT", TIME$
                    GOTO 200
                END IF

                READING(CHAN) = RAD

                'PRINT CHANNEL OUTPUTS (IN BITS) ON SCREEN
                LOCATE CHAN + 8, 10
                PRINT USING "########.##"; READING(CHAN)

                'PRINT CHANNEL OUTPUTS (IN ENGINEETING UNITS) ON SCREEN
                ENGR(CHAN) = (READING(CHAN) - CALC(CHAN)) / CALM(CHAN)
```

```
            LOCATE CHAN + 8, 50
            PRINT USING "########.###"; ENGR(CHAN)
            LOCATE CHAN + 8, 1
            PRINT GAIN(CHAN)

        NEXT CHAN


550     'TAKE ADDITIONAL READING OF LVDT 1~3 AT GAIN=1
        FOR CHAN = 1 TO 3
            cmnd$ = "AD" + STR$(CHAN) + STR$(1) + STR$(OFFSET(CHAN))
            PRINT #12, cmnd$

            FOR q = 1 TO 1600
              LOCATE 4, 1
              PRINT "Q=", q
              NEXT q

              IF LOC(12) > 1 THEN
                LOCATE 4, 30
                PRINT "LOC(12) IS:", LOC(12)
                INPUT #12, RAD
              ELSE
                LOCATE 21, 1
                PRINT "TIMEOUT", TIME$
                GOTO 200
              END IF

              DDD(CHAN) = RAD

             'PRINT CHANNEL OUTPUTS (IN BITS) ON SCREEN
              LOCATE 19, CHAN * 15
              PRINT USING "########.##"; DDD(CHAN)

        NEXT CHAN


600     'JUDGE AND CORRECT THE ADU ERRORS
        PRINT #12, "ERROR"
        FOR q = 1 TO 2000
            LOCATE 4, 1
            PRINT "Q=", q
        NEXT q

        IF LOC(12) > 1 THEN
            LOCATE 4, 30
            PRINT "LOC(12) IS:", LOC(12)
            INPUT #12, ER$
        ELSE
             LOCATE 21, 1
             PRINT "TIMEOUT", TIME$
             GOTO 200
        END IF

        IF ER$ <> "O.K." THEN
            LOCATE 20, 1
            PRINT "ERROR WAS: ", ER$, TIME$
            GOTO 200        'RESET THE ADU
        END IF

700     'TAKE THE READING FROM THE BACK GDS CONTROLLER
        PRINT #14, "C" + CHR$(22) + CHR$(255);
```

```
            FOR q = 1 TO 2000
            NEXT q

        PRINT #14, "R";

            FOR q = 1 TO 3000
            NEXT q

        'JUDGE THE TIMEOUT
        IF LOC(14) > 10 THEN
            LOCATE 4, 30
            PRINT "LOC(14) IS:", LOC(14)
            INPUT #14, Z$
            LOCATE 1, 1
            PRINT Z$
        ELSE
            LOCATE 21, 1
            PRINT "TIMEOUT", TIME$
            GOTO 350
        END IF

        pressure = VAL(MID$(Z$, 2, 4))
        VOLUME = VAL(MID$(Z$, 6, 6))
        status = ASC(Z$)
        IF (status AND 1) THEN pressure = -pressure
        IF (status AND 16) THEN VOLUME = -VOLUME
        LOCATE 19, 50
        PRINT VOLUME, "mm3"

800     'MAIN SUBROUTIN TO KEEP THE STRESS PATH
        IF JJJ = 1 THEN
          GOSUB 12500
        END IF

900     'RECORDING THE DATA AT SPECIFIED INTERVAL
        LOCATE 2, 42
        PRINT "LOGGING RATE:", INTERVAL(LIN)

        V2 = TIMER
        IF V2 < (INTERVAL(LIN) + 1) THEN
           V1 = 0
        END IF

        IF V2 > (V1 + INTERVAL(LIN)) THEN
          OPEN DIR$ FOR APPEND AS #11
          WRITE #11, DATE$, TIME$, READING(1), GAIN(1), READING(2), GAIN(2),
READING(3), GAIN(3), READING(4), READING(5), READING(6), READING(7), READING(8),
READING(9), READING(10), DDD(1), DDD(2), DDD(3), VOLUME
          CLOSE #11

          OPEN DEN$ FOR APPEND AS #13
          WRITE #13, DATE$, TIME$, INT(ENGR(1)), INT(ENGR(2)), INT(10 * ENGR(3)) / 10,
INT(10 * ENGR(4)) / 10, INT(10 * ENGR(5)) / 10, INT(10 * ENGR(6)) / 10, INT(100 * ENGR(7)) /
100, INT(1000 * ENGR(8)) / 1000, INT(1000 * ENGR(9)) / 1000, INT( _
10 * ENGR(10)) / 10
          CLOSE #13

          T# = T# + 1!
          LOCATE 3, 42
          PRINT "TOTAL LINES:", T#

          V1 = V1 + INTERVAL(LIN)
        END IF
```

```
        LOCATE 3, 1
        PRINT "NOW  :", TIME$, DATE$

        KEY(1) ON
        KEY(2) ON
        KEY(5) ON
        KEY(6) ON

      WEND

      END

6000  'SUB DECREASE LOGGING INTERVAL

      IF LIN > 1 THEN
            LIN = LIN - 1
      ELSE
            LIN = 1
      END IF
      RETURN

7000  'SUB INCREASE LOGGING INTERVAL

      IF LIN < 9 THEN
            LIN = LIN + 1
      ELSE
            LIN = 9
      END IF
      RETURN

8500  'SUB CHECK ENDPROGRAM
      IF LIN = 3 THEN
        GOSUB 9000
      END IF
      RETURN

9000  'ENDPROGRAM
      CLOSE #12
      CLOSE #14
      END

10000 'DETECT THE ERROR TYPE
       A = ERR
       B = ERL
       LOCATE 22, 1
       PRINT "DEVICE FOUND: ", A, B, TIME$
       RESUME 100

11000 'SET-UP LOGGING SCREEN
      'BITS READING ON THE LEFT & ENGINEETING READING ON THE RIGHT
      CLS
      LOCATE 8, 29
      PRINT "INSTRUMENT"
      LOCATE 10, 29
      PRINT "Axial LVDT-1"
      LOCATE 11, 29
      PRINT "Axial LVDT-2"
      LOCATE 12, 29
      PRINT "Radial LVDT"
      LOCATE 13, 29
      PRINT "Mid Pore Pressure"
      LOCATE 14, 29
```

```
PRINT "Base Pore Pressure"
LOCATE 15, 29
PRINT "Cell Pressure"
LOCATE 16, 29
PRINT "Loadcell"
LOCATE 17, 29
PRINT "Global strain-1"
LOCATE 18, 29
PRINT "Global strain-2"
LOCATE 19, 29
PRINT "Lower Chamber Pressure"

LOCATE 8, 70
PRINT "UNITS"
LOCATE 10, 70
PRINT "Bits"
LOCATE 11, 70
PRINT "Bits"
LOCATE 12, 70
PRINT "Bits"
LOCATE 13, 70
PRINT "kPa"
LOCATE 14, 70
PRINT "kPa"
LOCATE 15, 70
PRINT "kPa"
LOCATE 16, 70
PRINT "N"
LOCATE 17, 70
PRINT "mm"
LOCATE 18, 70
PRINT "mm"
LOCATE 19, 70
PRINT "kPa"

LOCATE 8, 1
PRINT "GAIN"

LOCATE 8, 10
PRINT "READING(BITS)"

LOCATE 8, 50
PRINT "ENGINEERING"

LOCATE 24, 1
PRINT "F1-DECREASE, F2-INCREASE, F10-STOP "

RETURN

12000   'SUBROTUIN TO RAMP THE LOWER CHAMBER

'SET HIGH PRESCION FOR CELL AND LOWER CLAMBER CONTROLLERS
Cmd$ = CHR$(28) + CHR$(255)

CALL Send(0, 3, Cmd$, DABend)
FOR q = 0 TO 10000
NEXT q

CALL Send(0, 5, Cmd$, DABend)
FOR q = 0 TO 10000
NEXT q

'RAMP THE LOWER CHAMBBER, RAMPDIR=1—UPWARDS, -1—DOWNWARDS
```

```
        IF RAMPDIR = 1 THEN
          md1$ = CHR$(1) + "175" + CHR$(255)
          md2$ = CHR$(11) + "32000" + CHR$(255)
          md3$ = CHR$(5) + "0" + CHR$(255)
          md4$ = CHR$(39) + CHR$(255)
        ELSE
          md1$ = CHR$(1) + "175" + CHR$(255)
          md2$ = CHR$(3) + "0" + CHR$(255)
          md3$ = CHR$(5) + "32000" + CHR$(255)
          md4$ = CHR$(7) + CHR$(255)
        END IF

        CALL Send(0, 5, md1$, nullend)
        FOR q = 0 TO 1000
        NEXT q

        CALL Send(0, 5, md2$, nullend)
        FOR q = 0 TO 1000
        NEXT q

        CALL Send(0, 5, md3$, nullend)
        FOR q = 0 TO 1000
        NEXT q

        CALL Send(0, 5, md4$, nullend)

        RETURN

12500   'SUBROUTION TO KEEP THE STRESS PATH OR HOLD THE TARGET STRAIN
        'PRC—CELL PRESSURE; PRL—DEVIATOR STRESS
        'STRN—LOCAL AXIAL STRAIN; STRR—LOCAL RADIAL STRAIN
        data$ = SPACE$(20)

        PRC = ENGR(6)

        PRL = 1000 * (READING(7) - LIRD) / CALM(7) / (3.1415927# * 2500)

        STRN1 = (READING(1) - LV1) * RS1 / 70
        STRN2 = (READING(2) - LV2) * RS2 / 70
        STRN = (STRN1 + STRN2) / 2

        STRV = 1000 * (VOLUME - VOL0) / (3.1415927# * 50 * 50 * 200)

        STRR = (READING(3) - LV3) * RS3 / 200

        LOCATE 21, 10
        PRINT STRN, STRV, STRR
        LOCATE 22, 1
        PRINT PRC + PRL, PRL

        'ADJUST LOGGING RATE AND JUDGE THE TARGET STRAIN AUTOMATICALLY
        IF KKK = 1 THEN

           IF RAMPDIR = 1 AND STRR > -.05 THEN LIN = 2
           IF RAMPDIR = 1 AND STRR < -.05 THEN LIN = 3
           IF RAMPDIR = -1 AND (STRR - SRT) < .1 THEN LIN = 2
           IF RAMPDIR = -1 AND (STRR - SRT) > .1 THEN LIN = 3

           IF (RAMPDIR = 1 AND STRR < SRT) OR (RAMPDIR = -1 AND STRR > 0) THEN
              KKK = 0
              LOCATE 22, 35
              PRINT TIME$
```

```
            LIN = 2

            PRLT = PRL
            PRCT = PV - PRLT
            LOCATE 22, 55
            PRINT PRLT

            OPEN DSM$ FOR APPEND AS #15
            WRITE #15, "RAMP OVER", DATE$, TIME$, NMC, READING(1), READING(2),
ENGR(4), PRLT
            CLOSE #15

            Cmd$ = CHR$(0) + CHR$(255)
            CALL Send(0, 5, Cmd$, DABend)
            FOR q = 1 TO 5000
            NEXT q

          END IF
        END IF

        'KEEP THE STRESS PATH WITH A CONSTANT TOTAL VERTICAL STRESS
        IF KKK = 1 THEN

          GAPE = PRC + PRL - PV
          LOCATE 22, 35
          PRINT PRC + PRL

          IF ABS(GAPE) >= 2! THEN
             SS = INT(2 * (PV - PRL + DFC))
             md$ = CHR$(4) + STR$(SS) + CHR$(255)
             CALL Send(0, 3, md$, DABend)
          ELSE
             IF GAPE > 0! THEN VV = 72
            IF GAPE <= 0! THEN VV = 8

            IF ABS(GAPE) > .5 THEN mdv$ = CHR$(VV) + "60" + CHR$(255)
            IF ABS(GAPE) > .25 AND ABS(GAPE) <= .5 THEN mdv$ = CHR$(VV) + "30" +
CHR$(255)
            IF ABS(GAPE) > .15 AND ABS(GAPE) <= .25 THEN mdv$ = CHR$(VV) + "15" +
CHR$(255)
            IF ABS(GAPE) > .05 AND ABS(GAPE) <= .15 THEN mdv$ = CHR$(VV) + "5" +
CHR$(255)
            IF ABS(GAPE) <= .05 THEN mdv$ = CHR$(VV) + "1" + CHR$(255)

            GOSUB 12800

          END IF

          LOCATE 22, 50
          PRINT VV

        END IF

        'HOLD THE TARGET STRAIN DURING THE REST PERIOD
        IF KKK = 0 THEN

           PRCT = PV - PRL

           RESTCOUNT = RESTCOUNT + 1
           LOCATE 20, 50
           PRINT RESTCOUNT, RESTL

           'ADJUST THE LOGGING RATE AUTOMATICALLY
```

```
IF RESTCOUNT = 15 THEN
   LIN = 3
END IF

IF RESTCOUNT = 90 THEN
   LIN = 5
END IF

IF RESTCOUNT = RESTL - 40 THEN
   LIN = 2
END IF

'CHANGE THE MODULAR AT THE END OF REST PERIOD
IF RESTCOUNT > RESTL THEN
  KKK = 1
  RAMPDIR = RAMPDIR * (-1)
  RESTCOUNT = 0
  PASSPORT = 1
  LIN = 3

  OPEN DSM$ FOR APPEND AS #15
  WRITE #15, "RAMP BEGIN", DATE$, TIME$, RAMPDIR, LV1, LV2, ENGR(4), PRL
  CLOSE #15

  GOTO 300
END IF



'ADJUST THE CELL PWP TO KEEP THE TOTAL VERTICAL STRESS CONSTANT
IF TTT = 3 THEN

   IF ABS(PRC - PRCT) > .1 AND ABS(PRC - PRCT) < 3! THEN

      IF (PRC - PRCT) >= .3 THEN mdv$ = CHR$(72) + "15" + CHR$(255)
      IF (PRC - PRCT) > .1 AND (PRC - PRCT) < .3 THEN mdv$ = CHR$(72) + "3" +
CHR$(255)
      IF (PRC - PRCT) > -.3 AND (PRC - PRCT) < -.1 THEN mdv$ = CHR$(8) + "3" +
CHR$(255)
      IF (PRC - PRCT) <= -.3 THEN mdv$ = CHR$(8) + "15" + CHR$(255)

      GOSUB 12800
   END IF

   IF ABS(PRC - PRCT) >= 3! THEN
     SS = INT(2 * (PV - PRL + DFC))
     md$ = CHR$(4) + STR$(SS) + CHR$(255)
     CALL Send(0, 3, md$, DABend)
   END IF

   LOCATE 21, 1
   PRINT TTT
   TTT = 5
END IF

'KEEP THE TARGET RADIAL STRAIN
IF TTT = 5 THEN

   IF (RAMPDIR = 1 AND ABS(STRR - SRT) > .01) OR (RAMPDIR = -1 AND
ABS(STRR) > .01) THEN

      IF RAMPDIR = 1 THEN
```

```
            IF (STRR - SRT) < -.01 THEN mdv$ = CHR$(72) + "1" + CHR$(255)
            IF (STRR - SRT) > .01 THEN mdv$ = CHR$(8) + "1" + CHR$(255)
          END IF
          IF RAMPDIR = -1 THEN
            IF STRR > .01 THEN mdv$ = CHR$(8) + "1" + CHR$(255)
            IF STRR < -.01 THEN mdv$ = CHR$(72) + "1" + CHR$(255)
          END IF

          GOSUB 12900
        END IF

        LOCATE 21, 1
        PRINT TTT
        TTT = 3
      END IF

    END IF

    RETURN

12800 'SUBROUTINE TO USE VOLUMN CONTROL FOR CELL PRESSURE CONTROLLER

    Cmd$ = CHR$(24) + CHR$(255)
    CALL Send(0, 3, Cmd$, DABend)

    FOR q = 1 TO 20000
    NEXT q

    'mdv$ = CHR$(VV) + STR$(VM) + CHR$(255)
    CALL Send(0, 3, mdv$, DABend)

    FOR q = 1 TO 1000
    NEXT q

    RETURN

12900 'SUBROUTINE TO USE VOLUMN CONTROL FOR LOWER CHAMBER CONTROLLER

    Cmd$ = CHR$(24) + CHR$(255)
    CALL Send(0, 5, Cmd$, DABend)

    FOR q = 1 TO 20000
    NEXT q

    CALL Send(0, 5, mdv$, DABend)

    FOR q = 1 TO 1000
    NEXT q

    RETURN

14000 'REDUCE THE REST PERIOD LENGTH
    IF RESTL > 600 THEN
      RESTL = RESTL - 600
    END IF
    RETURN

14500 'INCREASE THE REST PERIOD LENGTH
    RESTL = RESTL + 600
    RETURN
```

Appendix B

Simplified method for embedded integral abutment design

A simplified method is proposed to estimate the horizontal stress change behind embedded integral abutments for the purpose of preliminary approximation. The following assumptions are adopted:

1) The E_{ulr}/p_o'~ε_h curve, which is derived from stress path testing on a representative soil element at mid retained height, is assumed to adequately represent the stiffness-strain behaviour of the soil at all depths behind the abutment.

2) The horizontal strain change $\Delta\varepsilon_h$ induced in the soil behind a smooth rigid abutment can usefully be idealised as uniform, with its magnitude equal to d/h (Bolton and Powrie, 1988). In this case, d is the temperature-induced abutment top displacement and $d=\Delta T\cdot\alpha\cdot L/2$, where ΔT is the effective bridge temperature change, α is the deck temperature coefficient, and L is the bridge deck length. h is the length from the pivot to the wall crest and it can be assumed that $h=0.95\cdot H$ (H is the whole length of the abutment). Therefore, the horizontal strain can be expressed as

$$\Delta\varepsilon_h = (\frac{\Delta T\cdot\alpha}{1.9})\cdot\frac{L}{H} \qquad \text{(equation B.1)}$$

3) The effective earth pressure coefficient K is assumed to be unity before cyclic loading, to take account of the effects of wall installation (Clayton and Milititsky, 1983). Further reduction due to the excavation in front of the abutment is ignored, since its magnitude depends on the detailed construction sequence and technique, and such a simplification leads to a conservative but safe estimation of K.

Therefore, for a given geometry of an embedded abutment and a certain temperature change, the horizontal stress change behind the abutment can be estimated using the following the steps:

1) the horizontal strain change $\Delta\varepsilon_h$ behind the abutment can be estimated first, using equation B.1.
2) Then for a soil at a specified depth, the magnitude of E_{ulr}/p_o' at that horizontal strain level can be determined from the E_{ulr}/p_o'~ε_h curve. The value of p_o' can also be derived at this depth.
3) Finally, the horizontal stress change $\Delta\sigma_h$ can be estimated as:

$$\Delta\sigma_h = 2 \cdot \Delta\varepsilon_h \cdot E_{uh} = 2 \cdot \Delta\varepsilon_h \cdot \left(\frac{E_{uh}}{p_o'} \right) \cdot p_o' \qquad \text{(equation B.2)}$$

By combining the conservative assumption K=1, an ultimate horizontal earth pressure distribution behind embedded abutments can be established for the purpose of a preliminary design estimate.

Example

The embedded integral abutment shown in Figure 1.3a is used here as an example. It has a retained height of 8m and a total length of 20m, at the end of a 60m concrete deck. It is assumed to be embedded in overconsolidated stiff clay, and for simplicity, no ground water is present. The bulk unit weight of the soil is assumed to be 20kNm^3.

For an extreme annual effective bridge temperature change ΔT =43°C, the abutment top displacement d=16mm, which leads to a horizontal strain change in the soil behind the abutment of $\Delta\varepsilon_h \approx 0.08\%$ (equation B.1).

The $E_{uh}/p_o' \sim \varepsilon_h$ curve from the stress path testing on Atherfield I Clay in this research is used here (Figure B.1a). For $\Delta\varepsilon_h$ =0.08%, E_{uh}/p_o'=300.

Therefore the horizontal earth pressure change $\Delta\sigma_h$ can be calculated using equation B.2:

$$\Delta\sigma_h = 2 \cdot \Delta\varepsilon_h \cdot \left(\frac{E_{uh}}{p_o'} \right) \cdot p_o' = 2 \times 0.08\% \times 300 \times p_o' = 0.48 p_o' (kPa)$$

For soil at 4m depth, p_o'=80kPa, $\Delta\sigma_h$= 38.4kPa. For soil at 8m depth, p_o'=160kPa, $\Delta\sigma_h$ = 76.8kPa. Thus the profile of the horizontal stress change can be drawn. Compared with the initial mean effective stress, the deviator stress change is moderate and well below the failure envelope, as defined in Figure 5.24.

The extreme situation can be obtained by overlapping the horizontal stress change with the initial pressure distribution (K=1), as shown in Figure B.1b.

This simplified method will lead to a preliminary estimate of the horizontal stress change and distribution with the depth behind an embedded integral abutment. A further more refined pressure distribution needs to take account of soil-structure interaction and full numerical modelling is necessary, using a suitable soil model capable of simulating the non-linearity of small strain stiffness behaviour obtained from stress path testing with small-strain measurement.

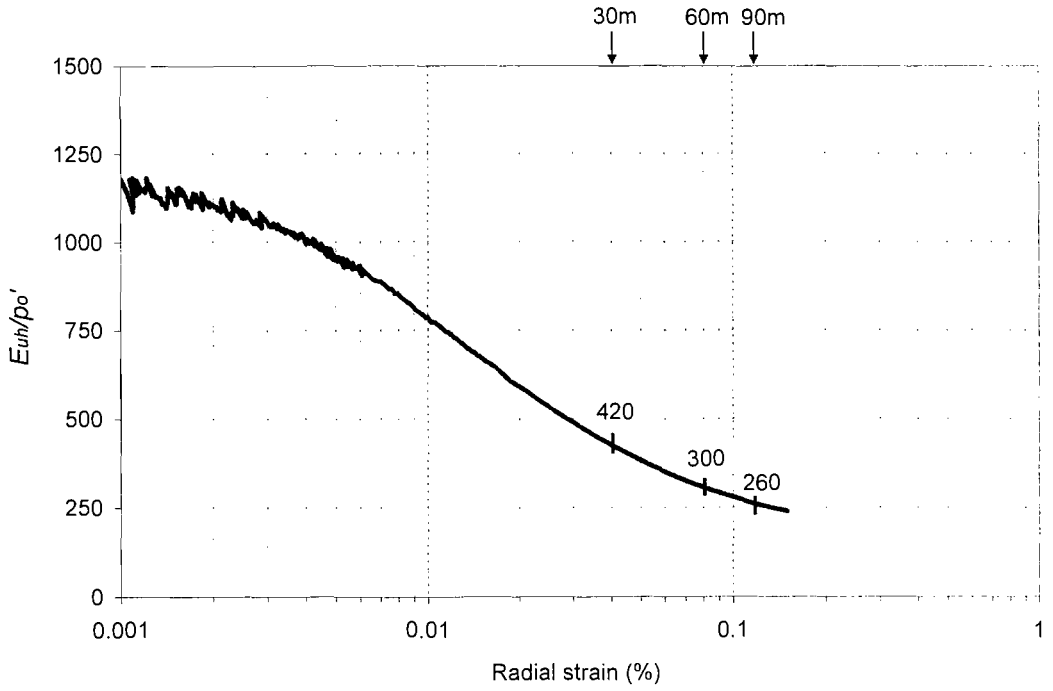

(a) The E_{uh}/p_o'~ε_h curve

(By assuming abutment length H=20m and ΔT=43°C, the concrete deck length is marked on the top at corresponding horizontal strain level)

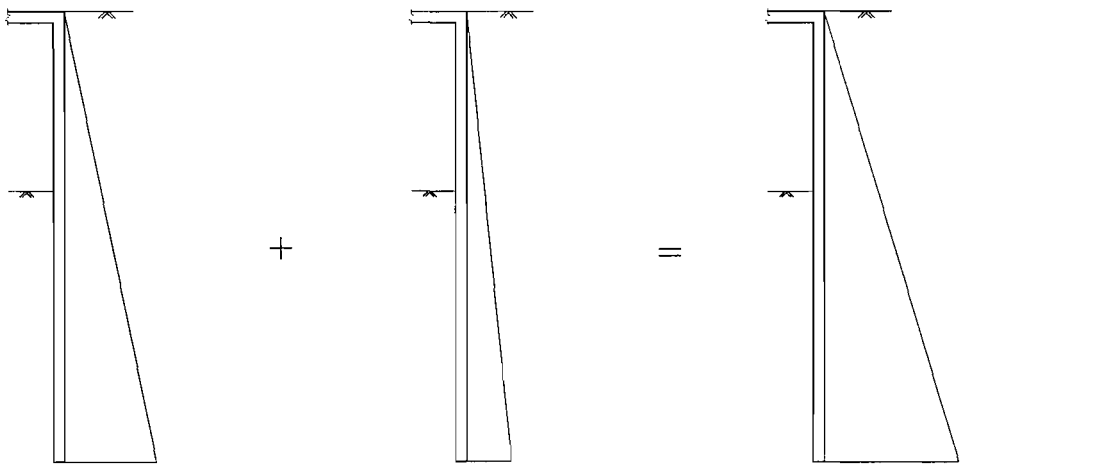

(b) Derivation of the ultimate horizontal earth pressure

Figure B.1 Simplified method to estimate the horizontal earth pressure behind an embedded integral abutment